PhD Academic Event
Graduate School of AE

TU Delft

28th of February 2020


33
olonomical Design of Novel
Composite Wing Structures

CONTENT

PREFACE

On Friday, the 28th of February 2020, the annual PhD academic event was held. This event was organized by the PhD Board of the Faculty of Aerospace Engineering in cooperation with the Graduate School of AE. This year the event took place at the Science Centre Delft in the Mekelzalen. The goal of the event was to promote interdisciplinary discussions and cooperation within the different aerospace departments.

A total of 132 PhD candidates participated in the event. It was possible for the PhD candidates to participate in a poster presentation (120 people), a pitch competition (10 people), or to do a demonstration of their research (2 people). During the two poster presentation rounds, all PhD candidates could vote for their top 3 best posters. This resulted in a first prize for Dora Klindzic, a second prize for Gijs de Rooij, and a third prize for Agnes Broer. This year the pitch competition was serious business! In only 2 minutes the PhD candidates had to let their message come across. The professional jury, consisting of dr. ir. Corine Meuleman, from the valorisation centre, dr. Tine Tomažič, head of R&D at Pipistrel, prof. dr. Henri Werij, dean of our faculty, and Nancy van Veen, secretary of the graduate school. After carefully evaluating the pitches with respect to their presentation style, slide quality and clarity of the story, three winners were chosen: the first prize went to Dirk Van Baelen, the second prize went to Sihao Sun, and the third prize to Reynard de Vries. Last but not least, the best demonstration awards went to Bruce LeBlanc and Diana Olejnik. Additionally, the keynote speaker dr. Tine Tomažič offered all prize winners a flight in an electric aircraft!

The last poster presentation session was followed by a fantastic keynote from dr. Tine Tomažič. During the reception after the keynote, beer was flowing richly and delicious snacks could be consumed.

All in all, it was a successful event! Thanks to everybody for their participation.

Kind regards,

PhD council of Aerospace Engineering

ABOUT THE GRADUATE SCHOOL OF AEROSPACE ENGINEERING

The Faculty of Aerospace Engineering counts more than 200 academic members of staff and approximately 250 post doctoral researchers and PhD candidates. The faculty is active in almost all areas of aerospace sciences and technologies, such as the development of future aircraft and spacecraft concepts, and also performs research in wind energy and other energy technologies. The state-of-the-art aerospace engineering laboratories include unique facilities that are also used in many international collaborative projects.

The prevalent PhD research culture at TU Delft is that of independence and motivation, critical thought and academic rigour. Doctoral students are given the freedom to determine their own learning programme and encouraged to develop independence in experimentation and research under supervision. The Graduate School of Aerospace Engineering fosters interdisciplinary exchange and collaboration and supports PhD candidates in their scientific research and personal development through a customized Doctoral Education Programme and other activities.

THE PhD COUNCIL

The annual PhD scientific event is organized by the PhD Council of the Faculty of Aerospace Engineering in cooperation with the Graduate School of AE. The main goal of the PhD Council is to act as a sounding board for all the PhD candidates in the faculty. In cooperation with the Graduate School of AE, they organise different social and scientific events, help improve communication and implement developments within the Faculty Graduate School. These are the members of the PhD Board of Aerospace Engineering representing their own department and section:

- Gourav Mahapatra, section AS
- Reynard de Vries, section FPP
- Bram Jongbloed (chair), section AMT
- Colin Van Dercreek, section ANCE
- Mario Coppola, section C&S
- Marta Gavioli, section ASCM
- Luis Laguarda Sanchez, section Aero

The members of the PhD Board can be contacted via PhD-Board-AE@tudelft.nl


KANTOOR 1

KEYNOTE SPEAKER

DR. TINE TOMAŽIČ | HEAD OF R&D AT PIPISTREL

A very inspiring keynote was given by dr. Tine Tomažič, who is the director of research & development at Pipistrel. Pipistrel is a Slovenian general-aviation and sailplane manufacturer, and is currently the only company in the world with a commercially available, EASA-certified electric aircraft. The company is involved in European research projects on hybrid-electric propulsion together with TU Delft, and is currently developing a hybrid-electric two-seater aircraft. In the keynote, Tine gave an overview of the history of electric-aircraft developments, explaining how this technology can both decrease the emissions and increase the revenue of general-aviation aircraft. Nevertheless, only a limited amount of electric aircraft have flow up to date, due to the technological, infrastructural, and certification challenges involved. Throughout the talk, Tine shared his personal experience within Pipistrel, showing how they started the development of their first electric aircraft in the NASA Green Flight Challenge in 2011. Finally, the keynote ended with an important message: the development and certification of new technologies such as electric propulsion can only be achieved by working together.

MEET THE JURY

DR. TINE TOMAŽIČ
Head of R&D at Pipistrel

DR. IR. CORINE MEULEMAN
Valorization Centre

NANCY VAN VEEN
Secretary of the Graduate School of AE

PROF. DR. HENRI WERIJ
Dean of the Faculty of Aerospace Engineering

CATEGORIES OF THE EVENT

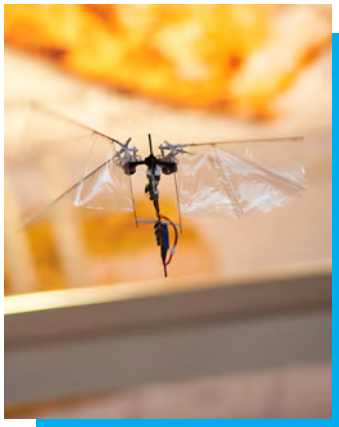

DEMONSTRATIONS

A demonstration of the research with a small, supporting explanation.

Page 20.

ELEVATOR PITCHES

A pitch of the research with a supporting slide.

Page 24.

POSTERS

A scientific poster illustrating the research conducted.

Page 38.


81
Can spot welded joints be safer than continuous welded joints?
Motivation
Initiation
Fatigue damage growth
A spot as a joint
Multi-spot is multi-joint
TUDelft

THE WINNERS

BEST PITCH

1.

DIRK VAN BAELEN

2.

SIHAO SUN

3.

REYNARD DE VRIES

BEST POSTER

1.

DORA KLINDZIC

2.

GIJS DE ROOIJ

3.

AGNES BROER

BEST DEMONSTRATIONS

DIANA OLEJNIK

BRUCE LEBLANC


TUDelft
TUDelft
TUDelft

DEMONSTRATIONS

DIANA OLEJNIK

TO BE AS NIMBLE AS A BEE

The end goal of this 4-year project, launched in 2017, is to develop a tail-less flapping wing robot with good wind-gust-rejection capabilities. At MAVLab, TU Delft, we are focusing on the design of bio-inspired wing-actuation mechanisms as well as on bio-inspired control algorithms. Our collaborators at the Experimental Zoology group at Wageningen UR use high-speed cameras to study the response of bumblebees and blowflies to various types wind gusts. This will provice new insights into the interplay between the sensory systems and the control architecture used in gust mitigation, which will be validated with the developed flapping wing robot carrying comparable sensors.

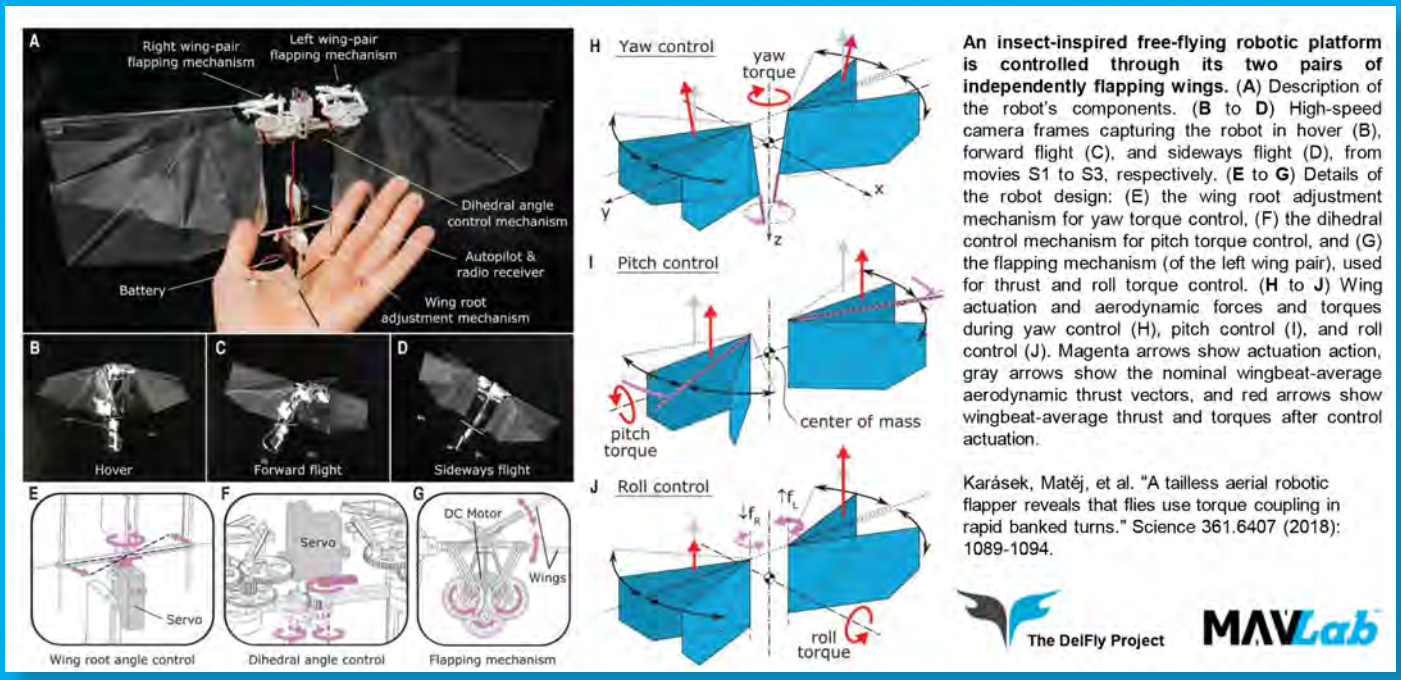

Thrust Control and Design with IPC VAWT

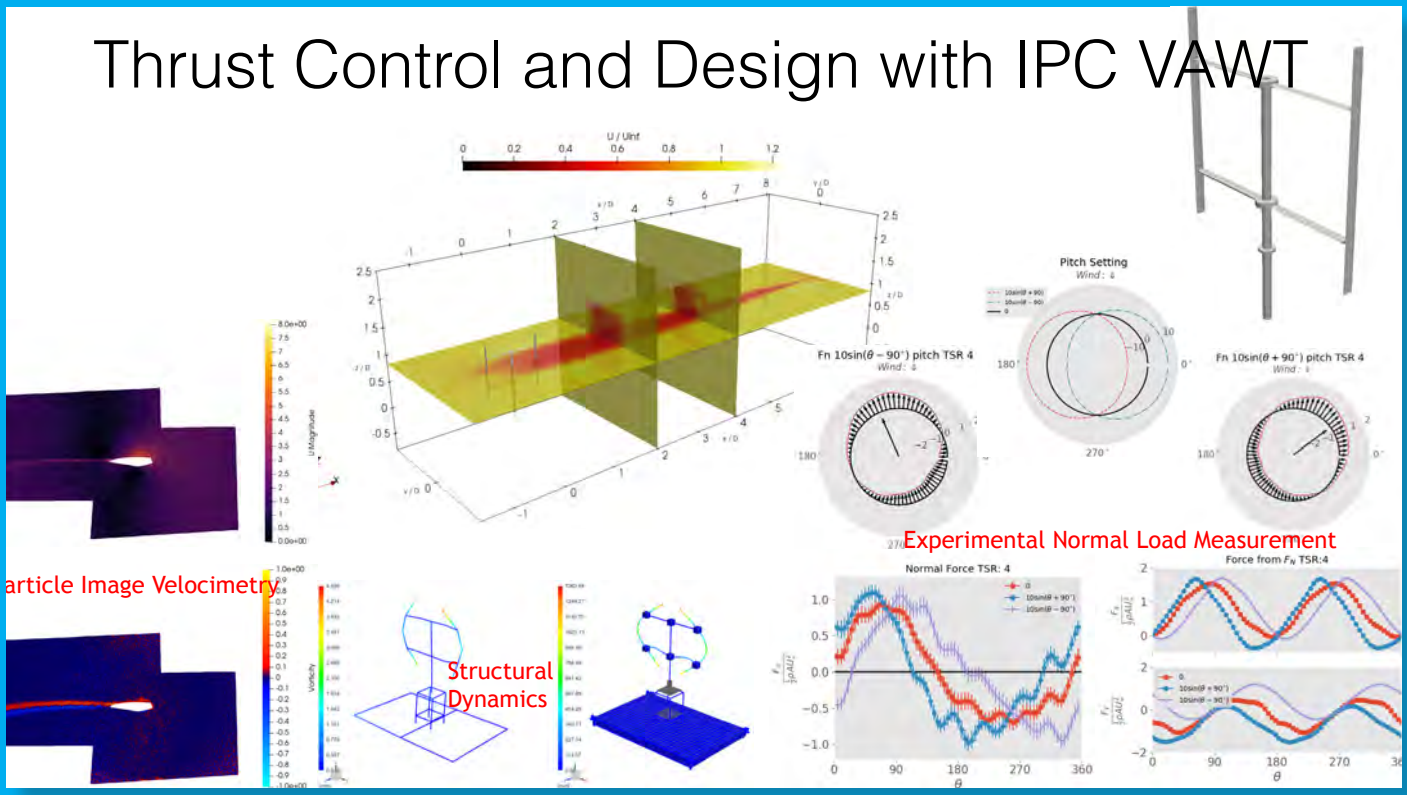

ELEVATOR PITCHES


TU Delft
SENNHEISER

DEPARTMENTS

Department of Control and Operations
Department of Aerodynamics , Wind Energy, Flight Performance and Propulsion
Department of Aerospace Structures and Materials

PHD PRESENTERS

Dirk van Baelen
Marie Bieber
Sven Pfeiffer
Jelmer Reitsma
Sihao Sun
Sagar Adatrao
Nando van Arnhem
Pieter-Jan Proesmans
Martijn Roelofs
Reynard de Vries
Luc Kootte

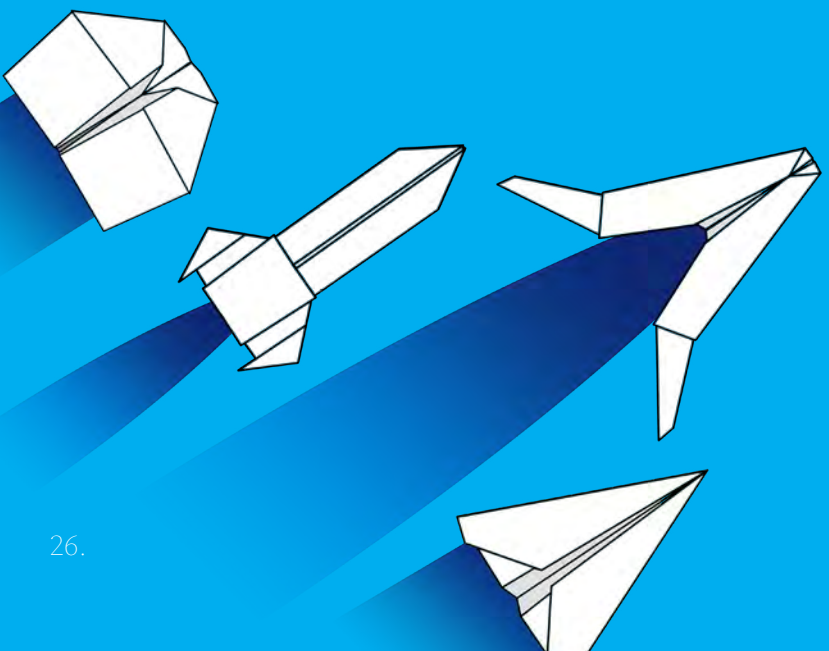

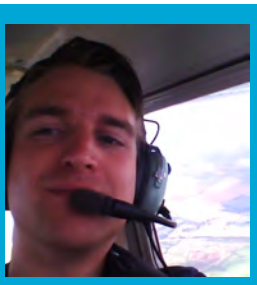

Dirk Van Baelen
Control & Operations
Control & Simulation
Joost Ellerbroek
René van Paassen
David Abbink
Max Mulder

d.vanbaelen@tudelft.nl

TU Delft

Haptic feedback for Flight Envelope Protection

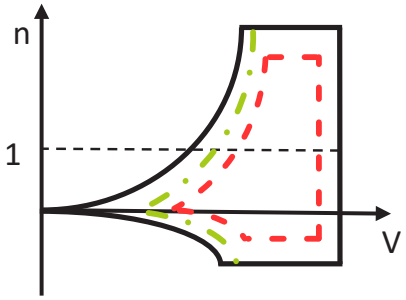

In an emergency, pilots need to operate the aircraft near the limits.

Haptic feedback through the side stick can give intuitive feedback.

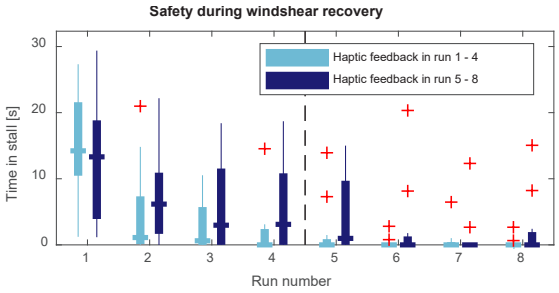

With haptic feedback, participants learn faster to stay out of stall.

Marie Bieber
Control & Operations
Air Transport Operations
Bruno Santos
Jacco Hoekstra
M.T.Bieber@tudelft.nl

TU Delft

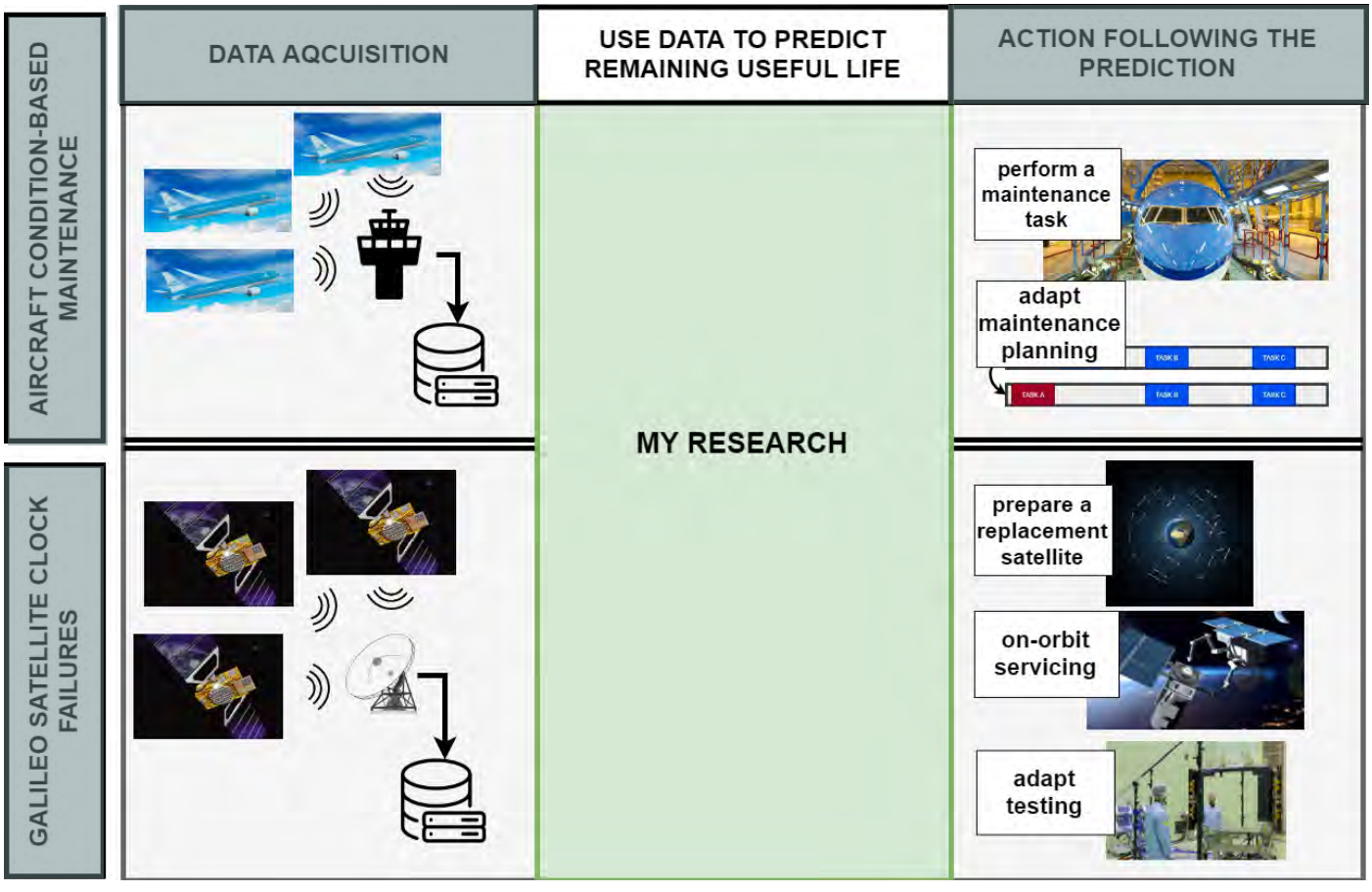

Indoor Localization for Drones with UWB

1. Emerging indoor applications for drones

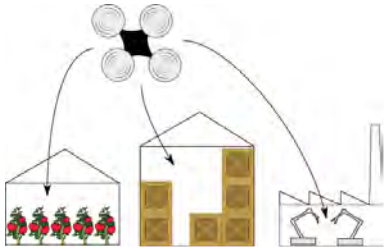

Greenhouses Warehouses Inspection

2. Problem: We can't use GPS for localization

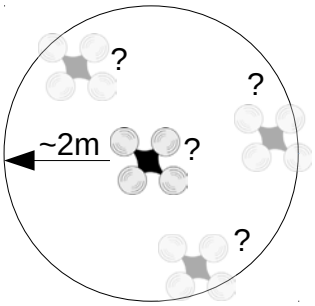

GPS: Low accuracy and bad reception in buildings

3. Solution: Multilateration with Ultra-Wideband

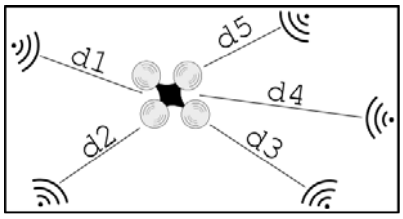

4. Challenges: Improve accuracy & decrease # of Beacons

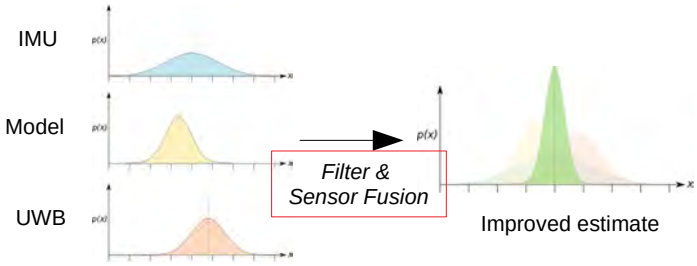

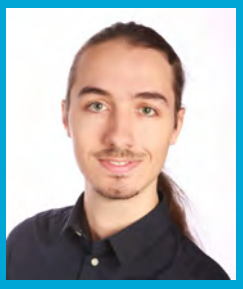

Sven Pfeiffer
Control & Operation
Control & Simulation
C. De Wagter
G.C.H.E De Croon
s.u.pfeiffer@tudelft.nl

TU Delft

Jelmer Reitsma
Control & Operations
Control & Simulation
Flight Deck Engineering
Human Factors
Daily supervisors:
René van Paassen
Clark Borst
Promotor:
Prof. dr. ir. Max Mulder
Email:
J.P.Reitsma@tudelft.nl

TU Delft

Supporting Operational Alerting on Modern Commercial Flight Decks

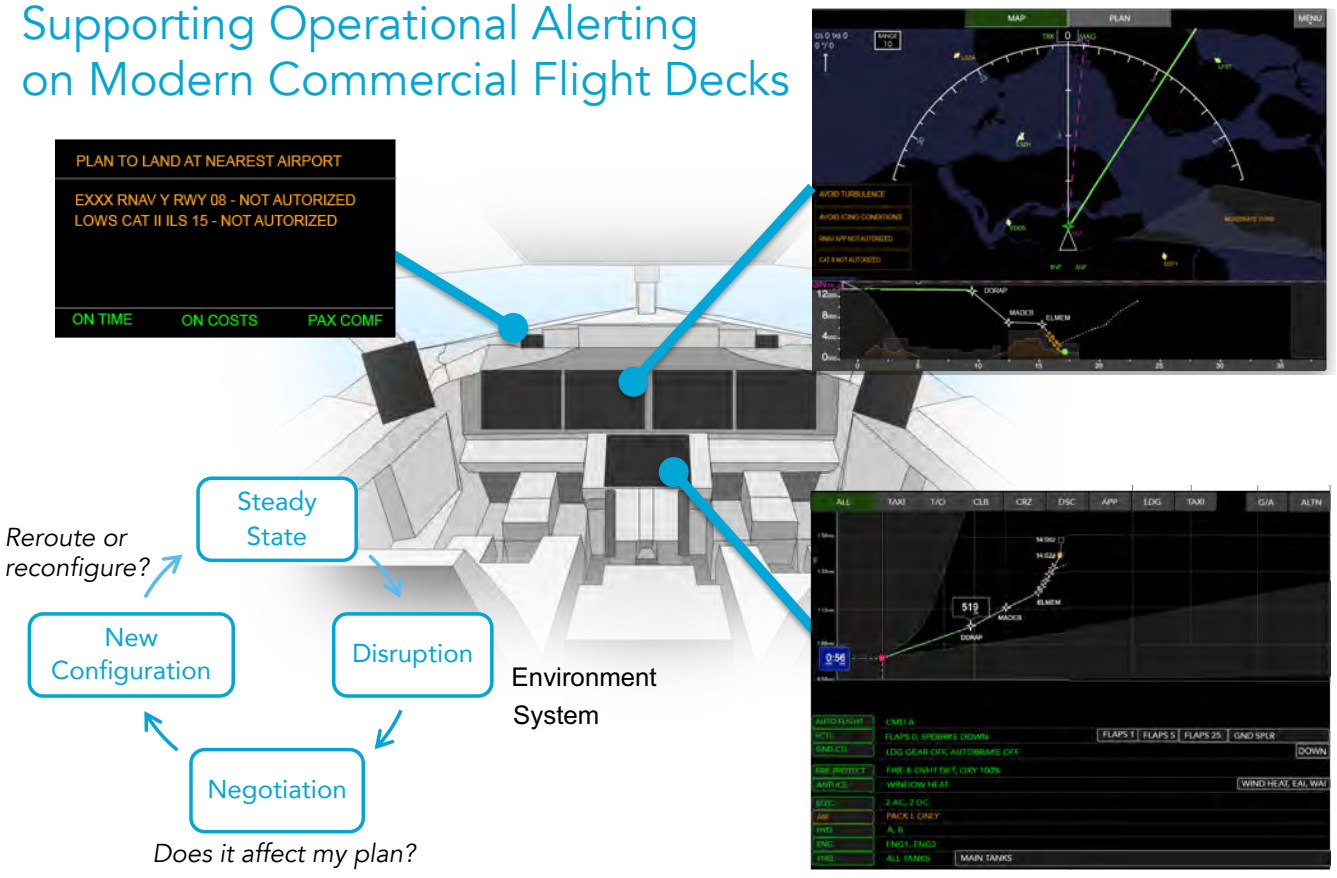

Quadrotor Fault-Tolerant Flight Control

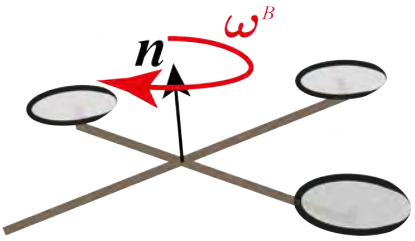

Problem

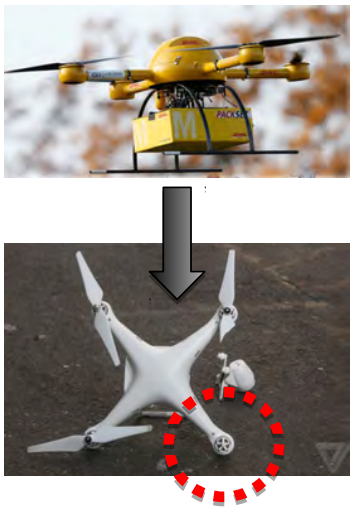

In-flight Rotor Failure

Solution

Fault Tolerant Flight Control

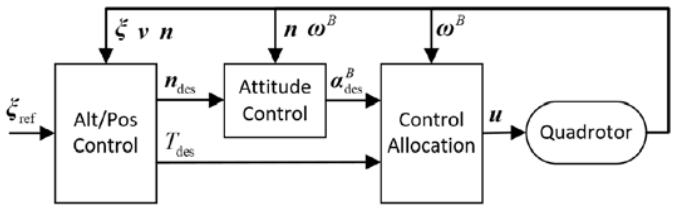

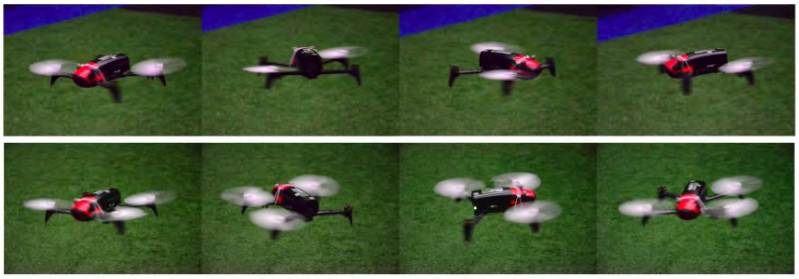

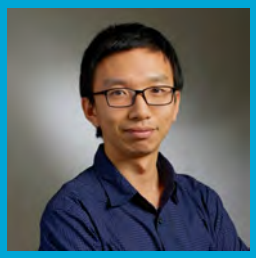

Sihao Sun
Control and Operations
Control and Simulations
Dr.ir. Coen de Visser
Dr.ir. Guido de Croon
s.sun-4@tudelft.nl

TU Delft

Name:
Sagar Adatrao
Department:
AWEP
Section:
Aerodynamics
Daily supervisor:
Dr. Andrea Sciacchitano
Promotor:
Prof. Dr. Fulvio Scarano
S.Adatrao@tudelft.nl

TU Delft

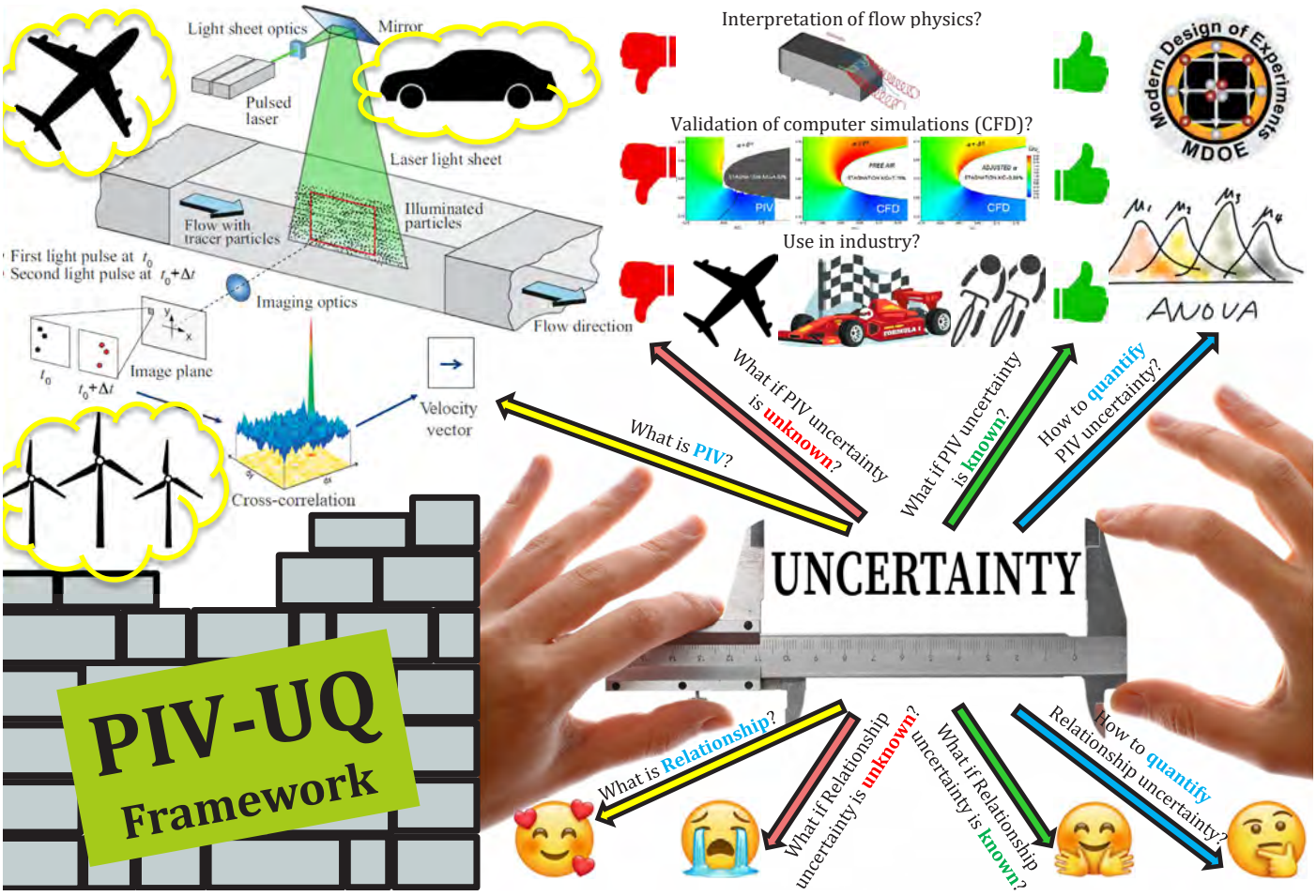

Nando van Arnhem
AWEP
FPP
Dr. R. Vos
Prof. L.L.M. Veldhuis
n.vanarnhem@tudelft.nl

TU Delft

Sustainable Aircraft Design

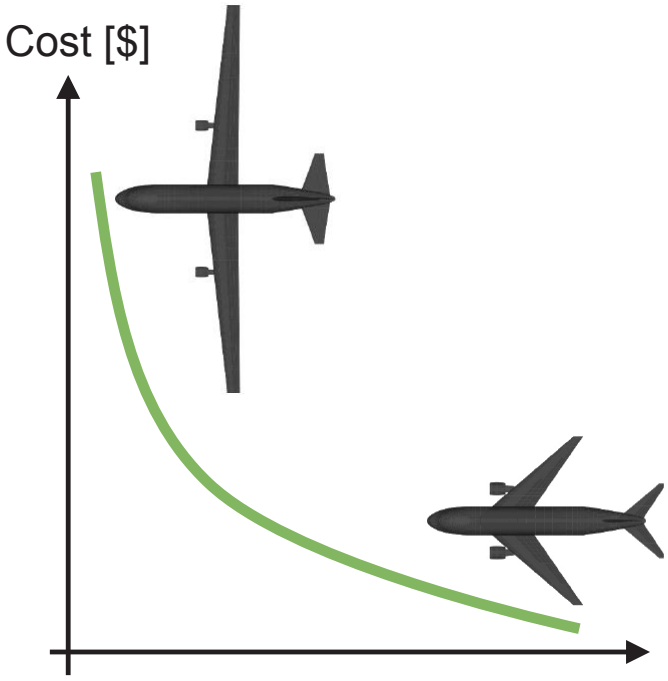

GLOWOPT

1. Select market requirements
2. Create climate functions
3. Design & optimise aircraft
4. Evaluate aircraft

Images adapted from Henderson et al. (2012)

Pieter-Jan Proesmans
Flight Performance & Propulsion
AWEP
Dr.ir. Roelof Vos
Prof.dr.ir. Leo Veldhuis
P.Proesmans@tudelft.nl

TU Delft

Martijn Roelofs
AWEP
FPP
Roelof Vos
Leo Veldhuis
M.N.Roelofs@tudelft.nl

TU Delft

Physics-based decision support for technology selection

	Scores		
t_1	—	—	—
t_2	—	—	—
t_3	—	—	—

$E = mc^2$

$\sum \boldsymbol{F} = m\boldsymbol{a}$

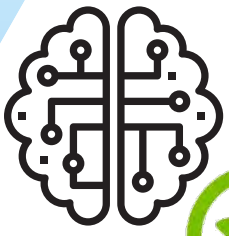

Aerodynamic Performance & Conceptual Design of Hybrid-Electric Aircraft with Over-the-Wing Distributed Propulsion

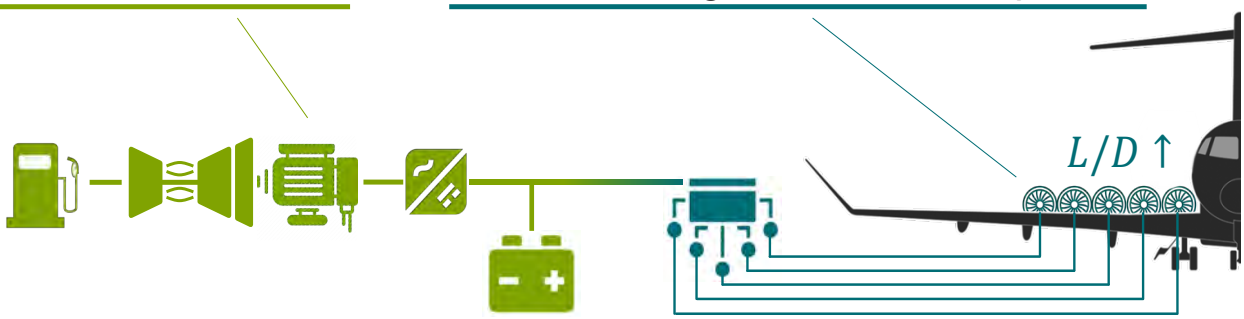

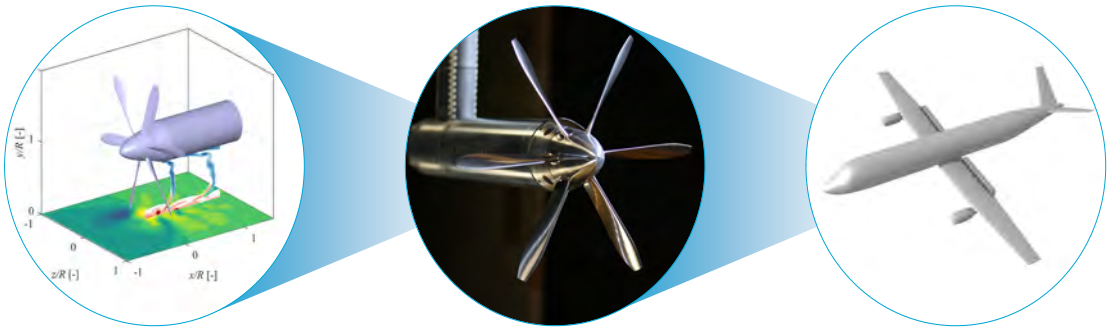

1. Study aerodynamic interaction

2. Determine system performance

3. Evaluate impact at aircraft level

Clean Sky 2

Name: Reynard de Vries
Department: AWEP
Section: FPP
Daily supervisor: Roelof Vos
Promotor: Leo L. M. Veldhuis
R.deVries@tudelft.nl

TUDelft

Luc Kootte

ASM: ASCM

Prof. Chiara Bisagni

l.j.kootte@tudelft.nl

Sponsored
by European Office of
Aerospace Research and
Development,
United States Air Force.

TUDelft

A Methodology for predicting skin-stringer separation in postbuckled composite structures

Objective

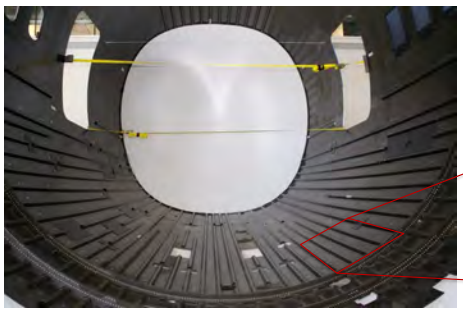

Boeing 787 fuselage

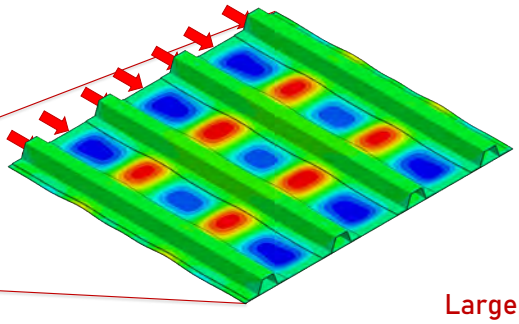

Multi-stringer panel

Large, complex and expensive

Small, targeted and cost-effective

Methodology

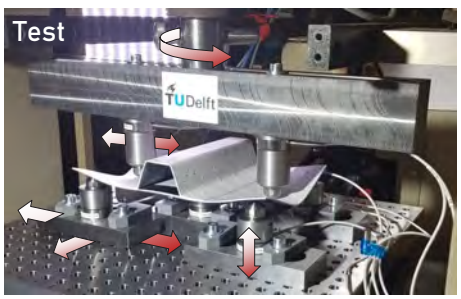

Adaptive multi-point test set-up

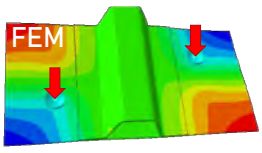

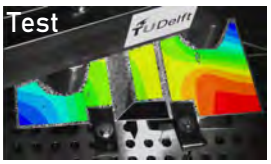

Out-of-plane deformation

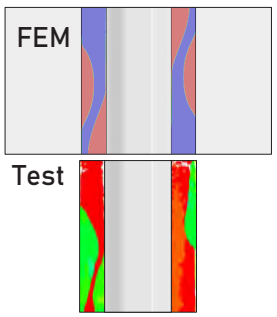

Interface separation

Single-stringer panel

POSTERS

Monocular-Based Data Fusion for the Relative Pos Estimation of Uncooperative Spacecraft

Motivation

The estimation of the relative position and attitude (pose) of an inactive target by an active servicer sp task in the design of current and planned space missions, due to its relevance for close-proximity oper **rendezvous with a space debris** and/or **in-orbit servicing** (Fig.1). Pose estimation systems based solely **camera** are recently becoming an attractive alternative to systems based on active sensors or stereo c reduced mass, power consumption and system complexity [1]. Unfortunately, the pose estimation pro complicated by the fact that the target satellite is, especially in the context of ADR, **uncooperative**, nam non functional and/or not able to aid the relative navigation.

The Mission

This activity refers to a co-sponsored PhD between Delft University of Technology, ESA's ESTEC, and Airbus DS Bremen. The research is currently driven by the challenges in close-proximity operations around an uncooperative spacecraft, and it is focused on three main aspects:

- **On-board Image Processing** which extracts features from a 2D monocular image
- **Pose Estimation** which handles the image processing output to return the relative pose
- **Navigation filter** which fuses the measurements from the different sensors and determines both statistical and systematic errors of relevant uncertain parameters affecting the relative motion in terms of attitude and position of both chaser and target spacecraft.

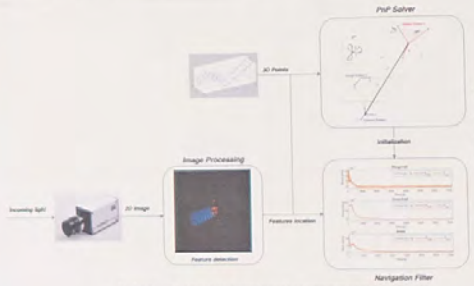

Fig. 2: Schematic of the adopted model-based pose estimation scheme.

Image Processing (IP)

The proposed IP implements a **Convolutional Neural network (CNN)** to detect *heatmaps* around pre-selected features on the target [3] (Fig.3-4). In addition, a novel method is investigated in which the heatmaps' shape is exploited to derive a covariance representation of the detected features (Fig.5). This is done in order to incorporate feature uncertainties in both the pose estimation step and in the navigation filter [4].

- Refined **Pose Estimation accuracy**
- Reliable **measurements covariance**
- Improved **Filter robustness**

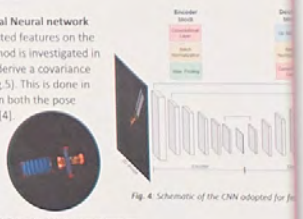

Fig. 3: Example of CNN-detected heatmaps.

Fig. 4: Schematic of the CNN adopted for fe

References

[1] Sharma, S., Ventura, J. and D'Amico, S. [2018]. "Robust Model-Based Monocular Pose Initialization for Noncooperative Spacecraft R Rockets, volume 55, No.6, pp. 1-16.
[2] Pasqualetto Cassinis, L., Fonod, R., Gill, E. [2019]. "Robustness and Applicability of monocular pose estimation systems for relative n spacecraft". Progress in Aerospace Sciences, volume 110.
[3] Pasqualetto Cassinis, L. et al. [2019]. "Comparative Assessment of Image Processing Algorithm for the Pose Estimation of Uncoopera on Satellite Constellations and Formation Flying, Glasgow, UK.
[4] Pasqualetto Cassinis et al. [2020]. "CNN-based Pose Estimation System for Close-Proximity Operations Around Uncooperative Space Mechanics Conference, Orlando, FL, USA.

TUDelft

56

Wind turbine blade fault detection: An aeroacoustics approach

1. Introduction

2. Methodology

- Research objective:
- Approach:

3. Experiment & test

- Aeroacoustic measurement for airfoil with pitch fault:

4. Future work

References:

TUDelft

DEPARTMENT OF SPACE ENGINEERING

We educate and research to advance the frontiers of space systems and missions, spaceflight and planetary science for the benefit of society.

Space is an indispensable part of our daily life. It is crucial for meeting today's and tomorrow's societal needs, such as finding answers to climate change, population growth, and global access to information. Spaceflight also enables us to explore our solar system. The exploitation of Space will accelerate with better science, skilful engineers, and capable services for the benefit of mankind. At the same time, growing risks must be tackled by securing access to space and reducing space debris. The Department of Space Engineering is unique world-wide in its capabilities to innovate for Space: from concept to application and from launch to end-of-life. It educates scientists and engineers and inspires research to make the Space domain more valuable, accessible, and safe, and to better understand the Earth, our solar system, and beyond.

The Department operates a cleanroom facility for the design, integration, and verification of assemblies up to entire satellites. It is an active member of the TU Delft Space Institute.

ASTRODYNAMICS AND SPACE MISSIONS

Dora Klindzic
Yuxin Liun
Gourav Mahapatra
Jesse Reusen
Marc Rovira-Navarro
Teresa Steinke

SPACE SYSTEMS ENIGNEERING

Stefano Casini
Fiona Leverone
Ruipeng Liu
Lorenzo Pasqualetto
Victor Villalba Corbacho

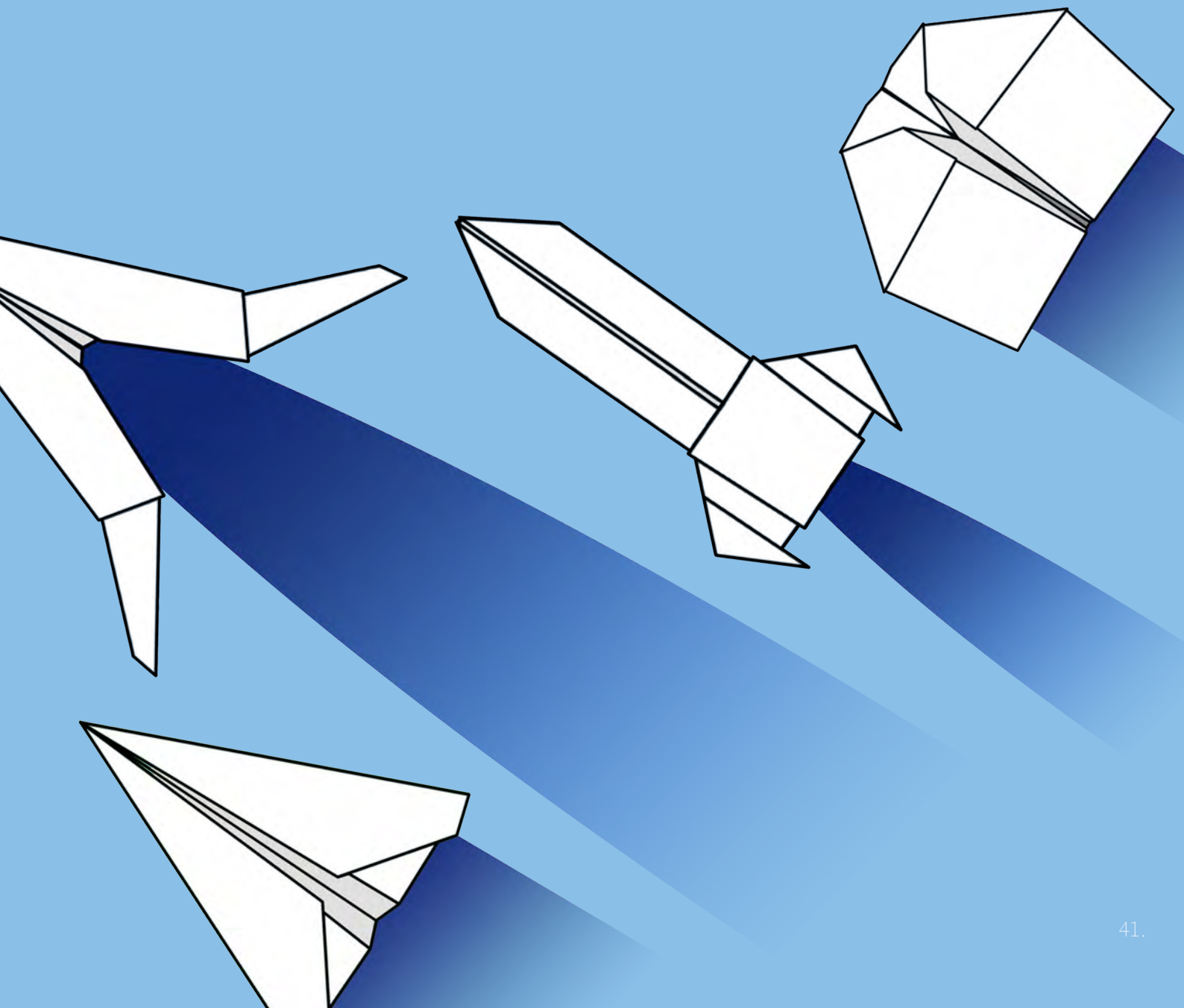

SE

A glimpse of Earth through LOUPE

Dora Klindžić
Space Engineering
Astrodynamics & S.M.
D.M. Stam, F. Snik,
M. Esposito, C. van Dijk
prom.: B. Vermeersen
d.klindzic@tudelft.nl

The Lunar Observatory for Unresolved Polarimetry of Earth (LOUPE) is a spectropolarimeter designed to observe the Earth as an Exoplanet.

What does a planet with life look like?

- **Liquid water** — detectable from rainbows and glories
- **Molecular oxygen** — O2A absorption band
- **Clouds & continents** — polarization of reflected starlight
- **Vegetation** — emission in green ("green bump") and infrared ("red edge")
- **Unresolved** — all spectral information contained in a point source for the observer

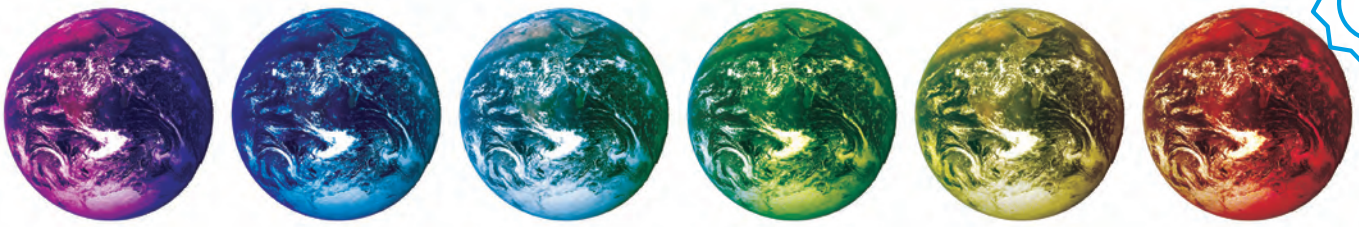

LOUPE combines hyperspectral imaging with linear polarization modulation.

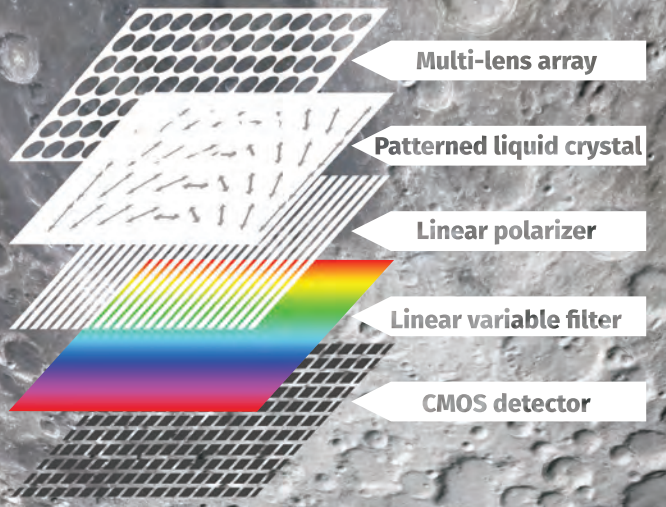

What is LOUPE's mission?

- Build a **compact** (<300g) space-qualified spectropolarimeter with no moving parts.
- Hitch a ride to the Moon on a lander or rover with minimal impact on total payload mass.
- Observe the Earth as if it were an **exoplanet** throughout different seasons and phases.
- Use the "ultimate selfie" to recognize **extraterrestrial life** on other planets!

TU Delft · cosine measurement systems · Universiteit Leiden, Leiden Observatory · LOUPE

Investigating Orbital Dynamics in CR3BP based on Machine Learning

PhD Candidate: Yuxin Liu
Department: Space Engineering
Section: Astrodynamics & Space Missions
Daily supervisor: Ron Noomen
Promotor: P.N.A.M Visser
Contact: yuxin.liu@tudelft.nl

1 2 3 4

Introduction

The flyby is a useful technique that saves propellant in deep space missions. The classical method of predicting a post-flyby effect is numerical integration. It provides accurate result but is time-consuming when trajectory optimization involved. The patched conics model is an efficient analytical method which assumes that the spacecraft is affected by the flyby body only within the sphere of influence of it. However, it is error-prone for some high-altitude flybys. A semi-analytical method was developed by Alessi and Sánchez for high-altitude cases but the spacecraft should be outside the Hill sphere to guarantee accuracy. In this work, a new Keplerian map is developed based on Gaussian Process Regression (GPRKM) to predict flyby effect accurately and efficiently.

Methodology

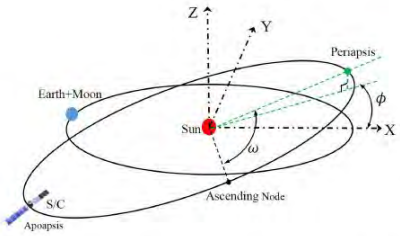

Fig. 1: Schematics of a three-body system before a flyby.

Schematic of CR3BP in the Sun-Earth-Spacecraft system. Both the before-flyby and post-flyby state of the spacecraft are denoted in five Kepler orbital elements except for the true anomaly. The true anomaly of initial state corresponds to apogee.

Step 1. Selection of the covariance function. The covariance function is a basic module of GPR model which expresses the relevance between two samples.

Step 2. Generation of training samples. Each sample consists of an input and an output. They are before-flyby and post-flyby states, respectively. The training samples provides empirical information for GPR model.

Step 3. Training the GPR model. The training samples are used to optimize the hyper-parameters of the covariance function.

Step 4. Predicting the post-flyby state for any before-flyby state using the trained GPR model.

Results and Conclusion

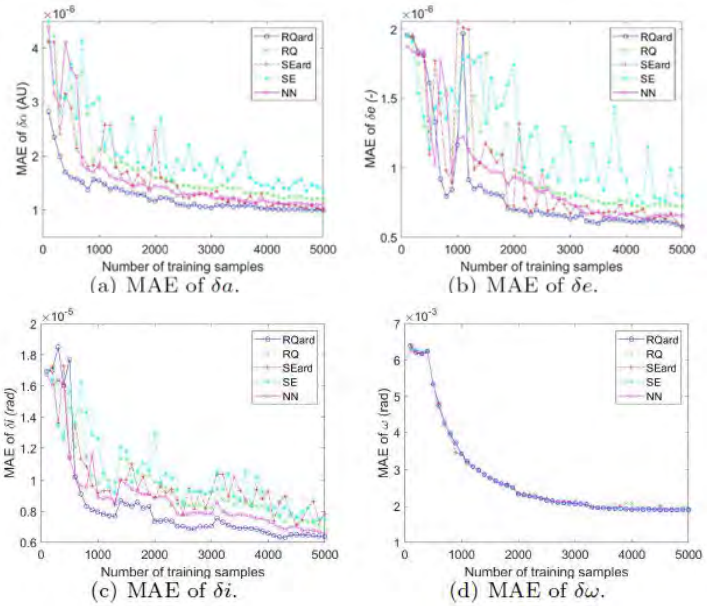

(a) MAE of δa. (b) MAE of δe. (c) MAE of δi. (d) MAE of $\delta\omega$.

Table 3: The performance of GPRKM compared to that of Alessi et al. [9] (fully reproduced here).

		δa [AU]	δe [-]	δi [rad]	$\delta\omega$ [rad]	$\delta\Omega$ [rad]
MAE	GPRKM	5.7×10^{-5}	3.4×10^{-5}	6.3×10^{-6}	1.9×10^{-3}	1.9×10^{-4}
	SKM	1.9×10^{-4}	7.6×10^{-5}	1.1×10^{-5}	2.2×10^{-3}	2.1×10^{-4}
	P-GRPKM	5.9×10^{-5}	5.0×10^{-5}	-	1.7×10^{-3}	-
Time* [s]	GPRKM	5.9×10^{-6}	1.5×10^{-6}	3.8×10^{-5}	3.6×10^{-6}	5.2×10^{-6}
	SKM	7.5×10^{-2}	7.5×10^{-2}	7.5×10^{-2}	7.5×10^{-2}	7.5×10^{-2}
	P-GRPKM	1.2×10^{-6}	1.2×10^{-6}	-	1.2×10^{-6}	-
	CR3BP	5.9×10^{-1}	5.9×10^{-1}	5.9×10^{-1}	5.9×10^{-1}	5.9×10^{-1}

Compared to a previous semi-analytical method, GPRKM has achieved a better accuracy. The CPU time for prediction is a factor 103 faster than that of this semi-analytical method.

Investigating Venus's clouds and hazes using CO_2 absorption bands in flux and polarization

Gourav Mahapatra (1), Loïc Rossi (2) and Daphne Stam (1)

(1) Faculty of Aerospace Engineering, TU Delft, The Netherlands (2) LATMOS/IPSL, CNRS, Guyancourt, France

Gourav Mahapatra

Astrodynamics & Space Missions
Group: Space Exploration
Daily supervisor: Dr. Daphne Stam
Promotor: Dr. LLA Vermeersen

1. Context

- The state of polarization of light that is scattered by particles is very sensitive to their size, composition and shape, even when the light is scattered multiple times between the particles.
- Hansen & Hovenier (1974) thus used Venus's polarization phase curve to determine that the upper cloud particles have an effective radius of 1.05 µm (and a variance of 0.07), and consist of 75 % sulphuric acid. This could not be derived from the flux phase curve!
- Later, the polarimeter on-board the Pioneer Venus orbiter helped to detect a layer of sub- micron sized haze particles above the clouds [2].
- We model total and polarized fluxes in the CO2 absorption bands between 1.4 and 1.5 µm to ultimately derive cloud top and haze opacity variability from SPICAV/Venus Express (VEx) data.
- We define the degree of polarization *P* of sunlight that is reflected by (a region on) Venus as the ratio of the (linearly) polarized flux to the total flux.

2. The SPICAV instrument onboard Venus Express

- SPICAV was a spectrometer on-board the VEx spacecraft with an infrared (IR) channel operating from 0.6 – 1.7 µm [3].
- SPICAV used a Acousto-optical tunable filter (AOTF) which captures light in two orthogonal polarization states enabling the possibility of deriving the degree of linear polarization.

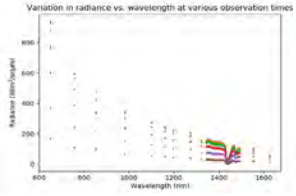

Figure 1. Example plot of Flux vs. wavelength from SPICAV data. Absorption at 1450 nm due to CO_2.

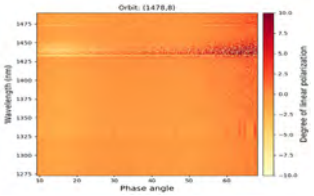

Figure 2. Contour plot showing variation of *P* with phase angle and wavelength.

- Figure 1 shows a set of sample radiance measurements at various times. Absorption at 1450 nm is clearly visible.
- Figure 2 shows the derived *P* data from SPICAV-IR. *P* is high in the absorption bands due to different ratios of single to multiple scattering and various particle types in the atmosphere.

3. Modelling approach

- Single scattering is calculated using Rayleigh (gas) and Mie scattering (clouds and hazes) [4] and the adding-doubling algorithm [5] is used to compute the light that is reflected by the atmosphere as a whole.
- Our 71 layer atmosphere model consists of CO2 gas and contains clouds and haze particles whose sizes are described by a log-normal particle size distribution, with for the clouds: rg =1.05µm, σ=1.2, and for the haze: rg = 0.15µm, σ = 1.91.
- Figure 3 shows the single scattering flux and polarization of light scattered by the gas, cloud, and haze particles.
- Figure 4 shows the aerosol (cloud and haze) vertical distributions we use to explore differences due to aerosol structure.

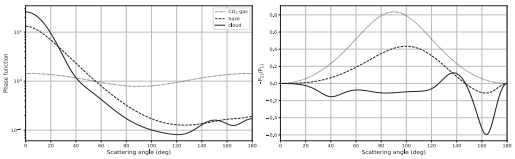

Figure 3. Phase function (left) and *P* (right) of incident unpolarized light that is singly scattered by the cloud (solid line), haze (dashed line) and the gas (dotted line) particles at 1.45 µm.

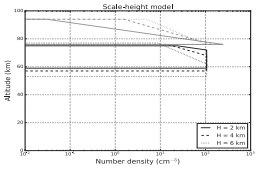

Figure 4. Vertical structure of various aerosol vertical distributions used in this work.

References

1. Hansen, J.E. and Hovenier, J.W., 1974. *JAS*, *31*(4), pp.1137-1160.
2. Kawabata, K., et al. *JGR: Space Physics* 85.A13 (1980): 8129-8140.
3. Korablev, Oleg, et al. *PLANET SPACE SCI* 65.1 (2012): 38-57.
4. De Rooij, W. A., and C. C. A. H. Van der Stap. *A&A* 131 (1984): 237-248.
5. De Haan, J. F., P. B. Bosma, and J. W. Hovenier. *A&A* 183 (1987): 371-391.
6. Rothman, Laurence S., et al. *JQSRT* 96.2 (2005): 139-204.
7. Stam, D. M., et al. *JQSRT* 64.2 (2000): 131-149.

4. Results: Variation with absorption optical thickness

- Figure 5 shows the reflected flux *F* and degree of polarization *P* for different atmospheric profiles as functions of the CO2 absorption optical thickness b^m_{abs}.
- Flux *F* decreases with increasing b^m while *P* can either increase or decrease.
- Clouds and haze increase *F* as compared to an atmosphere with only CO2 gas (panel A).
- Decreasing the cloud top altitude decreases *F* due to a larger amount of gaseous absorption across the b^m_{abs} range (panel C).

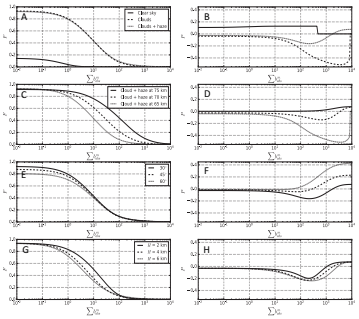

Figure 5. Variation of *F* and *P* with increasing total molecular absorption b^m_{abs} for atmospheres with 'scale-height' aerosol models.

- *F* decreases with increasing solar zenith angle due to the increasing path length and decreasing incident flux on the top of the atmosphere (panel E).
- *F* decreases with increasing scale height *H* due to the increase of scattering in higher layers (panel G).
- *P* decreases depending upon the absorption, the particles' vertical distribution, and/or the geometry.
- For a clear atmosphere, *P* is positive due to the positive single scattering polarization by gas (panel B, also Fig. 3).

- When the absorption is small (b_m^{abs} < 10), *P* is mostly determined by multiple scattering in the clouds (or in the gas, in case of the clear atmosphere), also in the presence of haze. For larger b_m^{abs} , *P* is increasingly determined by single scattering in the gas or the haze (if present) (panel B).
- For a given atmosphere structure, *P* increases with increasing solar zenith angle due to increasing scattering in higher atmospheric layers (panel F).

5. Results: Variation with wavelength

- Figure 6 shows the spectral variation of *F* and *P* for different atmospheric profiles (see Fig. 5) across the 1.4 – 1.5 µm range. Here, we used a 1 nm box convolution window to compute *F* and *P* across the absorption band.

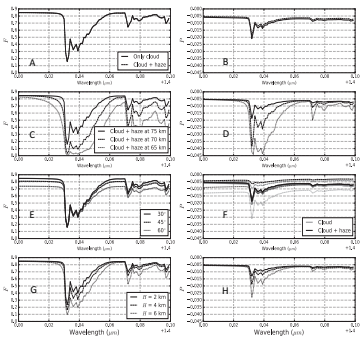

Figure 6. Variation of Flux (F) and Linear Polarization (P) with wavelength (1.4 - 1.5 µm) for atmospheres with 'scale-height' aerosol models.

- *F* is insensitive to the presence of a haze (panel A).
- *P* increases (in absolute sense) in the band because of the decrease of multiple scattering (panel B).
- Increasing the altitude of the cloud and haze particles, increases *F* in the band due to the increase in scattering in the higher atmosphere (panel C).
- Increasing the altitude increases *P* in absolute sense (panel D).
- Increasing the illumination angle decreases *F* in the continuum (see Fig. 5, panel E).

- The difference between clouds and clouds + haze cases is higher in *P* due to differences in single scattering properties (see Fig. 3).
- A change in *H* affects both *F* and *P* but differently as compared to a change in cloud top. This change in *F* is due to a variation in the amount of scattering and absorption by gas above the cloud (panel G). An increase in *H* yields an increase in *P* due to more single scattering in the upper atmospheric layers (panel H).

6. Conclusions and Future work

- Polarization across CO2 absorption bands is highly sensitive to the properties of cloud and haze particles, gas, and the illumination and viewing geometries.
- Polarization in the deepest parts of the CO2 band is determined by the single scattering properties of the particles in the upper layers of the atmosphere (at the given geometry) and can be either positive or negative (perpendicular or parallel to the reference plane).
- We will use SPICAV-IR flux and polarization data to constrain Venus's cloud top altitudes and haze properties.

Constraining dynamic models in North America using the static gravity field

Jesse Reusen[1], Wouter van der Wal[1], Bart Root[1,2], Javier Fullea[2]

[1]Delft University of Technology, Netherlands; [2]Dublin Institute of Advanced Sciences, Dublin, Ireland

Jesse Reusen
Aerospace Engineering
Astrodynamic & Space Missions
Supervisors: W. Van der Wal & B. Root
Promotor: L.L.A. Vermeersen
J.M.reusen@tudelft.nl

1. Introduction

The long-wavelength static gravity field in North America shows a negative anomaly up to about 50 mGal (Figure 1). The anomaly has been attributed to Glacial isostatic adjustment **(GIA)**, but also to deep mantle signal (dynamic topography). If either is true that would provide a unique constraint on the mantle. However, the anomaly can have other causes as well: topography and density anomalies in the crust and mantle. Our aim is to model all components with at least two alternative models for each component, and see which component has the largest uncertainty and can be constrained.

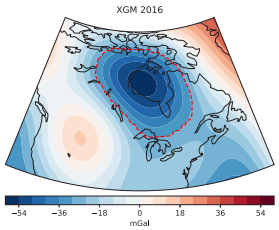

Figure 1: Gravity anomaly of global geopotential model XGM 2016 for spherical harmonic degrees 2-15. This range is selected because it contains most of the GIA signal.

2. Approach

The dynamic model employed here is based on a force balance. This balance is assumed to hold at a depth of 300 km. Because the reference column is laterally homogeneous, this means that the pressures at 300 km depth are equal, the assumption of isostasy. This assumption allows to fit one of the components. We assume that the geometry and density of the crust are reasonably well known. Therefore, we opt to adjust the density of the mantle just below the crust up to the Lithosphere Asthenosphere Boundary, (**LAB**) following Root et al. (2016, GJI)

Figure 2: The force balance. The forces involved are those caused by the weight of the crustal, lithospheric and asthenospheric layers, as well as an extra force due to incomplete GIA and a force due to dynamic topography. The forces in our model are set equal to the force at 300 km exerted by a reference column.

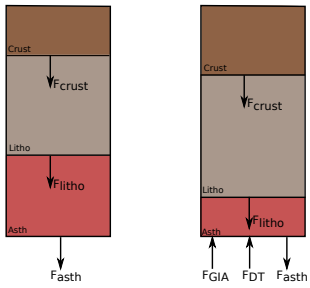

3. GIA and mantle convection

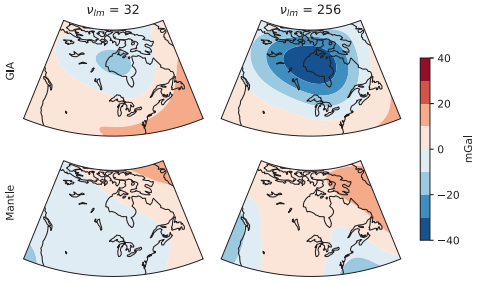

Figure 3: gravity anomalies due to GIA (top row) and mantle convection (bottom row), shown for two options of the lower mantle viscosity (values denoted in the title, in 10^{20} Pa s). The magnitude of the anomaly due to GIA depends heavily on the lower mantle viscosity. The sum of these contributions and that of the isostatically compensated crust should match the observations (Fig 1).

4. Reults – Preferred viscosity profile

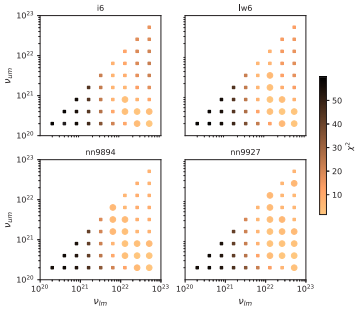

Figure 4: misfit between the model and the observations for different upper (ν_{um}) and lower (ν_{lm}) mantle viscosities. Each subplot indicates a different ice history. This ice history is used in the GIA model. Regardless of the ice history, larger lower mantle viscosities (x-axis) are favoured.

4. Reults – Gravity maps

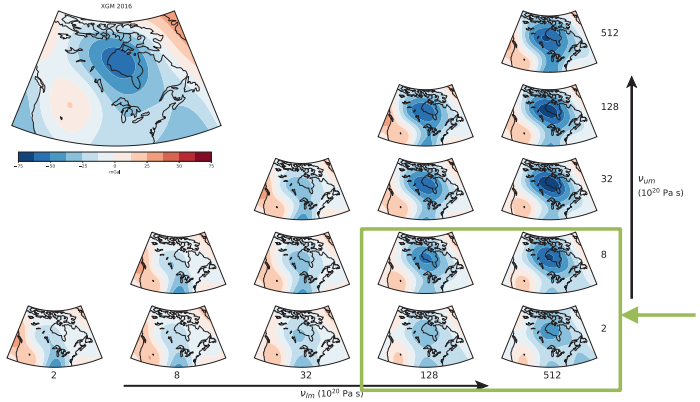

Figure 5: maps of model results (small subplots) and observations (top left), again for different upper (ν_{um}) and lower (ν_{lm}) mantle viscosities. Subplots on the right side (for larger lower mantle viscosities) match best.

8. Conclusions

- First time all components of the North America gravity field are included consistently with the assumption of isostasy: crust and lithosphere model, mantle density anomalies, dynamic topography, CMB topography and GIA.
- Lower mantle viscosity is shown to be the most sensitive parameter in the dynamic model.
- Best fitting viscosity profile has lower and upper mantle viscosities equal to $4x10^{20}$ and $2.56x10^{22}$ Pa s (Figures 4,5)
- Future work: Effect of 3D viscosity in models for GIA and dynamic topography.

This study is funded by:
esa STSE 3D Earth
NWO
ALW.GO.2017.035

SUBSURFACE OCEANS AND WHERE TO FIND THEM.

Marc Rovira-Navarro
Astrodynamics and Space Missions
W. van der Wal
B. Vermeersen
m.roviranavarro@tudelft.nl

Tides in Icy Moons

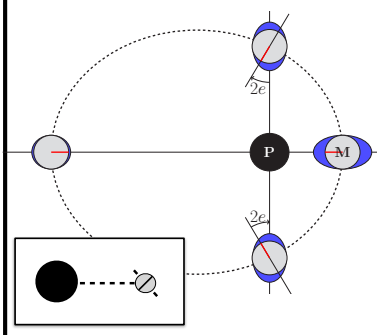

Some of the moons of the outer solar system **harbour subsurface oceans** (e.g., Europa, Enceladus). **Tidal dissipation** plays an important role in preventing these oceans from freezing and shaping the moons' surfaces.
Subsurface oceans can **extend the traditional habitable zone**. We want to understand under which conditions they form and how long they can persist.
We consider icy moons in our Solar System and explore the implications of our results for other planetary systems
Left: Schematic representation of a moon's eccentric (e) orbit. Along the orbit, the tidal bulge (blue) changes in amplitude an librates in longitude. The 0 degree meridian is indicated for reference. **Inset:** Sketch depicting the moon's obliquity which results in a latitudinal libration of the tidal bulge.

We study solid and ocean tides. We consider a simplified interior structure consisting of an ice shell, a subsurface ocean, a rocky mantle and a metallic core.
Right: General temperature profile inside an icy moon. Ts is the surface temperature which is in general less than 100K, the melting temperature Tm is pressure dependent water melting temperature and changes from 273 to 250K. The ice shell (grey) is divided in a conductive and convective layer. We assume the temperature to be constant within the ocean. The silicate mantle (brown) is similarly divided into a conductive and convective layer.

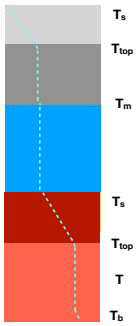

Solid Tides

The changing tidal potential **deforms** the **solid layers** of the moon, because these layers are **not perfectly elastic**, **energy is dissipated in the interior**. The amount of heat dissipation in the interior depends on the interior structure (e.g., ice shell thickness, mantle temperature). Using the viscoelastic theory for self-gravitating incompressible bodies we compute **tidal dissipation for different interior models of icy and rocky moons.** We consider two types of rheology (Maxwell and Andrade).
Right: Tidal dissipation within the silicate mantle and ice shell. Two cases are considered, a moon with a cold mantle (left) and a moon with a hot mantle (right).

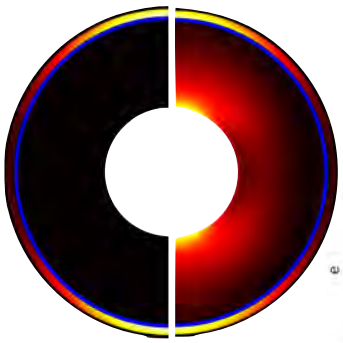

By assuming that the moon is in **thermal equilibrium** (heat generated in the inside equals heat conducted through the outer layer of the moon), we can compute equilibrium internal structures for different moon sizes and orbital parameters. We consider the Jovian system and compute the **region around the planet where subsurface oceans can exists.** We show that this region decreases with moon size. Extrapolating these results to other planetary systems shows that **subsurface oceans should be common in other planetary systems.**
Below: Equilibrium ice shell thickness for different orbital parameters. A moon with a rocky core of 1800km with and a 100km ice shell is considered.

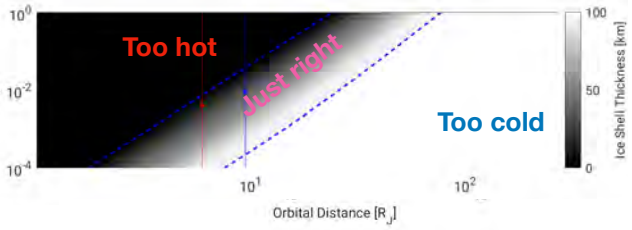

Ocean Tides

As happens on Earth, **tidal dissipation can also occur within the ocean.** It has been suggested that ocean tidal heating might be an important role in preventing subsurface oceans from freezing. (specially for small moons such as Enceladus). We investigate tidal dissipation and ocean currents for different ocean geometries.
If the ocean depth is small compared with the moon's radius, the **shallow water approximation** can be used.Under these considerations the **Laplace Tidal Equations** (LTE) can be used,
Lower right: Tidal dissipation in an ice-free Enceladan ocean for different ocean topographies (no topography and degree two and three ocean thickness variations)
Upper right: Tidal dissipation patterns for a 30km thick ocean due to the eccentricity (right) and obliquity tide (left)

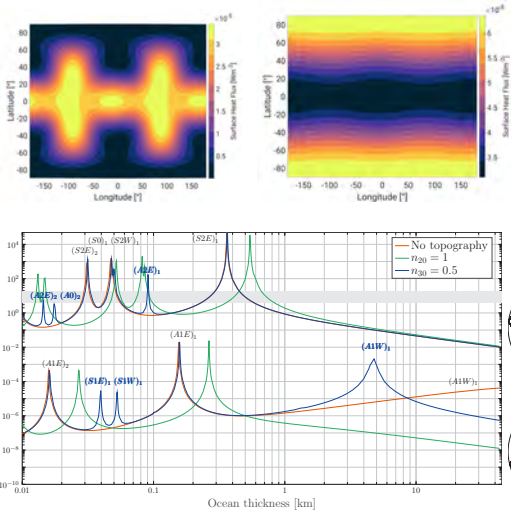

The **Laplace Tidal Equations** have been very successful in explaining tidal currents on Earth . However **the use of the LTE** might **not be justified for subsurface oceans**. For instance, the ocean depth to radius ratio in Enceladus is around 0.15 while on Earth it is just 0.001. **We challenge the LTE** and study the response of an unstratified ocean to tidal forcing. Without the LTE new kind of dynamics are possible. We focus on **internal inertial waves**, where the Coriolis force acts as restoring force.
Below: The properties of internal waves allows for the appearance of **wave-attractors**. A wave-attractor is a **trajectory in which energy accumulates.** The ocean geometry determines whereas a wave-attarctor appears or not.

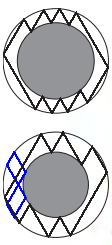

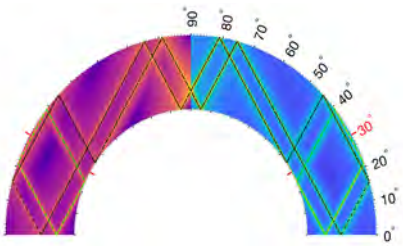

What do Io's volcanoes tell us about the interior

Teresa Steinke
Department: SpE
Section: A&S
Supervisor: Wouter van der Wal
Professor: Bert Vermeersen
e-mail: t.steinke@tudelft.nl

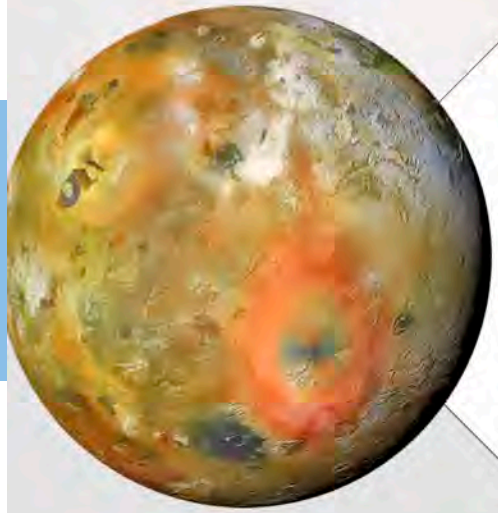

Introduction and Motivation

Tidal dissipation makes Jupiter's moon Io to the most active body in the Solar system. Most of the heat is lost through a large number of active volcanoes. The processes that cause the volcanic pattern of the moon are not fully understood yet. Here, we focus on the question: What is the influence of the viscosity and thickness of the layer beneath Io's crust on the total number, the density variation, and spatial relation of Io's observed volcanoes?

Spatial distribution of Io's volcanoes

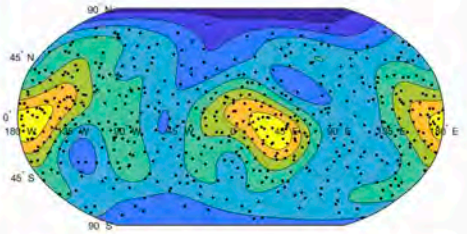

Graph shows the location of Io's volcanoes and the density distribution (in color) given in spherical harmonics up to degree 5. Credit: Duncan Sliedregt.

Model Approach

The number of up-streams and the amount of lateral heat flow in a convective system depend on the Rayleigh number. We use a scaling law by Viella et al. (2018) and Tackley (2001) to approximate the parameters defining the Rayleigh number of the system, i.e. the viscosity, the depth, and fraction of convective heat transport. This approach is independent of the location and assumed mechanism of tidal heating.

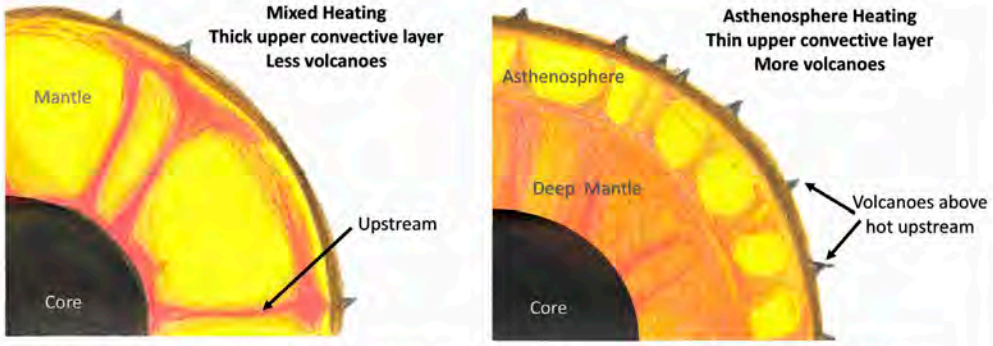

In Io's interior heat is transported by mantle convection and melt. Depending on the vigour of mantle convection up-streams appear more or less frequently per given area. Up-streams lead to a higher concentration of melt, invoking volcanism . Also the amount of heat that is transported laterally depends on the vigour (Rayleigh number) of the convective system. Thus, the Rayleigh number defines to what extend the non-uniformly produced tidal dissipation is smoothed.

Results and Conclusion

The strength of the tidally induced signal on Io's interior structure and surface depends on the thickness of the convective system, the mantle viscosity and whether the heat transport is dominated by convection or melt advection. The results favor either a thick mantle of high viscosity or a thin asthenosphere of low viscosity.

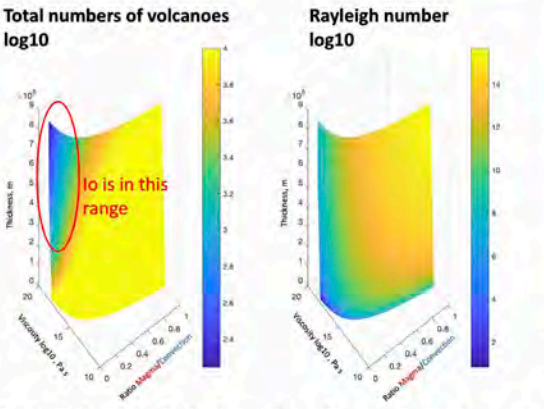

Total number and Rayleigh number of convective system as a function of interior parameters. Red circled area indicated the number of Io's observed volcanoes.

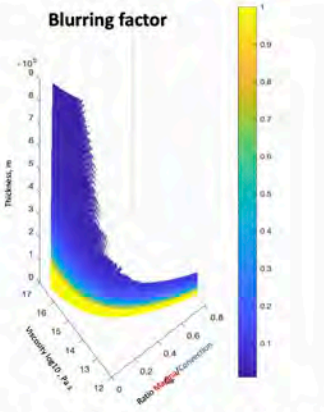

Blurring factor as a function of interior parameters. Only coloured area is in agreement with observed large scale density variations

Autonomous Navigation and AOCS for a Deep-Space CubeSat

Name: Stefano Casini
Department: SpE
Section: SSE
Daily supervisor: Dr. A. Cervone
Promotor: Prof. dr. E.K.A. Gill
S.Casini@tudelft.nl

Context and Motivation

The last years of space exploration have been characterized by an opening to CubeSats and small satellites (e.g. NASA MarCO, Fig.1), thanks to the recent growth in the space components miniaturization. **Commercial-of-the-shelf** (COTS) components have been widely used for Earth applications in the last 20 years, but recently their applicability for deep-space missions have been partially proved. In the **H2020 ITN Stardust-R** framework, **Near Earth Asteroids** will be chosen as target for deep-space missions. These mission scenarios will require a high degree of **autonomy** to assess real-time operations.

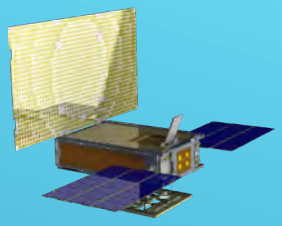

Fig.1: NASA Mars Cube One (MarCO)

Autonomous Celestial Navigation

Celestial navigation technique exploits **Line-of-Sight** (LOS) directions of visible bodies (planets, moons or large asteroids) to reconstruct the spacecraft state. The navigation filter is fed with LOS and ephemerides of the detect bodies. **Micro-Star Trackers** (Fig. 2) can detect LOS, similarly as they do for stars, although some complications are introduced by the variable magnitude, the different radiation environment and others.

Fig.2: ST200 micro-star tracker (courtesy of Hyperion Technologies B.V.)

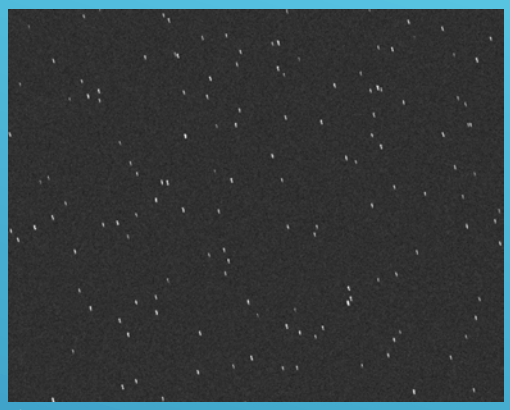

Fig.3: Space Image Simulator Output

Simulation and Testing

Software-in-the-Loop and Hardware-in-the-Loop tests are fundamental to validate components. A **Space Image Simulator** (SIS), capable of reproducing the **Star Tracker FOV** is important (Fig. 3). SIS has to take into account all the features characterizing the space imaging, such as sensor characteristics, optical aberrations, spacecraft dynamics for blurred images and various sources of noise.

Attitude and Orbit Control

Deep-Space introduces many **uncertainties** and **perturbations** which demand a very **accurate AOCS**, especially for real-time operations. **Reaction wheels** (Fig.4) for attitude control and **micro-propulsion** systems (Fig.5) for both attitude and orbit control represent the most promising hardware solutions to control CubeSats in Deep-Space. Micro-propulsion system selection strongly depends on the specific application and has to pass through a trade-off process.

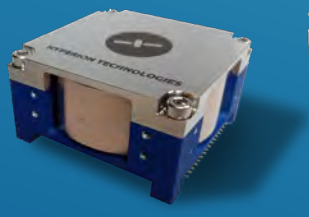

Fig.4: RW400 micro-reaction wheel (courtesy of Hyperion Technologies B.V.)

Fig.5: PM200 micro-thruster (courtesy of Hyperion Technologies B.V.)

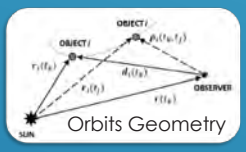

Visible Objects Detection, Deblurring and Noise Filtering, Centroiding and LOS Computation

Navigation Filter

Bodies Ephemerides

Spacecraft State Estimation

References

Franzese V. & Topputo, F., (2019), Line-of-sight deep-space autonomous navigation, Retrieved 2020-01-28, from https://arxiv.org/abs/1909.08459.
McNutt L., Johnson L., Clardy D., Castillo-Rogez J., Frick A. & Jones L., (2014), Near-Earth Asteroid Scout, In AIAA SPACE Conference and Exposition.
Walker R. et al., (2018), Deep-space CubeSats: thinking inside the box, Astronomy & Geophysics, 5:24-5:30.

Boosting satellite capabilities

Fiona Leverone
Department: Space Systems Engineering
Power and Propulsion
Supervisors: Dr. A. Cervone
Dr. M. Pini
Promotor: Prof. E. Gill
Contact: F.K.Leverone@tudelft.nl

What is the trend?

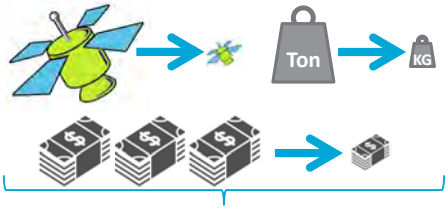

Satellites are getting **smaller** and **lighter**,
so that we can make space access more **affordable**.
This imposes strict **restrictions**, which limits **capabilities**
So,
How do we make these **small satellites** **highly competitive?**

What is the future?

By **coupling critical sub-systems** together can we **increase** the **capabilities** of current satellites?

What critical sub-systems can we couple?

- ✓ **Electrical power generation & storage:** Continuous operation
- ✓ **Propulsion capabilities:** Increase mission flexibility
- ✓ **Thermal control:** Survivability of components

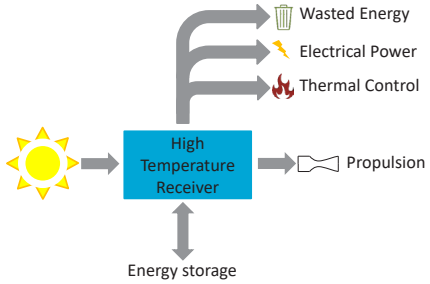

How does it work?

Electrical power generation & storage = **Organic Rankine Cycle** (ORC) and **Silicon** (Si) **thermal energy storage** (TES)

Advantages: High overall energy conversion efficiencies (20 to 30%)
Higher degradation resistance compared to conventional PV systems
High energy density & high specific energy

Propulsion System = **Solar thermal propulsion**

Advantages: Specific impulse > chemical propulsion systems
Transfer times < electric propulsion systems

While using **"free"** energy from the Sun

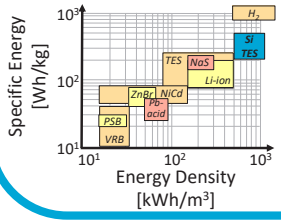

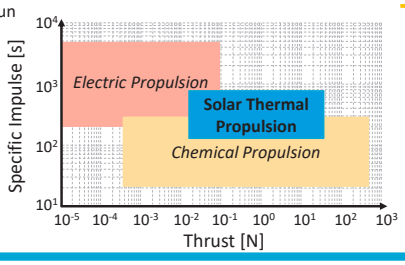

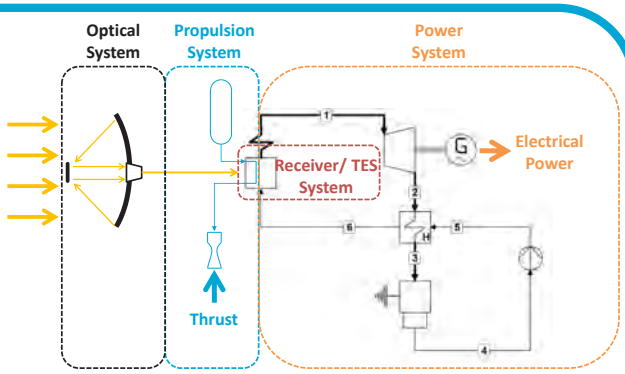

An **optical system** made up of concentrating mirrors and fiber-optic cables focus the sunlight onto a **receiver**. The thermal energy is either stored or used to generate thrust (≈4 N) via the **STP** system and power (≈500 W) via the **micro-ORC** system.

Is this feasible?

Yes,

- **STP** systems are potentially profitable over current mature propulsion technologies for **orbit transfer** missions that require **large velocity increments** coupled to a **short transfer** requirement.
- Best fluid combination **Toluene** (ORC) and **Water** (STP)
- Proposed integrated solar thermal system is **most suitable** for satellites that have a gross mass of **400 kg or more** (GTO to Lunar mission)

But,

- Low shared specific powers on the order of **10W/kg**
- Low micro-turbine efficiencies, **≈57%**

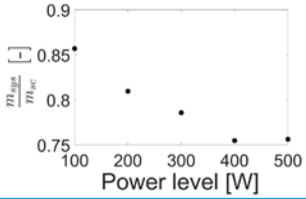

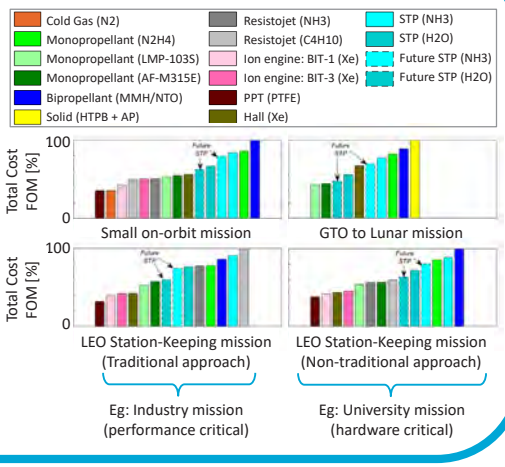

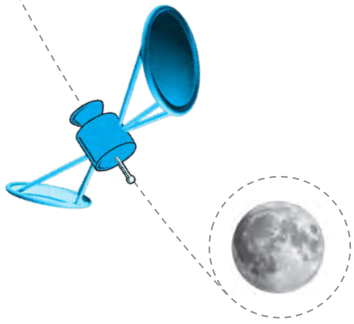

References
- Datas, A. et al., 2016. Ultra high temperature latent heat energy storage and thermophotovoltaic energy conversion. *Energy*, 107, pp.542-549.
- Gerrish, H.P., 2003. Solar thermal propulsion. *AIAA Space Propulsion Symposium*, Florida, USA.
- Leverone, F. et al., 2020. Design of a solar thermal propulsion and power system for mini-satellite lunar orbit insertion. *IEEE Aerospace Conference*, Montana, USA.
- Leverone, F. et al., 2019. Cost analysis of solar thermal propulsion systems for microsatellite applications. *Acta Astronautica*, 155, pp.90-110.
- Leverone, F. et al., 2019. Feasibility of an onboard micro-ORC system for small satellites. *ORC Conference*, Athens, Greece.

Space Robotics Intellectual Autonomy Technologies For On-orbit Servicing

Ruipeng Liu
Space Engineering
Space system engineering
Jian Guo
Eberhard Gill
R.Liu-1@tudelft.nl

1.PROBLEM

In current and future space applications, the need of designing spacecraft with a high level of on-board autonomy is emerging .Traditional notion as predefined and conservative sequences of on-board executed commands can fulfill the needs for satellites operating in a predictable environment. However, this approach is not adequate for spacecraft operating in unpredictable contexts, such as automated on orbit capture, maintenance, repair or assembly. They need to overcome long communication delays and outages, and the reduction of costs in ground segment operations, which can address long-term planning instead of day-to-day procedures, and most significantly , to deal with uncertainty or accent by itself.

2.CONCEPT

Spacecraft intelligent autonomous control
Spacecraft intelligent autonomous control is a technology that combinate the artificial intelligence and intelligent control that makes spacecraft can works in an uncertain environment. When the internal structure , parameters or external environment changed, by the way of AI based decision-making, planning & replanning, intelligent sensing technologes, spacecraft can continue to work by itself, and not rely on the help or support of ground stations or astronauts

SPACECRAFT AUTONOMY LEVELS

Level	Description	Functions
E1	Mission execution under ground control; limited on-board capability for safety issues	Real-time control from ground for nominal operations; execution of time-tagged commands for safety issues
E2	Execution of preplanned, ground-defined, mission operations on board	Capability to store time-based commands within an on-board scheduler
E3	Execution of adaptive mission operations on board	Execution of on-board operations control procedures
E4	Execution of goal-oriented mission operations on board	Goal-oriented mission replanning

OUR MISSION HERE

3.METHOD

Data Injection&Receiving Capability

The data injection receiving process can be automatically analyzed and processed to solve the problems of receiving, identifying to adapt to the repeated, intermittent (delayed), disordered.

Self-learning Ability

Load a large amount of data, files, programs, and execution sequences into the spacecraft. Based on the system's self-learning ability, it can quickly handle abnormal situations and identify and execute new tasks

System Self-management Ability

On-line monitoring capability, which solves the problems of real-time identification, isolation, alarming of abnormalities and faults. Monitoring the task execution process, ensure the execution of the task or at least maintain a safe state.

4.ARCHITECTURE

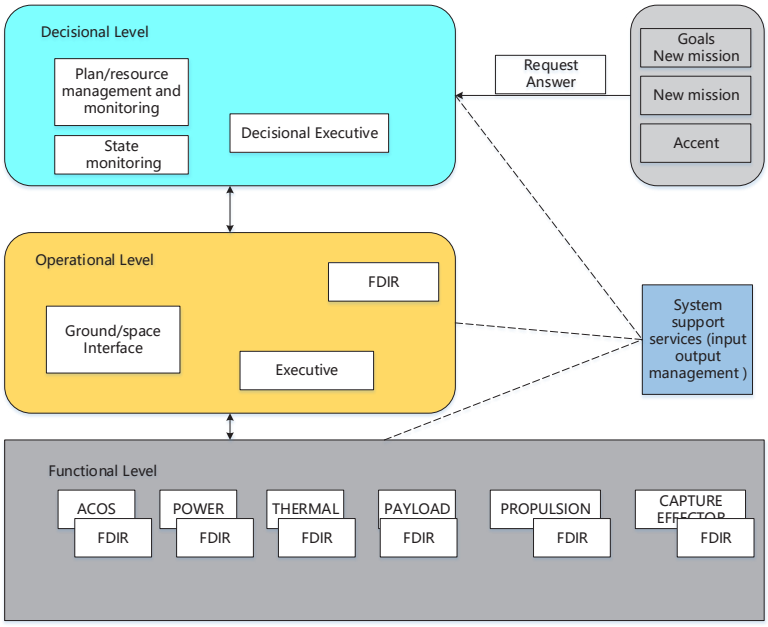

Monocular-Based Data Fusion for the Relative Pose Estimation of Uncooperative Spacecraft

Name: Lorenzo Pasqualetto
Department: SpE
Section: SSE
Daily supervisor: A. Menicucci
Promotor: E. Gill
L.PasqualettoCassinis@tudelft.nl

Motivation

The estimation of the relative position and attitude (pose) of an inactive target by an active servicer spacecraft is a critical task in the design of current and planned space missions, due to its relevance for close-proximity operations, i.e. the **rendezvous with a space debris** and/or **in-orbit servicing** (Fig.1). Pose estimation systems based solely on a **monocular camera** are recently becoming an attractive alternative to systems based on active sensors or stereo cameras, due to their reduced mass, power consumption and system complexity [1]. Unfortunately, the pose estimation problem is in this case complicated by the fact that the target satellite is, especially in the context of ADR, **uncooperative**, namely retained as non functional and/or not able to aid the relative navigation.

***Fig 1**: Future Mission Architectures requiring Rendezvous with Uncooperative Targets. Image credit by ESA.*

The Mission

This activity refers to a co-sponsored PhD between Delft University of Technology, ESA's ESTEC, and Airbus DS Bremen. The research is currently driven by the challenges in close-proximity operations around an uncooperative spacecraft, and it is focused on three main aspects:

- **On-board Image Processing** which extracts features from a 2D monocular image
- **Pose Estimation** which handles the image processing output to return the relative pose
- **Navigation filter** which fuses the measurements from the different sensors and determines both statistical and systematic errors of relevant uncertain parameters affecting the relative motion in terms of attitude and position of both chaser and target spacecraft.

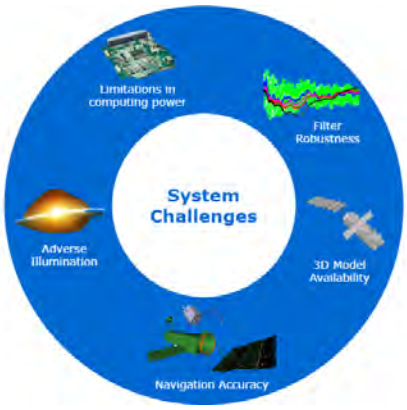

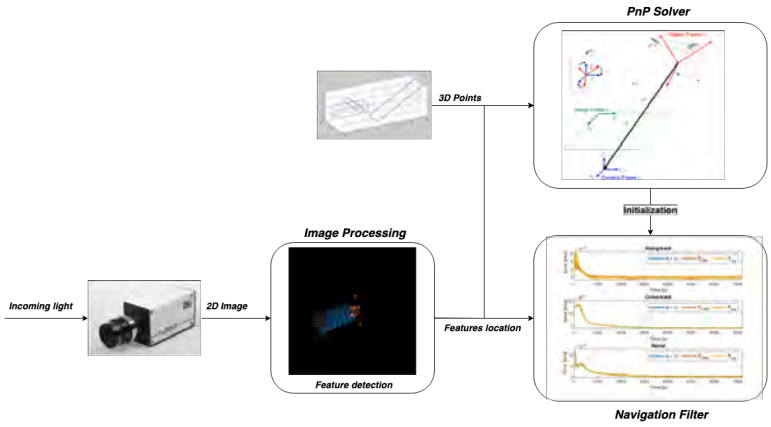

***Fig. 2**: Schematic of the adopted model-based pose estimation scheme.*

Model-based Monocular Pose Estimation

Monocular pose estimation consists in estimating the relative pose of a target spacecraft with respect to the servicer spacecraft by only using 2D images, either taken by a monocular camera or fused from more monocular cameras [2].

A **Model-based** monocular pose estimation method matches features extracted from a 2D image with a wireframe 3D model of the target. The relative pose is obtained by solving the **Perspective-n-Point (PnP)** Problem (Fig.2).

Image Processing (IP)

The proposed IP implements a **Convolutional Neural network (CNN)** to detect *heatmaps* around pre-selected features on the target [3] (Fig.3-4). In addition, a novel method is investigated in which the heatmaps' shape is exploited to derive a covariance representation of the detected features (Fig.5). This is done in order to incorporate feature uncertainties in both the pose estimation step and in the navigation filter [4].

- Refined **Pose Estimation accuracy**
- Reliable **measurements covariance**
- Improved **Filter robustness**

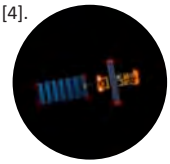

***Fig. 3**: Example of CNN-detected heatmaps.*

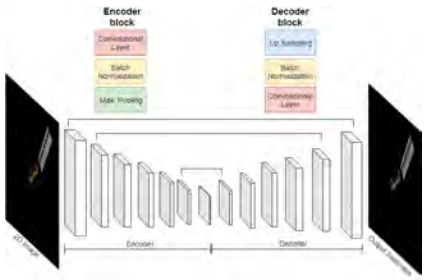

***Fig. 4**: Schematic of the CNN adopted for features detection.*

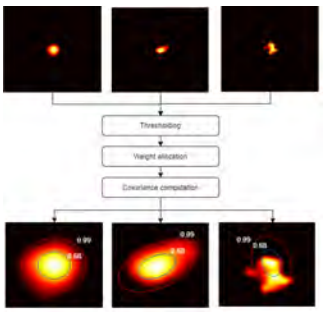

***Fig. 5**: Heatmaps-based covariance computation for each detected feature.*

References

[1] Sharma, S., Ventura, J., and D'Amico, S. [2018]. "Robust Model-Based Monocular Pose Initialization for Noncooperative Spacecraft Rendezvous", Journal of Spacecraft and Rockets, volume 55, No.6, pp. 1-16.
[2] Pasqualetto Cassinis, L., Fonod, R., Gill, E. [2019]. "Robustness and Applicability of monocular pose estimation systems for relative navigation with an uncooperative spacecraft", Progress in Aerospace Sciences, volume 110.
[3] Pasqualetto Cassinis, L. et al. [2019]. "Comparative Assessment of image Processing Algorithm for the Pose Estimation of Uncooperative Spacecraft", International Workshop on Satellite Constellations and Formation Flying, Glasgow, UK.
[4] Pasqualetto Cassinis et al. [2020]. "CNN-Based Pose Estimation System for Close-Proximity Operations Around Uncooperative Spacecraft", in 2020 AIAA Spaceflight Mechanics Conference, Orlando, FL, USA.

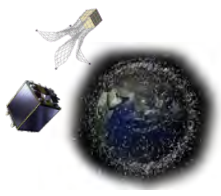

System modelling of a nanoactuator for the Deployable Space Telescope

Víctor Villalba Corbacho
Space Engineering
Space Systems Engineering
Hans Kuiper
Eberhard Gill
V.M.villalbacorbacho@tudelft.nl

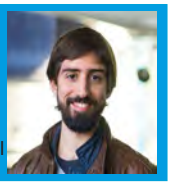

Problem

When designing a space telescope, bigger is better until you have to pay for the launch. A deployable telescope may overcome this by packaging a large optical system in a smaller bundle which unfolds in space, but this comes with drawbacks. One of these drawbacks is the need to position different mirror segments with nanometer repeatability in a dynamic environment. I have a paper explaining all the problems with that, but it is still under review.

Tell me more

For small displacements, which is the case here, the Freedom and Constraint Topologies (FACT) method gives an easy way to visualise the geometries which are possible to realise the degrees of freedom you want. With practical constraints to the attachment points and preserving symmetry, you choose a system that suits the need. Then you go on to materials choice, actuator choice, and onto simulations. Pepper did the stress simulations so we know this mechanism can hold the mirror though launch with a safety margin.

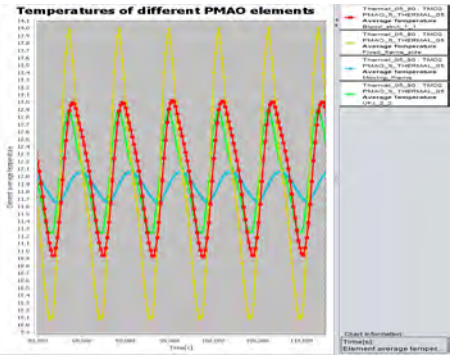

Classical athermalization approaches assume all of these lines are the same.

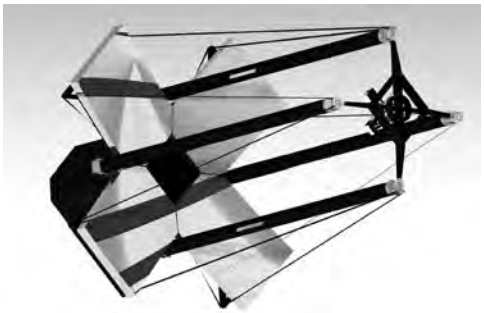

What a deployable telescope could look like.

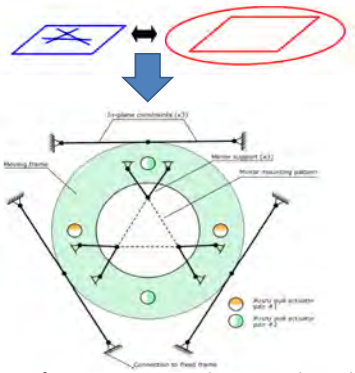

Schematic for an actuation mechanism as derived from FACT representation.

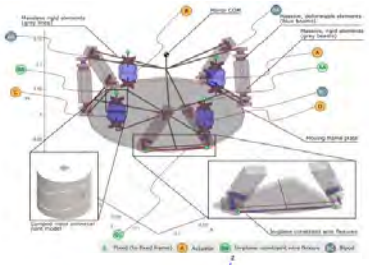

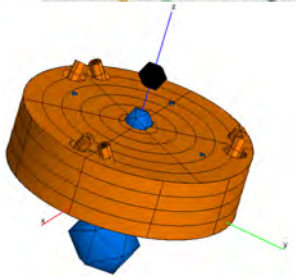

Mechanical and thermal models of the mechanism

Solution

In order to make constant adjustments to the positions of the mirrors, we need a 3 DOF mechanism capable of re-adjusting the mirror. Pepper proposed the latest mechanical design of such mechanism. It is a compliant frame powered by four piezoelectric actuators, which removes backlash, holds the mirror through launch, and has, in theory, angstrom repeatability. The proposed material for the setup its titanium 6Al4V.

Is this worth a Phd?

So far no. There are a few challenges to solve before considering the mechanism is feasible and done. In the portion of space close to Earth you see very large temperature changes between day and night. These changes tend to misalign the mirrors and distort the mechanism through its material's coefficient of thermal expansion. I have modelled these temperature changes for use on the future athermalization techniques. Later I will add that to a thermo-mechanical model to calculate the total drift.

Future plans

After I have the complete drift simulation, I want to reduce the modeling uncertainties. These include the efficiency of the piezoactuators, the distribution of elastic and inertial energy in the mechanism, and the elements of the conductance matrix. Hopefully my next poster will include the experiment I have devised to find these details out. Schematic below.

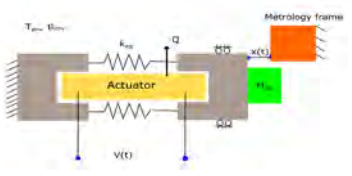

Possible set up to reduce modeling uncertainty. Ask me why it does not work.

References

Villalba, V., Kuiper, H. & Gill, E. Review on Thermal and Mechanical Challenges in the Development of Deployable Space Optics. Submitt. to J. Astron. Telesc. Instruments Syst. Under Rev. (2020).
Pepper, S. M. Design of a Primary Mirror Fine Positioning Mechanism for a Deployable Space Telescope. (Delft University of Technology, 2018).
Hopkins, J. B. & Culpepper, M. L. Synthesis of multi-degree of freedom , parallel flexure system concepts via Freedom and Constraint Topology (FACT) – Part I : Principles. Precis. Eng. 34, 259–270 (2010)
Bely, P. Y. The Design and Construction of Large Optical Telescopes. (Springer, 2003)


TUDelft
Jingna Pan

DEPARTMENT OF AEROSPACE STRUCTURES AND MATERIALS

The mission of the Aerospace Structures and Materials department is making load carrying structures of aircraft and spacecraft lighter, safer, cheaper and more environmentally friendly.

The ASM department researches novel materials, new (hybrid) material combinations, new structural concepts plus combinations there of. To support these objectives, the required (numerical) tools and methods are developed. Traditionally the 3 sections within the ASM department focus on complementary aspects of the mission and via synergy achieve an optimal, efficient and societal relevant implementation of our mission.

The Faculty of Aerospace Engineering has a highly advanced laboratory at it's disposal: the Delft Aerospace Structures & Materials Laboratory.

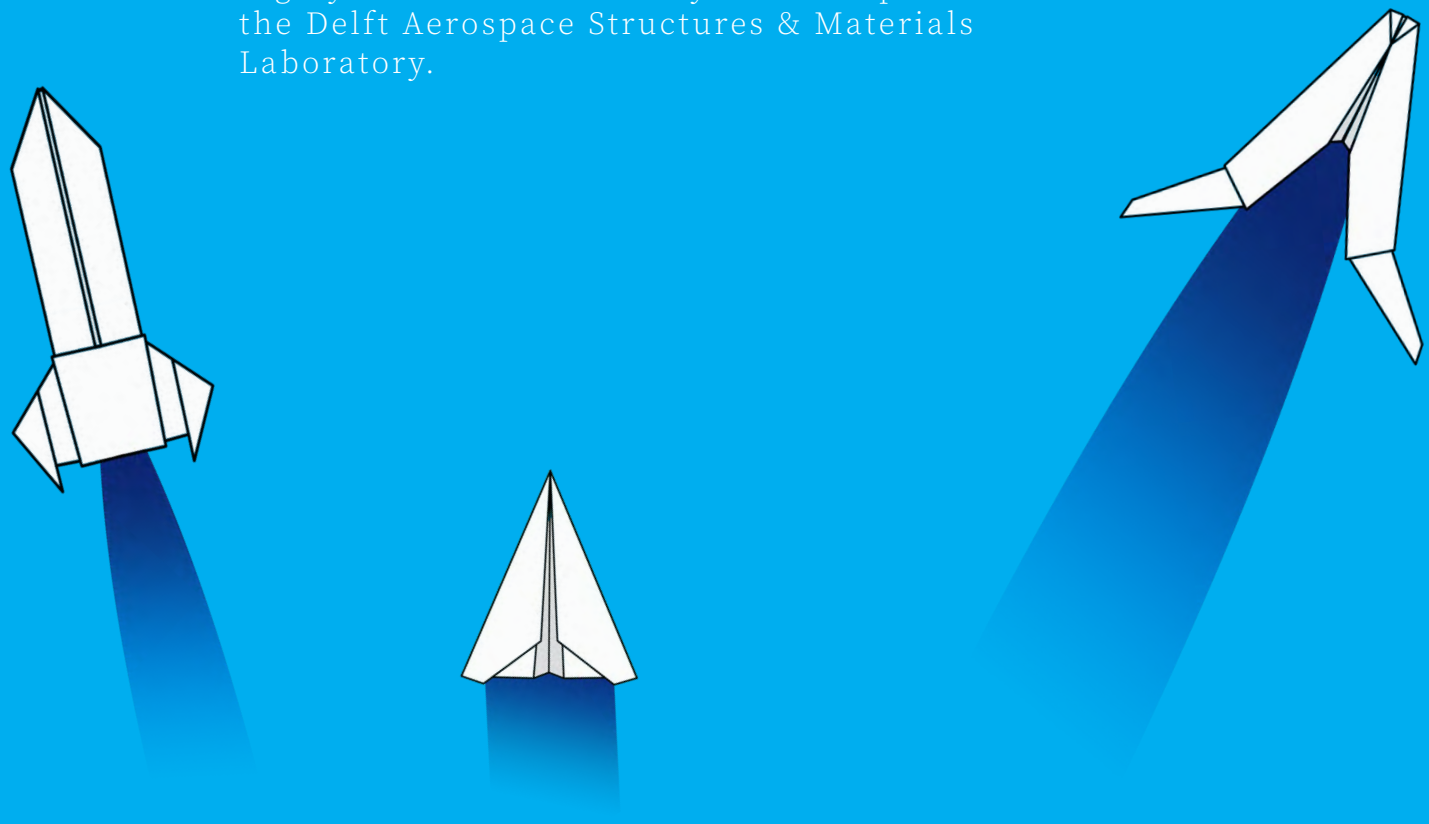

NOVEL AEROSPACE MATERIALS

Satya Ammu
Dimosthenis Giannopoulos
Anton Tuluk
Hugo Veldhuizen

AEROSPACE STRUCTURES AND COMPUTATIONAL MECHANICS

Xiaopeng Ai
Kevin van Dooren
Marta Gavioli
Natália C. Gomes de Paula
Javier Gutiérrez Álvarez
Niels van Hoorn
Andres Jürisson
Paul Lancelot
T. Mkhoyan
Hammad Rahman
Jens Semmelroggen
Bas Tijs
Giorgio Tosti Balducci
Yuqian Tu
Ines Uriol Balbin

STRUCTURAL INTEGRITY AND COMPOSITES

Agnes Broer
Luigi Fazzi
Lubin Huo
Nicolas P. Lavalette
Xi Li
Nakash Nazeer
Hongwei Quan
Eva Smeets
Nan Tao
Jesse van Kuijk
Megan Walker
Xiang Wang
C.M. de Zeeuw

AEROSPACE MANUFACTURING TECHNOLOGIES

Camila B. G. Brito
Ozan Çelik
Ujala Farooq
Deniz Ezgi Gülmez
Anja Haschenburger
Bram Jongbloed
Filipp Köhler
Shichen Liu
Chizoba Josephine Ogugua
Ioannis Tsakoniatis

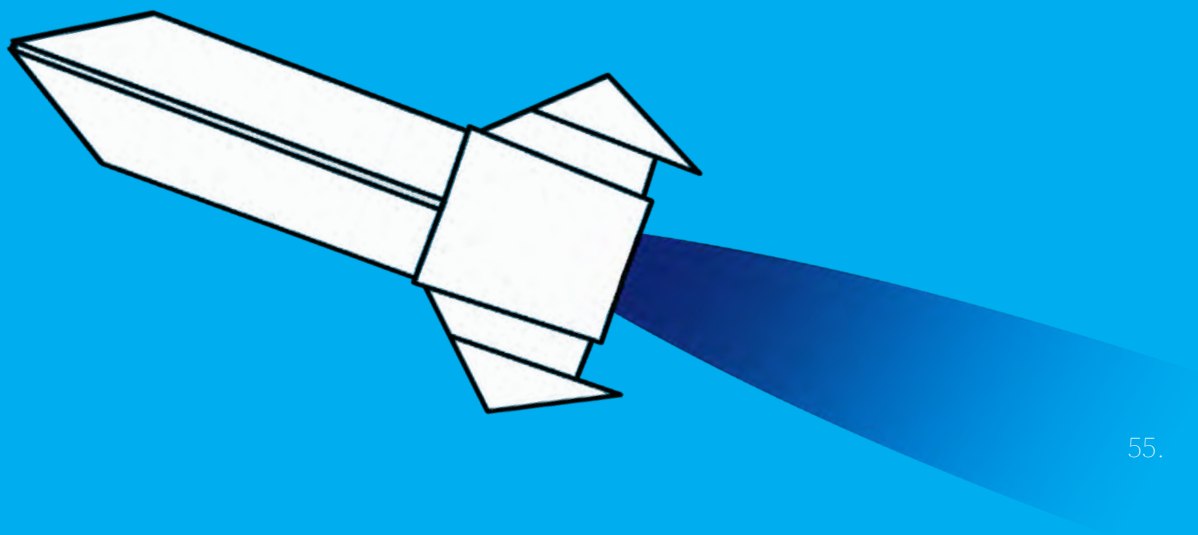

FLEXIBLE, LEAD-FREE ULTRASOUND TRANSDUCERS

Name Satya Ammu
Department ASM
Section NovAM
Daily supervisor Pim Groen
Promotor Pim Groen
S.K.Ammu@tudelft.nl

ASM

1. Goal

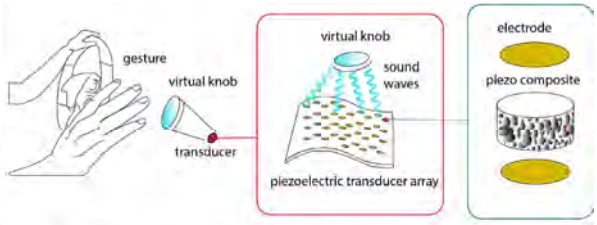

- Flexible piezoelectric transducer array
- Multiple piezo elements generate ultrasound waves
- These sound waves modulated to create pressure points/ shapes mid-air that are reflected back from a gesture

2. Materials and Method

Piezoelectric ultrasound transducers are usually made of *PZT* which is brittle and contain lead (Pb), a Substance of Very High Concern (SVHC))

Currently, most widely studied alternatives *PVDF* has good conformability but low piezoelectric properties (d_{33}) and low Curie temperature which limits their application in commercial applications.

Ceramic-polymer composites

Piezo ceramic powder- $K_{0,485}\ Na_{0,485}\ Li_{0,03}\ NbO_3$

High piezo-properties

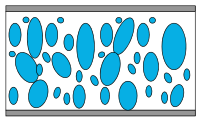

Random (0-3)

optimal combination of the high piezoelectric properties of ceramics with the conformability of polymers

Light weight
Flexible

Polymer- PDMS/ Epoxy/ PVDF

Screen printing composite transducer array

KNLN powder + polymer + solvent

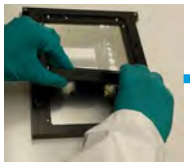

3. Predictions/ Experimental Results

Acoustic power density in [W/m^3]

$$p_{a,\,max} = \pi f_s \eta_{ma} Q_{m0} k^2_{eff} \varepsilon^T E^2_{max}$$

Where f_s = Series resonance frequency

η_{ma} = mechanoacoustic efficiency

Q_{m0} = unloaded mechanical quality factor

k^2_{eff} = Electro mechanical coupling coefficient

ε^T =dielectric constant

E^2_{max} =applicable electric field [V/m]

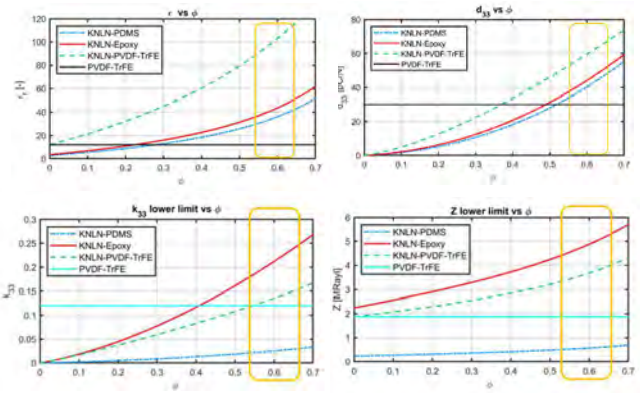

Piezoelectric performance comparison with PVDF

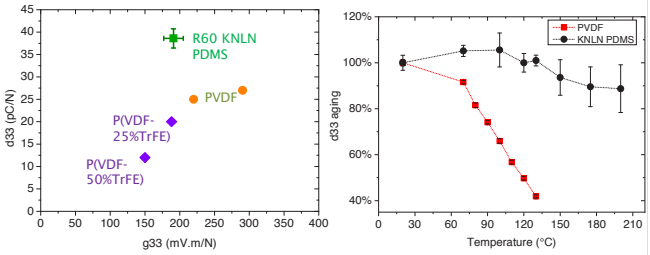

4.Conclusions

Screen printed, flexible composites of KNLN-PDMS show higher d_{33} than commercially available PVDF/ P(VDF- TrFE)

Their acoustic properties need to be verified as per predictions.

Flexibility of printed transducer

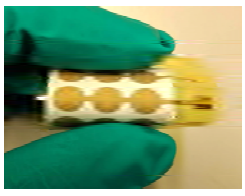

Energy Harvesting

Materials & Designs

Dimosthenis Giannopoulos
Aerospace Structures and Materials
Novel Aerospace Materials
Prof. dr. W.A. (Pim) Groen
D.Giannopoulos-1@tudelft.nl

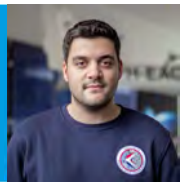

Introduction

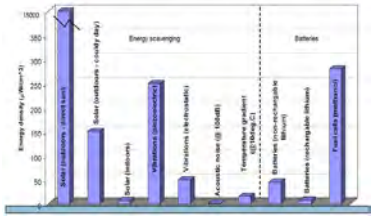

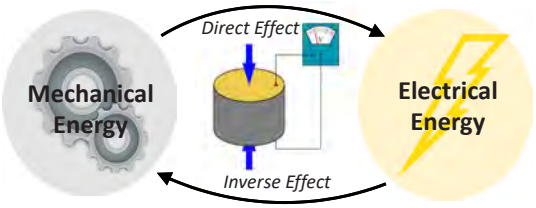

Materials and Methods

- Electrode-carbon paste
- Piezoelectric material-soft PZT
- Crosslinker-epoxy/nickel balls
- Substrate-Pernifer 45

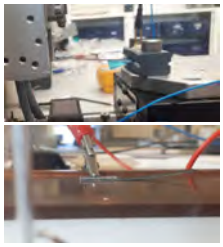

Modelling

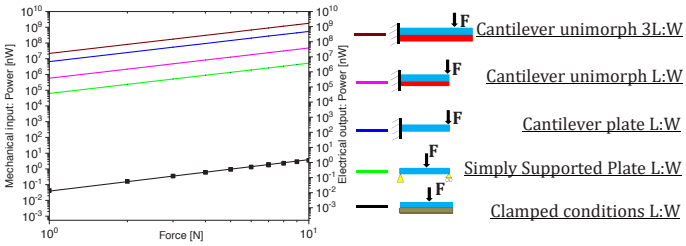

Mechanical characterization

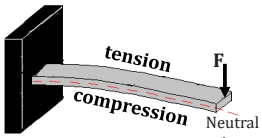

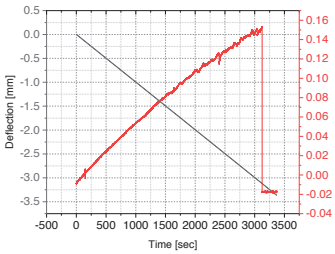

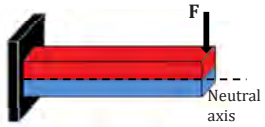

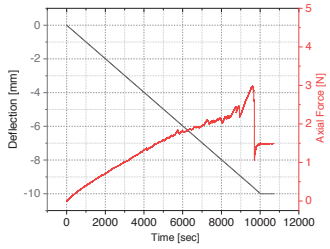

Boundary conditions

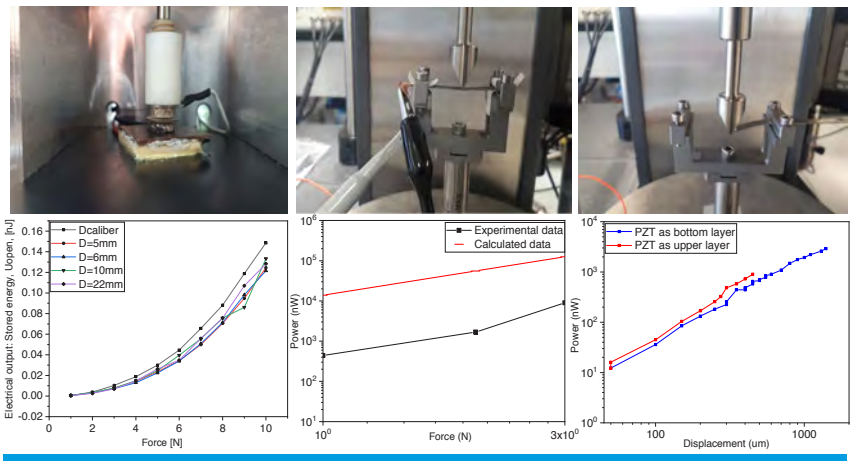

Energy harvesting

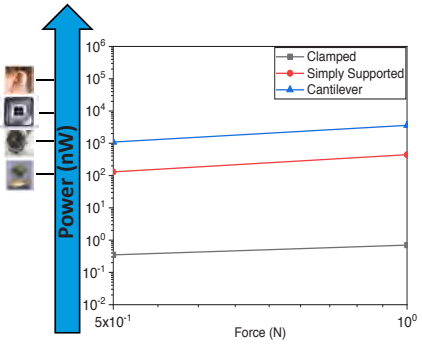

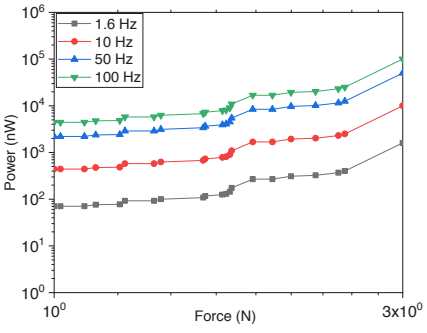

FEA

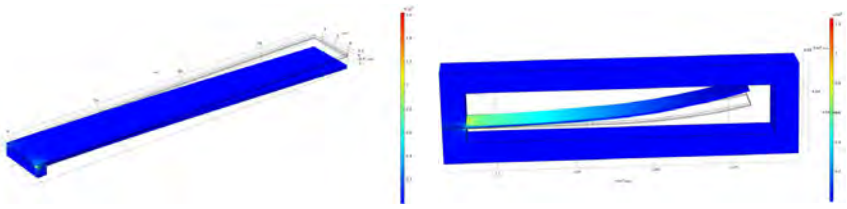

Effects of oxygen annealing on the bismuth ferrite conductivity

Anton Tuluk
Department: ASM
Section: NovAM

Promotor: Pim Groen
A.Tuluk-1@tudelft.nl

Abstract

Bismuth ferrite and solid solutions based on it are promising multiferroic materials for use in sensors and transducers. In particular $BiFeO_3$ is of interest due to the high Curie temperature and the possibility to use it as lead-free high temperature piezoceramics [1]. Although bismuth ferrite was discovered in the late 1950s, obtaining its pure phase is challenging due to the easily forming secondary phases of sillenite ($Bi_{25}FeO_{39}$) and mullite ($Bi_2Fe_4O_9$) [2]. The main problem limiting the use of bismuth ferrite is the high leakage currents. Which may be associated with oxygen defects occurring at the sintering stage. In this work, the effect of annealing in a controlled atmosphere on the conductivity of bismuth ferrite was studied.

Experimental

The raw materials were first grinding separately too increase the reactivity of the oxide powders and after that mixed thoroughly in the aluminum jar with hexane for 5h with stabilized zirconia balls. Obtained powder were dried and calcined in alumina crucibles at different temperatures for 1h. For determined phase purity were used X-ray diffraction with Cu Kα radiation at room temperature. Pre-ground bismuth ferrite powder with the lowest content of secondary phases was used for sintering ceramics prepared in the form of tablets with a diameter of 14 mm axially compressed at a pressure of 150 MPa. Sintering was carried out in air at a heating rate of 600°C/h. For electrical measurements gold electrodes were deposited on ceramic pellets by magnetron sputtering.

Experiment description

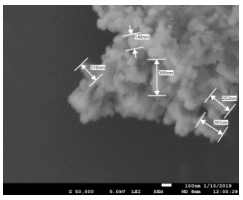

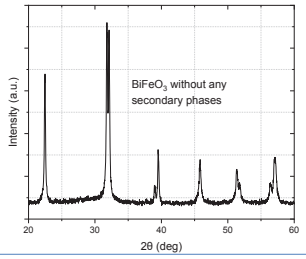

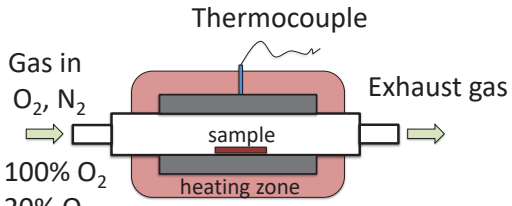

Samples before sintering

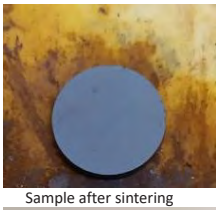

Sample after sintering

Sample after polishing and electroding

The effect of p_{O2} on conductivity $BiFeO_3$

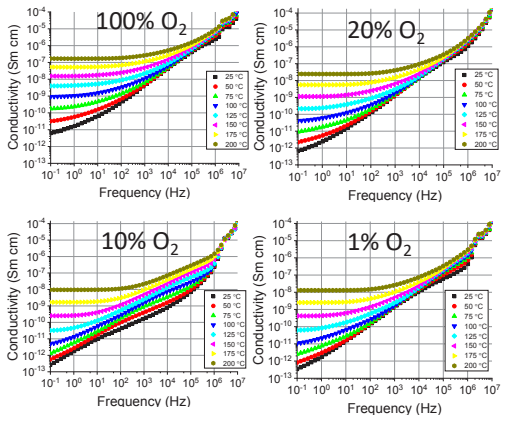

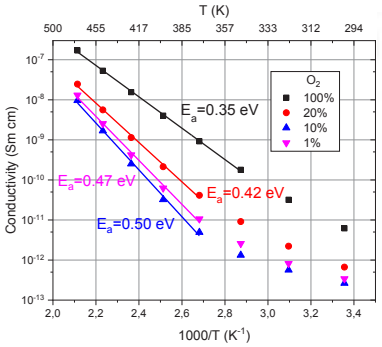

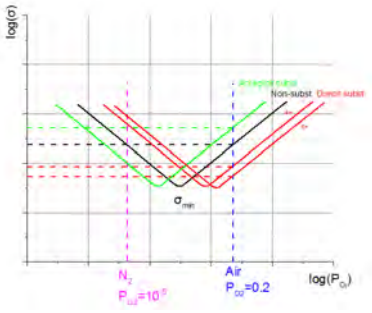

Alleged defective chemistry:

$$2Bi_{Bi}^{X} + 3O_{O}^{X} \xrightarrow{^{o}C} 2V_{Bi}''' + 3V_{O}^{\bullet\bullet} + 2Bi(g) + 3/2O_2(g)$$

$$2Fe_{Fe}^{X} + 1/2O_2(g) + V_{O}^{\bullet\bullet} \rightleftarrows 2Fe_{Fe}^{\bullet} + O_{O}^{x}$$

$$Fe_{Fe}^{\bullet} \rightarrow Fe_{Fe}^{x} + h^{\bullet}$$

Example of doping:

$$TiO_2 + Fe_{Fe}^{X} + 1/2V_{O}^{\bullet\bullet} \rightleftarrows$$

$$\rightleftarrows Ti_{Fe}^{\bullet} + 1/2Fe_2O_3 + 1/2O_{O}^{x}$$

[1] T. Stevenson, D. G. Martin, P. I. Cowin, A. Blumfield, A. J. Bell, T. P. Comyn, P. M. Weaver, *J.Mater Sci: Mater Electron*, 26, 9256–9267 (2015)
[2] T. Rojac, A. Bencan, B. Malic, G. Tutuncu, J.L. Jones, J.E. Daniels, and D. Damjanovic, *J.Am. Ceram. Soc.*, 97 [7], 1993–2011 (2014)

Carbon Dioxide Storage in Porous Organic Polymers

Hugo Veldhuizen[1], Alexandros Vasileiadis[2], Marnix Wagemaker[2], Tadhg Mahon[1], Durga P. Mainali[1], Lishuai Zong[1], Sybrand van der Zwaag[1], Atsushi Nagai[1]

Hugo Veldhuizen
Aerospace Structures & Materials
Novel Aerospace Materials
Dr. Atsushi Nagai
Prof. Sybrand van der Zwaag
H.V.Veldhuizen@tudelft.nl

1. Introduction

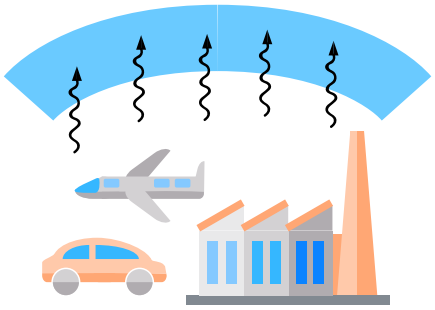

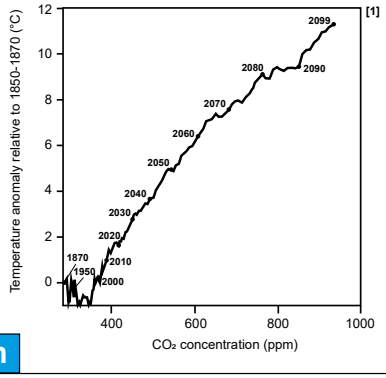

One of the largest challenges of our generation is limiting the increase of CO_2 in the atmosphere. 'Carbon' capture and storage by solid adsorbents is one of the few viable technologies that can mitigate current CO_2 emmisions.

Porous organic polymers have attracted interest in this context due to their nanoporous architecture, chemical and thermal stability, and their precise tunability.

2. Design and Characterization

Design and synthesis conditions

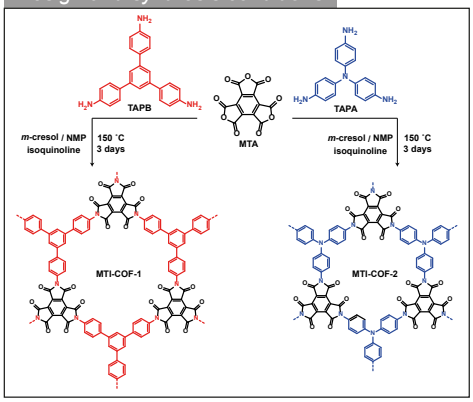

Molecular simulations to predict the crystal structure

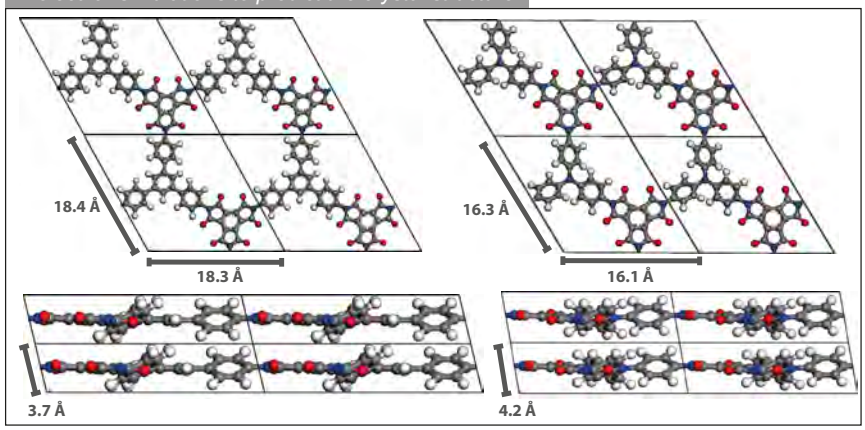

Characterizing porosity by N_2 and CO_2 sorption

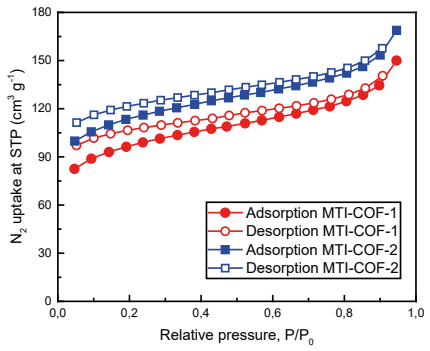

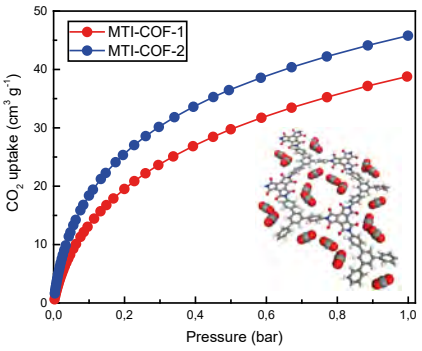

- Interestingly, both N_2 and CO_2 gas adsorbed better to **MTI-COF-2** than to **MTI-COF-1**, possibly due to the larger *c* parameter in the predicted crystal structure.
- Measured CO_2 capacities are on par with state-of-the-art porous polymers.

Visualizing microstructure by scanning electron microscopy

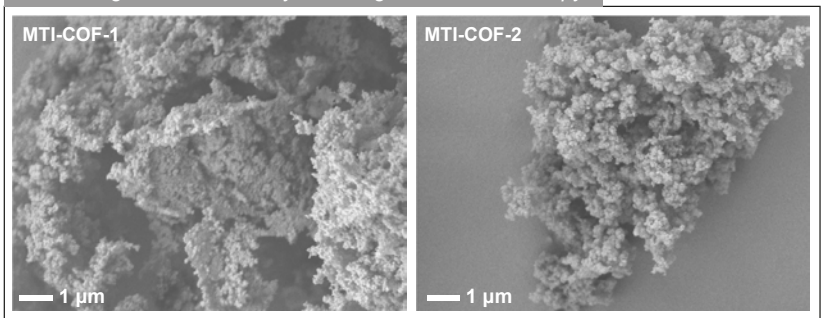

3. Conclusion and Outlook

- Two novel porous polymers have been synthesized that show good stability and excellent CO_2 adsorption capacities.[2]
- The next challenge will be the selective adsorption of CO_2 over water vapour.

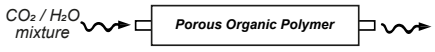

[1]Novel Aerospace Materials, Technische Universiteit Delft, Kluyverweg 1, 2629GB Delft, The Netherlands
[2]Storage of Electrochemical Energy, Technische Universiteit Delft, Mekelweg 15, 2629 JB Delft, The Netherlands

[1] IPCC, 2018: Global Warming of 1.5°C.
[2] H. Veldhuizen, A. Vasileiadis, M. Wagemaker, T. Mahon, D. P. Mainali, L. Zong, S. van der Zwaag, A. Nagai, *J. Polym. Sci. Part A: Polym. Chem.* **2019**, *57*, 2373-2377.

C1 Floating Node Method for the Modelling of Composites Damage and Failure

PhD Candidate: Xiaopeng Ai
Department: ASM
Section: ASCM
Daily supervisor: Dr. B. Chen
Promotor: Prof. Dr. C. Kassapoglou
Contact: x.ai@tudelft.nl

1 2 3 4

Background

Damage and failure predictions are indispensable for the design of composite structures. Floating Node Method (FNM) has demonstrated superior performance in capturing the complex crack networks that are developed during the progressive failure of composites. However, the high density of mesh needed to resolve the cohesive zone length for delamination prediction using cohesive elements makes the method computationally expensive.

Current status of FNM

The Floating Node Method is a discrete crack method which explicitly represent cracks in existing FE meshes through the use of additional Degrees of Freedom (DoFs) and element partitioning techniques.

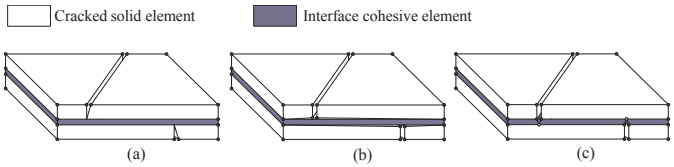

Figure 1: Three-dimensional coupling between matrix cracks and delamination

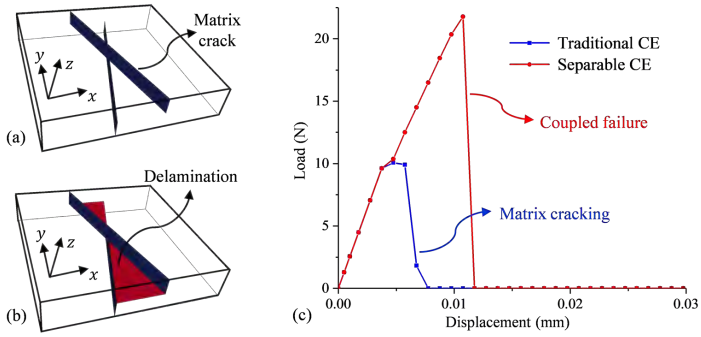

Figure 2: Comparison of numerical results between traditional CE and SCE

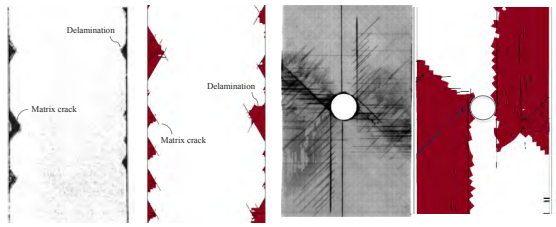

Figure 3: Comparison between experimental observations and numerical predictions

References

[1] B. Y. Chen, T. E. Tay, S. T. Pinho, and V. B. C. Tan, "Modelling the tensile failure of composites with the floating node method," Comput. Methods Appl. Mech. Eng., vol. 308, pp. 414–442, Aug. 2016
[2] B. Y. Chen, T. E. Tay, S. T. Pinho, and V. B. C. Tan, "Modelling delamination migration in angle-ply laminates," Compos. Sci. Technol., vol. 142, pp. 145–155, Apr. 2017.
[3] X. Lu, B. Y. Chen, V. B. C. Tan, and T. E. Tay, "A separable cohesive element for modelling coupled failure in laminated composite materials," Compos. Part A Appl. Sci. Manuf., vol. 107, pp. 387–398, Apr. 2018.
[4] R. Russo and B. Chen, "Higher Order Adaptively Integrated Cohesive," Proc. 18th Eur. Conf. Compos. Mater., no. June, pp. 24–28, 2018

C1 FNM: idea and tasks

The main idea of the proposed research in overcoming the efficiency bottleneck of FNM is to incorporate a recent CE technology into the FNM. The new CE has been shown to be able to overcome the cohesive zone limit, which enabled the use of CEs ten times larger than the current CE size.

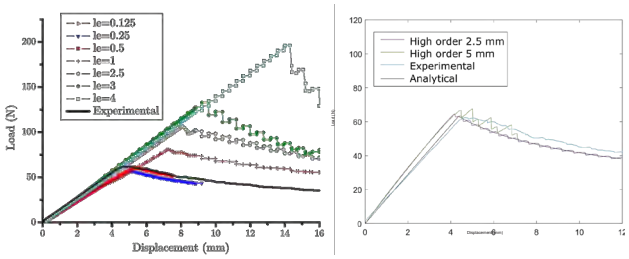

Figure 4: DCB load-displacement curves predicted with linear CEs (left, Turon et al. 2007) and C1 CEs (right, Russo & Chen 2018)

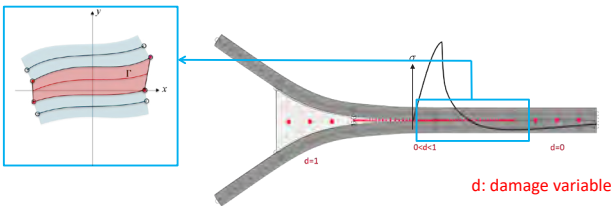

Figure 5: Adaptive integration and Cubic C1 CE

Plan of actions:
- Implement a C1-continuous triangular thin shell element for composite plies
- Develop a C1-continuous triangular adaptively-integrated CE for delamination
- Incorporate the elements of shell & cohesive into the FNM

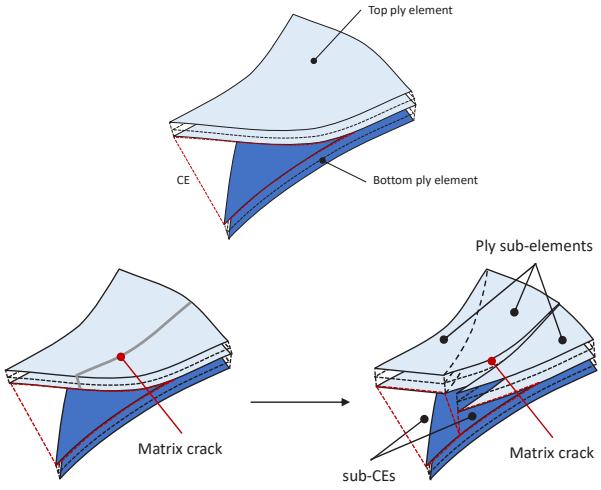

Figure 6: Incorporation of C1 ply & cohesive elements into FNM: partition with respect to a matrix crack

LAB-IN-A-BOX:
HANDS-ON EXPERENCES IN AEROSPACE STRUCTURES

Marta Gavioli
Department: ASM
Section: ASCM
Supervisor: C Bisagni
Promotor: C Bisagni
Contact: mgavioli@tudelft.nl

Laboratory learning activities are hands-on experiences that introduce students to experimental procedures, tools and equipment proper of the discipline.

STRUCTURES

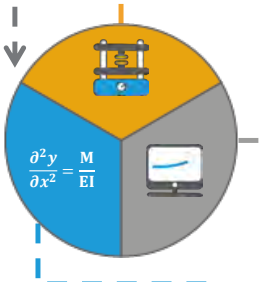

NUMERICAL MODELLING

ANALYTICAL MODELLING

At **bachelor level**: students tend to focus only on the maths (differential calculus, matrix algebra), they struggle with visualising the **phenomena behind the formula.**

EXPERIMENTAL WORK

The activity effectiveness **depends**, among many factors, on the **learning tasks** and the **instructional approach.**

However, lack of resources and time make it challenging to provide students with enough and meaningful experimental practice.

LEARNING GOALS

- **DEVELOPING EXPERIMENTAL ABILITIES:** Students learn how to use experimental tools and procedures.
- **DEVELOPING SCIENTIFIC APPROACH TO ENQUIRY:** Students learn how to design experimental investigations and train evidence-based reasoning.
- **REINFORCING CONTENT:** Students gain a better understanding of the disciplinary concepts linking theory to practice.

DESIGN-BASED RESEARCH METHODOLOGY

Aimed both at testing and refining learning theories and also advancing teaching practice.

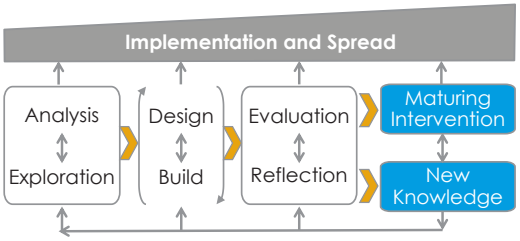

McKenney, S., Reeves, T. C. (2019). Conducting Educational Design Research.

LEARNING MATERIAL

- Inquiry-based instruction engage students in the learning process.
- Experimental practice provides new explanatory mechanisms to be used in the learning process.
- Coordinating multiple representations scaffolds the intertwining of model-based and evidence-based reasoning, improving conceptual understanding.

BEAM BENDING PORTABLE SET-UP

- Students can observe and measure the deflection of the beam under different load and boundary conditions.
- Lab-in-a-box provides several components, leaving students free to set up the experiment.
- Low cost, portable (in class or at home), team of 2/3 students can work together.

ASM

TU Delft

4TU. CENTRE FOR ENGINEERING EDUCATION

Ecolonomical Design of Novel Composite Wing Structures

Natália C. Gomes de Paula
Department: ASM
Section: ASCM
Daily Supervisor and Promotor:
Assoc. Prof. Roeland De Breuker
N.C.GomesdePaula@tudelft.nl

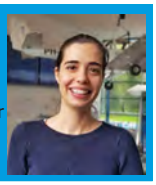

1 Background

Although transport aircraft wing structures are nowadays highly optimized, environmental aspects are only weakly integrated into design. The increasing demand for sustainable aviation, however, puts forward the need for considering environmental impacts at earlier design stages and using a more comprehensive approach than only accounting for flight emissions. Life cycle assessment (LCA) [1] is a methodology well-established in other sectors that has been gradually applied in the aeronautical industry and which complies with such requirements. Within the scope of an LCA study, all inputs from and all outputs into the environment are computed throughout the product life.

Apart from bringing environmental considerations into design, another central aspect of the ecolonomical concept is the economic viability. Therefore, the trade-offs occurring between cost and environmental impact minimization, and possibly with other design objectives, as the structural weight, are to be taken into account.

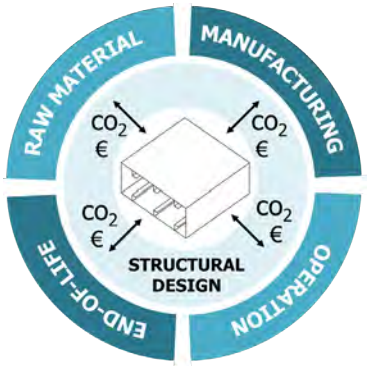

The project investigates an integrated design approach which considers cost and environmental constraints.

2 Objectives

The PhD project aims to develop an integrated tool for aerostructural optimization that includes economic and environmental analysis at a preliminary design stage, which:

- provides enough flexibility for the evaluation of novel technologies;
- accounts for changes and impacts at all phases of the life cycle;
- enables scenario-based sensitivity analysis for technology assessment;

This research is part of the EcoDesign Solutions consortium, which works on a multiscale approach to address and incorporate sustainability throughout the aircraft development cycle, including the study of novel materials, manufacturing techniques, and required changes in the structural design process.

3 Approach and Current Work

Current work focuses on how to estimate the costs and the environmental impacts occurring during the manufacturing stage. A unified process-based approach is considered for both assessments and combines unit operations to compose a preliminary manufacturing plan. The unit operations include the main processes for the fabrication of a single component, the assembly of components as a part, and quality inspection procedures. The time required for the execution of a process is the main parameter quantified and is highly influenced by the part complexity [2]. The integration of this preliminary manufacturing plan into a structural sizing tool will enable the identification of the main ecolonomical drivers and the distinction between alternative design concepts.

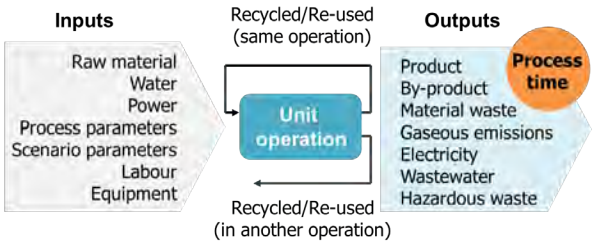

Diagram defining a unit operation. The illustration is based on the representation provided in [3].

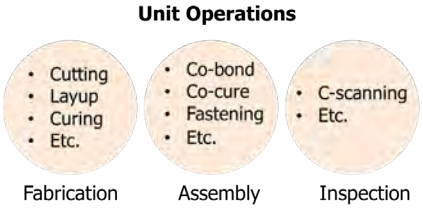

Examples of unit operations within each category.

4 References

[1] International Organisation for Standardization, ISO 14040:2006(E), *"Environmental management – Life cycle assessment – Principles and framework"*, Standard, 2006.

[2] Gutowski, T., Hoult, D., Dillon, G., Neoh, E.-T., Muter, S., Kim, E. and Tse, M., *"Development of a theoretical cost model for advanced composite fabrication"*, Composites Manufacturing, Vol. 5, No. 4, pp. 231-239, 1994.

[3] Choi, A. C. K., Kaebernick, H., and Lai, W. H., *"Manufacturing processes modelling for environmental impact assessment"*, Journal of Materials Processing Technology, Vol. 70, No. 1-3, pp. 231-238, 1997.

THERMOMECHANICAL BUCKLING FOR AEROSPACE APPLICATIONS

Javier Gutiérrez Álvarez
ASM
ASCM
Daily sup.: Chiara Bisagni
Promotor: Chiara Bisagni
j.gutierrezalvarez@tudelft.nl

HEAT AS A MORPHING TRIGGER

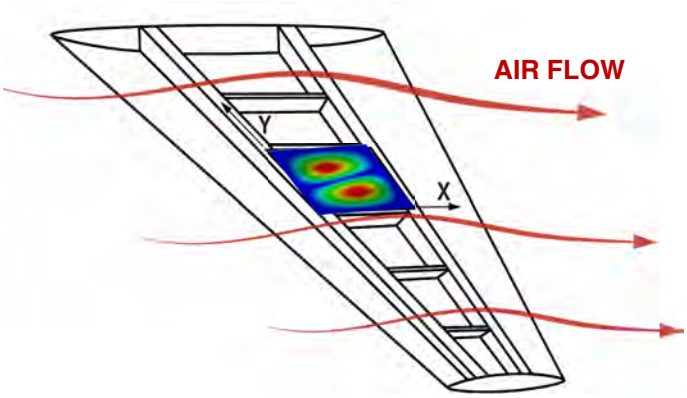

Research Objectives

- Study **thermomechanical buckling** and use it for **passive morphing / shape change** in **supersonic** regime.
- Research approach:
  Analytical +
  Numerical +
  Experimental

THERMAL BUCKLING AND MODE JUMPING EXPERIMENTS

HEATING DIAGRAM
AS4/8552, $[30/-30/5/-5]_s$

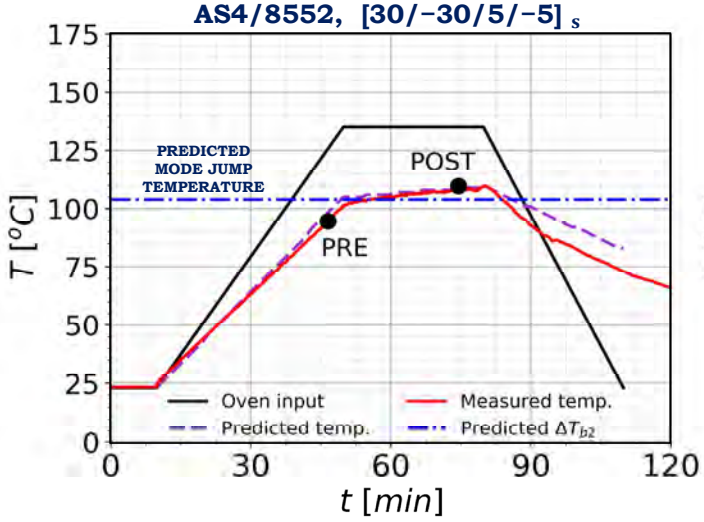

DEFLECTION CURVES FOR DIFFERENT PLATES

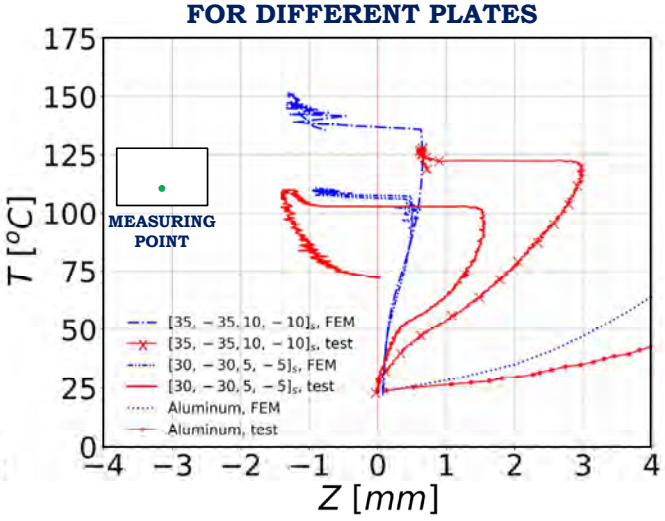

BUCKLING SHAPES

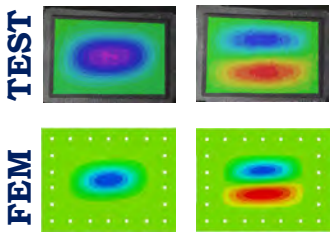

TEST SETUP

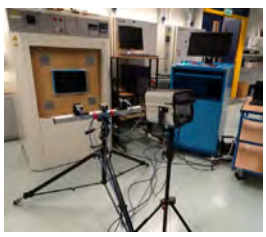

FUTURE WORK

- TEST: Mode jumping in **mechanically loaded** and **heated plates**
- APPLICATION: **change of shape / morphing** in aerospace structures

ASM

System Identification of Flexible Aircraft

Andres Jürisson
Department: ASM
Section: ASCM
Supervisor: Dr. ir. R. De Breuker
Supervisor: Dr. ir. C. De Visser
Promotor: Dr. ir. R. De Breuker
Contact: A.Jurisson@tudelft.nl

Background

The pursuit for improvement in performance and efficiency is pushing the aircraft designs towards higher aspect ratios while using lighter materials. This also results in aircraft with a closer interaction between the rigid-body responses and the structural dynamics. The traditional system identification approaches, used for determining the aircraft stability coefficients etc., assume that the aircraft is perfectly rigid and therefore are not able to accurately capture this interaction and the effects on aircraft response and loads .

Objective

Develop a methodology for obtaining a flight mechanics and loads model from a flexible aircraft flight test data in unsteady airflow conditions.

Why?

- Improve the understanding of the aircraft
- Validate the numerical models
- Expand the aerodynamic model coverage
- Monitor aircraft health
- Improve controller design

How?

1) Acquire system responses

Measure the aircraft responses to various manoeuvers at different flight conditions.

2) Determine suitable model structure

Find a model structure which can capture the dynamics of interest.

3) Estimate the parameters

Determine parameters of the model that would minimize the difference between the measured response and the response predicted by the model.

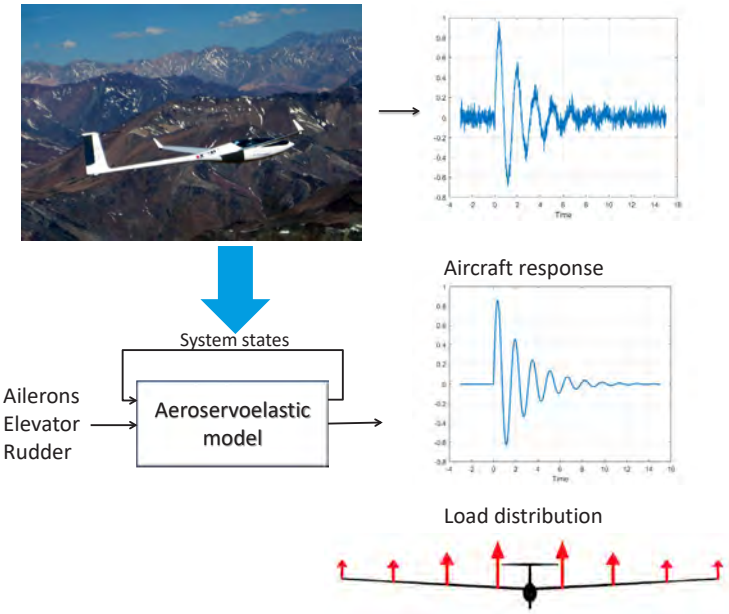

Challenges

- How to measure the structural dynamics?
- How to model and capture the unsteady aerodynamics?
- What are the required changes to conducting flight testing?
- How sensitive is the resulting model to modifications of the aircraft?

Test platform for research

- Diana 2 (1/3 scale) glider drone
- 5 m wingspan
- 24.8 aspect ratio
- Electric engine for take-off
- Extended sensor suite

Acknowledgements

This research project is conducted in collaboration with Netherlands Aerospace Centre (NLR).

Transonic Flight and Movables Loads Modelling for Wingbox Sizing

Paul Lancelot
ASM
ASCM
Dr.ir. Roeland De Breuker
Prof. Chiara Bisagni
p.m.g.j.lancelot@tudelft.nl

Non-linear unsteady hybrid aeroelastic model

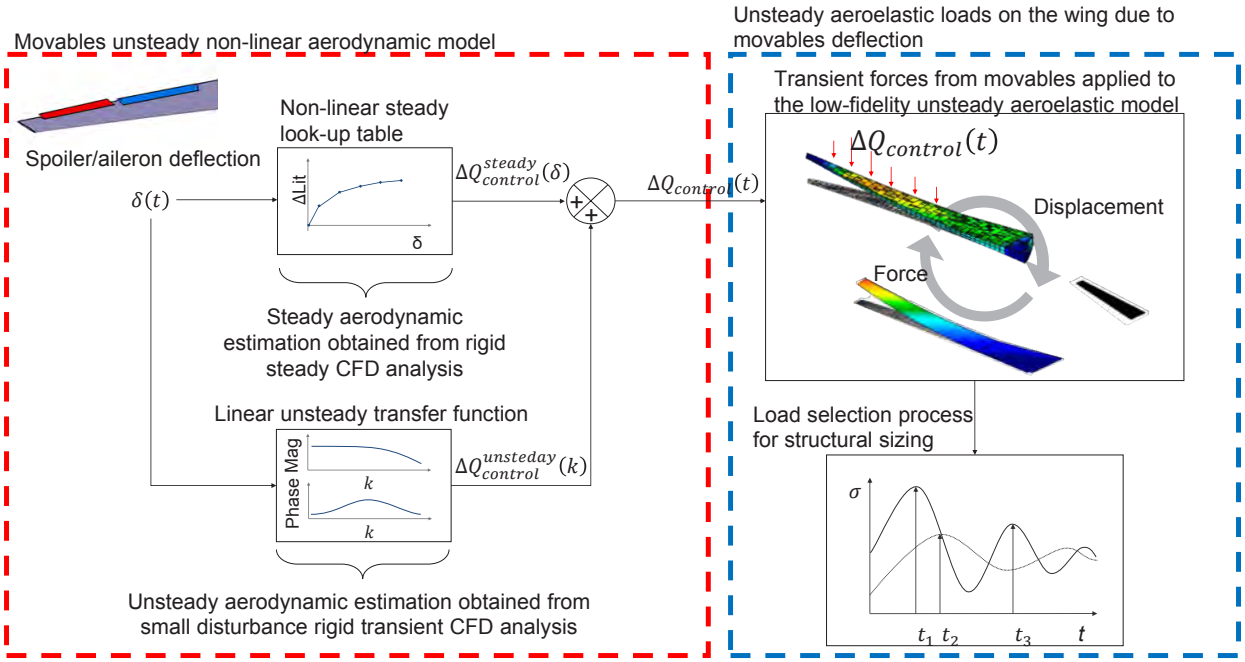

Accuracy of the hybrid model against high-fidelity results

Transonic dynamic high-fidelity simulation (FLUENT/NASTRAN)

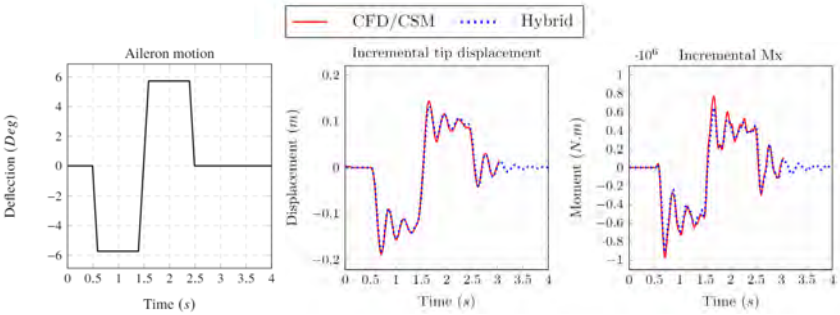

Influence of the aerodynamic fidelity on the aircraft GLA

Feed-forward gust load alleviation system (GLA):

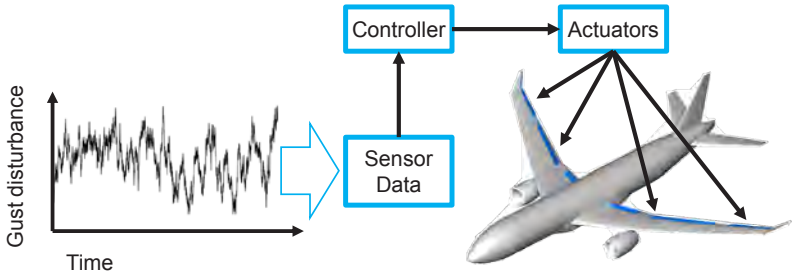

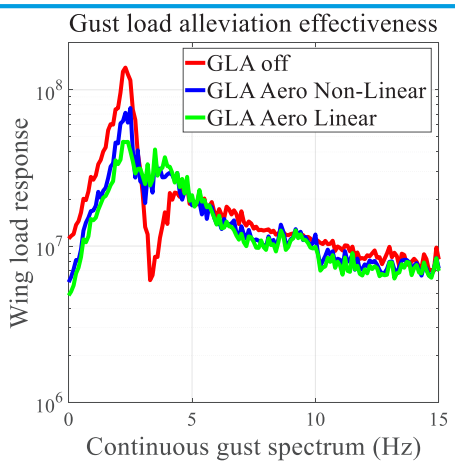

Fast Symmetry Detection with Deep Learning and GeConv

SMART-X

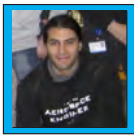

PhD Candidate: T. Mkhoyan
Department: ASM
Supervisor 1st: Dr.ir.R. De Breuker
Supervisor 2nd: Dr.ir.C.Visser
Promotor Dr.ir.R. De Breuker
Contact: T.mkhoyan@tudelft.nl

ASM

Aim

This study: Develop Fast 2-axis reflectional symmetry detection routine for estimation of aircraft wing orientation. Two methods developed and compared: traditional computer vision (*GeConv*) versus pure Deep learning (*RotNet*).

High level: Robust machine learning pipeline for prediction of wing deflection for aeroservoelastic control from raw images.

The Experiment

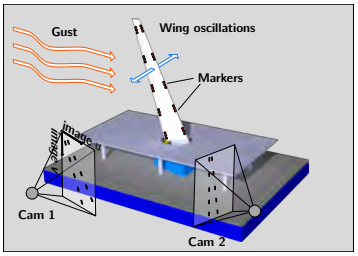

Visual based model-free control

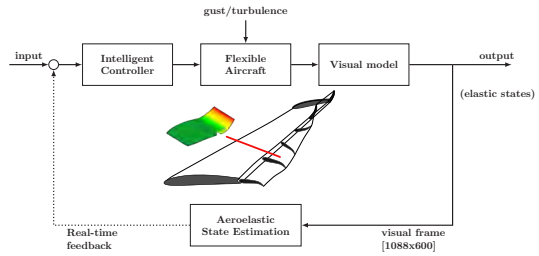

GeConv

Image filters and clustering (DBSCAN):

Sort and rotate points:

$$\mathbf{P}_{\theta hull} = sort(\mathbf{P}, sort(\boldsymbol{\theta}_{cp_k})); \ \mathbf{R} = \begin{bmatrix} \cos(\theta_k) & -sin(\theta_k) \\ \sin(\theta_k) & cos(\theta_k) \end{bmatrix}$$

Geometric convolution and symmetry score:

$$\mathbf{P}_{\theta_k} = (\mathbf{R} \cdot (\boldsymbol{\theta}_{\mathbf{k-1}} - \boldsymbol{\theta}_{cp})^T)^T + \boldsymbol{\theta}_{cp}$$

$$\theta_{Vsymm} = min(|mean(|\sin(|\boldsymbol{\theta}_{k_{cp}}|)|)|), \theta_{Vsymm})$$
$$\theta_{Hsymm} = min(|mean(|\cos(|\boldsymbol{\theta}_{k_{cp}}|)|)|), \theta_{Hsymm})$$

GeConv: Geometric Convolution process

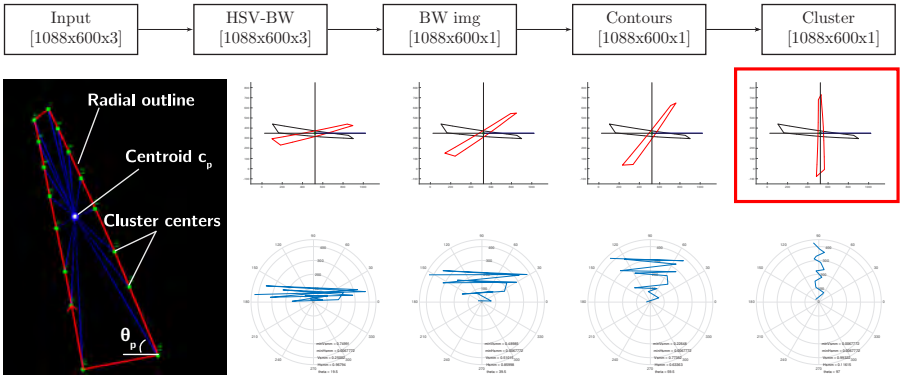

DCNN structure

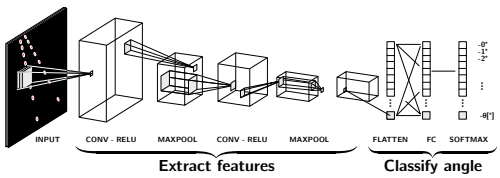

DCNN: training Deep Convolutional Neural Network

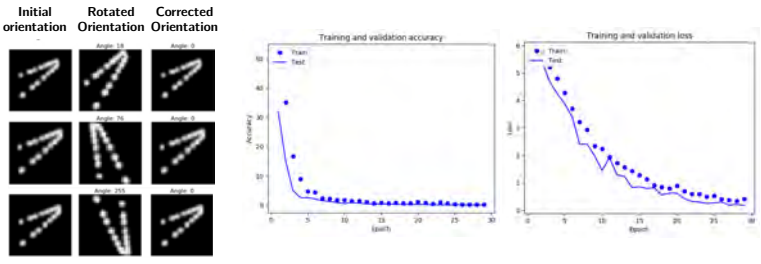

Planning Smart-X

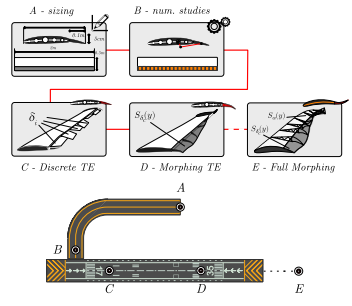

Current work with DCNN

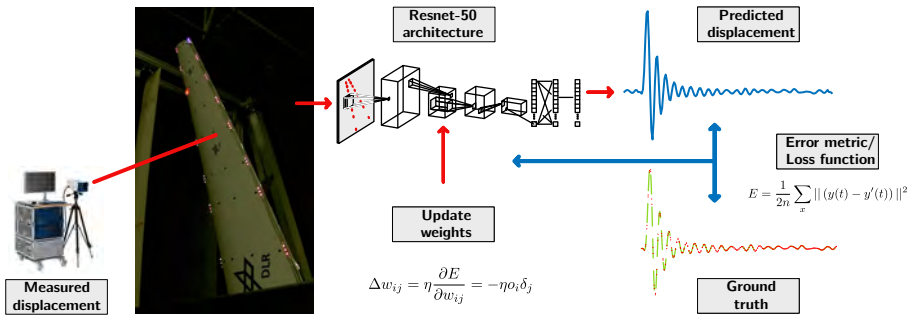

Aeroelastic Tailoring and Performance Optimization through Wing Box Material, Inner Layout and Shape Optimization

PhD Candidate: Hammad Rahman
Department: ASM
Section: ASCM
Daily supervisor: Saullo Castro
Promotor: Roeland De Breuker
h.rahman@tudelft.nl

Introduction

The weight of the aircraft can be reduced by controlling its wing aeroelastic performance and it is the prime focus of aircraft designers because of the associated fuel savings. The wing aeroelastic performance can be controlled by passively alleviating its aeroelastic loads. These loads are highly dependent on the stiffness of the wing, which is a function of wing material, its shape and internal structural layout.

A significant amount of work has been done on stiffness tailoring of the wing material. Hence the next steps are to investigate the possibility of passive loads alleviation by tailoring the inner structure of the wing and carrying out simultaneous performance optimisation through shape optimisation.

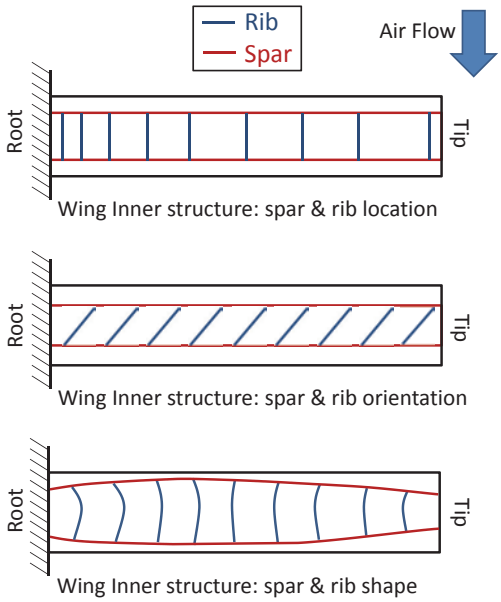

Research Goals

This PhD project aims to achieve following objectives:

- Investigation of variation in sizing parameters including thickness and shape of the spar, rib and stiffener on wing aeroelastic performance
- Optimization of sizing parameters, orientation, numbers and location of spar, rib and stiffener, simultaneously
- Investigation of mutual influence of inner wing box layout tailoring and skin material stiffness tailoring (straight & tow-steered fibers)
- Investigation of wing sweep and taper ratio on stiffness distribution
- Simultaneous optimization of wing shape and stiffness

Expected Work

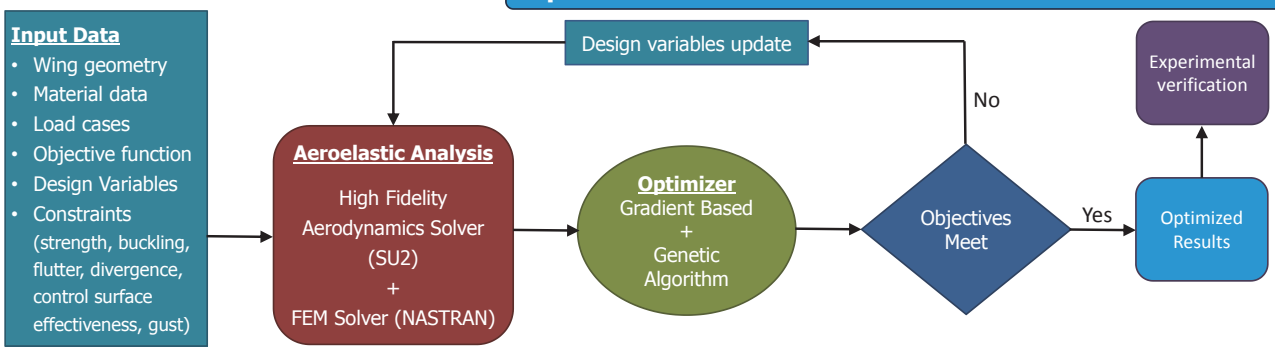

[1] Sodja, J., Werter, N. and De Breuker, R. (2018) 'Design of a flying demonstrator wing for manoeuvre load alleviation with cruise shape constraint', (January), pp. 1–16. doi: 10.2514/6.2018-2153
[2] Francois, G., Cooper, J. E. and Weaver, P. M. (2016) 'Impact of the wing sweep angle and rib orientation on wing structural response for un-tapered wings', 57th AIAA/ASCE/AHS/ASC Structures, Structural Dynamics, and Materials Conference. doi: 10.2514/6.2016-0472.
[3] Francois, G., Cooper, J. E. and Weaver, P. M. (2015) 'Aeroelastic tailoring using Rib/spar orientations: Experimental investigation', 56th AIAA/ASCE/AHS/ASC Structures, Structural Dynamics, and Materials Conference. doi: 10.2514/6.2015-0439.

Analysis and test of a thermoplastic composite welded joint

Name	Jens Semmelroggen
Department	ASM
Section	ASCM
Daily supervisor	Prof. C. Bisagni

J.M.Semmelroggen@tudelft.nl

1 | 2 | 3 | 4

Introduction

The use of thermoplastic composites to manufacture aircraft primary structures promise cost reductions during manufacture due to the ability to use various welding techniques. The behaviour of welded joints during crash scenarios is not well understood. Experiments can be used to reduce the uncertainty posed by these novel joining methods. The objectives of this work are to:

- Develop a methodology to predict the behaviour of welded joints subjected to loads encountered during a survivable crash scenario and determine if welding is sufficient for use in critical joints.
- Compare the performance of welds to fasteners in critical joints.

The two welded joints of interest for this work are the conduction welded joints identified in the figure on the right.

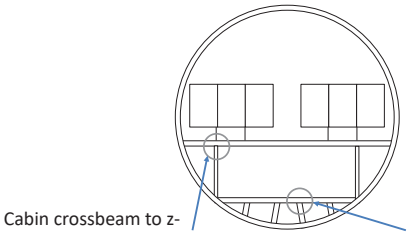

Methodology

A combination of numerical and experimental testing will be used to investigate the failure behaviour of the welded joint.
A numerical drop model of a fuselage section “Global Model” is used to obtain loads acting on the welded joint under investigation. Loads obtained from the Global Model are applied to a higher fidelity local model incorporating the welded interface. To validate the methodology, a simplified joint is to be designed and tested.

Figure: Global model. Parts connected with rigid ties

Figure: Local model. Parts connected with TIEBREAK contact

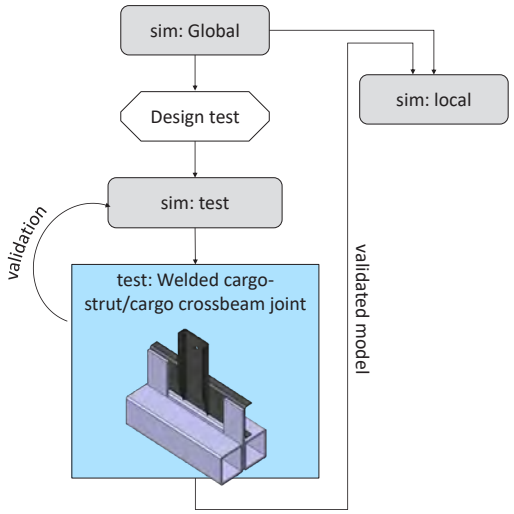

Figure: Flow chart of experimental and numerical approach

Present Work

The focus of the current work is with the design of the experimental setup to test the welded joint. The test should provide a level of abstraction of the loading experienced by the real welded joint. Key requirements for the test setup include:

- The test setup should provide a representative loading case.
- The ability to study the effect of different ratios of mode I an II opening modes on the strength of the joint.
- The ability to test welded as well as fastened joints.

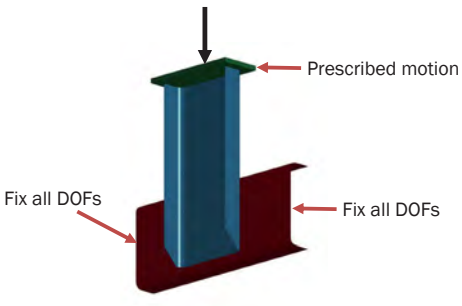

Figure: Finite element model for exploring test concepts

This project has received funding from the Clean Sky 2 Joint Undertaking under the European Union's Horizon 2020 research and innovation programme under grant agreement No 776455.

Horizon 2020 European Union Funding for Research & Innovation

Virtual testing of thermoplastic composites

Matrix dominated failure of thermoplastic composites and welded joints

Bas Tijs
Company : GKN Fokker
TU Delft dep. : ASM - ASCM
Supervisor : Prof. C. Bisagni
Dr. A. Turon
Email : Bas.Tijs@fokker.com

1 | 2 | 3 | 4

Research objective

Research objective:
"The objective of this research is to accurately predict matrix dominated failure of thermoplastic composites and welded joints while taking into account the influence of the manufacturing process."

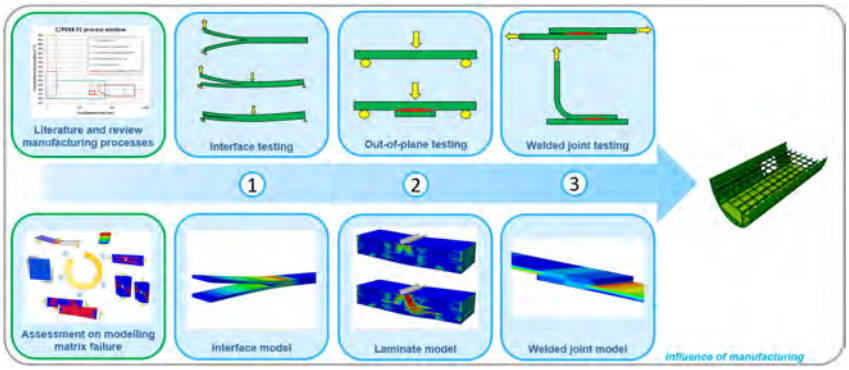

Modelling matrix failure

The simulation strategy developed and validated for thermoset composites in [1] has been implemented in a **new numerical framework** to evaluate **thermoplastic composites**. It was found that special attention needs to be paid to **matrix dominated failure modes** due to the much **higher fracture toughness and ductility** of the material and that traditional strain based **continuum damage models** have difficulty in accurately predicting the **highly complex failure mechanisms** and their interactions during **large deformations**.

The new continuum damage model is able to accurtely predict the failure mode of an open-hole tension test and thermoplastic welded single lap shear joint as shown in Figure 1 and 2. The internal failure modes are dominated by large shear deformations within the ply splits and a strong interaction with delaminations is observed.

Open-hole tension strength

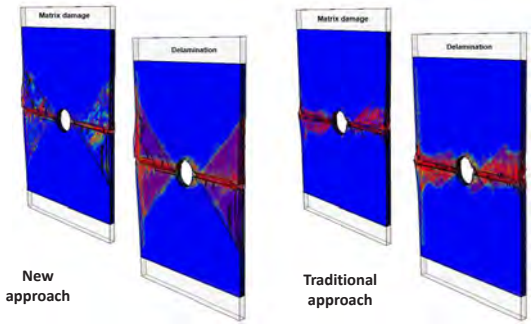

Figure 1: Failure mode of an open-hole laminate [2]

Shear strength of welded joints

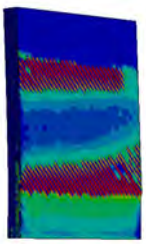

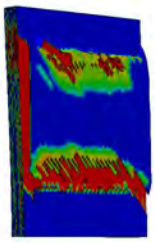

Matrix splitting (before coupon failure)

Delamination of first ply (after coupon failure)

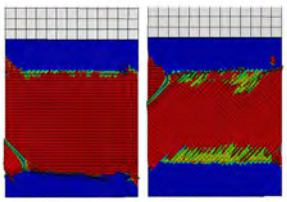

Simulation

Experiment

Figure 2: First ply peel-off in welded single lap shear coupon

[1] B.H.A.H. Tijs, C.S. Lopes, A. Turon, C. Bisagni, J. Waleson, J.W. van Ingen and S.L. Veldman, Virtual Testing of Thermoplastic Composites: Towards a Hybrid Simulation-Physical Testing Pyramid, Proceedings of the 18th European Conference on Composite Materials, Athens, Greece, June 2018.
[2] B.H.A.H. Tijs, A. Turon, C. Bisagni, The importance of accounting for large shear deformations on modelling matrix failure of thermoplastic and thermoset composites, Proceedings of the 7th ECCOMAS Thematic Conference on the Mechanical Response of Composites, Girona, Spain, Sept 2019.

This work has received co-founding from the Clean Sky 2 Joint Undertaking under the European Union's Horizon 2020 research and innovation programme under grant agreement No 776455.

TU Delft | Fokker | Clean Sky 2

Quantum-Aided Optimization of Composite Laminates

Giorgio Tosti Balducci
Department: Aerospace Structures and Materials
Section: Aerospace Structures and Computational Mechanics
Daily supervisor: B. Chen
Promotor: R. De Breuker
G.B.L.TostiBalducci@tudelft.nl

	1	2	3	4

Introduction

Quantum computers (QCs) are one of the current frontiers of research and going beyond purely theoretical promises, they recently achieved supremacy over classical computers [1]. Engineering optimization problems are often computationally demanding, making them a perfect candidate for testing the speed-up that QCs can provide.

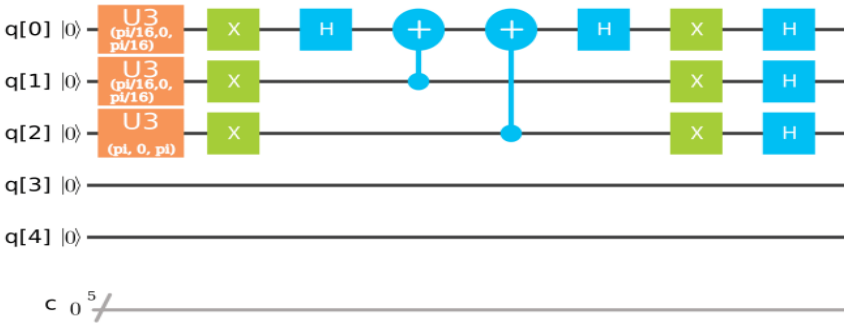

Source: Coles et al., 2018, Quantum implementations for beginners. *arXiv:1804.03719v1*

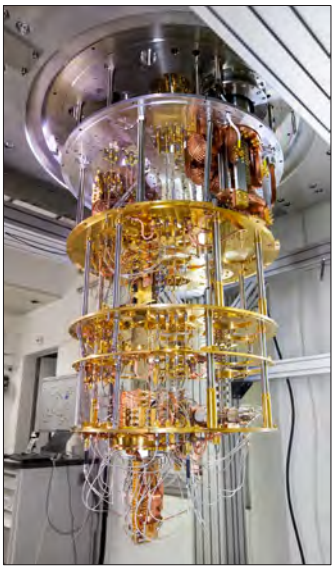

Source:https://en.wikipedia.org/wiki/Quantum_computing

Source: http://www.automateddynamics.com/resources/innovation/cobonded-structures

Composite panels optimization

Combinatorial minima search problems can most benefit from quantum mechanical effects. Optimization of composite laminates for different objectives falls in this category, if the design space is considered as the tensor product of any combination of stacking sequences, plies thickness and angles. Moreover, design of stiffened panels can also be optimized discretely, by choosing the best combination of stiffeners number, shapes, locations and orientations.

Quantum-aided composites optimization

The advantage of quantum optimization algorithms is two-fold. Most of them don't make use of gradients, thus avoiding local minima traps and additionally they minimize the number of function evaluations before the optimum is reached. This research is aimed at implementing and testing routines based on quantum search algorithms, such as Grover's, QAOA and quantum annealing in a hybrid solver with classical function evaluations. By doing this, it will be assessed whether optimal composite designs are achieved with a substantially reduced computational cost and how this scales with an increasing number of variables.

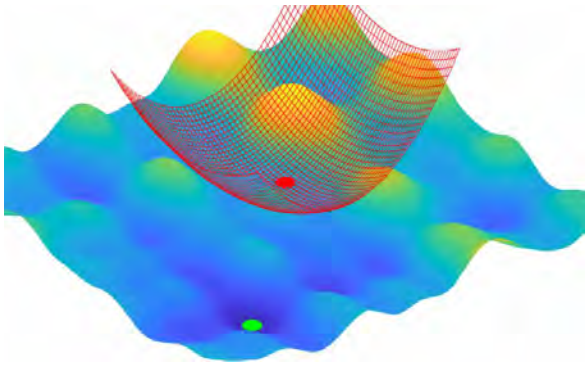

Source: Geiping et al., 2018, Composite Optimization by Nonconvex Majorization-Minimization. *arXiv:1802.07072v2*

References
[1] Arute F., et al., 2019. Quantum supremacy using a programmable superconducting processor. Nature, 574(7779), pp.505-510.

Ditching and Water Impact of Aerospace Structures

Name: Yuqian Tu
Department: ASM
Section: ASCM
Daily supervisor: Chiara Bisagni
Promotor: Chiara Bisagni
Y.Tu@tudelft.nl

Objectives

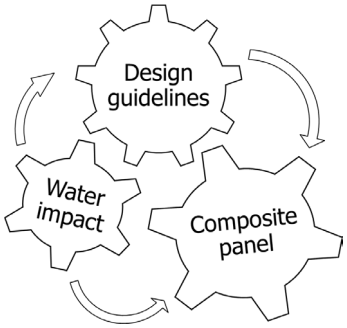

Background

Ditching in the Hudson River (Day, 2009)

Open Issues

- Ditching and water impact of composite structures
- Aircraft component design and optimization of composite structures related to ditching and water
- The research of aircraft impact on rough water

Parameters

Design parameters
- Panel curvature
- Panel thickness

Impact parameters
- Impact velocity v
- Impact angle α

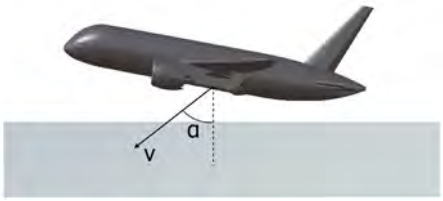

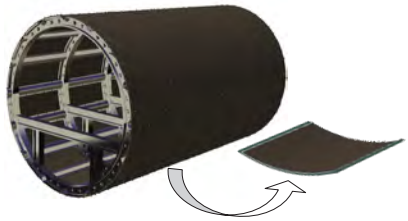

Analysis Outputs
- Pressure
- Deformation
- Composite failure
- Deceleration

Test Setup

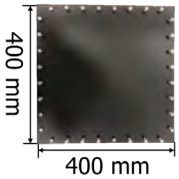

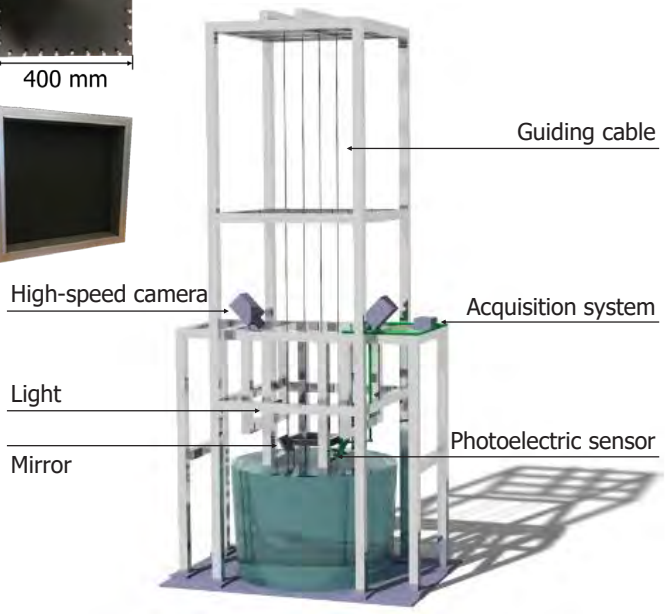

Numerical Results

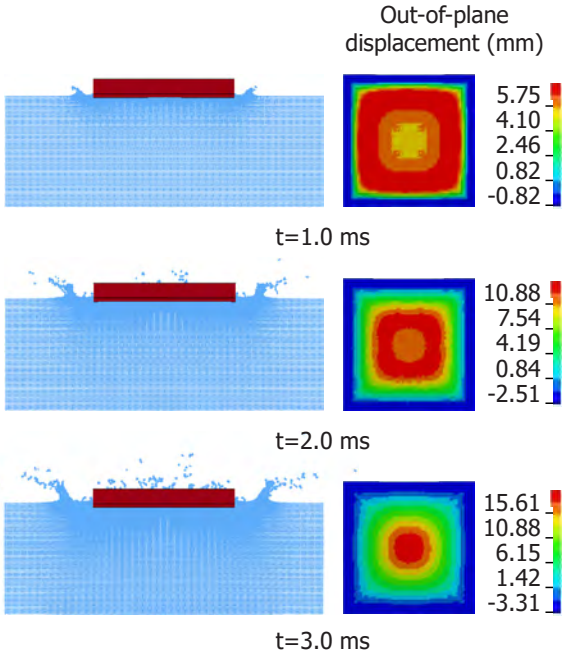

Conclusions

Preliminary investigation of design guidelines towards composite panels under ditching and water impact
- Numerical model setup using LS-DYNA
- Manufacture of the first flat panel
- Design of test setup

ASM

Future Launch Vehicle Structures: Design for Buckling using a Scaling Methodology

Ines Uriol Balbin
ASM
ASCM
Chiara Bisagni
i.uriolbalbin@tudelft.nl

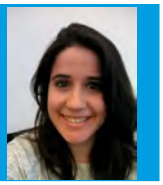

Challenge:

Large cylindrical shells often constitute a primary structural element in launch-vehicle structures, where axial buckling is a critical design load.

Objective:

Develop a scaling methodology to investigate the buckling phenomenon of launch-vehicle-like cylindrical shells

Methodology: Scaling based on nondimensional buckling equations

$$\left(\alpha_b^2\frac{\partial^3\hat{B}_1}{\partial z_1^3}+\beta\frac{\partial^3\hat{B}_1}{\partial z_1\partial z_2^2}\right)+\left(\frac{1}{\alpha_b^2}\frac{\partial^3\hat{B}_2}{\partial z_2^3}+\beta\frac{\partial^3\hat{B}_2}{\partial z_1^2\partial z_2}\right)=\left(\mathscr{P}\frac{\partial^2\hat{W}}{\partial z_1^2}-\sqrt{12}\,Z_2\,\frac{\partial^2\hat{F}}{\partial z_1^2}\right)$$

$$\chi_1\hat{B}_1-\alpha_b^2\frac{\partial^2\hat{B}_1}{\partial z_1^2}-\frac{1}{2}(\beta-\nu_b)\frac{\partial^2\hat{B}_1}{\partial z_2^2}-\frac{1}{2}(\beta+\nu_b)\frac{\partial^2\hat{B}_2}{\partial z_1\partial z_2}=\chi_1\frac{\partial\hat{W}}{\partial z_1}$$

$$\chi_2\hat{B}_2-\frac{1}{\alpha_b^2}\frac{\partial^2\hat{B}_2}{\partial z_2^2}-\frac{1}{2}(\beta-\nu_b)\frac{\partial^2\hat{B}_2}{\partial z_1^2}-\frac{1}{2}(\beta+\nu_b)\frac{\partial^2\hat{B}_1}{\partial z_1\partial z_2}=\chi_2\frac{\partial\hat{W}}{\partial z_2}$$

$$1/\alpha_m^2\,\frac{\partial^4\hat{F}}{\partial z_2^4}+\alpha_m^2\frac{\partial^4\hat{F}}{\partial z_1^4}+2\mu\frac{\partial^4F}{\partial z_1^2\partial z_2^2}=\sqrt{12}Z_2\frac{\partial^2\hat{W}}{\partial z_1{}^2}$$

Similar buckling response can be achieved by keeping the nondimensional parameters constant throughout the scale changes

Approach:

INPUT	Orthotropy parameters: **μ** and **β**	• Defined by the material properties and layup • Represent the structure stiffness
	Geometry parameters: **α_m** and **α_b**	• Defined by the material properties, layup, length and radius • Linked to the ratio between radius and length
	Batdorf-Stein parameter: **Z2**	• Defined by the material properties, layup, radius and thickness • Represents the ratio between radius and thickness

By keeping these **5 parameters** constant throughout the scale changes, similar buckling response can be achieved

OUTPUT	Nondimensional buckling load: $\mathscr{P}$	• Represents the axial buckling load of a shell
	Nondimensional axial displacement: **U**	• Represents the displacement normalized by the stiffness

Results:

Large test

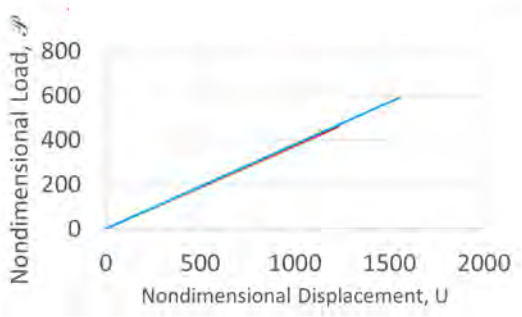

Scaled test

Stiffness of both shells is similar, and different knockdown factors account for the difference in the nondimensional buckling load

Development of a Validated Numerical Analysis Methodology for Thermoplastic Composite Stiffened Structures

Kevin van Dooren
Department : ASM
Section : ASCM
Daily supervisor : Prof. C. Bisagni
K.S.vandooren@tudelft.nl

1	2	3	4

Objectives

The main objective is to develop a **validated numerical analysis methodology**, with the main focus on **thermoplastic sub-component level** structures.

This numerical methodology will be developed to study **thermoplastic stiffened primary structures** resulting from different manufacturing technologies, such as **thermoplastic welding**, with the goal to reach higher levels of **TRL**. The numerical methodology aims to capture the **post-buckling behavior, initiation and propagation of damage and final failure** of thermoplastic stiffened primary structures. The **failure mode** of thermoplastics have shown to be very dependent on its **manufacturing method**, which increases the difficulty to capture the failure modes as seen in experimental testing.

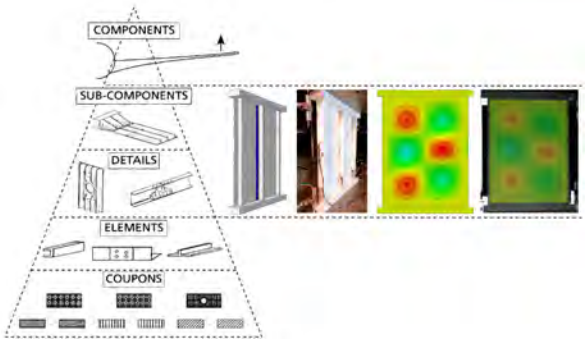

Figure 1: Building block approach

Previous Work: Analysis and Testing of a Thermoplastic Stiffened Panel with Butt-joint Construction

Two panels manufactured by GKN Fokker were analyzed and tested at TU Delft [1,2]. The panels included a crack of 70 mm in the skin-stringer interface, which is a representation of Barely Visible Impact Damage (BVID). The failure mode of interest is skin-stringer separation due to buckling.

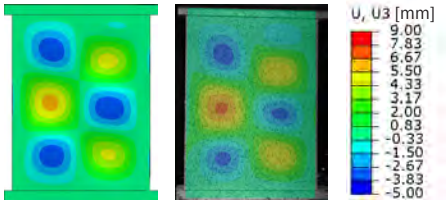

Figure 2: Comparison of buckling shape between FE (left) and test (right).

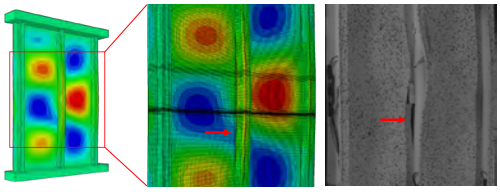

Figure 3: Comparison of crack opening.

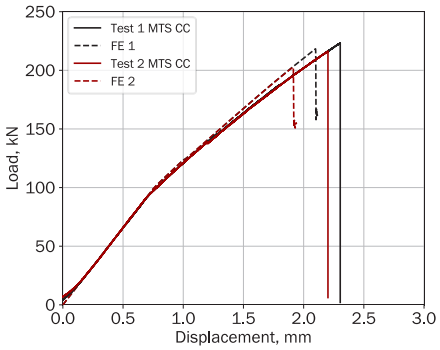

Figure 4: Load displacement comparison between test and finite element

Stunning

This work is executed as a part of the STUNNING project, "SmarT mUlti-fuNctioNal and INtegrated TP fuselaGe" , which aims to develop a thermoplastic multifunctional fuselage demonstrator.

Current Work: Design of Thermoplastic Stiffened Test Panels Representative of the STUNNING Multifunctional Fuselage

A three-stringer test panel representative of the STUNNING multifunctional fuselage is currently being designed to investigate skin-stringer separation of the welded interface due to buckling. The buckling shape is determined by the analysis of a fuselage section, consisting of a skin with five stringers and four frames. The three-stringer test panel is then designed to show the same buckling shape to be able to investigate the phenomena on a lower scale and more cost-effective manner.

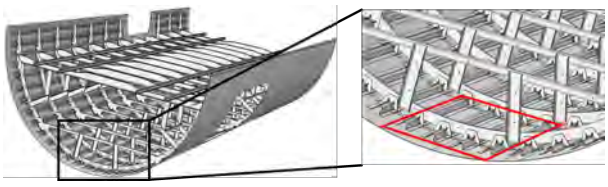

Figure 5: Area of interest of the STUNNING multifunctional fuselage.

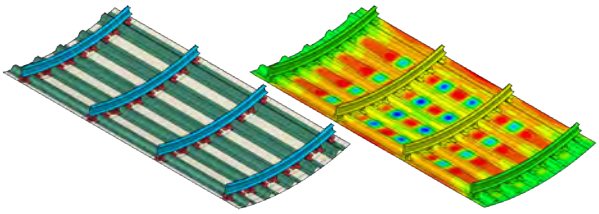

Figure 6: Buckling shape determination of large scale panel.

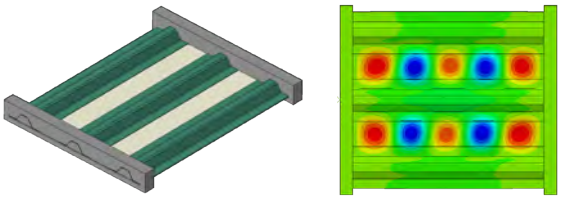

Figure 7: Preliminary test panel design.

References

[1] K.S. van Dooren, E. Labans, B.H.A.H. Tijs, J.E.A. Waleson and C.Bisagni. "Analysis and Testing of a Thermoplastic Composite Stiffened Panel under Compression". ICCM22 – 22nd International Conference on Composite Materials, Melbourne, Australia, 2019.
[2] J.W. van Ingen. "Thermoplastic Orthogrid Fuselage Shell". SAMPE Journal, Vol. 52, No. 5, pp. 7-15, 2016.

Acknowledgement
The work presented received funding from the Clean Sky 2 Joint Undertaking under the European Union's Horizon 2020 research and innovation programme under grant agreement No 776455.

Experimental impact damage tolerance evaluation of thick composite structures

Low- and high-velocity impact followed by compression-after-impact

Niels van Hoorn
Department: ASM
Section: ASCM
Dr. S.R. Turteltaub
Prof. Dr. C. Kassapoglou
N.vanHoorn@tudelft.nl

ASM

INTRODUCTION

Gear rib of the Affordable Low Cost Aircraft Structures (ALCAS) airliner wing [1].

Carbon Fibre Reinforced Polymer materials are being increasingly used in highly-loaded aerospace components, resulting in thick composite structures (e.g., 20-100mm)

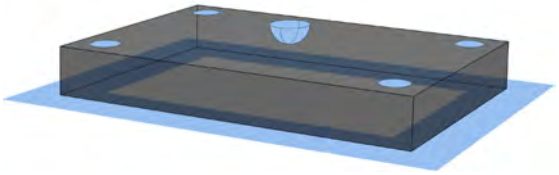

The impact problem according to the ASTM D7136 standard [2]. It illustrates centre impact with a 16mm diameter impactor on a 150x100mm specimen clamped at four corners.

Problem:
Impact events are critical in designing a damage tolerant composite structure

Knowledge gap:
Experimental data for impact on thick composite structures is limited

Solution:
A new testing campaign is carried out to be used for validation of numerical models

IMPACT EXPERIMENTS

40 impacts: 10 tests instances with each four specimens

Thickness	20mm	40mm
Energy level	55J	100J
Layup	Quasi-Isotropic (QI)	Anisotropic
Impactor	Large-mass drop-tower	Small-mass gas-cannon

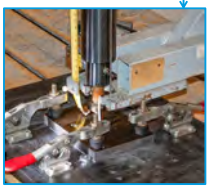

Illustration of the drop-tower with a 2.274kg impactor

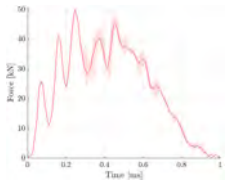

Example of a force-time history of a 55J large-mass impact

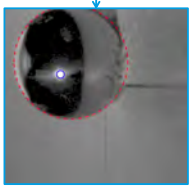

150,000fps high-speed images tracking the impactor

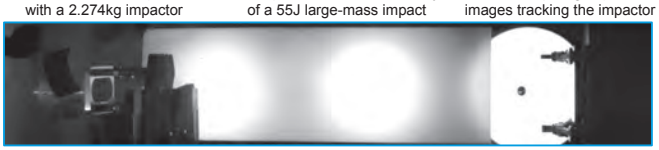

Small-mass gas-cannon with 20,000 fps high-speed images measuring the impactor velocity.

Damage inspection to determine the characteristic damage state

Ultrasonic C-scans | X-ray CT-scans | Dent depth

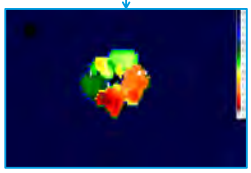

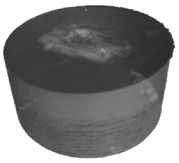

2D visual inspection of cross-sections

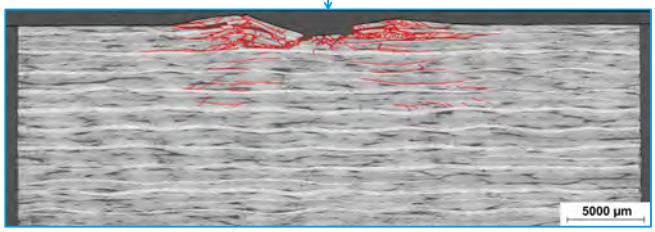

Illustration of impact damage due to a 55J large-mass impact on a 20mm thick specimen.

COMPRESSION-AFTER-IMPACT EXPERIMENTS

Experiments to determine the Compression-After-Impact (CAI) strength

Compression using 2,000kN static test bench

Example of a 40mm thick specimen with a 100J small-mass impact at the point of failure (i.e., 1234kN).

Two high-speed cameras at 20,000fps tracking damage mechanisms

Front view

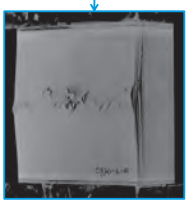

Rear view

Results: CAI strength as function of thickness and impact energy

Large-mass drop-tower

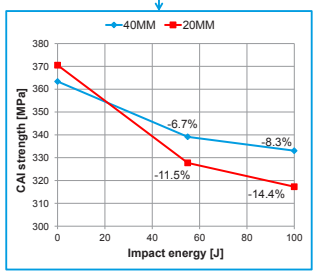

Small-mass gas-cannon

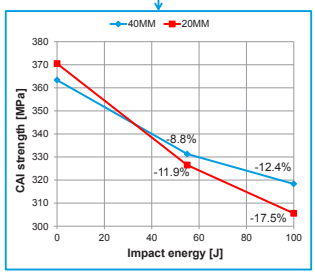

CONCLUSIONS

- ✓ The experimental data is used for the validation of numerical models
- ✓ Anomalies for small-mass impact, compared to large-mass, are that...
  - ...the delaminated area is significantly higher for 20mm specimens (+112% @ 100J)
  - ...the layup has a considerable effect on the dent depth (+60% for the QI layup @ 55J)
- ✓ Residual CAI strengths show a relatively small effect of impact damage

[1] H.P.J. de Vries. Development of a main landing gear attachment fitting using composite material and resin transfer moulding. Techreport NLR-TP-2009-732, NLR – Netherlands Aerospace Centre, December 2010.
[2] ASTM International. *Standard test method for measuring the damage resistance of a fiber-reinforced polymer matrix composite to a drop-weight impact event,* number ASTM D7136/D7136M-15, West Conshohocken, PA, 2015

TU Delft

nlr Dedicated to innovation in aerospace

Fokker

GKN AEROSPACE


TUDelft
TUDelft

Damage diagnostics utilizing sensor data fusion

Agnes Broer
Department: ASM
Section: SI&C
Supervisor: D. Zarouchas
Promotor: R. Benedictus
Contact: a.a.r.broer@tudelft.nl

1. Objective

Develop a multi-sensing structural health monitoring (SHM) framework in order to diagnose impact damage in stiffened composite aircraft structures on all four SHM levels, namely 1) detection, 2) localisation, 3) type, and 4) severity.

2. Motivation

Each sensing technique provides limited information on the damage in a structure. Combining them can reduce uncertainty, improve resolution, and increase confidence. This leads to an improved image of the damage in a structure.

3. Method

In order to develop an SHM framework based on data fusion, a test campaign is performed in which the damage in a composite panel is monitored using several SHM techniques.

4. Case Study

Four skin-stiffener panels are tested in compression-compression fatigue loading (post-buckling). Each specimen is impacted with an energy of 10 J before the fatigue test. Variation is introduced by changing the location of impact.

Composite Panel

Four skin-stiffener panels are tested in fatigue compression after impact (FCAI). Each panel is a carbon-epoxy skin panel with one T-stiffener and has been sensorised.

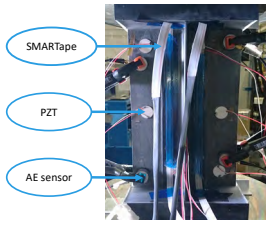

Impact Locations

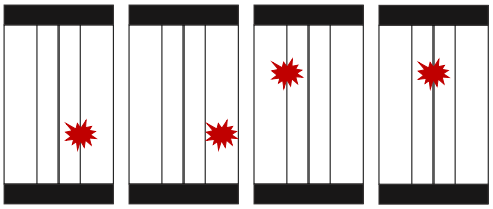

5. Experimental Setup

Lamb wave detection system
- Pitch-catch & pulse-echo mode
- Detect, localise, and size skin damage

SMARTape system
- Placed on each stiffener foot
- Two sensing techniques:
  1. Rayleigh-scattering based distributed strain sensing
  2. Fibre Bragg Grating sensors
- Localise and size disbond
- Monitor disbond growth

Digital image correlation system
- Focused on skin
- Out-of-plane displacement and strains in skin

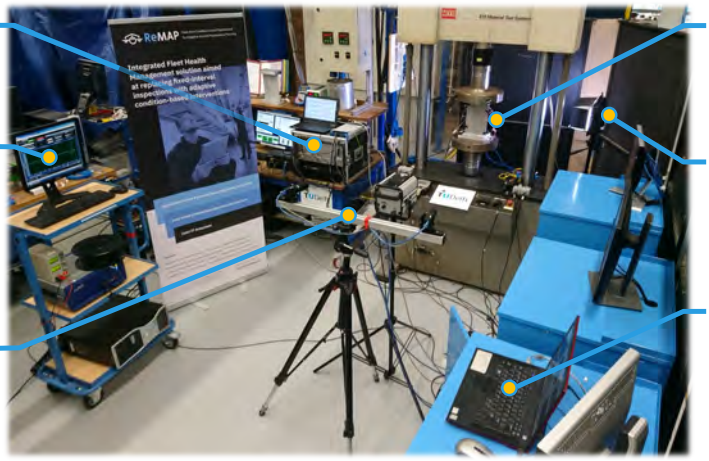

Composite panel
- Panel placed inside test bench
- Damage monitored using 5 different sensing systems

Camera system
- Focused on stiffener foot
- Initiation and propagation of disbond

Acoustic emission acquisition system
- Damage initiation and propagation
- Damage classification
- Damage localisation using multiple AE sensors

6. Outlook

An experimental campaign was presented in which data from multiple sensors was collected for the development of an SHM framework. An SHM framework utilizing data fusion will be able to detect, localise, classify, and quantify the severity of damage growth in aircraft structures.

This project has received funding from the European Union's Horizon 2020 research and innovation programme under grant agreement No 769288

h2020-remap.eu

Numerical Modelling and simulation of fibre Bragg grating (FBG) sensors

Luigi Fazzi
AS&M
SI&C
Dr. R.M. Groves
Prof. Dr. R. Benedictus
L.Fazzi@tudelft.nl

FBG spectrum affected by birefringence

FBG sensors have interesting properties like immunity to electromagnetic interferences, and for the morphology of optical fibre (FO), the FBG sensor is the ideal candidate for surface mounting or embedding in aeronautical composite structures without affecting their mechanical performances. The nature of the deformations influences the response of the FBG sensors differently. In fact, theoretically, the FO cross-section can be considered as perfectly circular. However, transverse loads on the FO cause a deformation in its shape resulting in birefringence effects. This causes a change in the reflected and the transmitted output spectrum of the FBG sensor.

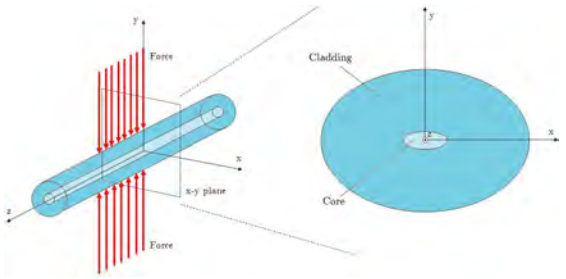

FO cross-section geometry change caused by transverse load

Numerical simulations show that an increase in the uniform transverse load leads to a more accentuated peak separation and a widened spectrum. The reason is the birefringence causes the coupling of the electromagnetic waves polarized along the slow (x) and fast (y) axes. We treated this effect with Coupled-Mode theory and obtained the FBG spectra using the Transfer Matrix method to solve the coupling equations.

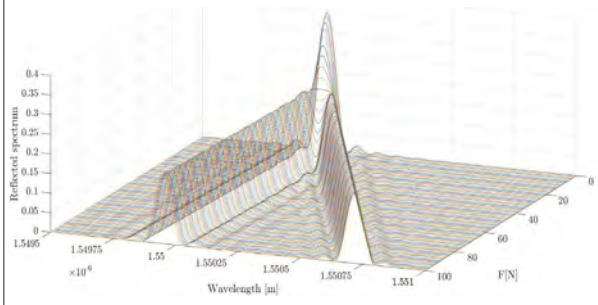

Evolution of FBG spectra with increasing transverse loads in plane strain state

The birefringence effects on FBGs were experimentally investigated applying a uniform transverse load with a block of steel. The recorded peaks wavelengths have been compared, and are in good agreement with the experimental results. A future goal could be to achieve the same result when FBG sensors are into composites.

Bragg peak in Tilted FBG sensors

Tilted FBG can couple some portion of the core light to the cladding modes drastically modifying the transmission spectrum in relation to the tilt angle induced.

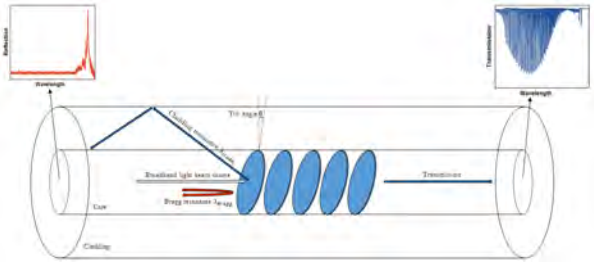

Schematic of mode coupling in tilted FBG sensors

Although a straightforward numerical calculation of coupled-mode differential equations offers precise results,
this reveals to be time consuming and computationally inefficient. To overcome these issues, we used the Transfer Matrix Method to solve the Coupled-Mode Method equations along the tilted FBG length. In this work, we consider weakly tilted FBGs with a tilt angle in the range θ<20°. In this case, the light is coupled from fibre fundamental LP01 mode to a backward propagating Bragg mode and also backward propagating cladding modes. Considering only the forward-backward core mode coupling, we obtained the following trend of the Bragg peak with the variation of the tilt angle:

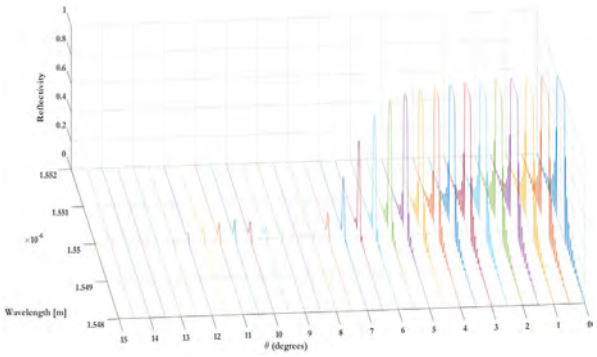

Evolution of Bragg peak in TFBG with increasing of tilt angle

This numerical method allows the determination of the reflected or transmitted Bragg peak and provides its spectral shape before the TFBG sensor is manufactured, by considering changes of the optical fibre parameters, apodization profile, and/or the depth and phase of the core refractive index modulation. The future work concerns the application of this method to simulate the coupling between the forward propagating core mode and the backward propagating cladding modes.

Comparison of the response of CFRP laminates subjected to low-velocity fatigue and fatigue indentation loading

Name: Lubin Huo (2nd year)
Department: ASM
Section: SIC
Daily supervisor: R.C. Alderliesten
Promoter: R.C. Alderliesten
L.Huo@tudelft.nl

Introduction

Fatigue of composite laminates caused by repeated transverse impact loading has been studied in the past few decades[1-3]. Composite material systems under transverse impact fatigue loading with different incident energies corresponding to different fatigue life (i.e. the total number of impacts till degradation of the composite mechanical properties). In general, with high impact energy, the material system could be perforated with few impacts, while for low-velocity impact , it may require thousands of impacts to perforate the specimen. Obviously, semi-automatic motorized drop-weight impact devices (i.e. manual operation is unavoidable for each impact) are not suitable for the study of low-velocity impact fatigue. Relevant studies [4-7] have shown that, with comparable boundary and loading conditions, quasi-static indentation and low-velocity impact can yield similar damage characteristics for the same material systems. Furthermore, in contrast with low-velocity impact, quasi-static indentation has the advantages that force-deflection curves can be directly recorded instead of numerically integrating force-time curves. Furthermore, the impact locations are more consistent, and damage initiation and propagation can be observed more easily. Therefore, it would be significant if quasi-static indentation could be applied repeatedly (fatigue indentation) loading to reproduce low-velocity impact fatigue loading.

Tests procedures

To that aim, the transverse fatigue loading responses of CFRP composite laminates were compared, tested either in impact fatigue loading or in repeated indentation loading. The laminates consisted of 150 × 300 × 2.5 mm panels made by hand-lay-up using unidirectional carbon/epoxy prepreg M30SC/DT120 [8, 9] supplied by Delta-Tech S. p. a., with a layup sequence $[45, 0, -45, 90]_{2s}$. In both cases, the panels were subjected to 225 transverse load cycles (i.e. low-velocity impacts or quasi-static indentations), and these loads were applied to the panels by a 30 mm diameter hemispherical steel impactor or indenter. The specimens were under the same clamp boundary condition and two similarity principles were used to generate more similar loading conditions. The first principle is called force quasi-static indentation (FQSI), because it applies the quasi-static indentation with a rate of 3 mm/min to the same maximum force as obtained with the force-time curve from drop-weight 2.41m/s impact with 8.4 J incident energy. The second principle is referred to as an energy quasi-static indentation (EQSI), because the 3 mm/min indentation is applied with the same energy of 6.5 J. This resulted in lower than low-velocity indent energy mainly because of the vibration and loud noises during low-velocity impact that would be consuming part of the energy. The reason for choosing 6.5 J quasi-static indentation was a preliminary test showing that 6.5 J quasi-static indentation and 8.4 J low-velocity impact yield similar peak forces for the cases in this study.

(a) Drop-weight impact tower (b) Quasi-static indention test set-up

Fig. 1. Test rigs.

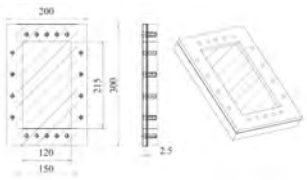

Fig. 2. Test specimen clamped in indicated by the hatched area.

Results and discussion

The responses were evaluated based on force-displacement curves that were divided into loading and unloading stages, as shown in Fig. 3, and based on the morphologies of the damages which were obtained through KEYENCE® laser microscopy and subsequently AutoCAD® software package to obtain the damage profiles, shown in Fig. 4. The comparison of force-displacement curves suggests that quasi-static indentation fatigue loading have similar loading behaviour as repeated low-velocity impacts, but that the EQSI principle fits better than FQSI principle. However, neither FQSI or EQSI could induce similar behaviour to low-velocity impact during the unloading stage. This may be the result of the dynamic response of low-velocity impact, which is not present during the quasi-static indentations. Fig. 4. shows that the damage patterns of these three damage specimens all have a pine tree shape which indicate that the specimens under low-velocity impact fatigue loading and quasi-static indentation fatigue loading have similar damage mechanisms, although FQSI seems to be closer to low-velocity impact loading than EQSI in terms of damage amount in this study.

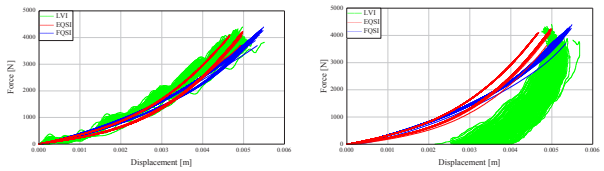

(a) Loading stage (b) Unloading stage

Fig. 3. Peak of force vs number of impacts and indentations.

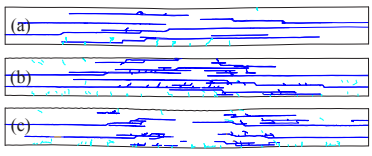

Fig. 4. Damage morphologies of the specimens caused by different loading. (a) 225 times quasi-static indentations with the energy of 6.5 J, (b) 225 times low-velocity impact with the energy of 8.4 J, (c) 225 times quasi-static indentations with the same peak of force of low-velocity of impacts. (cyan for isolate matrix cracks and blue for delaminations).

References

1. Wyrick, D.A. and D.F. Adams, Residual strength of a carbon/epoxy composite material subjected to repeated impact. Journal of Composite Materials, 1987. 22: p. 749-765.
2. Belingardi, G., M. Cavatorta, and D. Salvatore Paolino, Repeated impact response of hand lay-up and vacuum infusion thick glass reinforced laminates. International Journal of Impact Engineering, 2008. 35(7): p. 609-619.
3. Maria Pia Cavatorta and D.S. Paolino, Damage variables in impact testing of composite laminates, in Composite Materials Reasearch Progress, L.P. Durand, Editor. 2008, Nova Science Publishers. p. 237-256.
4. Bull, D.J., S.M. Spearing, and I. Sinclair, Investigation of the response to low velocity impact and quasi-static indentation loading of particle-toughened carbon-fibre composite materials. Composites Part A: Applied Science and Manufacturing, 2015. 74: p. 38-46.
5. Wagih, A., et al., A quasi-static indentation test to elucidate the sequence of damage events in low velocity impacts on composite laminates. Composites Part A: Applied Science and Manufacturing, 2016. 82: p. 180-189.
6. Lagace, P.A., et al., A Preliminary Proposition for a Test Method to Measure (Impact) Damage Resistance. Journal of Reinforced Plastics and Composites, 1993. 12(5): p. 584-601.
7. Weirdie, B.L. and P.A. Lagace, On the use of quasi-static testing to assess impact damage resistance of composite shell structures. Mechanics of composite materials and structures an international journal, 1998. 5(1): p. 103-119.
8. Toray Industries, I., High-performance carbon fiber Torayca.
9. Tech, D., DT120 Versatile High Toughness Epoxy Matrix. 2015.

Design and Optimization of Hybrid Composite Trusses

Nicolas P. Lavalette
Aerospace Structures & Materials
Structural Integrity & Composites
Supervisor: O.K. Bergsma
Promotor: R. Benedictus
n.p.lavalette@tudelft.nl

MOTIVATION

The goal of this research project is to develop a new kind of load-carrying structures to be used in aerospace applications, by combining the high axial strength and low density of CFRP pultruded members with the axially loaded nature of trusses.

PROBLEMATICS

- Current truss optimization methods do not consider as variables the strength and weight of the joints.
- The small scale of the structures and the nature of its members require the design of an adhesive joint, with a model able to predict its strength.

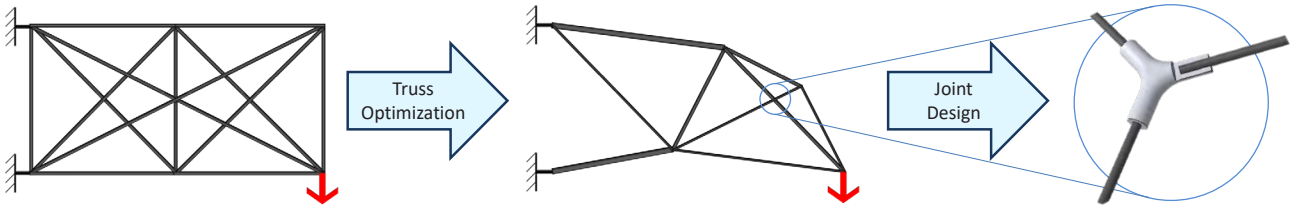

The solution found to join the truss members together is to adhesively bond them to a metallic node (aluminum or titanium). The joint needs to be optimized for the best strength/weight ratios, and implemented in the truss optimization algorithm.

NUMERICAL MODELLING

The adhesive used is the **Araldite 2015-1**. Its ductility allows it to redistribute stresses by undergoing a large amount of plastic deformation before failing.

Cohesive Zone Modelling (CZM) is used to predict the strength of the joint. It models the initiation and propagation of damage in the adhesive up to failure. A **trapezoidal traction-separation law** is used for this adhesive.

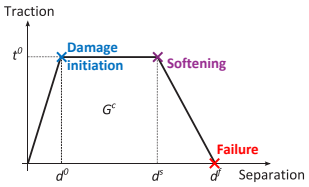

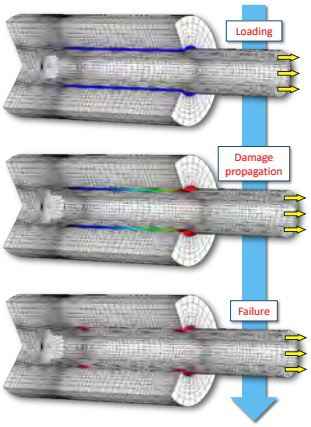

JOINT OPTIMIZATION

A **multi-objective optimization** of the joint is done using a **Genetic Algorithm** (Matlab-Python-Abaqus interface), to determine the configurations with the highest strength and the lowest weight.

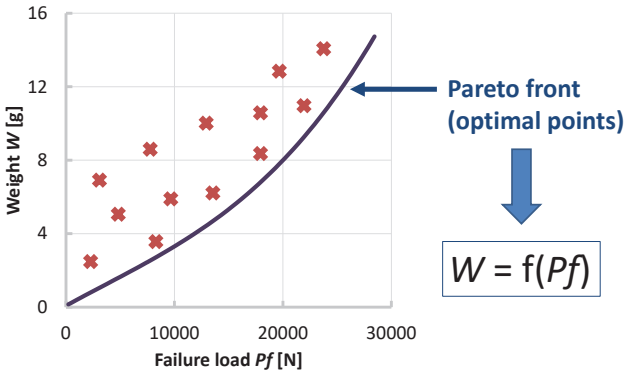

TRUSS OPTIMIZATION

A **genetic algorithm** is used to optimize the **topology** (nodes connectivity), **size** (member diameter) and **shape** (nodes coordinates) of the composite truss, for the minimum weight.

The relationship resulting from the joint optimization gives to each joint a weight penalty, which is added to the structure's total weight.

- **Hybrid Aluminum-CFRP truss:**

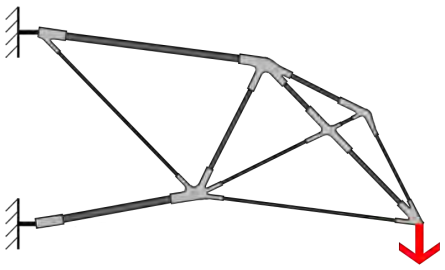

Adding the joints **AFTER** the optimization:
Weight = **0.52 kg**

Adding the joints **DURING** the optimization:
Weight = **0.45 kg**
~15% weight reduction

- **Full Aluminum truss (for comparison):**

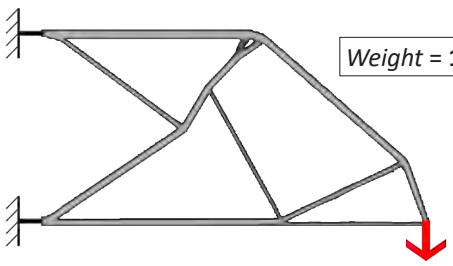

Weight = **1.51 kg**

Loading Rate Effect on the Damage Accumulation Process of CFRP Cross-Ply Laminates under Tensile

Xi LI

Aerospace Structures & Materials
Structural Integrity & Composites
Dr. D. Zarouchas
Prof.dr.ir. R. Benedictus
Xi.Li@tudelft.nl

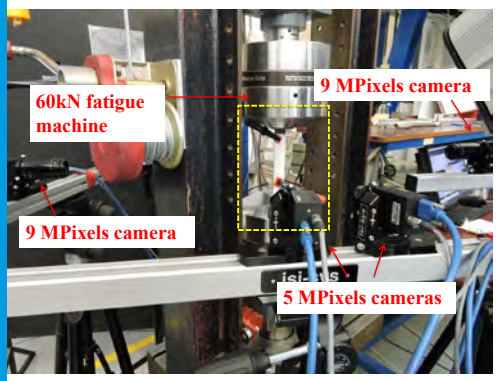

Specimen:

Layup - [0₂/90₄]s

Thickness - 1.5mm

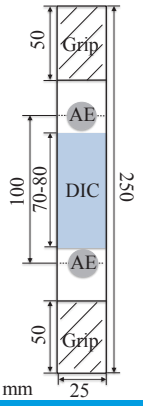

Control mode	Loading rate	Running time (s)
Load	0.019 kN/s	1470.25 ± 40.14
	0.19 kN/s	140.72 ± 1.78
	1.9 kN/s	14.21 ± 0.03
	19 kN/s	1.54 ± 0.01
Displacement	1 mm/min	196.80 ± 3.05

Methodology:

In-situ damage monitoring including edge observation, DIC and AE was applied during the tension.

RESULTS

(①0.019 kN/s ②0.19 kN/s ③1.9 kN/s ④19 kN/s ⑤1 mm/min)

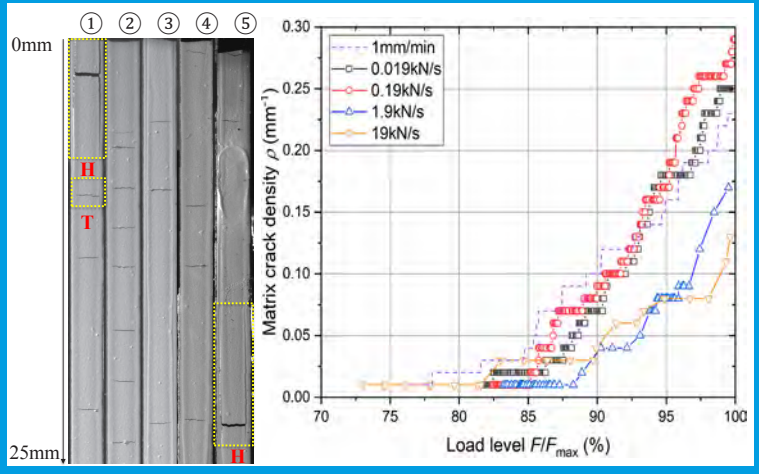

Transverse strain at the exterior 0 ply before final failure

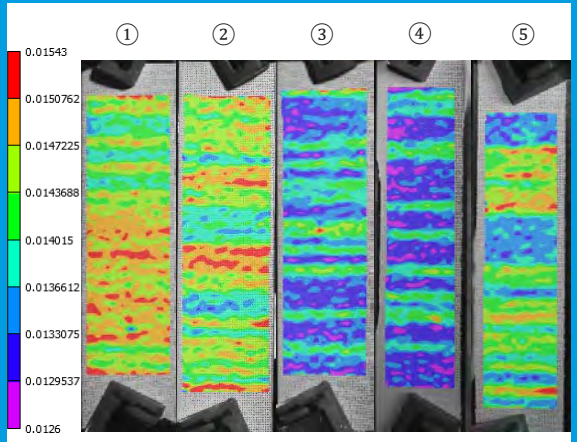

Edge observation

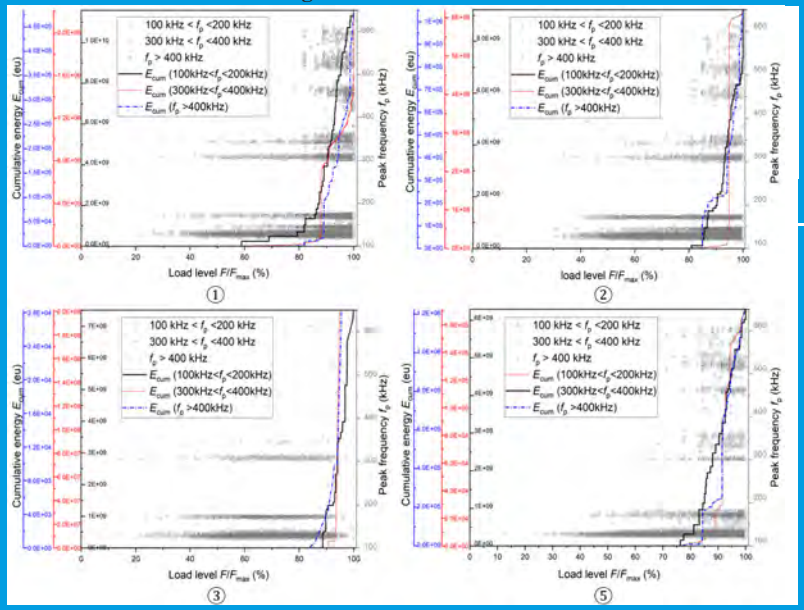

AE

DIC

	Axial modulus (GPa)	Tensile strength (MPa)	Failure strain
①	51.45 ± 0.65	706.81 ± 14.91	0.0144 ± 0.0002
②	50.54 ± 0.70	684.99 ± 7.82	0.0140 ± 0.0002
③	51.26 ± 1.01	691.01 ± 15.69	0.0136 ± 0.0001
④	51.32 ± 2.18	673.72± 8.34	0.131 ± 0.0000
⑤	51.52 ± 0.32	699.33 ± 6.94	0.0141 ± 0.0002

Mechanical properties

CONCLUSIONS

- Axial modulus and strength are less sensitive to different loading rates than the failure strain, which typically decreases with the increase of loading rates.
- More matrix cracks at the inner 90 plies generated with lower loading rates.
- Under all loading rates, matrix crack density remained constant or presented a slow growing trend up to the load level around 85% and then significantly increased up to the final failure.
- The largest strain concentration through the loading direction (38 mm) was found at 0.019 kN/s.
- Peak frequency provides sufficient distinction between different AE signal groups (i.e. 100-200 kHz, 300-400 kHz and > 400 kHz). The highest cumulative AE energy during the tests was related to the AE activities at the 100 kHz to 200 kHz peak frequency range.

Development of a Fibre Optic Shape Monitoring System for a Morphing Wing Section

Nakash Nazeer
Department: ASM
Division: SI&C
Daily supervisor/Promotor:
Dr. R.M. Groves
Email: N.Nazeer@tudelft.nl

Fibre Bragg grating (FBG) sensing

The grating in figure forms the sensing region and is capable of modulating the amplitude and phase of incoming light with respect to external disturbances. These gratings are 'written' by exposing the fibre to light with specific wavelengths.

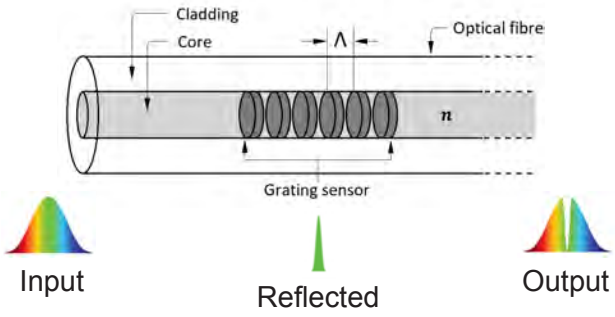

$$\lambda B = 2n_{eff}\Lambda$$

Λ: Periodic spacing
λ_B: Grating wavelength
$neff$: Core refractive index

On undergoing perturbations, a narrowband of the incident optical field, by successive, coherent scattering from the index variations is reflected with a central wavelength. This wavelength is referred to as Bragg wavelength λ_B. This shift in wavelength is used to measure the strain acting on the fibre.

Morphing wings and Structural Health Monitoring (SHM)

Wings or wing sections capable of changing their shape on-demand are defined as morphing capable. To achieve ideal aerodynamic and structural performance the wing needs to adapt its shape to different flight conditions. That being said, SHM of these structures is of great importance.

Being light weight, highly sensitive and embeddable, optical fibres are perfect for this purpose.

To prove the potential of the developed sensing method, a cantilever panel was tested successfully along with its capability of measuring bending, torsion and location of loads acting on it.

The next step is to incorporate this system in a composite smart-wing. The sensor system would provide critical information on the deflection and shape of its morphing sections hence enhancing its reliability and performance.

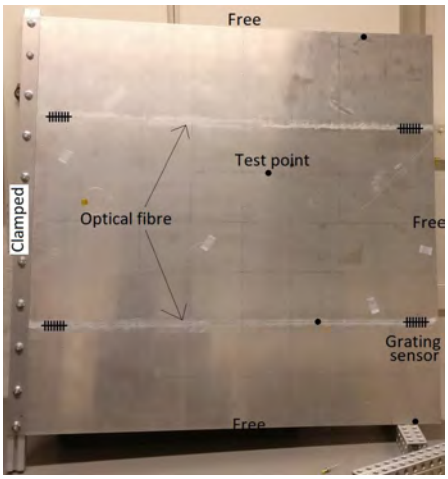

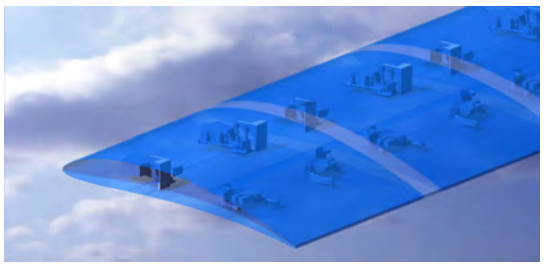

This work is part of the smart sensors project that falls under the strategic project SmartX in the Aerospace Structures and Materials department, Faculty of Aerospace Engineering. The project is focussed on the design and development of a smart wing technology.

The plastic dissipation during fatigue crack growth

Name: Hongwei Quan
Department: ASM
Section: SI&C
Daily supervisor: R.C. Alderliesten
Promotor: R.Benedictus
h.quan@tudelft.nl

1.Introduction

Fatigue failure is one of the major types of failure in aerospace engineering, and aluminum is one of the most common materials used in aerospace structures. So knowledge on the fatigue behavior of aluminum alloys is therefore a prerequisite in aerospace to design against fatigue failure.

2.Literature review and basic questions

Various studies tried to use plastic energy dissipation to predict fatigue crack growth. The basis is the relation between plastic energy dissipation per cycle (*dW/dN*) and fatigue crack growth rate (*da/dN*).

[1] proposed a linear relation between *da/dN* and the total energy dissipated per cycle (dW_{tot}/dN) with that dW_{tot}/da is considered as a material property. Meanwhile, [2-6] proposed a linear relation between *da/dN* and the plastic dissipation over the reversed plastic zone per cycle dW_{re}/dN.

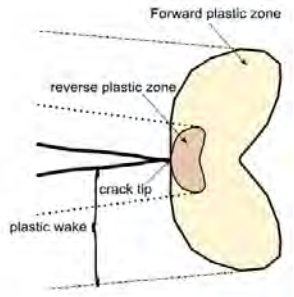

Plastic regions developing during cyclic loading around a crack tip. Figure from [7]

To verify or falsify the hypothesis on the relationship between *dW/dN* and *da/dN*, two questions had to be answered:

Do *da/dN* and *dW/dN* relate linearly during fatigue crack growth?

Does the relation between *da/dN* and *dW/dN* remain the same at different stress ratios?

3.Experimental methodology

The 7075-T6 CCT specimens were tested. The test was performed at 3 stress ratios, R = 0.1, 0.5 and 0.7. The fatigue crack growth rate was calculated from the crack lengths measured visually. The plastic dissipation value was obtained by applying the displacement field measured by DIC as the boundary condition to the finite element model in simulation.

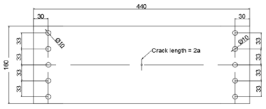

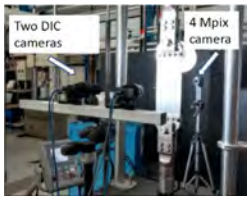

Figure . The CCT specimens and set-up

4. Results

- Fatigue crack growth rate *da/dN*

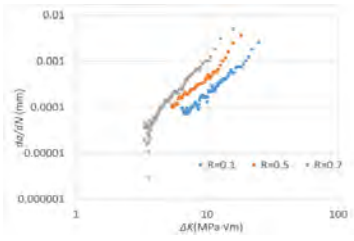

$$\frac{da}{dN} = C(\Delta K)^m$$

R	C	m
0.1	6.093×10^{-7}	2.502
0.5	1.213×10^{-6}	2.598
0.7	3.943×10^{-7}	3.526

- Plastic dissipation *(dW/dN)*.vs. *ΔK*

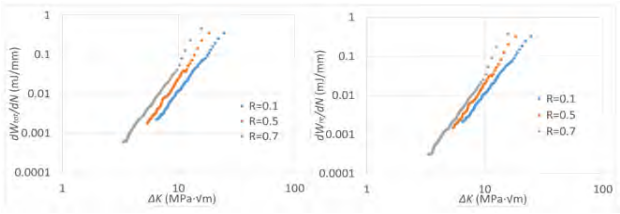

(Left) Total plastic dissipation per cycle in unit thickness .vs. *ΔK;* (Right) Plastic dissipation per cycle in reversed plastic zone in unit thickness .vs. *ΔK*

The relation between *dW/dN* and *ΔK* could be fitted very well in a power law:

$$\frac{dW}{dN} = A(\Delta K)^b$$

Table. The parameters in equation above

R	Total plastic dissipation		Plastic dissipation in reversed plastic zone	
	A	b	A	b
0.1	1.517×10^{-6}	3.878	1.411×10^{-6}	3.886
0.5	1.201×10^{-6}	4.305	8.598×10^{-7}	4.371
0.7	3.614×10^{-6}	4.176	1.401×10^{-6}	4.389

- The value of *dW/da*

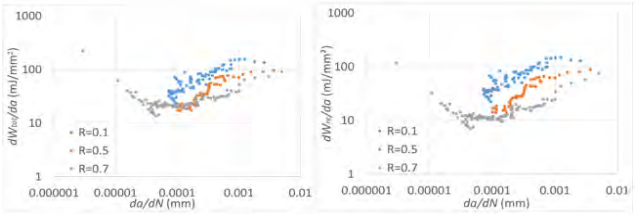

The value of *dW/da* against *da/dN*. (Left) *dW* means the total plastic dissipation; (Right) *dW* means the plastic dissipation only in the reversed plastic zone

If the hypothesis on the linear relationship between *dW/dN* and *da/dN* is correct, the value of *dW/da* should be almost constant, which does not agree with the experimental results.

5. Explanation and conclusion

It is concluded that both the total plastic dissipation and the plastic dissipation in the reversed plastic zone show a nonlinear relation with *da/dN* for 7075-T6. Hence, the value of *dW/da* for 7075-T6 is not constant, implying that the plastic dissipation cannot be used to predict the fatigue crack growth rate for 7075-T6. Because the value of *m (in Paris' relation)* is much smaller than *b (in the relation between dW/dN and ΔK)*.

However, when *m* is close to *b* (*b* normally close to 4), the plastic dissipation could be regarded as approximately linearly related to the fatigue crack growth rate. If that condition is met, the plastic dissipation might be a good method to predict fatigue crack growth rate.

6. References

1. Smith, K. V. (2011). Engineering Fracture Mechanics, 78(18), 3183-3195.
2. Klingbeil, N. W. (2003). International Journal of Fatigue, 25(2), 117-128.
3. Daily, J. S., & Klingbeil, N. W. (2004). International Journal of Fatigue, 26(7), 727-738.
4. Baudendistel, C. M., & Klingbeil, N. W. (2013). International Journal of Fatigue, 51, 96-104.
5. Daily, J. S., & Klingbeil, N. W. (2006). International journal of fatigue, 28(12), 1725-1738.
6. Daily, J. S., & Klingbeil, N. W. (2010). International Journal of Fatigue, 32(10), 1710-1723.
7. Nittur, P. G., Karlsson, A. M. (2014). Engineering Fracture Mechanics, 124, 155-166.

Can spot welded joints be safer than continuous welded joints?

Eva Smeets
Department: ASM
Section: SI&C
Daily supervisor: Calvin Rans
Promotor: Rinze Benedictus
E.T.B.Smeets@tudelft.nl

1	2	3	4

Motivation

Sustainability and safety are big drivers for aerospace design. An understanding of the development of damage is key to predict safety and damage tolerance. The aim of this project is to explore the potential for exploiting patterns of discrete welds of various shapes and sizes to create joints with improved damage tolerance and damage detectability.

EcoDesign demonstrator

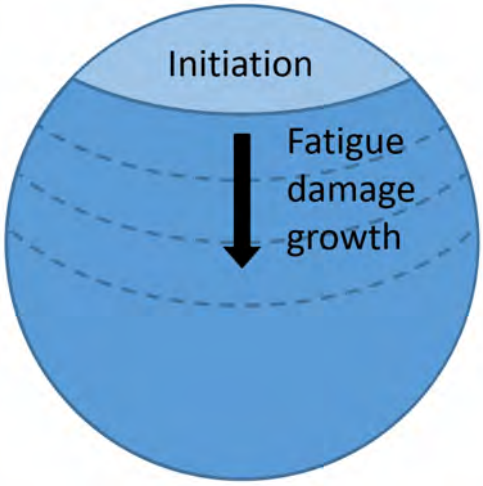

A spot as a joint

The first part is the modelling of the damage behaviour of a single spot weld.

Important aspects

- Damage initiation
- Damage growth

Multi-spot is multi-joint

Unique opportunity for damage tolerance due to damage arresting behaviour.

Important aspects:

- Damage progression
- Pattern optimization

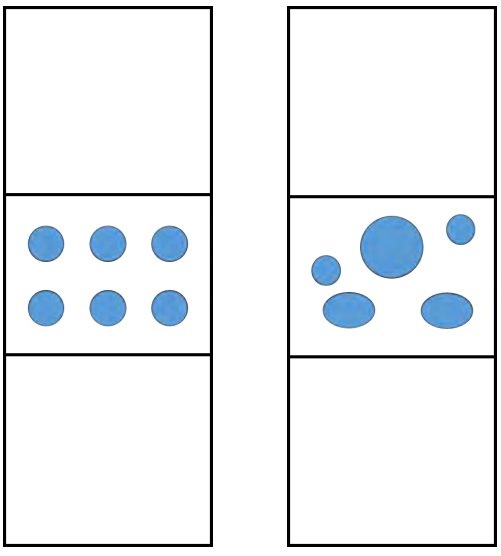

ASM

Shearography Nondestructive Evaluation for Thick GFRP Laminate with Delaminations

Name Nan Tao
Department ASM
Section SI&C
Daily supervisor Andrei Anisimov
Promotor Roger Groves
Rinze Benedictus
n.tao@tudelft.nl

Material	Fatigue & Damage Tolerance	Non-Destructive Testing & Structural Health Monitoring	Manufacturing, Joining & Production	Structure

Background

Shearography is a non-destructive full-field speckle interferometric method for measuring the surface strain field. It has been nearly applied for non-destructive evaluating (NDE) of composite structures by looking for defect-induced strain anomalies. However, the NDE of large and thick composite using shearography is rarely reported. Therefore in this work we aim to develop a shearography inspection system for large and thick composite structures

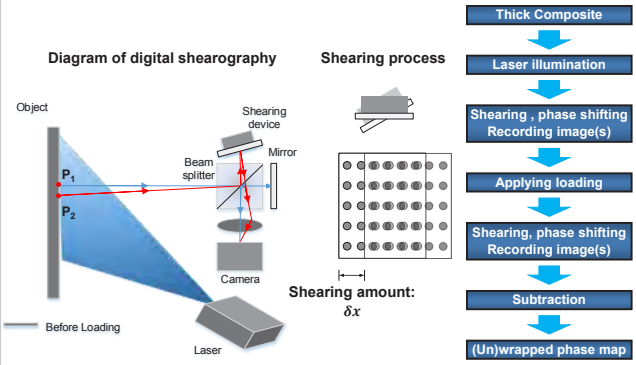

3D Shearography Setup

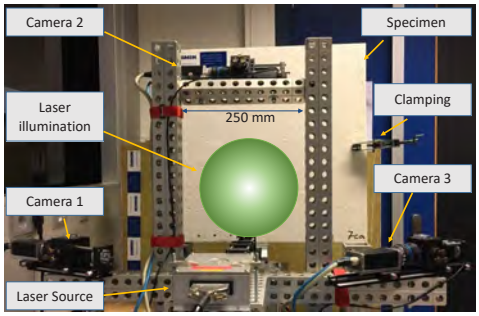

Phase shifting

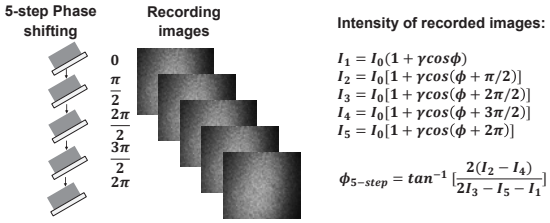

Intensity of recorded images:

$$I_1 = I_0(1+\gamma cos\phi)$$
$$I_2 = I_0[1+\gamma cos(\phi+\pi/2)]$$
$$I_3 = I_0[1+\gamma cos(\phi+2\pi/2)]$$
$$I_4 = I_0[1+\gamma cos(\phi+3\pi/2)]$$
$$I_5 = I_0[1+\gamma cos(\phi+2\pi)]$$

$$\phi_{5-step} = tan^{-1}\left[\frac{2(I_2-I_4)}{2I_3-I_5-I_1}\right]$$

Current Results

Analytical modelling of thermal deformation of a simply supported epoxy plate (intact plate)

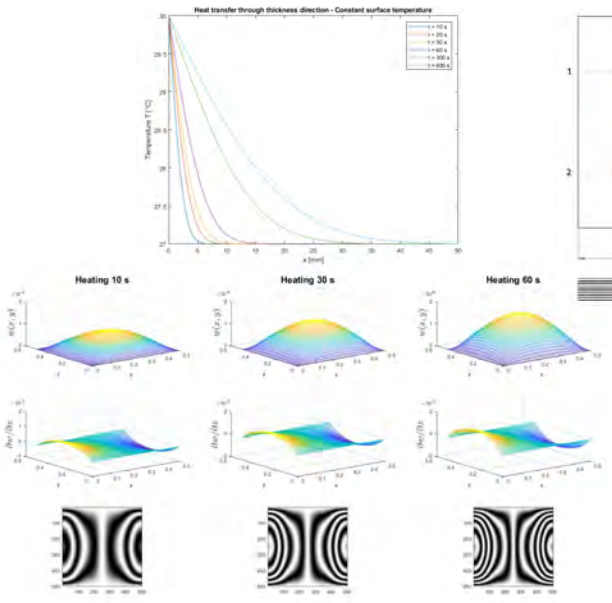

Shearography non-destructive testing for a GFRP laminate with delaminations

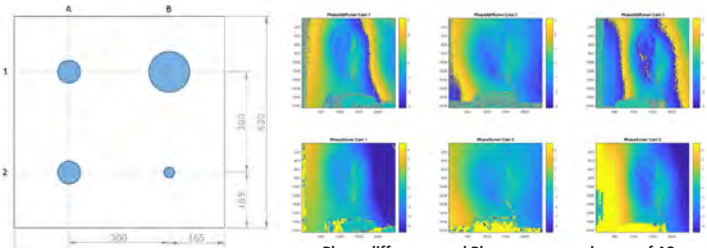

Phase difference and Phase unwrapped maps of A2

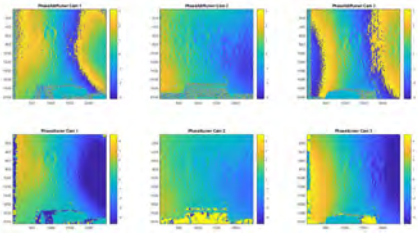

Phase difference and Phase unwrapped maps of B2

Interaction between stress ranges and stress ratios during variable amplitude fatigue crack growth

Jesse van Kuijk
Aerospace Structures & Materials
Structural Integrity & Composites
Daily supervisor: René Alderliesten
Promotor: Rinze Benedictus
J.J.A.vanKuijk-1@tudelft.nl

Background

In 1963, Paris and Erdogan[1] proposed that fatigue crack growth rate follows a power law relationship. Subsequent fatigue crack growth models following this power law relationship are phenomenologically derived, and have *no physical basis*. A physics based model needs to be developed to understand fatigue. The energy equation[2] is used to observe changes in various energy dissipation terms, measured by the potential drop through-the-cycle technique.

The energy equation

$$\frac{dW}{dN} = \frac{dU_a}{dA}\frac{dA}{dN} + \frac{dU_p}{dV_p}\frac{dV_p}{dN} + \frac{dU_e}{dV_e}\frac{dV_e}{dN}$$

Work applied =
Fracture surface energy dissipation +
Plastic volume energy dissipation +
Elastic energy

Potential Drop Through-The-Cycle

Potential Drop (PD) measures the change of electric potential over a crack during fatigue crack growth, relating it to the crack length and growth rate. A new setup is created, measuring Through-The-Cycle: PD TTC. Thousands of measurements can be taken during a single fatigue cycle. The current work describes a method for analyzing the crack tip plasticity and fracture surface energy dissipation.

Results

- Each cycle shows a similar behavior of the potential.
- Relative change in potential increases during the fatigue life.
- Potential follows loading curve when the crack is closed.
- Potential levels off to a plateau while the crack is open and growing.
- The opening stress S_{op}, closing stress S_{cl}, and their timings are inferred from this.
- PD TTC therefore can measure changes in opening stress and closing stress during the fatigue life.

Model

Two main effects are interacting. With increasing strain, the Poisson effect increases and the piezoresistivity decreases the electrical resistivity. The net curve of both is proportional to the loading, but with deviations due to plasticity and crack growth.

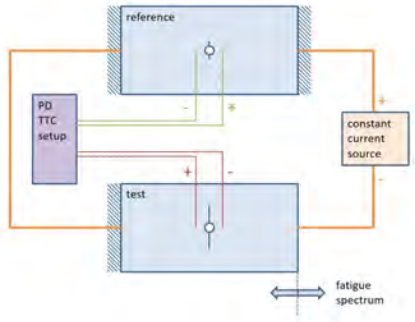

Figure 1. Schematic view of the PD TTC test setup with identical test and reference specimens. The ratio of the two potentials is used as output for crack length calculations.

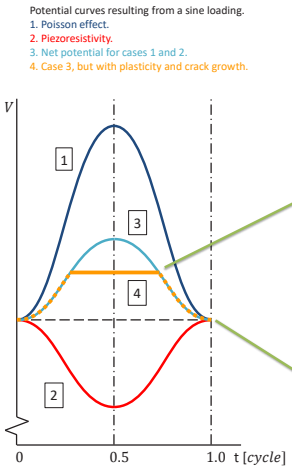

Figure 2. Schematic build-up of the measured potential signal (orange) through one cycle. The signal is proportional to the Poisson and piezoresistivity effects.

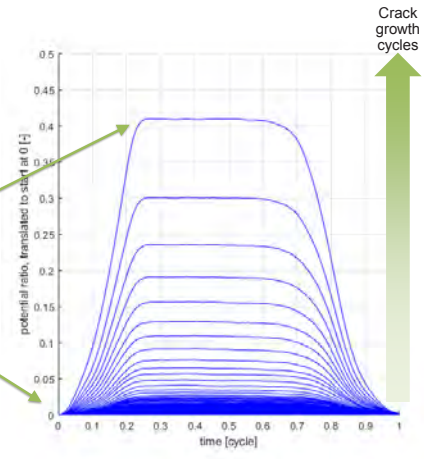

Figure 3. PD TTC measurements of a constant amplitude fatigue test with sine loading. All curves translated to start at zero for comparison. As the crack grows, the absolute range in potential per cycle increases.

Conclusions

- The Potential Drop Through-The-Cycle (PD TTC) technique gives information about fatigue crack growth phases, such as plasticity, crack opening, and crack closure.
- The development of these phenomena during the fatigue life can be tracked.
- These results can be used to enhance widely used models of fatigue crack growth, such as crack closure models and crack tip plasticity.

[1] P. Paris, F. Erdogan, *A critical analysis of crack propagation laws.* Transactions of the ASME (1963) 528-533
[2] R.C. Alderliesten, *How proper similitude can improve our understanding of crack closure and plasticity in fatigue.* Int. J. of Fatigue 82 (2016) 263-273

MODELLING THE FRACTURE OF METAMATERIALS

Megan Walker
ASM
SI&C
Calvin Rans
Rinze Benedictus
M.S.Walker@tudelft.nl

INTRODUCTION

- There exist in nature materials which are very light yet have a high fracture toughness; such as the exoskeleton of a lobster.
- These materials are composed of a repeating structure, mimicked in man-made materials such as the hexagonal honeycomb, referred to as metamaterials
- Almost no experimental work has been done to determine the fracture toughness, K_{IC}, of metamaterials.

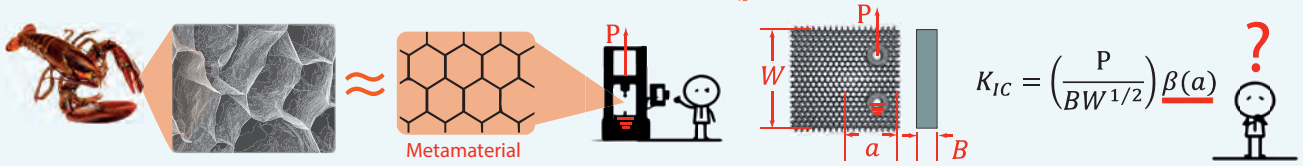

- Determination of K_{IC} requires the shape correction factor, β. in order to determine β we must first have a working model of the entire geometry.
- Modelling the entire geometry (i.e. producing a "micro-geometrical" model) could be quite computationally expensive.
- Some authors have reported success in modelling these structures using beam elements. This could be a computationally inexpensive solution to the problem.

Can beam elements be used to produce a micro-geometrical, numerical model of a CT specimen composed of a hexagonal honeycomb structure?

METHOD

- The general approach is to produce a numerical model and validate it using 3D printed specimens
- Several relative densities, ρ, were used to investigate the impact of beam slenderness.

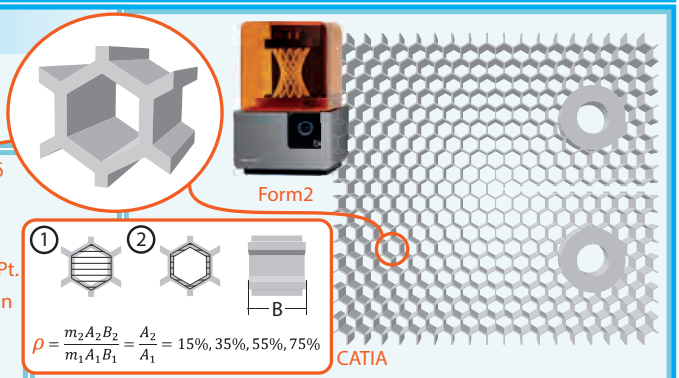

NUMERICAL

- Abaqus/Standard (implicit), Newton's Method
- Timoshenko (B21) elements
- Symmetry boundary conditions applied across Mirror line

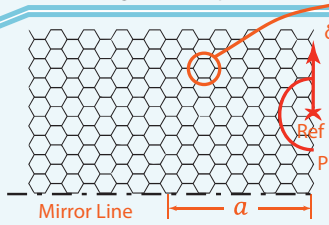

- The crack, a, is created by selectively removing the symmetry boundary condition
- Pin is rigid and is connected to Ref Pt.
- The force is determined by summing the reaction forces for a given displacement, δ, applied at Ref Pt.

EXPERIMENTAL

- Samples were designed using CATIA, output as .stl files then printed using a Form2 SLA 3D Printer.
- Samples were tested at a constant displacement rate of 10mm/min

RESULTS

- Several values of force were determined prior to the first fracture event (points a, b, c and d).
- For ρ=15, 35, 55 and 75% the forces as determined by the model were: 10.2, 4.3, 2.4 and 4.8 times larger, respectively.
- Fracture surfaces were quite tortous and uneven through the depth, B, of the sample.

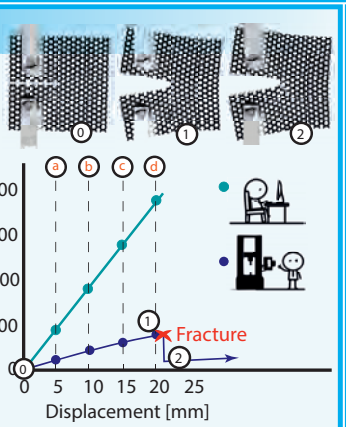

DISCUSSION

The differences between the model and the experiments may be due to the following:

1) The fracture surfaces seem to suggest that the samples were being subjected to an out-of-plane load during testing. If this was the case then only a portion of the cross-section would be loaded at a time. This would have a profound impact on the recorded force values.
2) The constitutive model used in Abaqus did not take plasticity into account. This would have the effect of making the model stiffer. However, β is an LEFM concept (i.e. a linear elastic concept). A preliminary investgation using a perfectly plastic constitutive model suggested that plasticity is extensive even at low levels of displacement. The material used may exhibit too much plasticity prior to fracture for LEFM to be applicable.

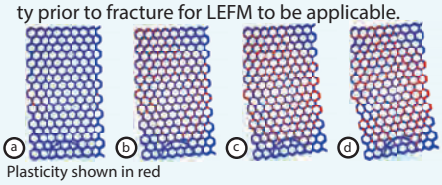

Plasticity shown in red

ONGOING INITIATIVES

- Fixtures have been redesigned to ensure that any out of plane loads are minimized.
- Samples were also redesigned to be thinner so as to mitigate the effect of out of plane loading.
- Various SLA polymers were tested and one was found to have a nearly perfect elastic/brittle behaviour. New samples will be tested from this material.
- In the event that this work is successful, future work will be done to investigate the impact of plasticity, as these preliminary experiments have suggested that it has a significant effect.

Development of Distributed Fiber Optic Sensing for Structural Health Monitoring

Name: Xiang Wang
Department: ASM
Section: SI&C
Daily supervisor:Dr. Roger Groves
Promotor: Prof. Rinze Benedictus
Xiang.Wang@tudelft.nl

Fiber optic sensing for Structural Health Monitoring

Fiber optic sensing is an effective way for structural health monitoring. It can detect the structural operating conditions including the shape of the structure, operational attitude, temperature field, strain field, etc. The performance of the sensors will effect the final result of the structural health monitoring. Therefore, developing high performance sensors is always an important theme for structural health monitoring.

Mie scattering for sensing

Mie scattering has the advantages of high intensity signals in optical fiber, which has the potential to have a better signal-to-noise ratio when obtaining data related to structural health monitoring.

Some simulations of Mie scattering from spherical particles with different size parameters and relative refractive index (the ratio of the refractive index of particles to the medium) are shown below to give the understanding of the influence from these parameters.

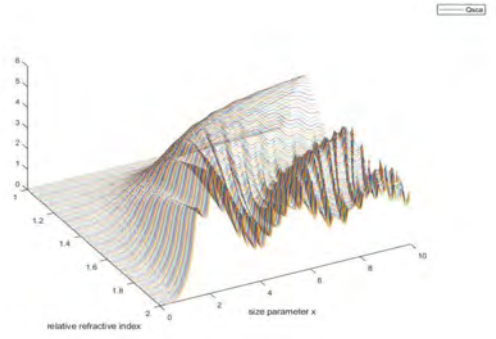

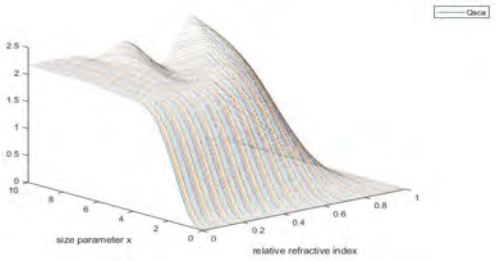

By analysing the characteristics of scattered light from particles between two optical fibers, the understanding of the behaviour of small particles along the sensing fiber will be deepened.

The figure for investigating the behavior of small size spherical particles (from nanometers to micrometers) is shown below:

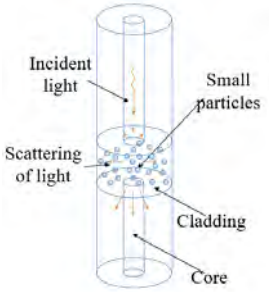

Experiment setup

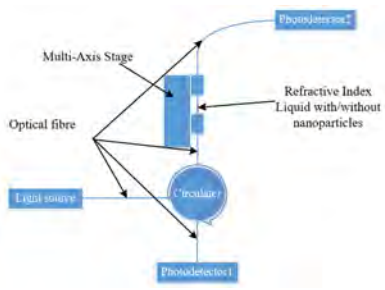

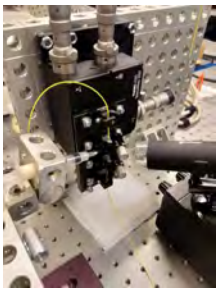

Objectives

The main research objective of this project is

- Investigate in the characteristics of Mie scattering in optical fibers
- Develop high sensitive distributed fiber optic sensor for structural health monitoring based on Mie scattering

INFLUENCE OF CLAMP POSITION ON STATIC ULTRASONIC WELDING OF THERMOPLASTIC COMPOSITES

Camila B. G. Brito
Aerospace Structures & Materials

Irene F. Villegas
Clemens Dransfeld
C.Brito@tudelft.nl

ULTRASONIC WELDING

- Suitable for thermoplastics
- No foreign material
- In-situ monitoring
- High-speed

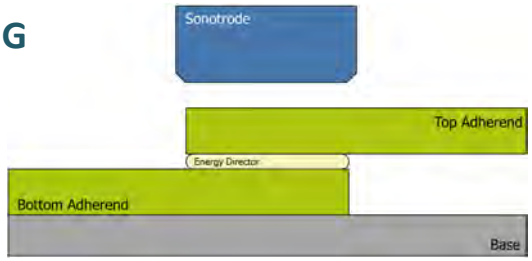

Parameters of interest:

- **Time** for energy director to flow
- **Power** consumed during the process

Clamp Position

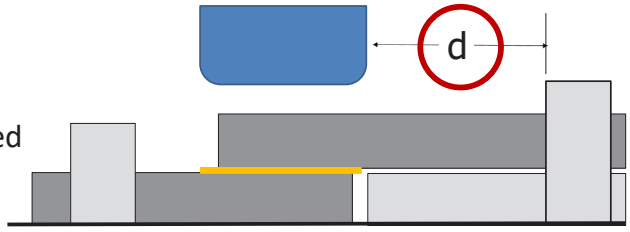

Angle effects

- Misalignment created between adherends

Vibration Effects

- Damping coefficient
- Spring constant

Power x Time - Δd

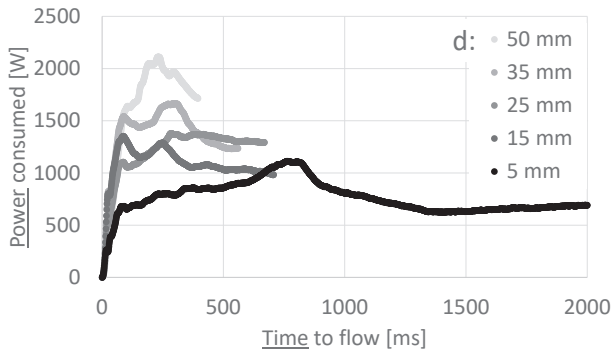

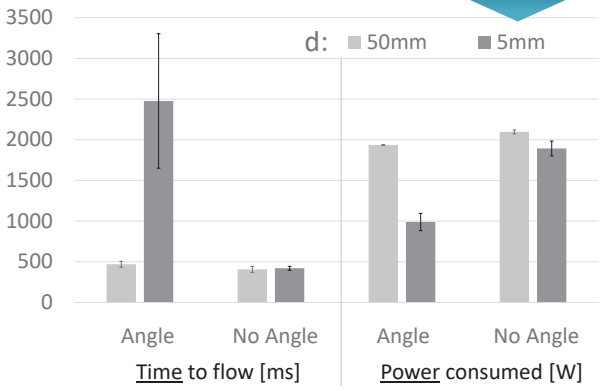

✓ CONCLUSION: Main effects come from **angle**.

Angle X d

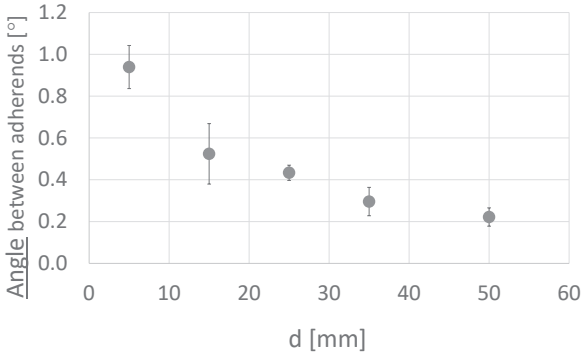

Fracture Surfaces

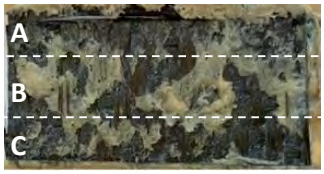

- A: melted
- B: melted
- C: melted

- A: intact
- B: melted
- C: overheated

✓ CONCLUSION: Increasing angle leads to different heating rates within the welding area

Consolidation During Laser Assisted Fiber Placement

Ozan ÇELİK
Aerospace Structures & Materials
Aerospace Manufacturing Technologies
Julie Teuwen, Daniël Peeters
Clemens Dransfeld
ozan.celik@tudelft.nl

Effects of Rapid Laser Heating on Deconsolidation State of CF/PEEK Tapes

Problem: During the process, rapid and intense heating of the thermoplastic composite material is required due to high melting temperatures (above 300°C) of high performance thermoplastic resins and very short processing times (0.01-0.3 seconds). The effect of the heating phase on the microstructure of the tape is unknown.

Experiments: A Philips VCSEL laser heater was used to heat CF/PEEK tapes to the same temperature with different heating time and heated length. Temperature and surface profile was measured in-situ with a thermal camera and laser surface scanner.

Results:

- Even if the laser radiation is uniform, non-uniform temperature occurs and it follows the tape profile
- The thickness and arc length of the tape increases during the heating phase
- Tape deformation starts from the glass transition temperature
- Heated length affects the mode of deformation and heating time affects the maximum out-of-plane deformation

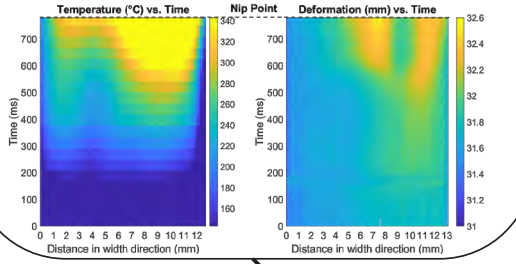

Influence of Thermal Contact Resistance on Thermal History in LAFP

Problem: Temperature history of the newly placed tape is affected by the degree of intimate contact at the interface. Air pockets at the interface create thermal contact resistance and reduce the heat transfer from the tape to the substrate. The relationship between the degree of intimate contact at the exit of the roller and the temperature history is unknown.

Experiments: A thermal camera was mounted at the outlet of the compaction roller of a LAFP machine, where the intimate contact between the tape and the substrate is already established. Laminates with different degrees of intimate contact were manufactured by changing the compaction force but keeping all the other parameters constant. The temperature history of the newly placed tape was recorded and cross-sectional microscopy images were taken from the samples to measure degree of intimate contact.

Preliminary results: The thermal images show significant differences when the compaction force was changed. At the low compaction force, the tapes at the center compact less due to the reduced pressure. They exhibit a higher temperature at the exit of the compaction roller and cool down slower

Future work: The relationship between the degree of intimate contact, the resulting TCR and the temperature history will be investigated using an optical-thermal model of the process.

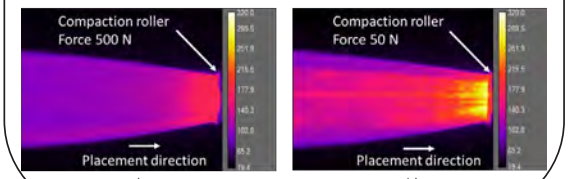

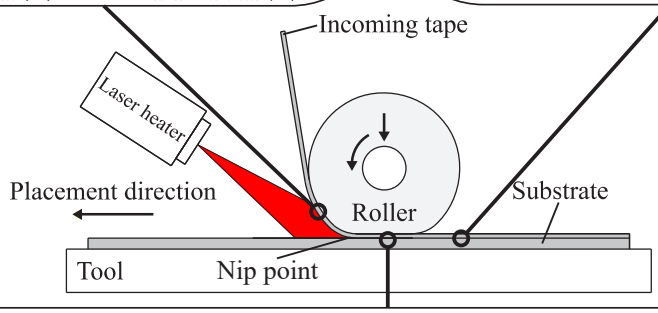

Intimate Contact Development During Laser Assisted Fiber Placement: Microstructure and Effect of Process Parameters

Problem: Intimate contact development is the first step of consolidation and very important for the quality of the final product. So far, it has been assumed that intimate contact develops with the squeeze flow of surface asperities. This assumption is derived from process models which were developed for conventional thermoplastic composite processing, e.g. press consolidation. The mechanisms for intimate contact development at short time spans typically found in the LAFP process, taking the microstructural changes due to laser heating into account, is unknown.

Experiments: One-layer samples were prepared with a LAFP machine with different process parameters. The final degree of intimate contact of the samples was measured with a novel method which considers the non-homogeneous nature of the contact surface.

Modeling: A heat transfer finite element model of the process was formulated to estimate the temperature history of the tape in the compaction region. The estimated temperature history was then combined with the measured roller pressure and the degree of intimate contact was calculated with the state-of-the-art intimate contact models.

Results: The concept of *effective intimate contact*, which is based on the resin content at the surface, is introduced and a methodology to measure it from surface micrographs is provided. Squeeze flow models could not predict the measured degree of effective intimate contact. It is shown that in addition to the squeeze flow mechanism, through-thickness percolation flow of the resin needs to be considered to explain the effective intimate contact development.[1]

[1] Çelik, O., Peeters, D. M. J., Dransfeld, C. A., Teuwen, J. J. E., Intimate Contact Development During Laser Assisted Fiber Placement: Microstructure and Reffect of process parameters, Submitted to Composites: Part A Applied Science and Manufacturing (Under review)

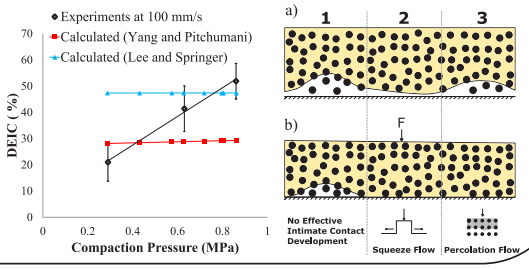

Toughening of epoxy using thermoplastic multilayers: an interface/interphase study

Ujala Farooq
Aerospace Structures and Materials
Aerospace Manufacturing Technologies
Supervisor: Dr. Julie Teuwen
Promotor: Prof. Clemens Dransfeld
u.farooq@tudelft.nl

Objective

The use of thermoplastic multilayers, instead of bulk resin modification, is proposed to improve the toughness of the epoxy resin by the synergetic mechanism comes from inhomogeneity effect along with the morphology gradient. The proposed methodology will also solve the problem of viscosity enhancement, that occurred in bulk resin modification, by infusing unmodified liquid epoxy into the thermoplastic films.

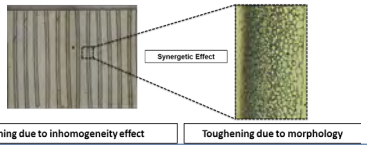

Theory

The crack resistance and fracture toughness of epoxy is extremely poor at room temperature due to its high cross-linked density. The dominant solution is to incorporate a second phase (i.e., thermoplastics) into the epoxy matrix through bulk resin modification. The novelty of this research is, however, to incorporate the multi-layers scaffold of poly(ether imide) (PEI) into tri-functional and tetra-functional aerospace grade epoxy system, in order to develop an ideal model system to investigate the crack propagation with hierarchical dual scale toughening.

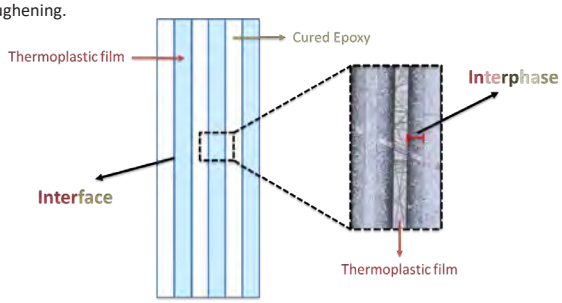

Infusion of epoxy into multilayers (scaffold) of thermoplastic

The thickness of the interphase (i.e., gel layer) in PEI/epoxy system is strongly dependent on the following parameters:

- **PEI film thickness**
- **Curing temperature**
- **Curing time**

Experimental

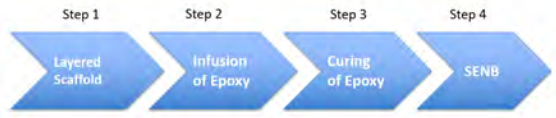

The development of scaffold using four steps

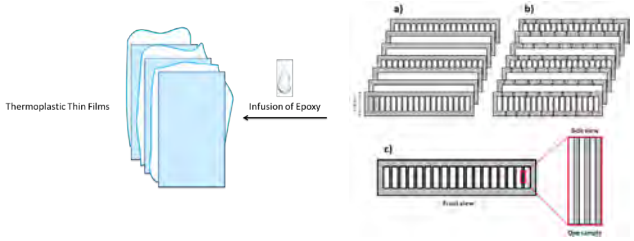

Order of films stacking. Every two 'ladders' have 2 spacers in between to reach 33vol% PEI content. a) without channels b) with channels c) cutting of single sample from scaffold

Results and Discussion

- Scaffolds produced from 60 µm PEI film differed in the dissolution behavior from the scaffolds produced from 25 and 50 µm PEI film.
- In the former case, PEI films dissolved partially upon infiltration reaching a 90% dissolution at higher curing temperatures.
- In the latter case, PEI films were able to dissolve completely at temperatures higher than 180°C.

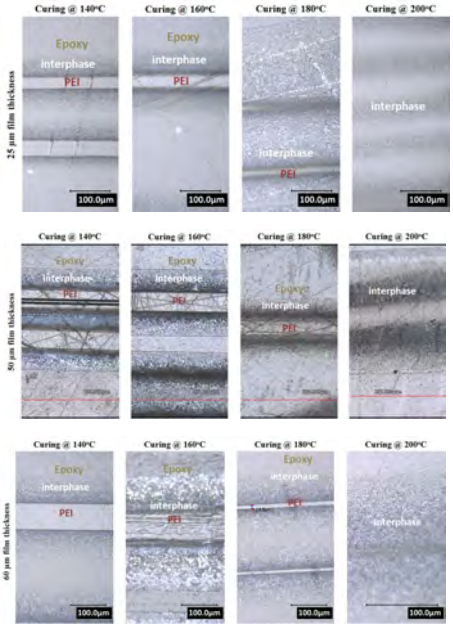

Microscopic images of solvent-etched PEI scaffolds made of 25,50 and 60 µm thick PEI film infiltrated with epoxy and cured at different temperatures.

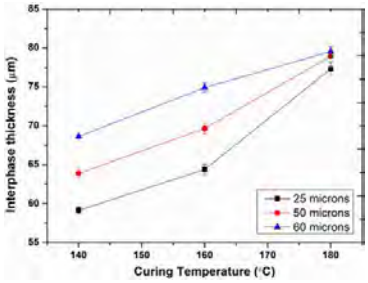

Influence of curing temperature on PEI/EP interphase thickness

Conclusions

This study presents the formation of dual scale morphologies in PEI/epoxy system. The gel layer was formed at the PEI/epoxy interface due to the diffusion of epoxy monomers into the glassy thermoplastic and its partial dissolution. The gel layer thickness increases both with increasing curing temperature and PEI film thickness.

References

P. Vijayan P, D. Puglia, M.A.S.A. Al-Maadeed, J.M. Kenny, S. Thomas, Elastomer/thermoplastic modified epoxy nanocomposites: The hybrid effect of 'micro' and 'nano' scale, Materials Science and Engineering: R: Reports, 116 (2017) 1-29.

J. Teuwen, J. Asquier, P. Inderkum, K. Masania, C. Brauner, I. Villegas, C. Dransfeld, Gradient interphases between high-Tg epoxy and polyetherimide for advanced joining processes, in: ECCM18: 18th European Conference on Composite Materials, 2018.

High performance composites based on discontinuous fiber architectures

Deniz Ezgi Gülmez
Department: ASM
Section: AMT
Daily supervisor: Jos Sinke
Promotor: Clemens Dransfeld
D.E.Gulmez@tudelft.nl

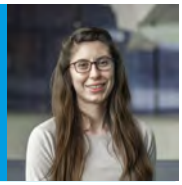

SCOPE: The application of thermoplastic high performance fibers reinforced polymers(CFRPs) requires faster processing methods, increased design freedom and attractive recycling routes, while further improving lightweight performance and damage tolerance.

TARGET: Novel manufacturing methods for discontinuous CFRPs using thermoplastics matrices with bioinspired hierarchical composite architectures and constitutive models to describe their mechanical properties.

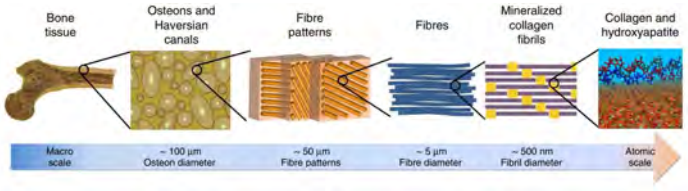

[Buehler 2013]

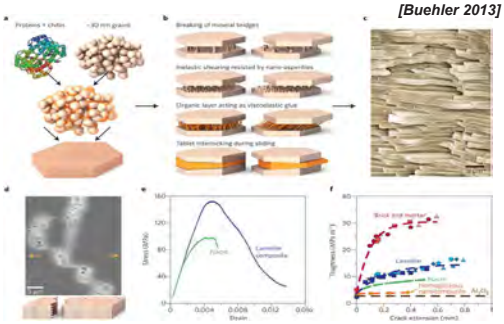

[Wegst 2015]

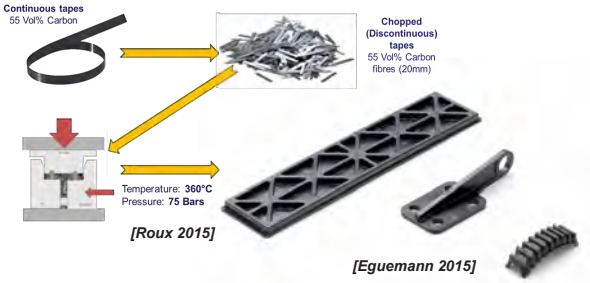

[Roux 2015]

[Eguemann 2015]

BACKGROUND

Structural materials in nature such as bone or nacre develop outstanding properties by combining stiff and ductile constituents into hierarchical structures. It is appealing to investigate whether the concept of bioinspired discontinuous structures can be applied to aerospace composite materials, aiming to achieve unprecedented combinations of strength, damage tolerance and manufacturability, while offering the potential to use discontinuous fiber architectures from recycled production waste or end of life.

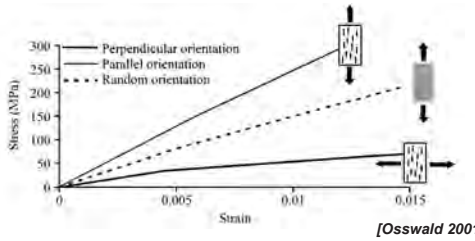

[Osswald 2001]

EXPLOITATION AND POSSIBLE FUTURE DEVELOPMENTS

- Modelling approach for composites with stochastic mesoscale architecture.
- Processing methods for application into complex structures
- Processing routes based on production waste from continuous fiber composites

OBJECTIVE

The projects aims at addressing three aspects:

- Multi scale modelling of mechanical response of composites based on chopped thermoplastic unidirectional tapes
- Development of fast manufacturing technology including local control of the orientation of chopped tapes.
- Recycling of thermoplastic composites made from chopped unidirectional tapes

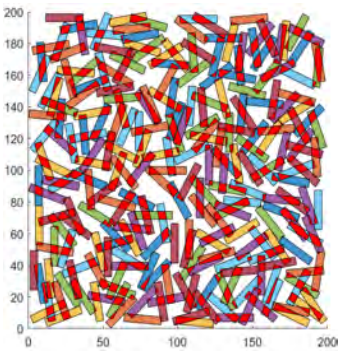

[Roux 2015]

Leakages in Vacuum Bagging

Influence of leakages on vacuum bagging and composite part quality

Anja Haschenburger
Department AE
Section AMT
Daily supervisor Dr. Jan Stüve
Promotor Prof. dr. ir. Rinze Benedictus
A.I.Haschenburger@tudelft.nl

MOTIVATION

A vacuum bag is required during the curing process of composite parts. The evacuated bag acts as a hermetic border between laminate and ambient, limiting the flow of resin to the outer part geometry and evenly applying pressure onto the part during resin curing. A high degree of evacuation is essential for manufacturing high performance composites for which reason the vacuum bag must be free of leakages which would allow for pressure equalization with the ambient.

Contemporary manual leakage detection methods are inaccurate, time-consuming and correspondingly expensive. To improve the process it is necessary to understand the influence of different leakages on the vacuum bag regarding pressure distribution, air flow and temperature as well as their impact on the part quality. The proposed PhD thesis aims to develop an accurate and fast leakage detection that is based on engineering analysis rather than on trial-and-error and to create a deeper knowledge regarding the main factors of influence of leakages in vacuum bagging on the part quality.

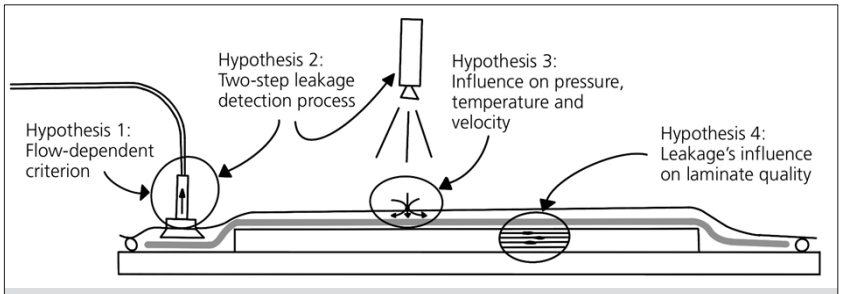

Figure 1: Schematic affiliation of all hypotheses shown on a vacuum bagging cross section

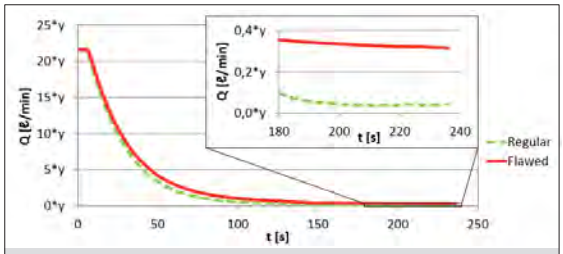

Figure 2: Characteristic flow elevation caused by leakage

HYPOTHESES

Principle hypothesis

There is a method to characterize the influence of leaks on vacuum bagging on component quality in terms of size, shape and location.

- **Hypothesis 1:** There is a flow-dependent criterion for the exact quantification and evaluation of the airtightness.
- **Hypothesis 2:** With the help of a two-step process, it is possible to determine the exact location of the leak and thus achieve a significant time saving in leak detection (>30%)
- **Hypothesis 3:** The influence of leaks on temperature, pressure distribution and velocity can be mapped with the help of flow simulation.
- **Hypothesis 4:** The impact of a leakage on the part quality in terms of porosity and voids can be physically explained and characterized.

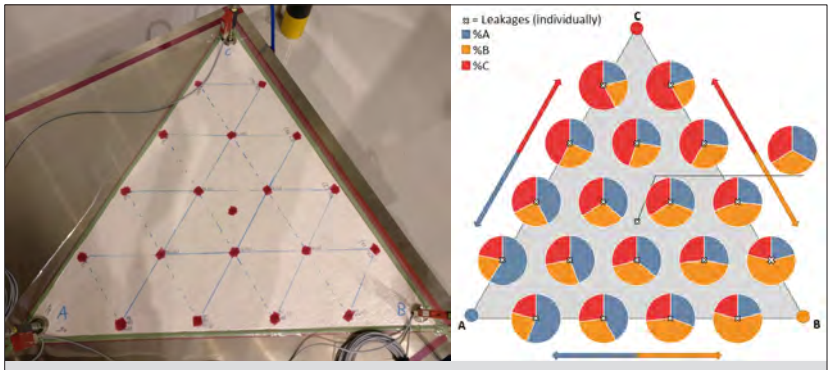

Figure 3: Triangular vacuum bag and distribution of leakage flow

RESULTS AND CONCLUSIONS

Leakages prevent the initial evacuation of the vacuum bag due to the continuous inflow of air. The existence of a leakage results in an elevated threshold flow in comparison to an airtight vacuum bag for which the flow rate continuously decreases until vacuum is reached. Comparison to the flow rate progression of an airtight vacuum bag allows for identification of leakages.

Based on the elevated flow rate, the occurring vacuum loss inside the vacuum bag can be predicted within a range of ten percent. Additionally, the size of the leakage can be determined.

The volumetric flow rate caused by a leakage evenly splits among multiple vacuum lines if not obstructed. The implementation of volumetric flow meters into every vacuum line allows for localization of the leakage, whereas more flow meters result in increased precision.

All figures by the author.

Continuous Ultrasonic Welding of Thermoplastic Composites

Bram Jongbloed
B.C.P.Jongbloed@tudelft.nl

Aerospace Structures & Materials
AMT/ASCM
Dr. Irene Fernandez Villegas
Prof. dr. ir. Rinze Benedictus

Back ground and motivation

Aircraft manufacturers are increasing their interest in carbon fibre-reinforced thermoplastic composites, since these materials can significantly reduce cost during part manufacturing and assembly as compared to carbon fibre-reinforced thermosetting composites. The main contributing factors are the ease of manufacturing (e.g. hot press forming), the reduction in the cycle time, the high material toughness, the recyclability of entire components and scraps produced during manufacturing, and the possibility to weld the thermoplastic composite components together. Recently, continuous ultrasonic welding has been shown to be a promising high-speed joining technique for thermoplastic composites [1]. For the continuous welding process the sonotrode moves over the to-be-welded overlap, while it applies the mechanical vibrations and static welding force.

The objective of this study was to identify and understand differences between the static and continuous ultrasonic welding process for thermoplastic composites in order to see whether we can use the available knowledge in static welding to further develop and understand the continuous process. The two processes were compared experimentally with respect to the melting of the interface, the required areal energy density and consumed power, the temperature evolution at the interface, and the effect of changes of the welding parameters welding force and vibrational amplitude on the optimum welding conditions.

[1] Jongbloed, B., Teuwen, J., Palardy, G., Fernandez Villegas, I., & Benedictus, R. (2019). Continuous ultrasonic welding of thermoplastic composites: Enhancing the weld uniformity by changing the energy director. *Journal of Composite Materials*.

Methodology

Material: CF/PPS [0/90]3s plates with an 0.20 mm thick mesh energy director (ED).
Three parameter cases of welding forces and vibrational amplitudes:
- 500 N and 80 µm
- 1500 N and 80 µm
- 500 N and 60 µm

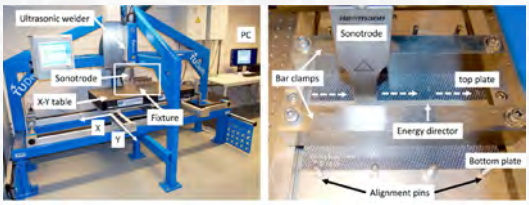

Continuous welding

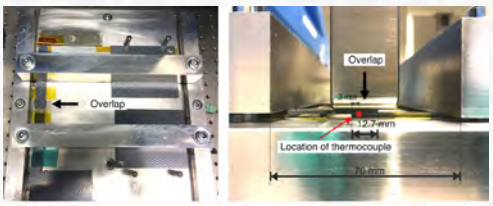

Static welding

Results and discussion

Continuous welding

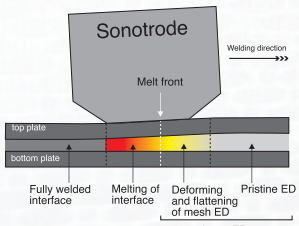

Consumed power & areal energy density

Case	Welding technique	Areal energy density $[J/mm^2]$	Average power [W]
500 N, 80 m	Static [440 ms]	2.0 ± 0.1	843 ± 41
	Continuous [35 mm/s]	3.6	1605
1500 N, 80 m	Static [335 ms]	2.4 ± 0.1	1352 ± 60
	Continuous [45 mm/s]	3.3	1869
500 N, 60 m	Static [940 ms]	2.9 ± 0.3	588 ± 54
	Continuous [15 mm/s]	4.8	916

Static welding

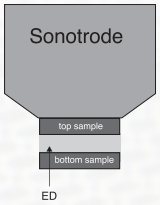

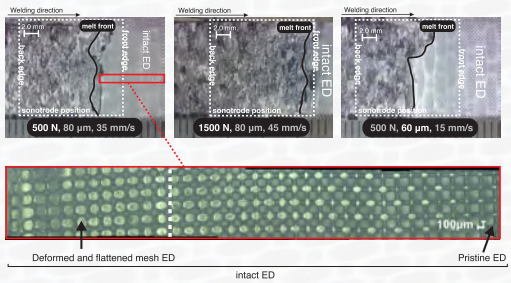

Melting of the interface

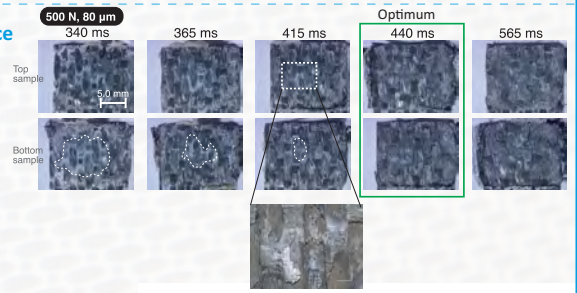

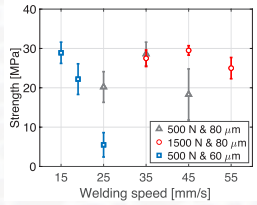

Effect of parameters force and amplitude

		Parameter case		
Optimum time	Based on	500 N and 80 m	1500 N and 80 m	500 N and 60 m
t_{static}	static experiments	440 ms	335 ms	940 ms
$t_{continuous}$	CUW experiments	429 ms	333 ms	1000 ms
Optimum speed	Based on			
$v_{continuous}$	CUW experiments	35 mm/s	45 mm/s	15 mm/s
$v_{calculated}$	t_{static}	34 mm/s	45 mm/s	16 mm/s

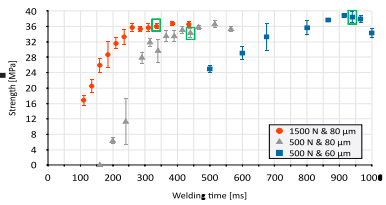

Conclusion

- During the continuous welding process the melt front moves in a straight line together with the sonotrode. While for the static welding process the melt front moves front the edges towards the middle of the weld.
- Continuous process has a higher power consumption than the static process. However, the temperatures measured at the interface are similar.
- Changes in welding force and vibrational amplitude have a similar effect on the optimum welding time and optimum welding speed. Therefore, it seems that they are related and that it is possible find an optimum welding speed based on the optimum welding time in continuous welding

Industrialised Continuous Ultrasonic Welding of Thermoplastic Composites

Filipp Köhler
Department: ASM
Section: AMT
Daily supervisor: I.F. Villegas
Promotor: C. Dransfeld;
A. Herrmann
Email: f.kohler@tudelft.nl

Background

The use of fibre-reinforced plastics for structural purposes in the aerospace industry increased significantly over the past decades due to their advantages over metallic materials. An important aspect is the joining of fibre-reinforced plastic components, since these are unavoidable in aircraft. Thermoplastic composites allow for fusion bonding processes to join parts. During these processes, the thermoplastic polymer melts upon heating, allowing molecular interdiffusion to take place due to the mobility of the polymer chains.

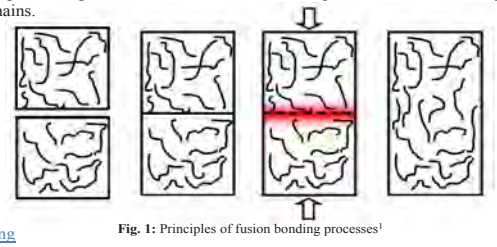

Fig. 1: Principles of fusion bonding processes[1]

Ultrasonic Welding

During the ultrasonic welding process, a sonotrode exerts static pressure and high-frequency low-amplitude transverse mechanical vibration on the adherends. A thin film of the same resin as the composite's matrix, called an energy director (ED), is placed in between the adherends. Due to its lower stiffness compared to the fibre-reinforced adherends, the ED is subjected to higher cyclic strain, thus generating more heat through viscoelastic effects, resulting in a localised heat generation at the interface. Over the past years, static ultrasonic welding has been the focus of an extensive amount of studies, leading to a good understanding of the static process. As a result, the possibility of performing sequential spot welds has shown to be a promising method for the attachment of composite brackets and clips. However, to apply the ultrasonic welding process in high performance aerospace structural components, a continuous process must be developed. Evolving ultrasonic welding from a static to a continuous process allows for higher loads to be transferred and minimizes stress concentrations.

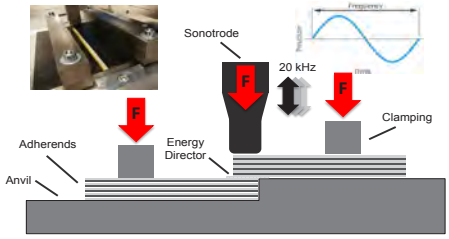

Fig. 2: Schematic of ultrasonic welding setup and process

Research Objective

The research aims at developing an industrialised and robust continuous ultrasonic welding process based on a robotic system to be able to join large aircraft primary structures. Those structures can have complex shapes as well as distinct topologies along the desired weld line and are most often made out of unidirectional continuous fibres.

Focus of research on fabric materials	⇒ Influence of unidirectional materials on welding process
No additional consolidation but proper clamping	⇒ Effect of subsequent consolidation on quality and process
Very stiff machinery with limited flexibility	⇒ Influence of less stiff robotic system on welding process
Start and end of weld line neglected due to different welding conditions	⇒ Influence of additional spot weld on quality and process

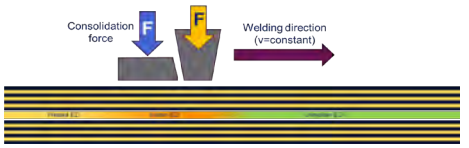

Fig. 3: Continuous ultrasonic welding process with subsequent consolidation

Welding of CF-UD Materials and the Influence of Heat Generation and Heat Transfer

This study aims to investigate how the fibre orientation in the layers adjacent to the weld line influence the welding process and the appearance of edge defects. Specific focus is put on heat generation and heat transfer due to the anisotropic thermal conductivity of unidirectional materials. Ultrasonic welding trials are carried out with and without embedded thermocouples in the weld line. The analysis is based on microscopic analysis of the weld line. Press consolidated laminates were used in two different configurations:

- Configuration 0°: 0/45/135/90/45/135/135/45/90/135/45/0
- Configuration 90°: 90/135/45/0/135/45/45/135/0/45/135/90

Welding was performed on a Ultraschalltechnik Herrmann static welder with a rectangular sonotrode. The process was controlled by vertical displacement. Reference welds were performed to identify the optimum weld parameters. Thermocouples were embedded at different locations. The temperature, power and displacement were sampled at a 1000 HZ rate.

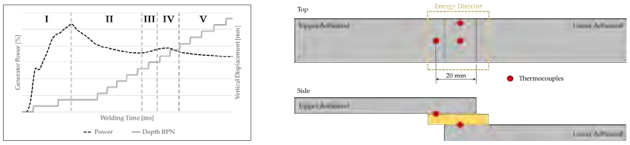

Fig. 4: Power-displacement diagram with highlighted welding stages obtained from reference welds (left) and location of thermocouples (right)

Comparing the fracture surfaces of two samples with configuration 0° and 90° the first shows severe fibre and polymer squeeze out at the longitudinal edges of the adherends. The fibre squeeze out affects the layers adjacent to the weld line but also beyond. The effect of fibre squeeze is also known from fabric materials but usually appears in later stages of process. The fibre orientation adjacent to the weld line does also affect the welding process. Initial melting of the energy director (first power peak in power-displacement diagram) appears at the same time for both configurations. But further melting of the energy director, until vertical displacement starts, takes longer for the 0° configuration. This stage of the welding process is dominated by heat conduction from the longitudinal edges towards the centre of the weld line. Due to the better thermal conductivity in fibre direction compared to the transversal direction heat conduction appears faster in the 90° configuration leading to faster melting of the complete energy director and shorter weld times.

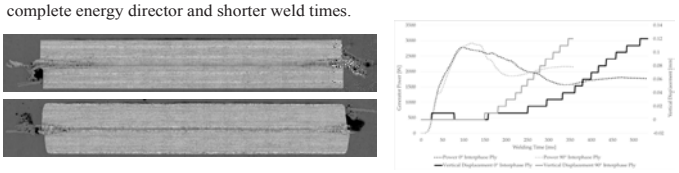

Fig. 5: Transversal microcuts for 0° (top) and 90° configuration (bottom) showing different degree of fibre squeeze out at edges (left) and comparison of welding time and start of vertical displacement for both configurations (right)

This can also be noted when comparing the temperature development during the welding process. Both configurations show an initial rapid increase at the longitudinal edges and in the centre. Afterwards temperature increase slows down especially at the centre of the weld line. But while for the 0° configuration the difference in temperature from longitudinal edge to centre remains at 150-180 °C the difference for 90° configuration is reduced to around 40 °C very quickly (after 250 ms)

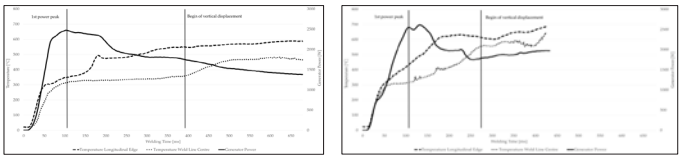

Fig. 6: Temperature development at longitudinal edges (dashed line) and weld line centre (dotted line) and power curves (solid line) for configuration 0° (left) and configuration 90° (right)

Conclusion

- The fibre orientation in the layers adjacent to the weld line highly affects the welding process
- A 0° orientation leads to very severe fibre squeeze out affecting several layers of both adherends
- 0° configuration shows longer overall weld times → can be attributed to worse thermal conductivity compared to 90° orientation
- This is confirmed by temperature development → after initial heating difference from longitudinal edge to centre for 0° configuration remains at high level

Future Work

- Use the knowledge of different thermal conductivity to avoid fibre squeeze out for 0° configuration

References:
I. F. Villegas, L. Moser, A. Yousefpour, P. Mitschang and H. E. N. Bersee, "Process and performance evaluation of ultrasonic, induction and resistance welding of advanced thermoplastic composites," *Journal of Thermoplastic Composite Materials*, vol. 26, no. 8, p. 1007–1024, 2013.
I. F. Villegas, "In situ monitoring of ultrasonic welding of thermoplastic composites through power and displacement data," Journal of Thermoplastic Composite Materials, vol. 28, no. 1, p. 66–85, 2015.
I.F. Villegas, B. Valle Grande, H. E. N. Bersee and R. Benedictus, "A comparative evaluation between flat and traditional energy directors for ultrasonic welding of CF/PPS thermoplastic composites," Composite Interfaces, vol. 22, no. 8, p. 717–729, 2015.
A. Benatar and T. G. Gutowski, "Ultrasonic welding of PEEK graphite APC-2 composites," Polymer Engineering & Science, vol. 29, no. 23, p. 1705–1721, 1989.
[1]E. Talbot, P. Hubert, M Dubé, and A. Yousefpour. Optimization of thermoplastic composites resistance welding parameters based on transient heat transfer finite element modeling. Journal of Thermoplastic Composite Materials, 26(5):699–717, 2013 (1)

Novel Manufacturing Process of Thermoset based Uncured Fibre Metal Laminates

PhD Candidate: Shichen Liu
Department: ASM
Section: AMT
Daily supervisor: Jos Sinke
Promotor: Clemens Dransfeld
Contact: S.Liu-7@tudelft.nl

Introduction

Fiber Metal Laminates (FMLs) — Metal alloys; Dry fibres; Matrix resins → Fibre prepregs

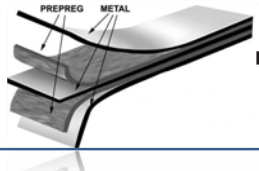

Benefits
- Improved fatigue;
- Better tailoring;
- Higher fire resistance;
- Less corrosion;
- High specific strength and stiffness

Background

Layup

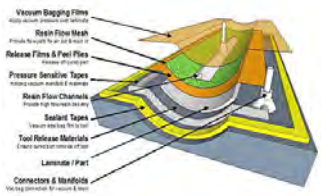

Autoclave

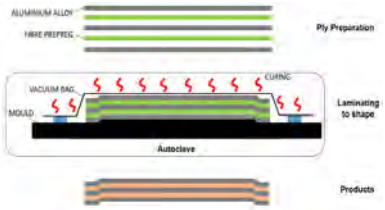

Traditional autoclave process

Related research challenges:

Formability of FML related to metal constituent;

Laminate formability limited by the failure strain of fibres:

Aramid fibres<2.5%; Carbon fibres<1%; Glass fibres<4%;

Fibres deform elastic until failure-High elastic energy involved:

Residual stresses and spring back;

Different and complex failure modes occurred:

Wrinkle, Buckling ,Delamination and Fracture (Both in metals and fibres).

Drawbacks of traditional autoclave process:

- Only suitable for manufacturing **monolithic** and **simple** parts having large radiuses and profiles.
- **High production costs and long production period** which are not economical for small sizes and more complexed shapes.

Research aims:

1. **Use for small sizes and more complex shapes and profiles;**
2. **Achieve the out-of-autoclave process and time-saving as well as cost-saving;**
3. **Apply in mass volume production for industrial application.**

Method

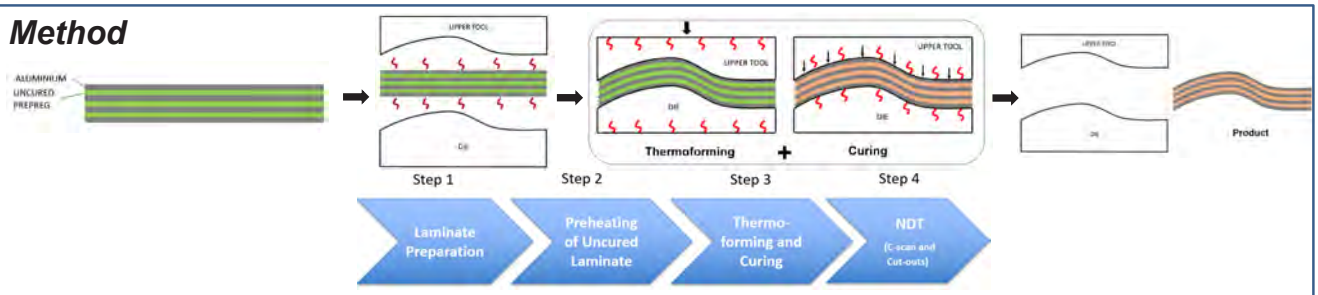

Novel Manufacturing Process of thermoset based uncured fibre metal laminates

Scientific Questions:

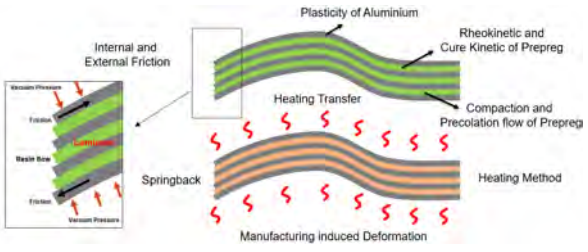

Plan

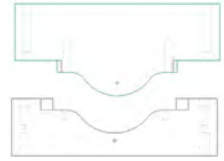

Mould design and shape

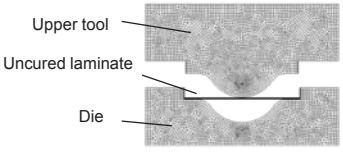

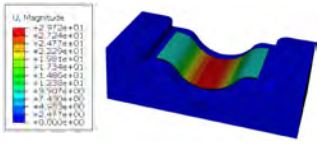

Numerical modelling of the process

References:

[1] J. Sinke, "Manufacturing of GLARE Parts and Structures," *Appl. Compos. Mater.*, vol. 10, no. 4–5, pp. 293–305, 2003.

[2] M. Smolnicki and P. Stabla, "Finite element method analysis of fibre-metal laminates considering different approaches to material model," *SN Appl. Sci.*, vol. 1, no. 5, pp. 1–7, 2019.

[3] L. Shichen, L. Lihui, and G. Shiwei, "An Investigation into the Formability and Processes of GLARE Materials Using Hydro-bulging Test," *Int. J. Precis. Eng. Manuf.*, vol. 20, no. 1, pp. 121–128, 2019.

Life Cycle Assessment of Novel Manufacturing Methods for Carbon Fiber Reinforced Polymers (CFRP)

Name Chizoba Josphine Ogugua
Department: ASM
Section: AMT
Daily supervisor: Jos Sinke
Promotor: Clemens Dransfeld
C.J.Ogugua@tudelft.nl

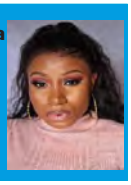

Introduction

The global transition to aircraft with composite architecture is projected to contribute 15%–20% of aviation CO_2 reduction targets by 2050. This reduction is attributed to high specific strength and stiffness, tailorability and fatigue resistance of Carbon Fibre Reinforced Polymers (CFRP) which can significantly reduce aircraft empty weight and in turn lead to reduction in fuel consumption and CO_2 emissions during operation.

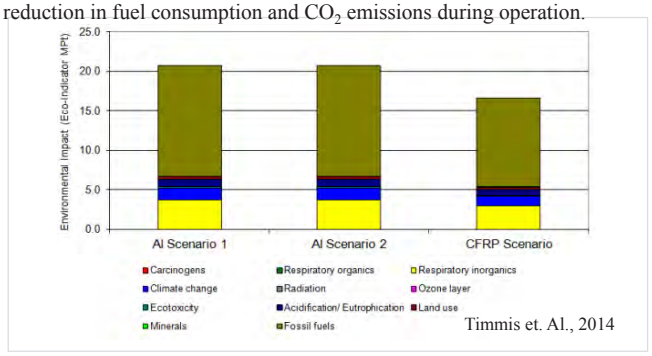

Timmis et. Al., 2014

Despite these benefits, manufacturing CFRP in the prepreg-autoclave route is a high energy, cost and labour intensive process with limited automation, long cycle times and challenges associated with recycling thermoset CFRP [2]. Several novel thermoplastics CFRP processing methods offer the potential for more efficient manufacturing and benefits through significant faster joining methods and attractive end-of-life scenarios. However, little work is known in the public domain focusing on accurate life-cycle assessment of such technologies in terms of energy consumption, environmental and health impacts.

Background

Life Cycle Assessment (LCA) is an ISO standardised methodology that has been used to access the environmental and health impacts of various composite manufacturing technologies. With emerging technologies, which are at their incipient stage and mainly function at lab to pilot scale, there is still a challenge of assessing the environmental impact at an early stage in a way that reflects the future impacts of these technologies when implemented on a full-industrial scale. Limitations including data representativeness of lab-scale results as well as production optimization have still not been addressed.

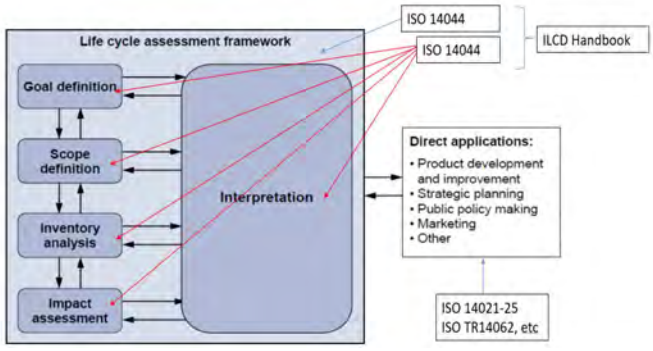

Methodology

This method combines LCA with Ex-ante principles to develop a framework for assessing new and emerging manufacturing technologies for Carbon Fibre Reinforced Polymers (CFRP).
This involves utilising data from lab-scale experiments to investigate the direct environmental impacts of selected CFRP manufacturing processes from a life cycle perspective then scaling up results to consider various multiscale industrial scenarios.

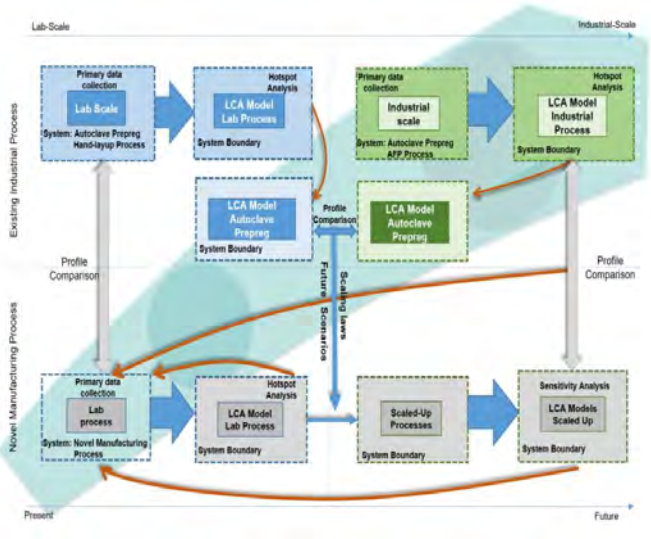

Objective

- Identify Process steps for CFRP Manufacturing
- Develop parametric Scaling Laws relating Energy flows and material flows to part parameters

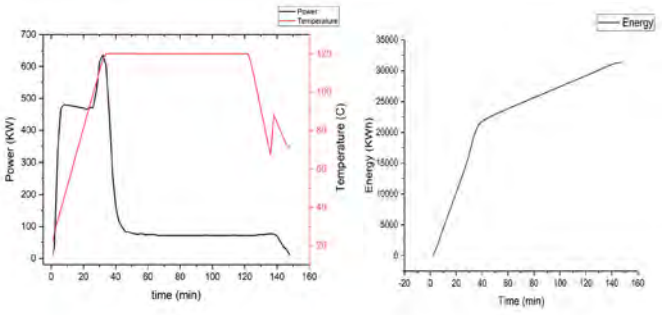

- Validate Scaling relationships
- Carry out LCA of various novel CFRP manufacturing processes using scaling relationships.
- Develop Life Cycle Based Framework for assessing new CFRP manufacturing technologies

Investigation of Fracture Toughness of Ultrasonically Welded Thermoplastics

PhD Candidate: Ioannis Tsakoniatis

Department: ASM
Section: ASCM
Supervisor: I.F. Villegas
Promotor: R. Benedictus
Contact: I.Tsakoniatis@tudelft.nl

Motivation

Carbon fibre reinforced composites offer very high specific properties. Thermoplastic composites offer several advantages compared to Thermosets:

- Reformability, lower manufacturing costs
- Recyclability
- **Weldability**

Fig.1: Composite fuselage section mechanically fastened (left) and welded part (right)[1].

Ultrasonic Welding

- Very fast process
- High frequency-low amplitude vibrations
- Melting of composite matrix through viscoelastic heating

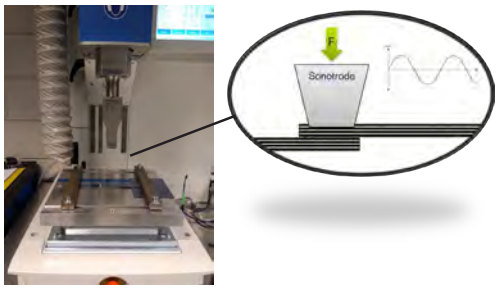

Fig. 2: Ultrasonic welding setup (left) and diagram of process(right).

Project Aim

- **Investigating up-scaling of weld area through static UW**
- **Investigation of fracture toughness of welds**

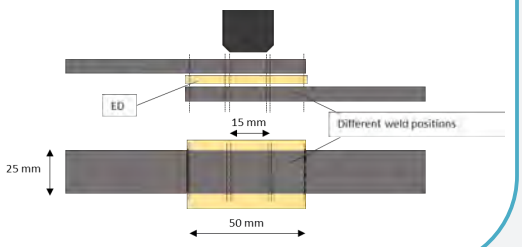

[1] Boeing fuselage photo, https://harpers.org/blog/2013/07/boeings-plastic-planes/
[2] I. F. Villegas, B. Valle Grande, H.E.N. Bersee, and R. Benedictus. A comparative evaluation between flat and traditional energy directors for ultrasonic welding of cf/pps thermoplastic composites, *Composite Interfaces*, 22(8):717–729, 2015.
[4]G. Pallardy, I. F. Villegas. Smart ultrasonic welding of thermoplastic composites, *Proceedings of the American Society for Composites - 31st Technical Conference, ASC* , 2016.

Research Objectives

1. *How can the weld area be increased to measure fracture toughness ?*
2. *What factors affect the process for sequential overlapping welds?*
3. *How do different weld configurations perform in static mode I?*
4. *Can the weld quality be accurately assessed through fracture toughness testing?*

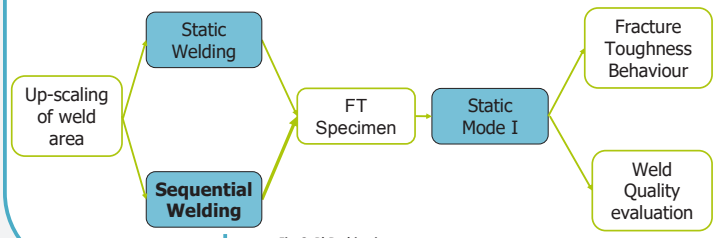

Fig. 3: PhD objectives summary

Sequential Overlapping welding

Different welding configuration studied to get to multiple sequential welds. Use of 2 Energy Director (ED) types and different position within overlap.

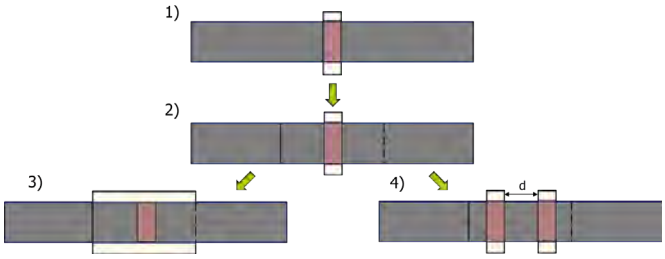

Fig. 4: Overlap configurations

Assessment of weld quality and study of physical changes through:

- Power and displacement output data
- Lap Shear Strength (LSS) testing
- Visual and microscopic Fractography

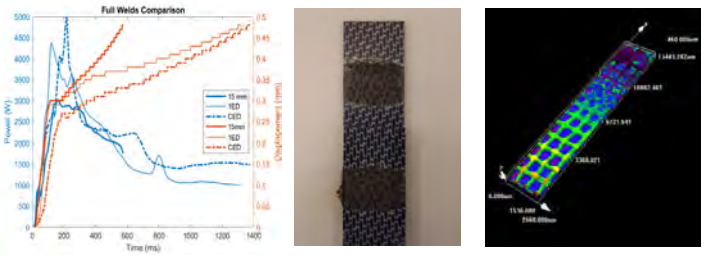

Fig. 5: Power curves (left), fracture surface from LSS (centre) and 3D microscopy image (right).

Conclusions

- ❖ Use of mesh ED provides more consistent high quality welds
- ❖ Welds with continuous ED required higher heating times, changes in vibrations
- ❖ Multiple welds achievable with higher energy director, proximity limit of identified

DEPARTMENT OF CONTROL AND OPERATIONS

The mission of the Control and Operations Department (C&O) is to improve the safety and efficiency of operations in aerospace.

Consequently, the action plan for C&O for the coming years is to:
- Increase its productivity related to the primary mission;
- Focus on making quality contributions to the body of knowledge;
- Invest in two key critical needs, namely managing the enormous growth of unmanned aerial vehicle operations and in operational emissions impact modelling.

The C&O department now houses all the aerospace operations expertise of the faculty, strengthening its focus and making it more visible to the outside world, thereby achieving more synergy and further improving the quality of the research and education.

CONTROL AND SIMULATION

Tom van Dijk
Daniel Friesen
Shushuai Li
Cheng Liu
F. Paredes-Valles
Marta Ribeiro
Gijs de Rooij
P.F. Scaramuzzino
Bo Sun
Yingfu Xu
Yu Ying
Christian Zammit

AIRCRAFT NOISE AND CLIMATE EFFECTS

Kathrin Deck
Colin van Dercreek
Tannaz Haji Mohammadloo
Salil Luesutthiviboon
Flávio D. A. Quadros
Alejandro Rubio Carpio
Ana Vieira

AIR TRANSPORT AND OPERATIONS

Chengpeng Jiang
Juseong Lee
Hao Ma
Matt Vert

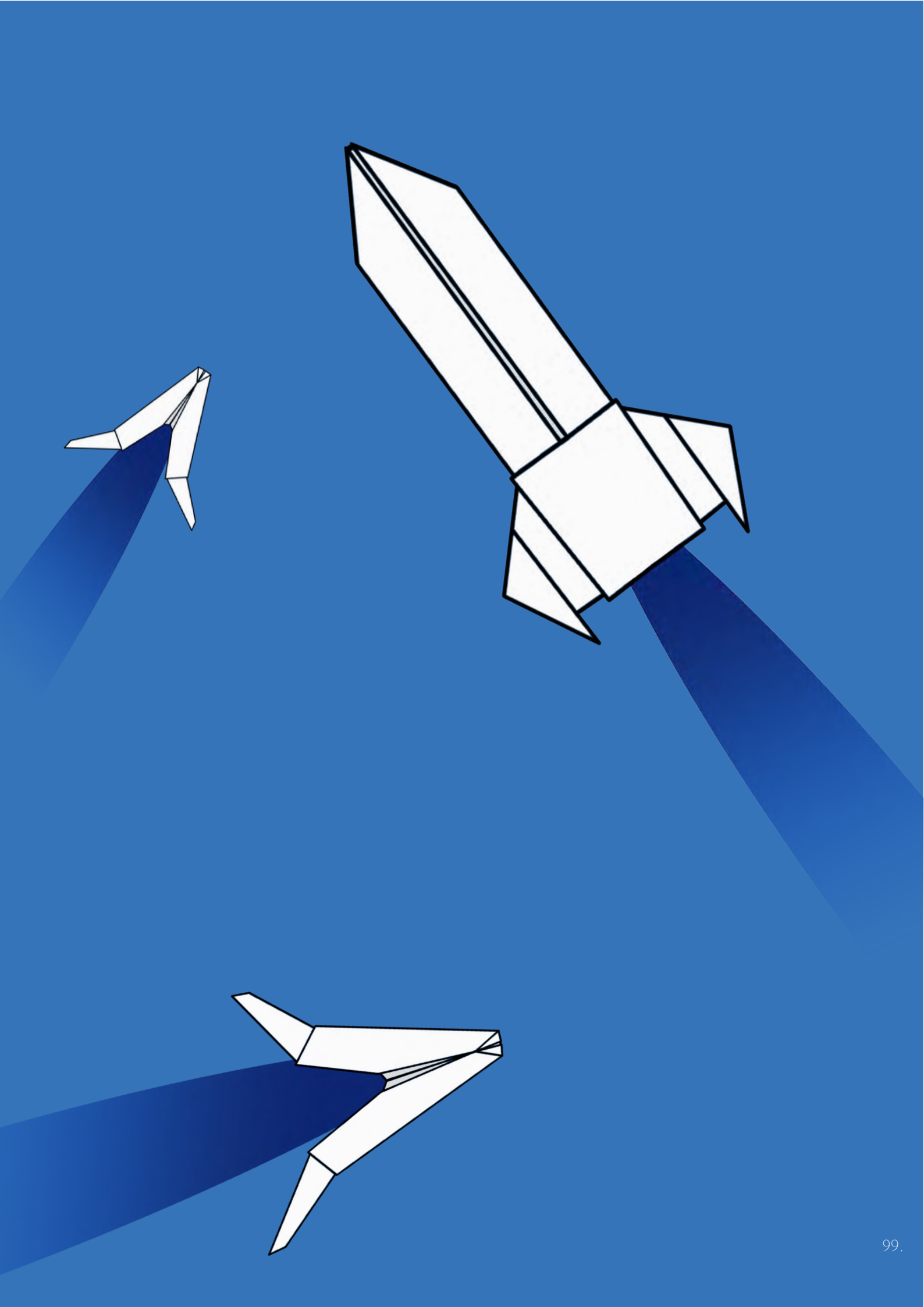

Monocular Visual Obstacle Avoidance for UAVs

Tom van Dijk
Control & Operations
Control & Simulation
Guido de Croon
Max Mulder
j.c.vandijk-1@tudelft.nl

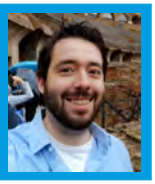

Goal: collision avoidance package for UAVs

Minimize ***cost***, ***weight***:
- Cheap microcontroller (STM32F4 ~€5)
- Single camera (less weight)

Why vision? Lightweight, low energy.

The '*standard*' approach:
Stereo vision and
Visual-Inertial Odometry

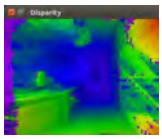

IMAV 2018 Awards

Outdoor Competition Winners
1st Place: ENAC/TU DELFT Team Paparazzi
2nd Place: Urban Ants BUT - Bialystok University of Technology

Conclusions: effective, but mid-high computational load, large stereo camera, sensitive to stereo matching errors.

Monocular vision: how do neural networks see depth in single images?

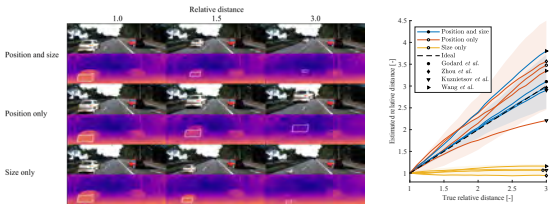

Conclusion: neural networks ignore the apparent size of objects and only use their vertical position in the image. [ICCV '19]

Future work:
Monocular vision ***on UAVs***:
how can neural networks handle changing viewpoints?

How to run monocular obstacle avoidance on a ***microcontroller***?
- Transfer neural network?
- Re-implement learned behavior?

Helicopter Automation

Daniel Friesen
Department: **Control & Operations**
Section: **Control & Simulation**
Supervisors:
Dr.ir. C. Borst
Promoters:
Dr. M. D. Pavel, Dr. P. Masarati
Contact: D.Friesen@tudelft.nl

Why?

The goal of this project is to contribute to an increase in helicopter safety and a decrease of helicopter accident rates. An accident analysis of the European Helicopter Safety Team concluded that in close to 70% of the analysed accidents, **pilot judgement & actions** played a role. Likewise, in close to 35% of accidents, **situation awareness** (or the loss thereof) was a contributing factor. [1,2]

These factors are not solely caused by any single root cause, but are **enabled by the whole human-machine-system architecture** [3]. The focus of this research is the influence of automation systems on the interaction between the pilot and the helicopter.

This project analyses the characteristics and effects of different automation systems for helicopters. It aims to provide knowledge and guidelines to improve helicopter human-machine-interaction and reduce the likelihood of errors and accident causes.

What is helicopter automation?

Automation is more than an autopilot. In a holistic approach, automation systems can cover any or all of the following processes that are required to control a system [4]:

[5]

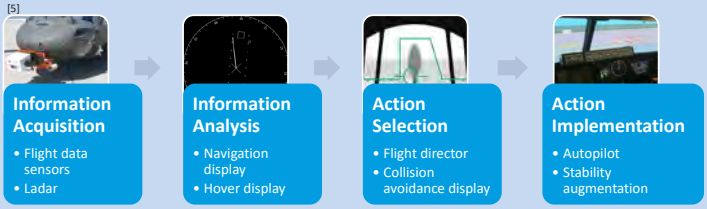

Do we try to replace the human with automation?

No. We try to improve the human-machine-interaction of helicopters by employing automation systems. These systems can support any of the above-mentioned activities.

Methodology

We investigate automation systems covering different time scales of operation: short term, mid term, and long term. Corresponding functions of flight management and control are **Stabilisation**, **Guidance**, and **Navigation**. [6]

We try to answer the question:

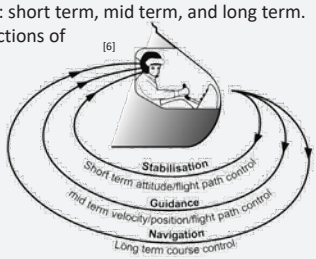

How can automation increase safety?

Stabilisation support

Example: *What are the characteristics of a safety-increasing hover display?*

Experimental Setup

What visual information does the pilot need?

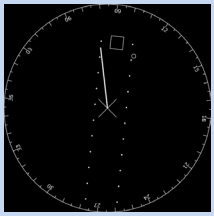

Prototype hover display design

How does the pilot control the helicopter?

What is the influence of the vehicle dynamics?

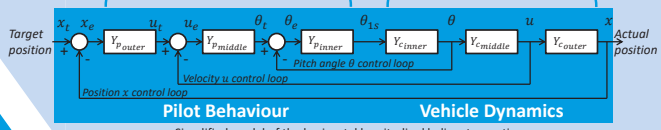

Simplified model of the horizontal longitudinal helicopter motion

Guidance support

Example: *What are the characteristics of a safety-increasing collision avoidance system?*

You're approaching an obstacle in your flight path…

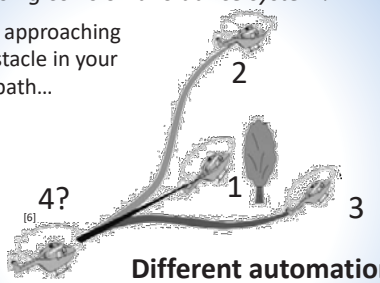

…what is the safest way to avoid a collision?

1. Stop
2. Pull up
3. Initiate a turn
4. A combination of all

Different automation approaches:
support pilot decision making or support quick reaction time

[6], adapted

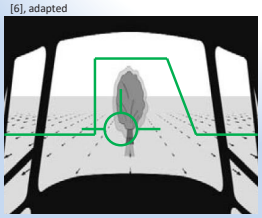

Provides pilot with information, pilot decides on best action

[6], adapted

Determines safest action autonomously, gives recommendation to pilot

Navigation support

Example: *What are the characteristics of a safety-increasing route planning system?*

What is the safest route to the target considering…

- Weather
- Fuel
- Other traffic?

[7]

Expected results

1. **Guidelines for automation design**
2. **A better understanding of the influence of automation on helicopter human-machine-interaction**
3. **Novel automation systems**

[1] European Helicopter Safety Team, Final Report - EHEST Analysis of 2000-2005 European Helicopter Accidents," 2010.
[2] European Helicopter Safety Team, Final Report - EHEST Analysis of 2006-2010 European Helicopter Accidents," 2015.
[3] Dekker, S. W., "Accidents are Normal and Human Error Does Not Exist: A New Look at the Creation of Occupational Safety," International Journal of Occupational Safety and Ergonomics, Vol. 9, No. 2, 2003, pp. 211–218.
[4] R. Parasuraman, T.B. Sheridan, and C.D. Wickens. A model for types and levels of human interaction with automation. IEEE Transactions on Systems, Man, and Cybernetics - Part A: Systems and Humans, 30(3):286–297, 2000.
[5] Szoboszlay, Z. P., McKinley, R. A., Braddom, L. S. R., Harrington, W. W., Burns, H. N., and Savage, J. C., "Landing an H-60 Helicopter in Brownout Conditions Using 3D-LZ Displays," AHS International Forum 66, Phoenix, Arizona, United States of America, 2010.
[6] Padfield, G. D., "The Tau of Flight Control," The Aeronautical Journal, Vol. 115, No. 1171, 2011, pp. 521–556.
[7] Iijima, T., Matayoshi, N., Nishi, T., and Wada, O., "Development and Flight evaluation of Airborne Weather Information System," 2012 IEEE/AIAA 31st Digital Avionics Systems Conference (DASC), IEEE, oct 2012, pp. 2C3–1–2C3–15.

This project has received funding from the European Union's Horizon 2020 research and innovation programme under the Marie Skłodowska-Curie grant agreement No 721920.

Visual relative localization of flying robots with deep neural networks

Shushuai Li
Control & Operation
Control & Simulation
Guido de Croon
Max Mulder
s.li-6@tudelft.nl

1 Introduction

In last decades, multiple robots have been widely studied, which however, rely heavily on external positioning systems like GPS. Since some deep learning methods are proposed for learning the 6D pose of objects, we hope the relative position between robots can be also learned from images.

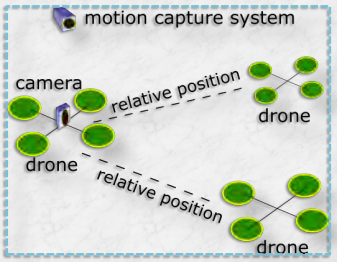

Fig 1. The scheme of 3D relative localization between flying robots by processing images with deep learning. Motion capture system provides the groundtruth of relative position, while camera gives inputs of images.

2 Research question

The composition of datasets:

- Images G_i (i<N=777) with the drone in different positions;
- 3D relative position X_i between the camera and the drone;
- Mask images M_i segmented manually.

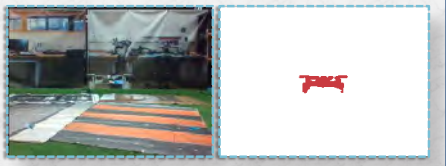

Fig 2. Examples of image G_i (left) captured by the camera, and the mask image M_i (right) segmented manually.

Question statement:

Design a deep neural network f, which takes images G_i as inputs and predicts the relative position X_i, and this regression problem can be written as follows:

$$min \sum_{0}^{N_{train}} \|f(G_i) - X_i\|$$

In the mean time, we hope to extend the network f to f' to predict the mask for image segmentation.

$$min \sum_{0}^{N_{train}} \|f'(G_i) - M_i\|$$

3 Experimental setting

The specifications of settings:

- Network type: U-net with 35 layers
- Layer type: Conv2d, ReLU, MaxPool, Upsampling
- Train/test size: 699/78 (randomly split)
- Batch size: 8 Epoch number: 40
- Loss function: Dice and BCE loss for segmentation, SmoothL1Loss for position regression
- Optimization: Adam with learning rate 1e-4

Neural network structure:

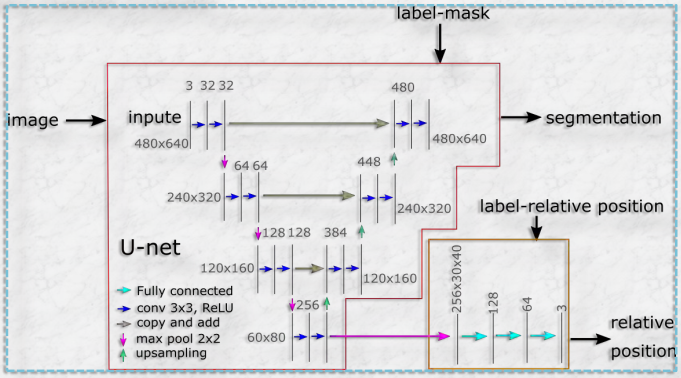

Fig 3. The structure of a typical U-net deep neural network, which takes an image as input and outputs the segmentation result. In training process, the labels consist of masks and relative positions. For relative position regression, only half U-net is used, plus a fully connected network.

4 Results

Fig 4. **The segmentation results** of the drone based on the validation datasets. From which we can see the U-net deep network can successfully detect the drone with different pixel sizes, indicating that the U-net consists of the information of the drone in the image.

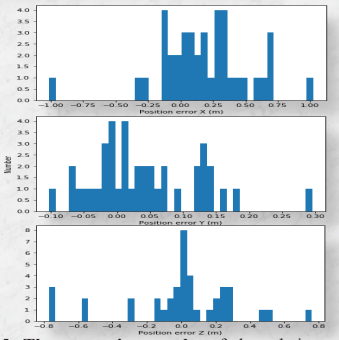

Fig 5. **The regression results** of the relative position between the camera and the drone. Prediction error of 3 dimensional position is shown in this figure, based on 40 pairs of images and goundtruth position from the validation datasets.

5 Discussion

From the segmentation results in Fig. 4 and the regression results in Fig. 5, we can obtain:

- Contraction part of the U-net consists of the information of the drone; fully connected network can regress the relative position between the drone and the camera.
- This neural network does not rely on pre-trained weights.
- Customized datasets can be found in website https://github.com/shushuai3/DLcourse-data

6 Conclusion

Conclusion:

- Trained network is capable of executing image segmentation of the drone;
- Deep neural network could learn the relative 3D position of an object by monocular image.

Future work:

- Current shortage is its robustness to complex background like webcam experiments;
- Improve the generality of this .

TU Delft

Hierarchical Reinforcement Learning (HRL) on Flight Guidance and Navigation

PhD Candidate: Cheng Liu
Department: Control & Operation
Section: Control & Simulation
Supervisor: Erik-Jan van Kampen
Promotor: G.C.H.E. de Croon
Contact: c.liu-10@tudelft.nl

I. Introduction

Reinforcement Learning (RL) is a machine learning algorithm which draws its inspiration from the way humans learn [1]. As shown in Fig. 1, Reinforcement Learning can be defined as the ability of an agent to improve upon its performance via experience from interacting with its environment.

There are two benefits to use RL for the Guidance and Navigation system:

- The system can adapt itself.
- It allows for a black-box approach.

II. Research Challenge

One of the fundamental scientific challenges when applying RL methods to flight guidance and navigation systems is the “curse of dimensionality”. Autonomous guidance and navigation problems often have high-dimensional spaces, multiple objectives, and consequently large number of states and actions. Besides, these systems often have partial observability instead of a perfect perception of their environment. Therefore, a continuous version of RL is required, in which a function approximator such as artificial neural networks will be used to generalize over the state space, representing state functions with a limited number of function-approximator parameters.

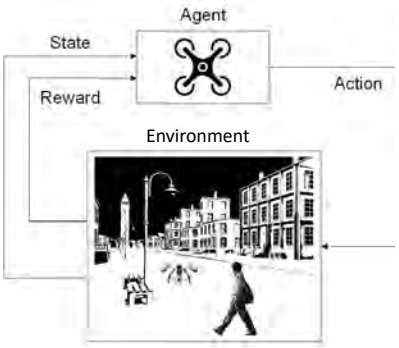

Figure 1. The RL agent-environment interaction (the agent is represented by a quadrotor)

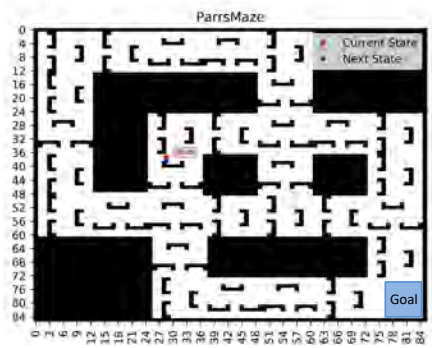

Figure 2. A 86x86 Parr’s Maze environment with obstacles to avoid and a goal to reach by the agent

V. Function Approximator: Artificial Neural Networks (ANNs)

An ANN with a single hidden layer containing a large enough finite number of sigmoid units can approximate any continuous function on a compact region of the network’s input space to any degree of accuracy (Cybenko, 1989). Fig. 3 illustrates the architecture of a deep convolutional network (DCN), a type of ANN that has proven to be very successful in applications including impressive reinforcement learning applications such as AlphaGo Zero [1]. It consists of alternating convolutional and subsampling layers, followed by several fully connected final layers. Each convolutional layer produces several feature maps. Combined with HRL methods, ANNs can be very powerful to solve the curse of dimensionality with high representation accuracy, but the design and training of ANNs lack the ability of generalization [2]. This research also aims to improve the generalization ability of the proposed HRL methods and approximation functions, for example, by using transfer learning methods.

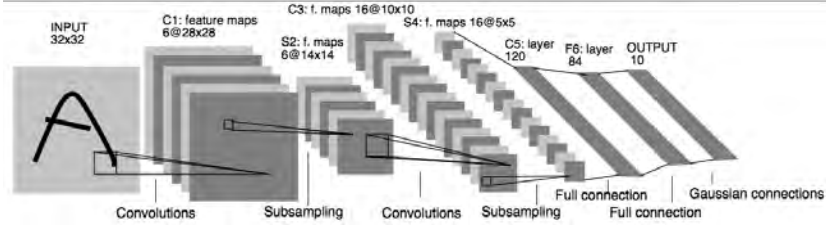

Figure 3. The Deep Convolutional Network [1]

III. Research Goal

This research aims to develop an intelligent flight Guidance and Navigation system, that can learn to guide and navigate the aircraft in unknown conditions. The goal of this research is to increase safety of flight, now and in the future, when there may be even less human presence in the cockpit.

IV. Hierarchical Reinforcement Learning

Hierarchical RL (HRL) is a RL method by which multiple objectives can be combined within one application. HRL follows the general algorithm design principle of divide and conquer so that hard goals, e.g. those with sparse long-term rewards are replaced with easy sub-goals (dense short-term rewards e.g.). As shown in Fig. 4, HRL can speed up learning for multi-objective tasks by allowing different objectives in different levels, and naturally reduces the uncertainty and ambiguity induced by partial observability at higher levels because some hidden variables can be estimated at different levels [3].

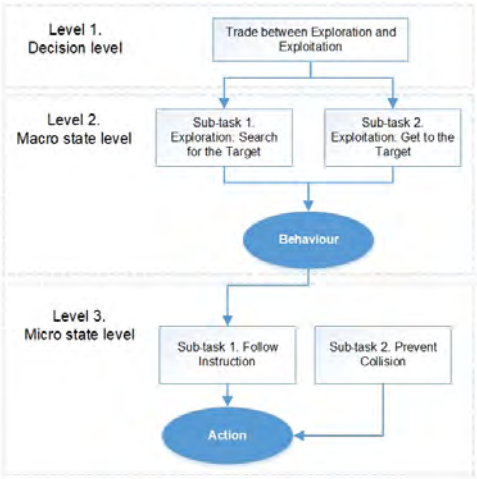

Figure 4. An architecture for Hierarchical Reinforcement Learning on maze navigation [3]

VI. References

[1] Sutton, R. S. and Barto, A. G. (2018). Reinforcement Learning: An Introduction (2nd Edition). MIT Press.

[2] Karimpanal, Thommen George and Bouffanais, Roland. Self- Organizing Maps as a Storage and Transfer Mechanism in Reinforcement Learning. ALA Workshop, ICML 2018.

[3] Ye Zhou, Erik-Jan van Kampen, Qiping Chu, Hybrid Hierarchical Reinforcement Learning for online guidance and navigation with partial observability. Neurocomputing 331 (2019) 443-457.

Neuromorphic Sensing, Computing, and Learning

F. Paredes-Valles
f.paredesvalles@tudelft.nl
Dep.: Control & Operations
Sec.: Control & Simulation
Supv.: Dr. G.C.H.E. de Croon
Prom.: Prof. dr. ir. M. Mulder

Event-based Cameras

Conventional cameras perceive the world as a series of frames. Although convenient for some computer vision applications, these frames contain highly redundant data, hence requiring inefficient and resource-intensive image processing methods.

Inspired by biological retinas, the pixel array of an event-based camera operates asynchronously by only transmitting local brightness changes at the time they occur [1]. The result is a stream of events at microsecond resolution, with very low latency and power requirements, and a wide dynamic range. Each event encodes information about its timestamp, its location in the array, and the polarity of the perceived change.

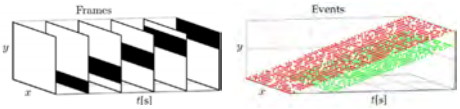

Output of frame- and event-based vision sensors.

Spiking Neural Networks

Taking further inspiration from nature, Spiking Neural Networks (SNNs) have been proposed as alternative to the computationally expensive Artificial Neural Networks (ANNs). Similarly to biological brains, the computation carried out by these neural models is asynchronous and spike-based. Additionally, they can be implemented in neuromorphic hardware for real-time performance, with very low latency and power consumption.

Despite these benefits, the nature of SNNs limits the application of the optimization algorithms normally employed in ANNs. Instead, learning in SNNs is dominated by variants of Spike-Timing-Dependent-Plasticity (STDP), a biologically plausible protocol that adapts the strength of a connection between two neurons based on their correlated activity.

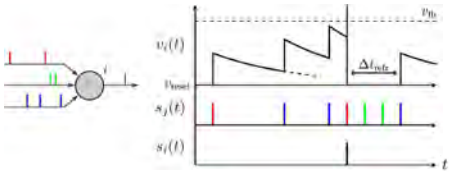

A model of a spiking neuron. The graphic shows the temporal course of the potential of the ith neuron, driven by a sample input spike train.

Bio-Inspired Visual Motion Perception

The combination of SNNs and event-based vision sensors holds the potential of highly efficient and high-bandwidth optical flow estimation. In [2], we presented the first hierarchical spiking architecture in which motion (direction and speed) selectivity emerges in an unsupervised fashion from the raw stimuli generated with an event-based camera. A novel adaptive spiking neuron model and stable STDP formulation are at the core of this neural network governing its spike-based processing and learning, respectively.

The SNN architecture exhibits the main properties of biological visual motion systems, namely feature extraction and local and global motion perception. Convolutional layers with synapses characterized by single and multiple transmission delays are employed for feature and local motion perception, respectively; while global motion selectivity emerges in a final fully-connected layer. The proposed solution was validated using synthetic and real event sequences, and against the state-of-the-art ANN on optical flow estimation from event-based data: EV-FlowNet [3].

Video

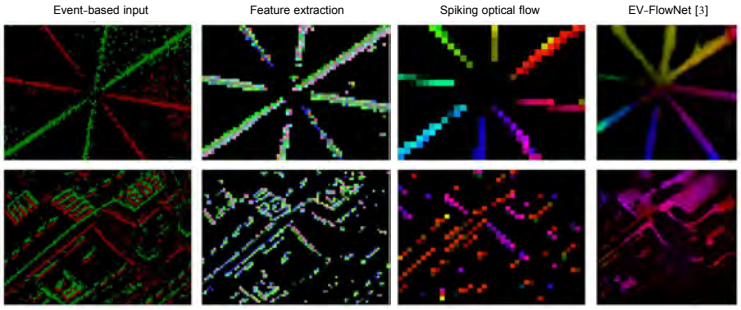

Qualitative results on real event sequences. The optical flow estimation of the EV-FlowNet ANN [3] is shown for validation. For the optical flow columns, motion direction is encoded in color hue, while speed in color brightness.

Research Goal

Neuromorphic computing is the boost artificial intelligence needs to operate efficiently in low-powered devices, such as the onboard computers of Micro Air Vehicles (MAVs). However, to date, little research has been performed towards solving, in a neuromorphic fashion, the main challenges for which conventional ANNs are employed in the field of robotics.

In this research, we focus on the estimation of optical flow using an event-based camera. We are interested in achieving this goal through a SNN that learns to extract this information using biologically plausible protocols, such as the aforementioned STDP. We want to investigate the consequences of such a perception mechanism in the control loop of an MAV.

To date, we have demonstrated that selectivity to the motion the input stimuli can emerge in a hierarchical SNN through STDP (see above). However, despite the compelling results, we are still far from the optimal architecture, and further research is required.

Additional Work: Autonomous Drone Racing

My team from the Micro Aerial Vehicle Lab (MAVLab) of TU Delft has won the first ever Artificial Intelligence Robotic Racing (AIRR) Circuit, with a final breathtaking victory in the World Championship Race held in Austin, Texas, last December. The team takes home the one million dollar grand prize, sponsored by Lockheed Martin and The Drone Racing League, for creating the fastest and most reliable self-piloting drone this season.

The AIRR Circuit consisted of a season with three races, of which we won two, and a World Championship in a winner-takes-all format. We competed against eight other teams from world-renowned universities and companies, all using the same drone. These vehicles had to navigate autonomously through a series of gates as fast as possible, and without using GPS.

Video

The RacerAI.
Picture credit: The Drone Racing League.

Team MAVLab at the World Championship Race.
Picture credit: Lockheed Martin.

References

1. Gallego, G., Delbruck, T., Orchard, G., Bartolozzi, C., Taba, B., Censi, A., ... & Scaramuzza, D. (2019). Event-based vision: A survey. arXiv preprint arXiv:1904.08405.
2. Paredes-Vallés, F., Scheper, K. Y. W., & De Croon, G. C. H. E. (2019). Unsupervised learning of a hierarchical spiking neural network for optical flow estimation: From events to global motion perception. IEEE Transactions on Pattern Analysis and Machine Intelligence (TPAMI).
3. Zhu, A. Z., Yuan, L., Chaney, K., & Daniilidis, K. (2018). EV-FlowNet: Self-supervised optical flow estimation for event-based cameras. *arXiv preprint arXiv:1802.06898*.

Conflict Resolution in High Densities

Marta Ribeiro
Control & Operations
Control & Simulation
Joost Ellerbroek
Jacco Hoekstra
M.J.Ribeiro@tudelft.nl

WHY

Drones provide new operational capabilities for industries and have grown as a consumer leisure product.

Drones must have **Sense & Avoid** in order to be allowed in civil airspace.

Air traffic control operators are not capable of guaranteeing safety at the expected high traffic densities.

GOALS

To create a conflict resolution model capable of guaranteeing safety at **high densities**.

To create a system capable of detecting and avoiding **rogue aircraft**.

METHODOLOGY

Research existent conflict resolution models & analysis of **gaps** and **bottlenecks**.

Development of a new detection and avoidance algorithm for high densities.

Testing in a fast-time, multi-agent simulation environment.

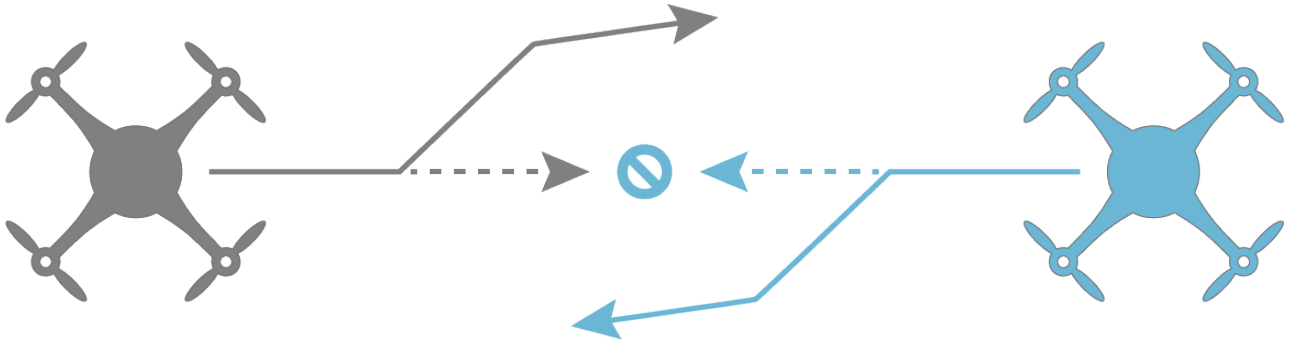

RESULTS

Bluesky [1] ATM simulation tool was used to test the safety and efficiency of the most researched conflict resolutions models.

The **Modified Voltage Potential** model improves the efficiency of the conflict avoidance maneuvers while guaranteeing safety [2].

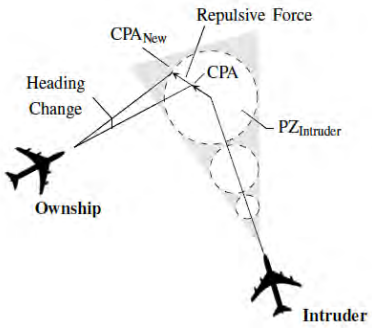

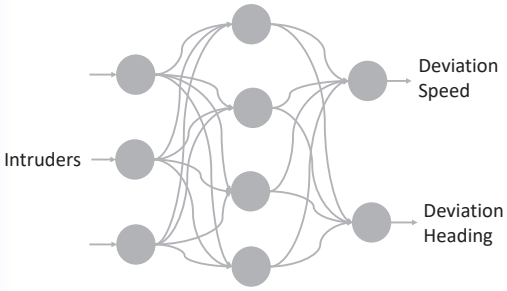

Reinforcement learning can improve the **efficiency** and **safety** of current geometric conflict avoidance models.

FUTURE

Improve resolution environment from 2D to 3D.

Analysis of **emergent behaviour** with conflict resolution in high traffic densities.

Conflict resolution with **rogue aircraft**.

References

[1] J. Hoekstra and J. Ellerbroek, "Bluesky ATC simulator project: an open data and open source approach" in Conference: International Conference for Research on Air transportation, 2016.

[2] M. Ribeiro, J. Ellerbroek and J. Hoekstra, "Analysis of Conflict Resolution Methods for Manned and Unmanned Aviation Using Fast-Time Simulations" in Ninth SESAR Innovations Days, 2019.

Gijs de Rooij
Control & Operations
Control & Simulation
Dr.ir. Clark Borst
Prof.dr.ir. Max Mulder
G.deRooij@tudelft.nl

1 | 2 | 3 | 4 Starting date: November 2019

2

Promoting human-machine teamwork in highly automated air traffic control

The current air traffic management (ATM) system is built around human operators giving commands to pilots. With increasing traffic densities, ATM is expected to shift towards a more automated system, while improving safety and minimising delays. Humans will, however, continue to play an essential role supervising these systems.

Our project therefore focusses on the human aspect. We are developing an interface that allows human operators to interact with the automation, while maintaining their vigilance and skill set. A key aspect is the ability to smoothly transition between supervisory and manual control. Human and automation should become team players, both able to hand- or takeover tasks when detecting the other actor or themselves to underperform.

Research objectives

Develop a human-machine interface that:
- supports a shared mental model
- allows operators to supervise automation and intervene if needed
- can smoothly transition between levels of automation

Develop a human-automation control & communication framework:
- communicate intentions, actions and decision-making criteria between human operator and automation

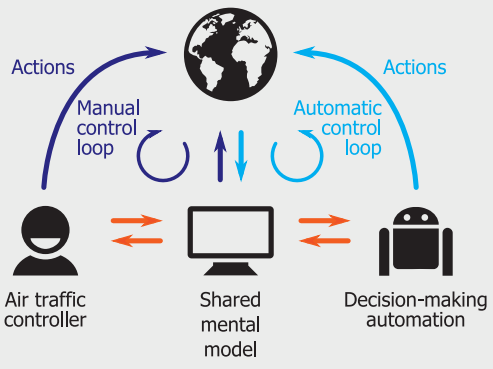

Experiment: task division/sharing

Our first experiment focuses on a partially automated environment that can help maintain manual skills and vigilance of controllers (ATCos). They perform (assisted) manual control on some aircraft, while simultaneously supervising full automation controlling several other aircraft. How can we best divide these responsibilities?

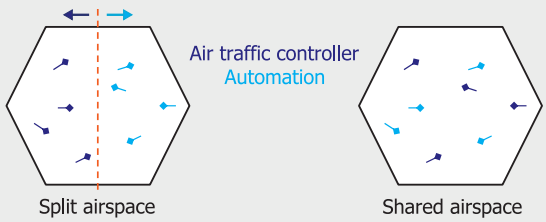

We expect ATCos to prefer the split airspace where they have to cooperate less with the automation. However, situation awareness is expected to be better in the shared airspace.

Further experiments will take a closer look at what (sub) tasks are to be shared between the ATCo and automation, how this division can smoothly transition and what kind of interface can help in creating a shared mental model.

Alleviating Flight Simulator Negative Transference for Helicopter Operations

PhD Candidate: P.F. Scaramuzzino
Department: Control & Operations
Section: Control & Simulation
Supervisors: Dr. Ir. D.M. Pool, Ir. O. Stroosma
Promotors: Dr. M.D. Pavel, Prof. Dr. G. Quaranta
Contact: p.f.scaramuzzino@tudelft.nl
Year 3

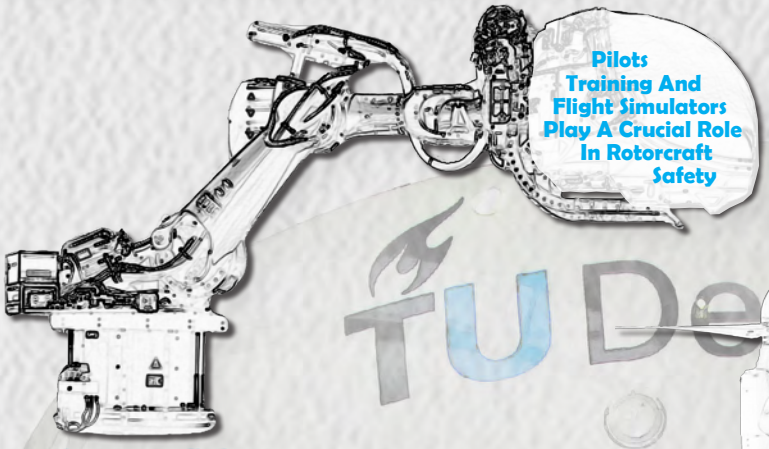

Research Motivation

The dramatically larger accident rate for rotary-wing aircraft compared to fixed-wing aircraft is limiting the increase in use and the public acceptance of rotorcraft. The analysis of accident data [1, 2, 3, 4] recognized training/Instructional interventions to be of prime interest for rotorcraft safety, since most of the accidents in the data set were the result of pilot-related factors. In particular, many efforts need to be dedicated to develop standard training program on autorotation and emergency aircraft handling and to improve simulator training for basic and advanced maneuvers.

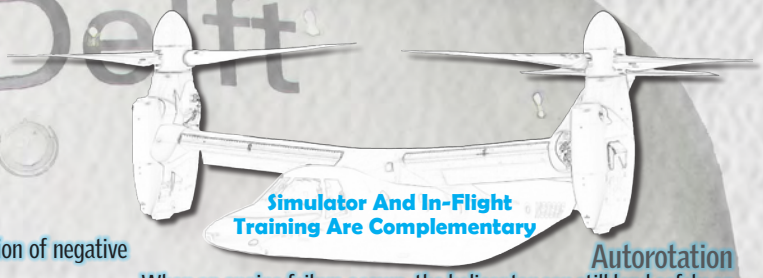

Simulator Vs In-flight Training

- In-flight training of advanced manoeuvres is expensive and risky
- Simulator training may be unrealistic, thus leading to the acquisition of negative skills that may be dangerous during actual flight

Therefore, the combination of simulator and in-flight training is desirable, especially during the training of hazardous scenarios.

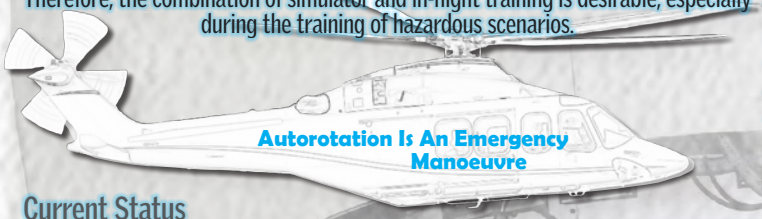

Autorotation

When an engine failure occurs, the helicopter can still land safely on the ground if the pilot quickly recognize the loss of power and respond properly, performing the so-called autorotation. In normal mode of operation, standard helicopter flight dynamics models consider the angular velocity of the rotor as a constant. During autorotation, this approximation is not valid any longer and an additional equation is required, i.e. the rotor torque:

$$\dot{\Omega} = \dot{r} + \frac{1}{I_R}\left(-Q_{mr} - g_{tr}Q_{tr}\right)$$

Current Status

Pilots' control strategy is strictly related to the helicopter dynamics they have to fly. To reproduce pilots' behavior correctly in the simulator, it is essential to understand how the helicopter dynamics stability in autorotation changes with respect to normal powered flight, so that it is possible to estimate how pilots should adapt to keep the helicopter under control in the event of a power failure. The dynamic behavior of the helicopter in the two flight conditions is substantially different, as can be noticed from the root loci comparison:

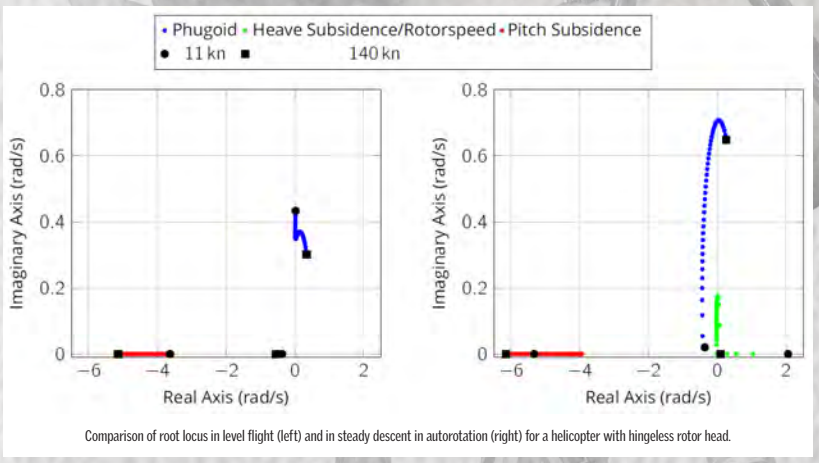

Comparison of root locus in level flight (left) and in steady descent in autorotation (right) for a helicopter with hingeless rotor head.

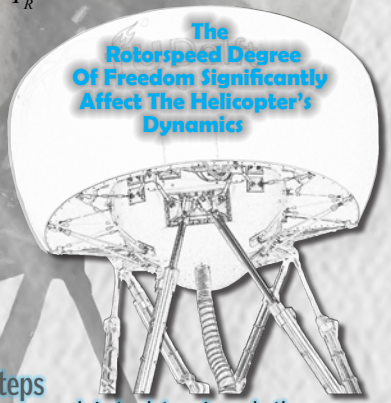

Goal/Next Steps

The goal of this research is to determine whether a certain system dynamics may lead to the development of a more robust control behavior that can be easily adapted to different system dynamics, thus leading to substantial benefits during initial autorotation training. This will be achieved through a series of quasi-Transfer-of-Training experiments.

Acknowledgements

This project has received fundings from the European Union's Horizon 2020 research and innovation programme under the Marie Skłodowska-Curie grant agreement No 721920.

References

[1] U.S. Joint Helicopter Safety Analysis Team. (2011). The Compendium Report: The U.S. JHSAT Baseline of Helicopter Accident Analysis (Vol. I).
[2] U.S. Joint Helicopter Safety Analysis Team. (2011). The Compendium Report: The U.S. JHSAT Baseline of Helicopter Accident Analysis (Vol. II).
[3] European Helicopter Safety Team. (2010). EHEST Analysis of 2000-2005 European Helicopter Accidents.
[4] European Helicopter Safety Team. (2015). EHEST Analysis of 2006-2010 European Helicopter Accidents.

TU Delft · POLITECNICO MILANO 1863 · NITROS ENGINEERING FOR ROTORCRAFT SAFETY

Global Dual Heuristic Programming Applied to Flight GNC Systems

PhD Candidate: Bo Sun
Department: Control & Operation
Section: Control & Simulation
Supervisor: Erik-Jan van Kampen
Promotor: Max Mulder
Contact: b.sun-1@tudelft.nl

Background

Difficulty to obtain the piecewise mathematical models of aerospace systems has been one of the main challenges for guidance, navigation and control (GNC) systems design. The demand can be trickier as the structures of aerospace systems become more diverse, and their working environments become more complex. Besides, current GNC systems have to work under similar, predictable circumstances, and complete designed tasks. They lack the capability of making decisions and cannot deal with the complicated situations by themselves.

One option to overcome these challenges is reinforcement learning (RL), which is a framework of bio-inspired, self-learning methods. RL improves the performance of GNC systems by interacting with environment through actions and receiving each time a reward, without the requirement for precise models.

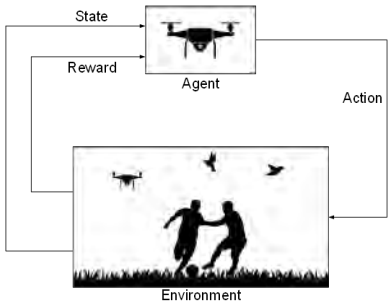

Figure 1. Working principle of RL. The aircraft aims to keep tracking shots of athletes steadily while avoid collisions with birds. It interacts with the environment through actions and collects a reward corresponding to the state transition.

Research goal

This research addresses the following question:

How can aerospace systems benefit from RL, to improve the autonomy and learning in an unknown and non-stationary environment, and meanwhile deal with dynamical uncertainties and partial observability?

Besides, when applied to aerospace systems, conventional RL methods are limited in some challenges, such as low sampling efficiency, the "curse of dimensionality" and not being able to utilize human knowledge. Three specific methods and/or applications are proposed to address the main research question and above challenges:

- Approximate methods ;
- Incremental techniques;
- Hybrid hierarchies.

Global Dual Heuristic Programming

A global dual heuristic programming (GDHP) technique is introduced for controller design using collected rewards. It combines the information of the cost-to-go and its derivatives, and takes advantage of the fast speed of heuristic dynamic programming (HDP) and the high accuracy of dual heuristic programming (DHP). Different from the traditional straight form, explicit analytical calculations are employed to compute the first and second-order derivatives online, so as to eliminate the inconsistent errors due to coupling and to improve the control performance.

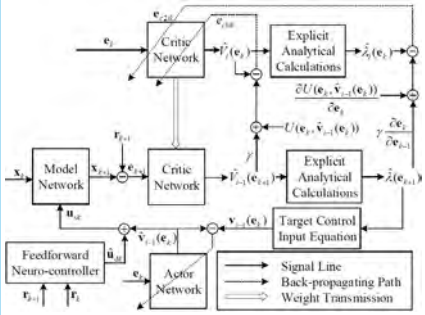

Figure 3. The architecture of the GDHP algorithm with explicit analytical calculations. A feedforward neuro-controller is introduced to approximate the desired control.

Incremental identification

RL methods require future information because they "bootstrap". Conventionally, neural networks (NNs) are used to approximate the global system dynamics. However, offline trained NNs cannot deal with uncertainties and sudden changes, while online trained NNs may cost much time to generate an accurate prediction. This research uses an incremental model to approximate the locally linearized model. A recursive least square (RLS) approach is introduced to identify the coefficients of linear model, avoiding the trouble of matrix inversion in ordinary least square technique.

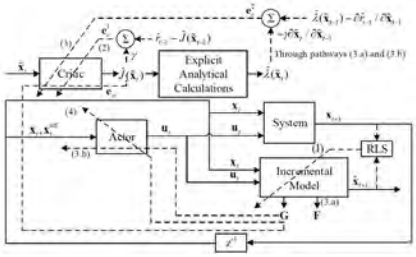

Figure 2. The architecture of the GDHP algorithm with explicit analytical calculations. Solid lines represent the feedforward flow of signals, and dashed lines are backpropagation pathways.

Cascaded actor network

Artificially building hierarchies can speed up RL learning processes because human prior knowledge is utilized. A structured cascaded actor network is used to provide specific relationships between the angular rate and the attitude angle, as shown in Fig. 4. Compared to the end-to-end structure, this cascaded network takes advantages of the physical properties of the aerospace systems and involves intermediate demands so as to provide more information for controller.

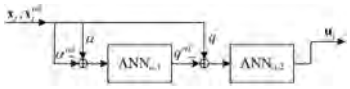

Figure 4. The architecture of the cascaded actor network for inner-loop longitudinal aircraft control. It utilizes practical physical dynamics of aircraft and speeds up the convergence of weights.

Future work

- Current algorithms require full state feedback, which may not be available in some aerospace applications. Therefore, further research should explore system identification techniques for output feedback or partial observability.
- Stability is essential for controller design. Further investigation into stability analysis of RL methods is recommended to improve the performance of controllers.
- Hierarchical structure is applied to a low level control problem. Further research can explore higher level applications, such as navigation and guidance problems of aerospace systems.
- The current research focuses on the method innovation and numerical simulation. Further research can attempt to apply proposed methods to higher degree-of-freedom models and experiments of real systems.

References

[1] B. Sun, and E. van Kampen. Incremental Model-Based Global Dual Heuristic Programming for Flight Control. IFAC-PapersOnLine, Vol. 52, Iss. 29, 7-12, 2019.

[2] B. Sun, and E. van Kampen. Incremental model-based global dual heuristic programming with explicit analytical calculations applied to flight control. Engineering Applications of Artificial Intelligence, Vol. 89, 103425, 2020.

[3] B. Sun and E. van Kampen. Launch Vehicle Discrete-Time Optimal Tracking Control using Global Dual Heuristic Programming. Submitted.

Model-Aided Visual-Inertial State Estimation for Autonomous Drone Racing

PhD Candidate: Yingfu Xu
Department: Control & Operations
Section: Control & Simulation
Daily supervisor: Dr. G.C.H.E.de Croon
Promotor: Prof. dr. ir. M.Mulder
Contact: Y.Xu-6@tudelft.nl

Background

The main goal of the project is to investigate methods that allows micro air vehicles to autonomously navigate at high speed in cluttered environments. The background and testbed of the project is the Autonomous Drone Racing (ADR) competition, in which the racing drone equipped with camera flies at high speed through continuous gates and tries to finish the whole track safely as soon as possible. Efficient visiual state estimation method is the main focus of the research.

Figure 1. (left) Wizards220X Racing drone platform carrying a forward-facing camera JeVois flying in IROS ADR (2019 Macau).

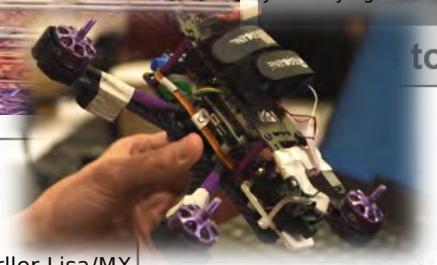

Software & Hardware

a. State estimation, planning and control: Paparazzi UAV [1] can run on microcontrller Lisa/MX (STM32F4). It is an open-source software en-compassing autopilot systems and ground station;

b. Visual detection: The JeVois smart camera is a small-size complete Linux computer. We run "snake gate" [2] algorithm to detect 4 corners of the light gate.

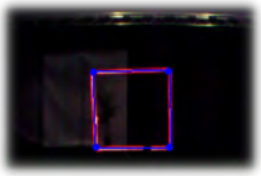

Figure 2. Onboard "snake gate" detection of JeVois smart camera.

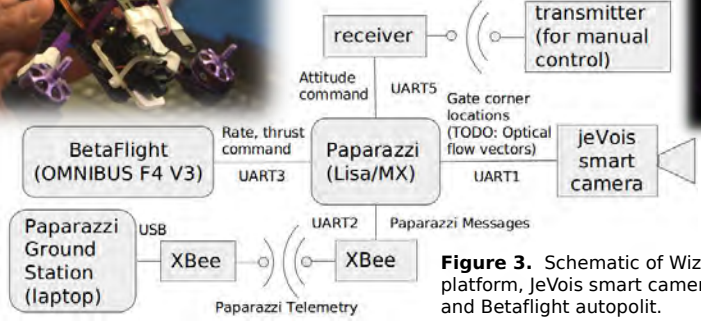

Figure 3. Schematic of Wizards220X Racing drone platform, JeVois smart camera, Paparizzi autopilot and Betaflight autopolit.

FlightGoggles Simulator

MIT FlightGoggles Simulator has high-quality simulated visual output of a challenging drone race track "abandoned factory". We implemented Drone Racing 2018 Solution [2] in 3 nodes of Robot Operation System (ROS).

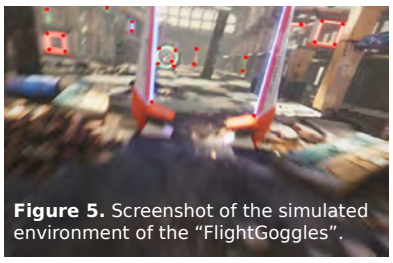

Figure 5. Screenshot of the simulated environment of the "FlightGoggles".

Model-Aided Visual-Inertial State Estimation

a. Visual-inertial odometry (VIO) uses camera(s) and inertial measurement unit (IMU) to estimate the state (position, velocity and attitude) of the robot. Our research aims at VIO for forward-facing monocular camera. Unlike popular VIO solutions that map the environment by estimating 3D locations of feature points, we work on tracking features between frames and calculate the relative motion using linear RANSAC methods, which are less accurate by more efficient. Focus of Expansion(FoE) indicating motion direction can be calculated by optic flow vectors after derotation. We also utilize dynamic model [3] of the quadrotor MAV to make up the drifting caused by visual tracking failure;

b. If flight speed is very high, motion blur is very likely to appear in images and decrease the robustness of feature tracking. We are working on deep-learning-based method to estimate speed infromation from blurry images.

Figure 4. (right) FoE calculated by translational optical flows in forward motion.

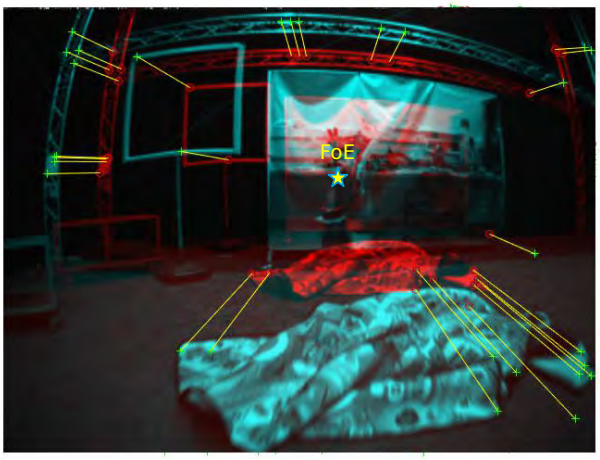

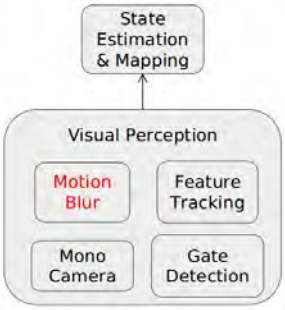

Figure 6. Main challenges for visual perception in high-speed flight.

References

[1] Paparazzi UAV. https://wiki.paparazziuav.org/wiki/Main_Page
[2] Li, Shuo, et al. "Visual model-predictive localization for computationally efficient autonomous racing of a 72-gram drone." arXiv preprint arXiv:1905.10110 (2019).
[3] Abeywardena, Dinuka, et al. "Fast, on-board, model-aided visual-inertial odometry system for quadrotor micro aerial vehicles." 2016 IEEE International Conference on Robotics and Automation (ICRA). IEEE, 2016.

Revealing Adverse Rotorcraft Pilot Couplings Induced by Flight Control System

PhD Candidate: Yu Ying
Department: C&O
Section: C&S
Supervisor: M. D. Pavel &
Erik-Jan van Kampen
Promoter: Max Mulder
Email: Y.Yu-2@tudelft.nl

Project Description

Rotorcraft-Pilot Couplings (RPCs) are annoying vehicle oscillations that arise from the pilot's effort of controlling rotorcraft. It is an adverse interaction between pilot and vehicle, which was known in the past under the name pilot induced/pilot assisted oscillations PIO/PAO. Helicopter RPCs are a subject of concern for helicopter's safety. The current practice of revealing adverse rotorcraft pilot couplings (RPC) shows significant gaps in predicting RPC and determining the reason for the occurrence of RPC. There are lots of work related to Cat. I PIO (linear) and Cat. II PIO (quasi-linear), but few researches focus on Cat.III PIO which is associated with nonlinearity, let alone Cat. III RPC. Furthermore, although the use of flight control system (FCS) is increasing the role of the vehicle FCS in triggering PIO remains unclear currently.

Thus, the aim of the project is to minimize Cat. III RPC to improve helicopter safety by: (1) understanding the mechanisms through which cat. III RPC can be triggered, especially, understanding the effects of control systems and their role in triggering Cat. III RPC; (2) proposing generalized available prediction criteria for Cat. III RPC; (3) giving guidelines to alleviate the existing Cat. III RPCs.

Potential trigger events of Cat. III PIO

There are no definition of Cat. III PIO, but Dr. McRuer described it as nonlinear pilot-vehicle oscillations due to Nonlinear vehicle-centered transitions or pilot-centered transitions. Transitions that may trigger Cat. III PIO is shown in Fig. 1.

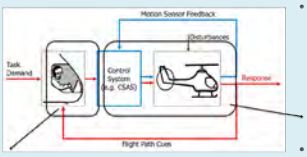

Source: Padfield, 1996

- Cues;
- Behavioral mode;
- Pilot equalization dynamics.
- Variation of vehicle dynamics;
  - ➢ Control mode transition;
  - ➢ Unpredictable failures.
- Nonlinearities
  - ➢ Actuator dynamics
  - ➢ Sensor dynamics
  - ➢ Inherit time delay
  - ➢ Control authority

Fig 1. Potential triggers of Cat. III PIO

Outline of the Research

The outline of this research is listed in Fig 2.

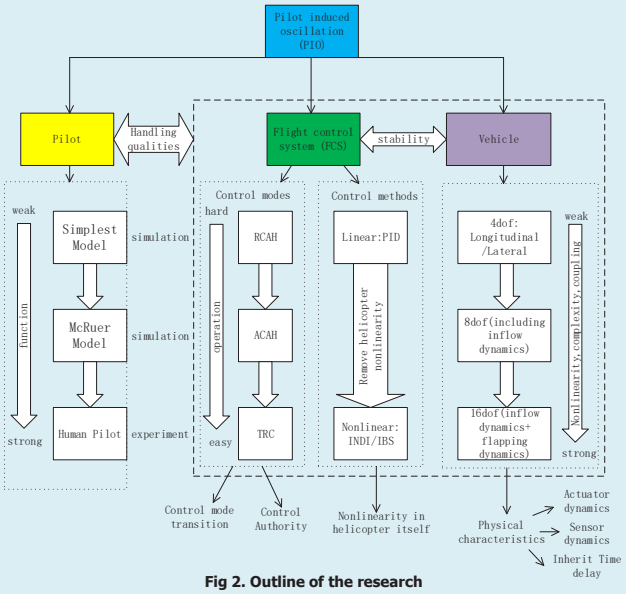

Fig 2. Outline of the research

RCAH: Rate Command Attitude Hold

ACAH: Attitude Command Attitude Hold

TRC: Translational Rate Command

PID: Proportional Integrative Derivative

INDI: Incremental Nonlinear Dynamic Inversion

IBS: Incremental Backstepping

Simplest Model: $K_p e^{-ts}$

McRuer Model: $K_p \frac{1+T_L s}{1+T_I s} \rightarrow \frac{\omega_n^2}{s^2+2\xi\omega_n s+\omega_n^2} e^{-\tau_p s}$

equalization — Physical limitations

Structure of Pilot Vehicle System

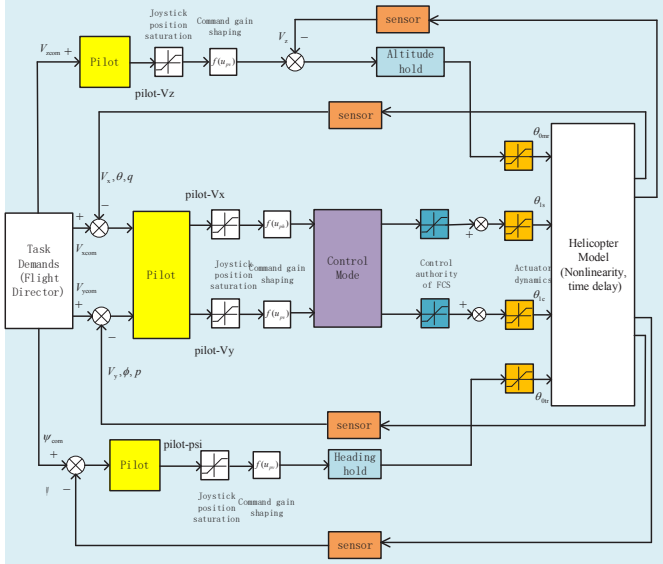

Fig 3. Structure of pilot vehicle system

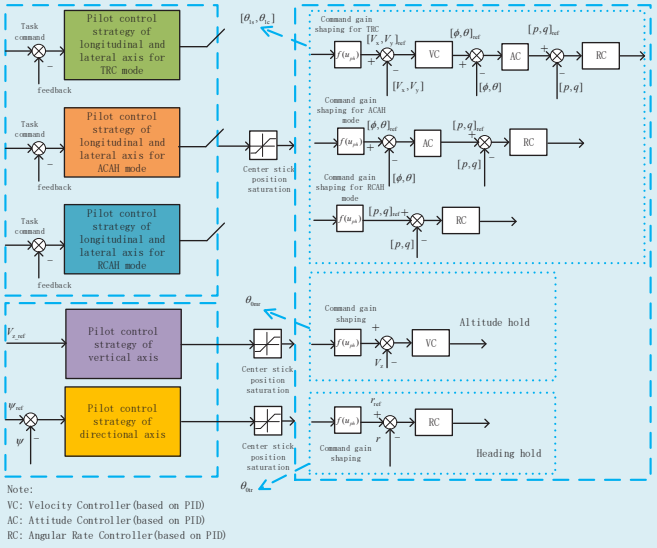

Fig 4. Pilot control strategy modes and FCS modes

Advancements for A* and RRT in 3D path planning of UAVs

Ing. Christian Zammit
Aerospace Engineering
Control & Simulation
Dr. ir. Erik-Jan van Kampen
Prof. dr. ir. Max Mulder
c.zammit@tudelft.nl

Introduction:

Unmanned Aerial Vehicles (UAVs) are slowly being integrated into all spheres of life. They are being proposed for a wide range of indoor and outdoor applications varying from surveillance, search and rescue to leisure flying. The inclusion of UAVs into the national airspace and military applications requires robust autonomous guidance, navigation control (GNC) systems that shall ensure safe navigation in view of uncertainties present within UAV systems and the environment in which they will operate. Advancements in Unmanned Aerial Vehicles (UAVs) design, actuator and sensory systems and control are making such devices financially available to a wide spectrum of users with various demands and expectations. To mitigate with this ever increasing demand robust, efficient and application-specific path planning is paramount.

Research Aim:

Investigate how interval methods can be applied to the problem of path planning for UAVs under uncertainties.

Research Questions:

1. What is the state-of-the-art in the field of path planning for UAVs?
2. Can these algorithms be utilised in real-time?
3. What is the effect, if any, on path planning performance if static obstacles are replaced with dynamic obstacles
4. In what ways do uncertainties affect path planning?
5. How can uncertainties modelled using interval methods effect path planning performance?

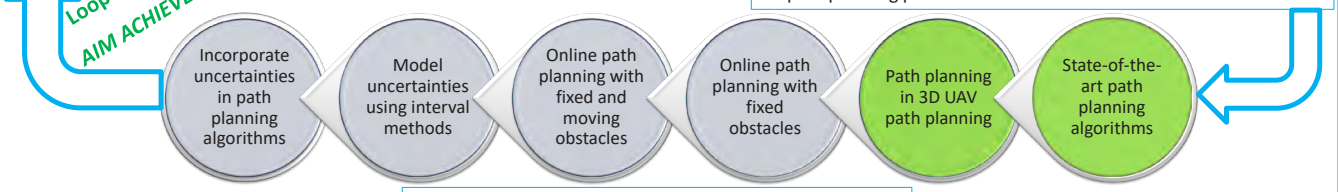

State-of-the-art Path Planning Algorithms:

1. *Graph-Based Algorithms → A* and its variants*
2. *Sampling-Based Algorithms → RRT and its variants*

A* Ripple Reduction Algorithm

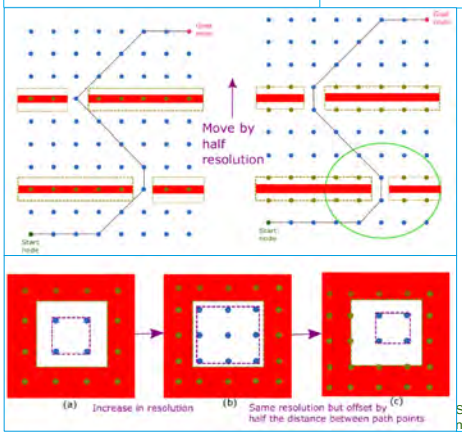

Smoothing Algorithm

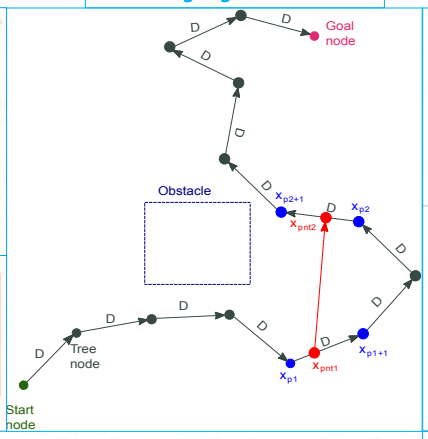

3x 3D Obstacle Scenarios

Cube 1x1x1; Start: 0,-0.5,0; Goal: 0,0.5,0

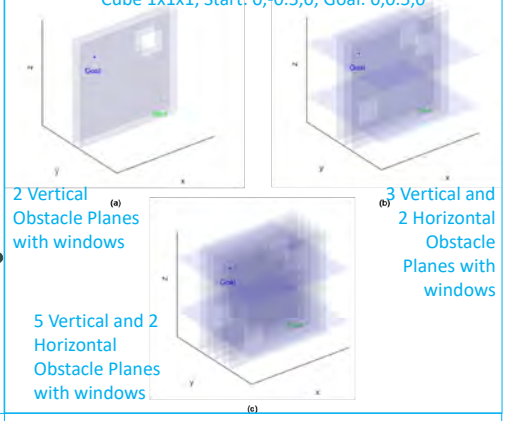

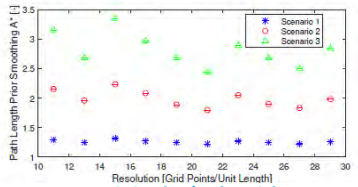

Original A* Algorithm

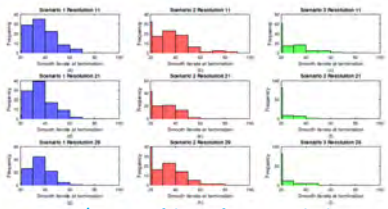

A* Smoothing Characteristics

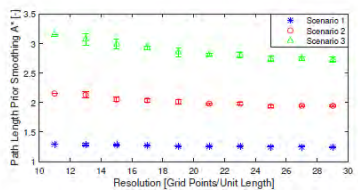

A* Ripple Reduction Algorithm

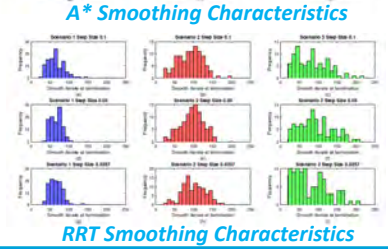

RRT Smoothing Characteristics

Salient Results:

A* Ripple Reduction Algorithm:

1. A* algorithm exhibited a ripple for different resolutions for the same scenario.
2. Path length ripple reduction by more than 46% in terms of standard deviation with respect to the original A*.
3. The path length and computational time will not be negatively compromised.

New Smoothing Algorithm:

1. The new smoothing algorithm measures the rate of improvement over the last predetermined number of iterates and stops if the improvement is low.
2. Results confirm an improvement of more than 10 multiples less computational time for all considered algorithms with less than 10% reduction for A* and between 25% and 45% for RRT and its variants..

Development of Climate Functions for Sustainable Aircraft Design

Kathrin Deck
Control & Operations
Aircraft Noise & Climate Effects
Daily supervisor: Feijia Yin
Promotor: Volker Grewe
K.T.Deck@tudelft.nl

Motivation

- Aviation contributes to climate change
  - CO_2 effects / emissions
  - Non-CO_2 effects (e.g. emissions of NO_x, formation of contrails)
- Further increase of air traffic is predicted
  (see [1])

➡ Reduce climate effect of aircraft / aviation
➡ Development of a climate impact assessment tool at the aircraft design level
➡ Focus on climate functions

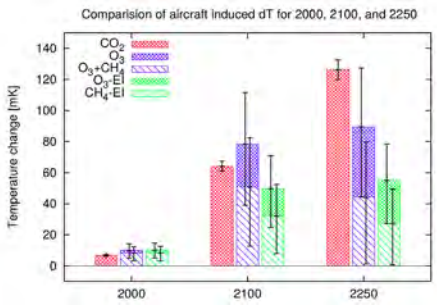

Contribution of Subsonic Aircraft Emissions to Climate Change *(Source: [4])*

Global-Warming-Optimized Aircraft Design (GLOWOPT)

- State of the Art:
  - Climate impact of aviation
  - Climate metrics
  - Climate optimized operation
  - Climate optimized design
- Representative Route Network and Fleet:
  - Air traffic forecast model
  - Prediction of future air traffic
- Climate Functions
- Aircraft Design Optimization:
  - Reference aircraft
  - Design parameters for optimization
- Assessment:
  - Climate impact of reference aircraft and optimized aircraft
  - Additional parameters like noise or air quality

(see [2])

Climate Functions

- Adequate climate metric
- Strategy for climate functions
- Calculation of the Climate Functions for Aircraft Design (CFAD)
  (see [2])

AirClim

- Linear response model
- Uses precalculated atmospheric data together with aircraft emission data

➡ Calculation of atmospheric concentration changes, radiative forcing changes and temperature changes
(see [4])

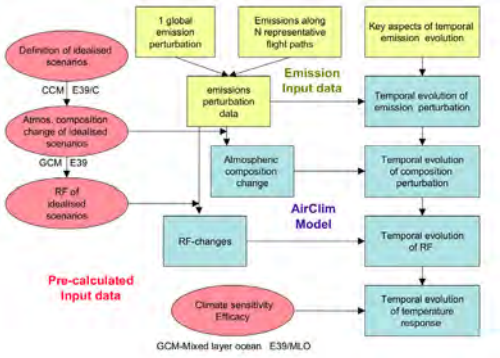

Overview of AirClim *(Source: [4])*

Overview of Common Climate Metrics

- Radiative Forcing:
  Changes in radiation resulting from concentration changes
- Global Warming Potential:
  Integrated radiative forcing over a time horizon
- Global Temperature Potential:
  Temperature change at a certain point in time
- Average Temperature Response:
  Integrated temperature change over a time horizon
  (see [3])

References
[1] Grewe, V. and Linke, F., 2017. Eco-efficiency in aviation. Meteorologische Zeitschrift, 26(6), 689-696, doi: 10.1127/metz/2017/0762.
[2] Project GLOWOPT: www.glowopt.eu (retrieved on 2020-01-30)
[3] Grewe, V. and Dahlmann, K., 2015. How ambiguous are climate metrics? And are we prepared to assess and compare the climate impact of new air traffic technologies? Atmospheric Environment, 106, 373-374, doi: 10.1016/j.atmosenv.2015.02.039.
[4] Grewe, V. and Stenke, A., 2008. AirClim: an efficient tool for climate evaluation of aircraft technology. Atmos. Chem. Phys., 8(16), 4621-4639.

Acknowledgements
This research is part of the project GLOWOPT and has received funding from Clean Sky 2 Joint Undertaking under the European Union's Horizon 2020 research and innovation programme under grant agreement No. 865300.

Design of Cavities for Low Noise Acoustic Arrays in Closed Test Section Wind Tunnels

Colin van Dercreek
Controls & Operations
Aircraft Noise and Climate Effects
Dr. Ir. Mirjam Snellen,
Dr.ir. Daniele Ragni &
Prof.Dr. Dick Simons
c.p.vandercreek-1@tudelft.nl

Introduction

Goal: Enable the testing of quieter airfoil and vehicle designs by increasing the signal to noise ratio of acoustic array measurements.

Application: Beamforming measurements in closed test section wind tunnels.

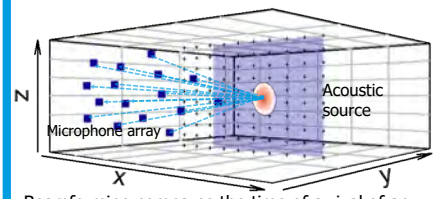

Beamforming compares the time of arrival of an acoustic wave at each microphone to quantify and locate acoustic sources.

Problem: Turbulent boundary layer pressure fluctuations cause low signal to noise ratios for wind tunnel wall mounted microphones.

Problem:

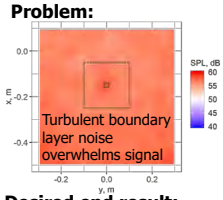

Desired end result:

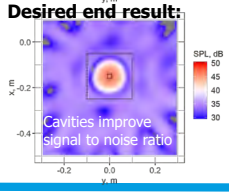

Approach: Cavities reduce the boundary layer pressure fluctuations measured by microphone arrays compared to flush mounted microphones.

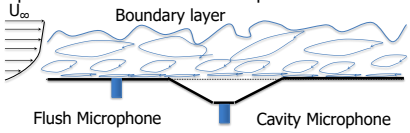

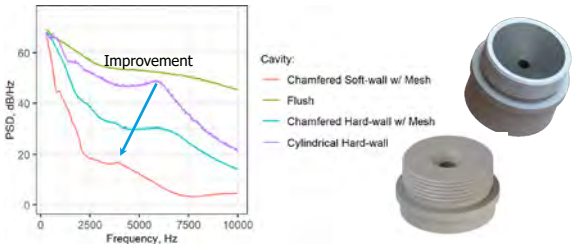

Modelling Approach

Boundary layer pressures are modelled as a sum of modes

Solve wave equation: $\frac{\partial^2 p}{\partial t^2} - c_0^2 \nabla^2 p = 0$

$$P(z,r,\theta) = \sum_{m=-\infty}^{\infty} \sum_{\mu=1}^{\infty} \left(A_{m\mu} e^{ik_{m\mu} z} + B_{m\mu} e^{-ik_{m\mu} z} \right) J_{m\mu}(r) e^{-im\theta}$$

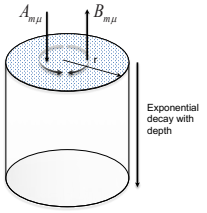

Cut-off frequencies due to geometry reduce propagating energy exponentially:

$$k_{m\mu} = \sqrt{\omega^2 - \alpha_{m\mu}}$$

Boundary layer is decomposed to a modal approximation:

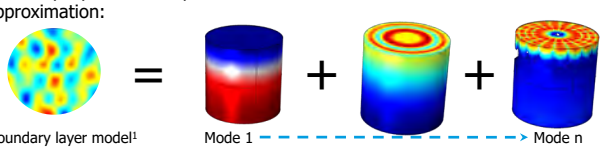

Boundary layer model[1] | Mode 1 | Mode n

Resulting model matches trends established experimentally:

- Soft walls increase SNR
- Chamfered sides increase SNR
- Stainless steel mesh increases SNR

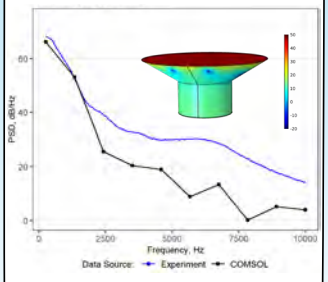

1. Maxit, L., "Simulation of the pressure field beneath a turbulent boundary layer using realizations of uncorrelated wall plane waves", *The Journal of the Acoustical Society of America* 140, 1268, 2016

Next steps:

- Combine Navier-Stokes model with acoustic model
- Optimize cavity designs to attenuate boundary layer noise

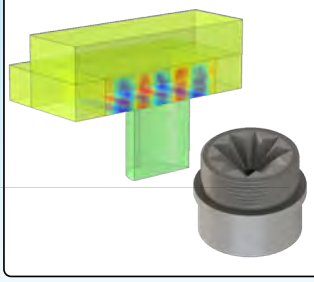

Experimental Approach

Measure the effect of cavity geometry on beamforming results

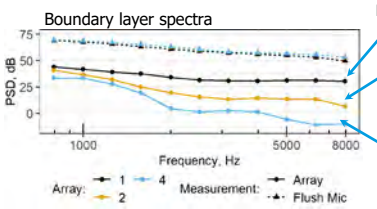

Cavity geometry significantly attenuates the boundary layer fluctuations at the microphone.

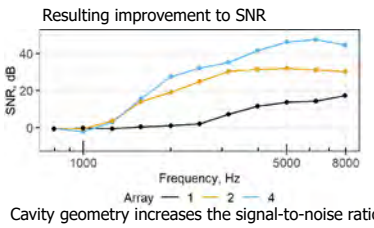

Cavity geometry increases the signal-to-noise ratio

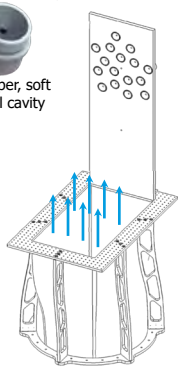

Experimental set-up enables comparison of different cavity geometries

Experiment showed that depth, mesh, area, and chamfer have significant effect on reducing boundary layer spectral energy.

Next steps:

- Measure flow within a cavity to evaluate transmitted modes due to the boundary layer.
- Test cavity geometries that result from model optimization
- Demonstrate improvement on array measurements compared to existing state of the art.

Project Outcome: Theoretical framework to design microphone cavities that increases the signal-to-noise ratio of acoustic measurements in wind tunnels.

Comparing Modeled and Measured Bathymetric Uncertainties:
Doppler Effect, Baseline Decorrelation and Additive Noise

Tannaz Haji Mohammadloo
Control and Operations
Aircraft Noise and Climate Effects
Dr. Ir. Mirjam Snellen
Prof. Dr. Dick G. Simons
T.Hajimohammadloo@tudelft.nl

Introduction

- Nowadays, multibeam echosounders (MBESs) provide high spatial coverage at relatively limited costs.

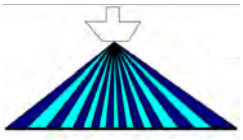

- However, the derived depths are affected by the uncertainties inherent to the MBES depending on a number of parameters, such as beam angle and sensors.

Current uncertainty prediction model

Depth uncertainty model developed by Hare in 1995 accounting for the contribution of

1) Echosounder
2) Angular motion sensor
3) Motion sensor and transducer alignment
4) Sound speed
5) Heave

The model Assumes independent contributors.

However, since the development of the depth uncertainty prediction model, improvements have been realized.

Objective

Accounting for the most recent insights in contributors to MBES depth uncertainties

1) Doppler Effect

Due to constant movement of the MBES

2) Baseline Decorrelation

Encountered in the MBES interferometry step and is due to the characteristics of the directivity pattern and a slightly different angular direction of the received signal on two sub-arrays.

3) Additive Noise

Signal-to-Noise ratio (SNR) decreases for outer beams increasing the depth uncertainty

Description of the Dataset

Oosterschelde estuary (Eastern Scheldt), the Netherlands

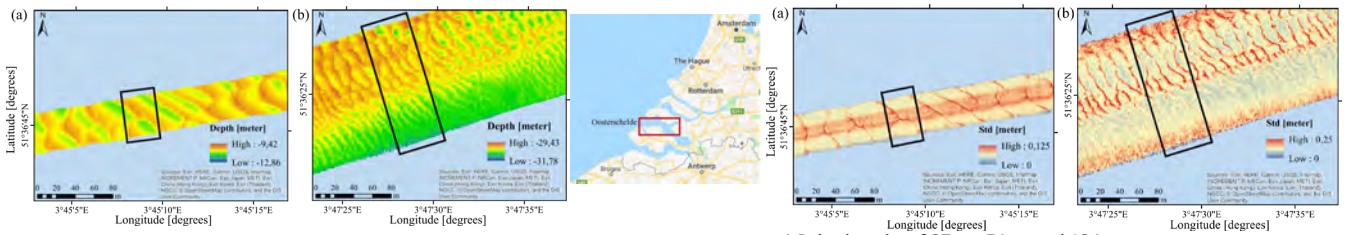

- ✓ Two surveys in 2018 in water depths of 10 m a) and 30 m b)
- ✓ Kongsberg EM2040c with a CW pulse shape and a center frequency of 300 kHz
- ✓ Pulse lengths of 27 μs, 54 μs and 134 μs
- ✓ Large standard deviation for a range of beams around nadir

Results

10 m water depth

Model of Hare [1995] | **Modified version of Hare [1995]**

30 m water depth

Model of Hare [1995] | **Modified version of Hare [1995]**

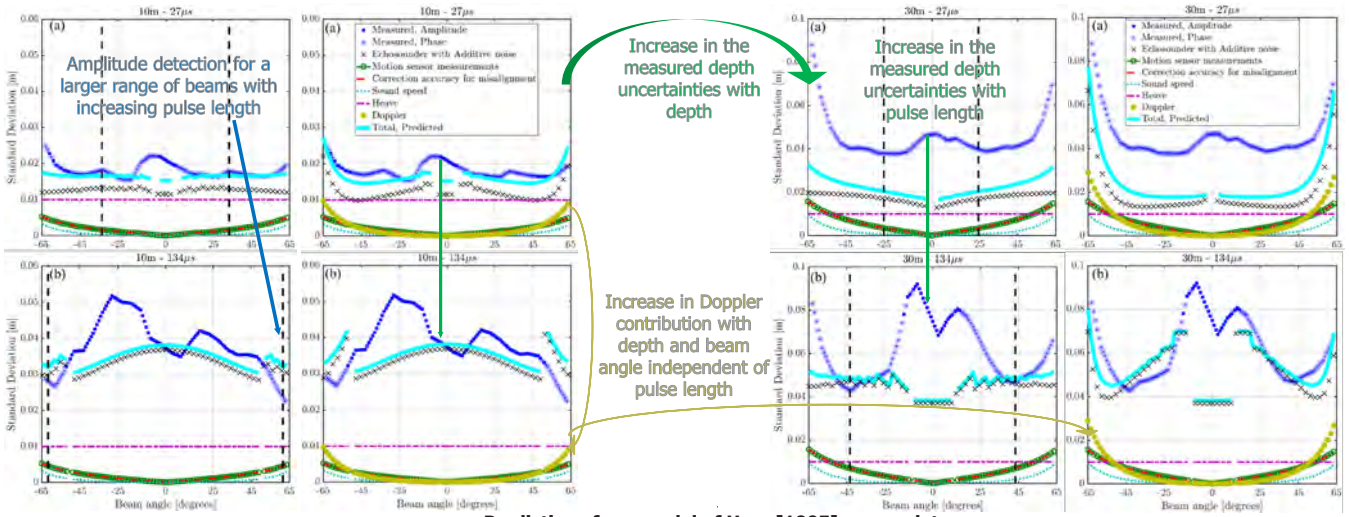

Predictions from model of Hare [1995] versus data

10 m

- ✚ Good agreement for (a) in the mid beam sector
- ➖ Underestimation occurs for (b)
- ➖ Underestimation increases for outer beams

30 m

- ➖ Consistent underestimation
- ➖ Discrepancy increases the outer beams

Predictions from modified version of Hare [1995] model versus data

- ✚ Improvement in model-data agreement for 10 m water depth for short pulse length
- ✚ Improvement in capturing the uncertainty increase with the beam angle for 30 m water depth
- ➖ Still, the increasing uncertainty with water depth is underestimated.

Conclusion

- ❖ Comparable levels of uncertainty based on the measurements and predictions
- ❖ Accounting for baseline decorrelation improves capturing the characteristics of uncertainty
- ❖ Accounting for SNR significantly improves the model-data agreement for outer beams.
- ❖ Failure in capturing the depth dependent uncertainty increase → requires further research
- ❖ Larger discrepancies in case of using amplitude detection → requires further research

TU Delft

Rijkswaterstaat
Ministry of Infrastructure and Water Management

Modeling pressure distribution on (partially) permeable airfoils:

the mimetic spectral element method (MSEM)*,**

Salil Luesutthiviboon
Department: Control & Operations
Section: Aircraft Noise & Climate Effects
Daily supervisors: Dr.ir. Mirjam Snellen, Dr. Daniele Ragni
Promotor: Prof.dr. Dick Simons
Contact: S.Luesutthiviboon@tudelft.nl

Background

- Recent research works have shown that airfoils with **permeable** trailing edge help to **attenuate** up to 10 dB of **turbulent boundary layer trailing-edge (TBL-TE) noise**.
- It is aimed to apply such airfoils on **wind turbine blades** in the near future to mitigate noise annoyance and therefore promote usage of clean energy.
- Despite the noise attenuation capability, permeable airfoils usually alter surface pressure distribution compared to solid airfoils, **reducing lift** force produced by the airfoil and potential power output of a wind turbine.
- Currently, there is no quick tool to **model the pressure distribution on permeable airfoils** that could **facilitate design** of permeable topology optimized for noise and lift.

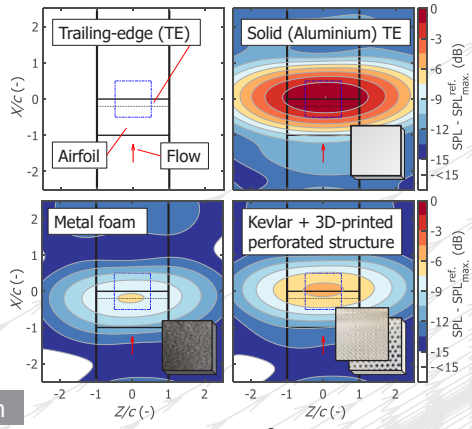

Visualization of TBL-TE noise attenuation by permeable TE inserts obtained from beamforming in terms of sound pressure level (SPL) relative to the maximum SPL of a reference (Solid) airfoil at a sound frequency of 1.25 kHz, chord based Reynolds number of 3.51×10^5

The MSEM

- The MSEM is a **variant of the FEM**
- It is capable of a giving a **machine-precision** solution in a relatively **short time**

Governing equations

The tool solves the **hybrid Darcy equation** which describe flow in a permeable domain Ω

$$\mathbf{u} + \mathbb{K}\nabla p = 0$$
$$\nabla \cdot \mathbf{u} = f$$

$\mathbf{u}$: Flow velocity
$\mathbb{K}$: Permeability tensor
p : Pressure
f : Source term
$\langle u \rangle_n$: Velocity, boundary
$\langle p \rangle$: Pressure, boundary

Boundary conditions (BCs)

$\mathbf{u}\cdot\mathbf{n} = \langle u \rangle_n$ along Γ_u
$p = \langle p \rangle$ along Γ_p

$\Gamma = \partial\Omega = \Gamma_u \cup \Gamma_p$

Computational domain

The domain is subdivided into 10 regions with prescribed BCs (not to scale)

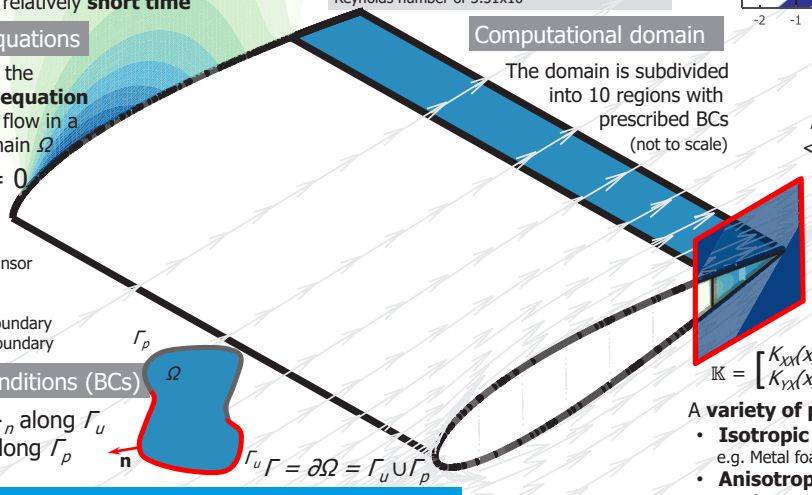

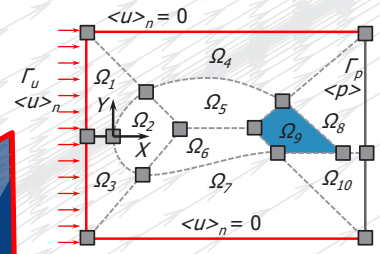

The permeability tensor $\mathbb{K}$

$$\mathbb{K} = \begin{bmatrix} K_{XX}(x,y) & K_{XY}(x,y) \\ K_{YX}(x,y) & K_{YY}(x,y) \end{bmatrix}$$

Given $K_{XY} = K_{YX} = 0$
Fully permeable: $K_{XX} = K_{YY} = 1$
Impermeable: $K_{XX} = K_{YY} \rightarrow -\infty$

A **variety of permeable** materials can be **modeled:**

- **Isotropic** permeability: $K_{XX} = K_{YY}$
  e.g. Metal foams
- **Anisotropic** permeability: $K_{XX} \neq K_{YY}$
  e.g. Customized 3D-printed structures

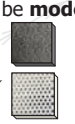

Permeable airfoil with varying permeability

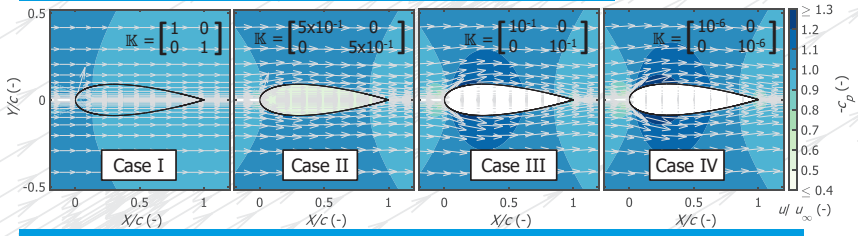

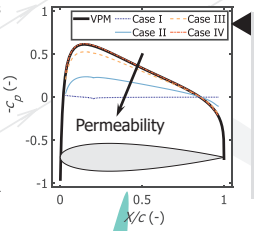

- The flow velocity within a permeable airfoil decreases as the permeability decreases.
- The reconstructed pressure coefficients c_p converge to the solution of the Vortex Panel Method (VPM) for a low permeability.

Airfoil with permeable trailing edge: Effects of anisotropy

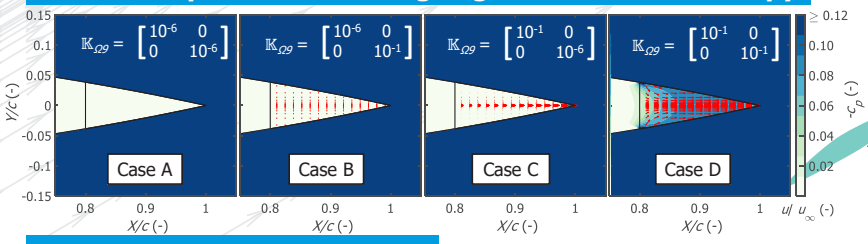

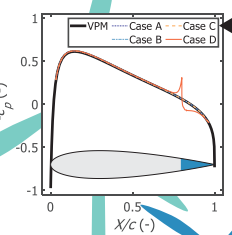

- The reconstructed pressure coefficients c_p on an airfoil with anisotropically-permeable trailing edge extent are more similar to that of a solid airfoil compared to an airfoil with isotropically-permeable trailing edge extent.

Conclusions and further steps

The current investigation at zero-degree angle of attack has shown that:

- The pressure coefficients on a permeable airfoil **converge** to the solution obtained from the VPM for a **low permeability**.
- **Anisotropic permeability** might be beneficial for maintaining the pressure distribution on the airfoil and **keeping reduction of lift minimal**.

Further steps are:

- Simulation at **nonzero** angles of attack and **cambered** airfoil and quantification of the **lift coefficient**
- **Comparison** with **experimental data**

* This research work is a part of the Innovative Permeable Materials for Airfoil Noise Reduction (IPER-MAN) project funded by STW (No. 15452)
** This part of the IPER-MAN project is carried out as a collaboration with Varun Jain and Dr. Marc Gerritsma from the Aerodynamics group at TU Delft

Air Quality Impacts of Civil Aviation Emissions

Flávio D. A. Quadros
Control and Operations
Aircraft Noise and Climate Effects
Dr. Irene Dedoussi
Dr. Mirjam Snellen
F.Quadros@tudelft.nl

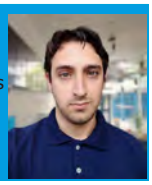

Introduction

Emissions

Combustion from aircraft engines and auxiliary power units release various pollutants into the atmosphere

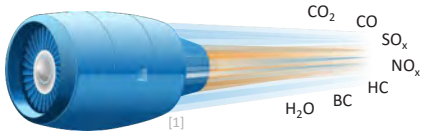

Global air-traffic is expected to grow significantly in the next few decades

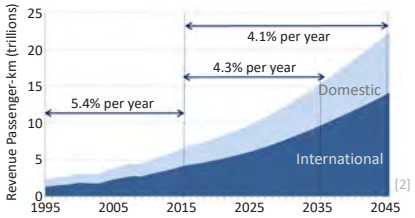

Climate impacts

Air Quality

Increased surface concentration:
+ Particulate matter ($PM_{2.5}$)
+ Ozone (O_3)

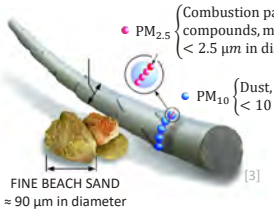

In the atmosphere, pollutants go through chemical reactions, photolysis, phase changes, transport, and deposition → The resulting changes have negative impacts on air quality

Human Health Effects

Increased mortality:
+ Cardiovascular diseases ($PM_{2.5}$)
+ Respiratory diseases (O_3)

Premature deaths per year due to population exposure to aviation-attributable PM2.5 and O_3 (90% confident intervals)[4]

North America	1500 (850-2300)
Europe	3700 (2100-5500)
Asia	8200 (3700-13 000)
Other regions	2700 (1400-4200)
World	16 000 (8300-24 000)

The worsening air quality is associated with increased disease mortality, with aviation resulting in an estimated 16 000 premature deaths globally in 2006

Methodology

Aircraft fuel burned in 2005

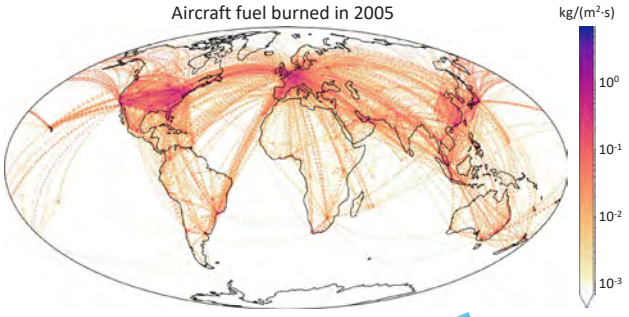

Emissions Inventory

The 4-D emission fluxes of the main species are estimated from the bottom-up using a number of resources:
- A global list of aircraft movements
- Engine emission certification data
- An aircraft performance model

Atmospheric Modeling

The air quality impacts of the aircraft emissions is estimated using the GEOS-Chem atmospheric chemical transport model

Pairs of simulations with and without aviation emissions are compared to provide aviation-attributable impact estimates

Simulations from a global model with a horizontal resolution of 4°x5° is coupled to higher resolutions 0.5°x0.625° simulation runs for North American, European and Asian domains

Surface $PM_{2.5}$ increase with a 10% increase in European aviation emissions

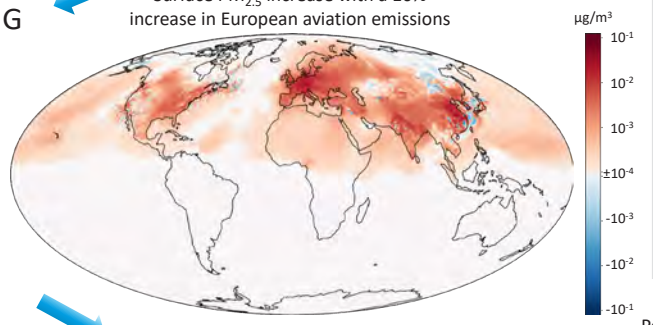

Impact Assessment

Exposure to $PM_{2.5}$ and O_3 attributable to aviation is calculated using population density data

Premature deaths are calculated from increased exposure to pollutants by concentration-response-functions derived from cohort studies in the epidemiological literature

Population density

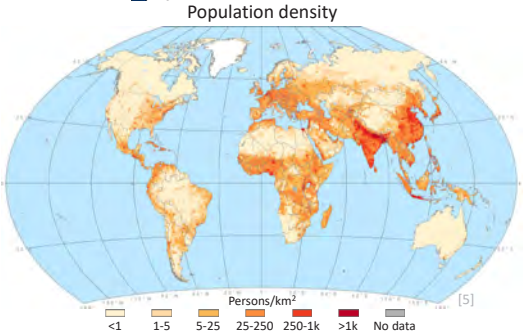

Goals

- ★ Compile a new aviation emissions inventory incorporating more recent data, newer emission index estimates, and an open-source aircraft performance model
- ★ Evaluate the evolution of air quality impacts from aviation over time due to increasing air traffic up to the present and into the future
- ★ Investigate the differences in air quality sensitivity to aviation emissions across different regions of the world
- ★ Run the GEOS-Chem model at high resolution in Europe with the updated emissions inventory to obtain a more precise estimate of the current air quality impacts of aviation in this region

References

[1] European Aviation Environmental Report 2019, EASA, EEA, EUROCONTROL
[2] ICAO Long-Term Traffic Forecasts – Passenger and Cargo, International Civil Aviation Organization, April 2018
[3] Particulate Matter (PM) Pollution, https://www.epa.gov/pm-pollution/particulate-matter-pm-basics, accessed 28/01/2020, US EPA
[4] Steve H L Yim et al 2015 Environ. Res. Lett. 10 034001
[5] Center for International Earth Science Information Network - CIESIN - Columbia University. 2018. Gridded Population of the World, Version 4 (GPWv4)

Noise Mitigation with Permeable Trailing Edges

PhD Candidate: Alejandro Rubio Carpio
Department: Control & Operations
Section: ANCE
Supervisors: F. Avallone & D. Ragni
Promotor: D. Casalino & M. Snellen
Contact: a.rubiocarpio@tudelft.nl

1 | 2 | 3 | 4

Motivation

- Broadband trailing edge noise represents the main source of noise in modern wind turbines.
- It is estimated that 1 dB noise reduction can increase energy production by 4 %.

[P. Sijtsma , 12th CEAS Workshop, 2008, Bilbao]

Metal Foams

- Porous microstructure (open-cell pore)
- Random pore arrangement

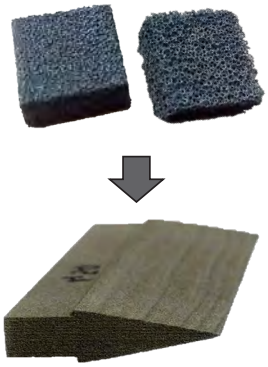

Perforated

- Straight channels linking suction and pressure side
- Fully parametrized pore arrangement

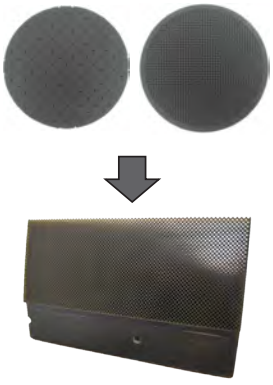

Diamond

- Based on the atomic arrangement in the diamond cubic crystal structure
- Pore-like micro-structure
- Fully parametrized pore arrangement

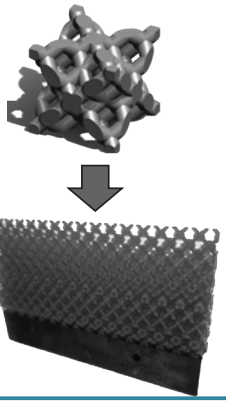

Model

- NACA 0018 airfoil
- Exchangeable trailing edges (last 20% of the chord)
- Chord: 20 cm
- Span: 40 cm
- Chord-based Reynolds number up to $4.6 \cdot 10^5$

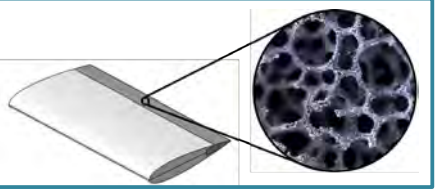

Noise Mitigation Mechanism

Flow Field

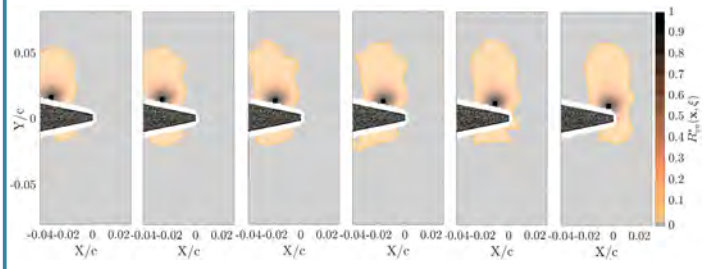

Noise Source Maps

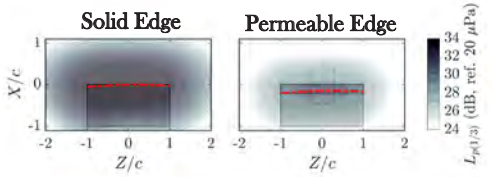

Flow at both sides of the trailing edge communicate within the permeable medium. Such phenomena allows for:

1. Decrease of the acoustic impedance jump at the trailing edge.
2. Streamwise distribution of noise sources.

Application

Noise Attenuation

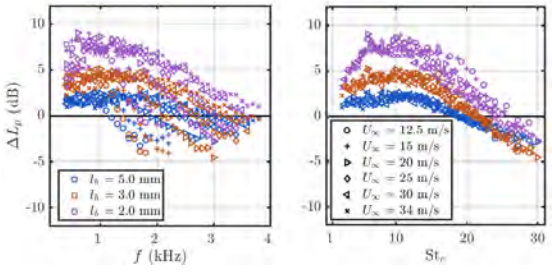

The frequency for noise mitigation is linearly dependent on flow speed.

Tonal Noise

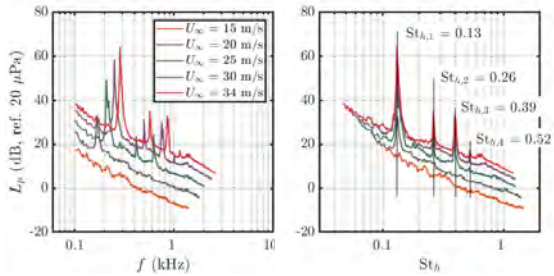

Highly permeable edges with ordered pore arrangement generate tones

References:

- A. Rubio Carpio, R. Merino Martinez, F. Avallone, D. Ragni, M. Snellen & S. van der Zwaag – Experimental characterization of the turbulent boundary layer over a porous trailing edge for noise abatement, Journal of Sound and Vibration 443 (537-558), 2018.
- A. Rubio Carpio, F. Avallone, D. Ragni, M. Snellen & S. van der Zwaag –Mechanisms of Noise Generation on Metal Foam Trailing-Edges, Physics of Fluids 31, 105110 (2019)
- A. Rubio Carpio, F. Avallone, D. Ragni, M. Snellen & S. van der Zwaag – Quantitative Criteria to Design Optimal Permeable Trailing Edges for Noise Abatement, Journal of Sound and Vibration, Submitted.

Improving Capabilities in Modelling Aircraft Noise Sources

Ana Vieira
Department: Control and Operations
Section: Aircraft Noise & Climate Effects
Daily supervisor: Dr. Mirjam Snellen
Promotor: Prof. Dr. Dick G. Simons
A.E.AlvesVieira@tudelft.nl

Noise reduction at the source

Typical aircraft noise sources

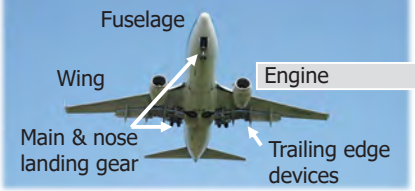

- Fan inlet
- Fan exhaust
- Jet
- Turbine
- Combustion

Sound quality metrics used to assess annoyance

Determine which characteristics of a sound contribute to annoyance

Loudness	Perception of the magnitude of a sound
Roughness	Assesses the fast loudness fluctuations (50 to 90 Hz)
Tonality	Measures the tonal prominence
Sharpness	Quantifies the high frequency content

Shielding of engine noise

Engine noise can be reduced by placing an obstacle between the noise source and the observer.

Fan noise shielded by

- Wings
- Fuselage

Comparison of noise shielding predictions with measurements

Test study – Fokker 70

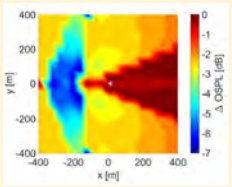

Prediction of noise shielding on the ground.

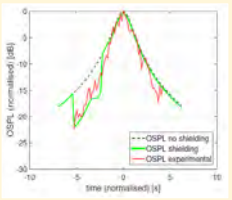

Overall sound pressured level of a flyover (measured and prediction).

Aircraft noise

Associated with risks for human health:
- Hypertension
- Increased risk of heart attack
- Sleep disturbance
- Stress

Flightpath 2050: ***Reduction of perceived noise by 65%***

Noise reduction at the source

Shielding of engine noise

Flyover measurements recorded at Schiphol Airport

Acoustic Array
- 64 microphones
- Underbrink spiral configuration
- Dimension 4m x 4m
- ADS-B transponder
- Optimal camera

Variability of tonality

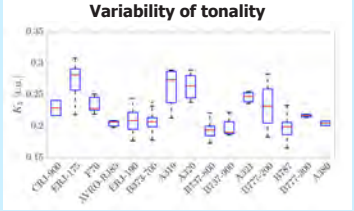

Variability of the sound quality metrics determined for the different aircraft types.

Operational conditions
+
Aircraft geometry
+
Engine characteristics

Prediction of loudness vs measurements

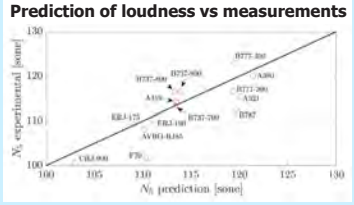

Result:
Empirical expressions to predict the sound quality metrics during the aircraft design phase.

Noise shielding measurements in the low speed wind tunnel

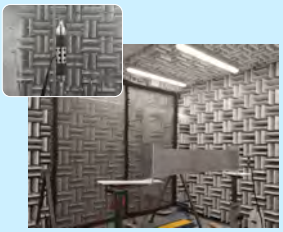

Assessment of noise shielding by a wing considering:
- Omni-directional source
- Propeller (with and without an incoming airflow)
- Beamforming used to localize the main sources associated to diffraction on the edges

Beamforming plot of a monopole source shielded by a wing

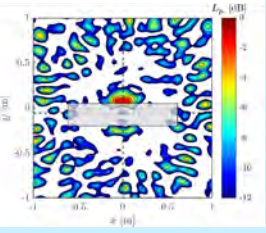

- The values of noise shielding are highly influenced by the directivity of the source.
- The curvature of the leading edge influences noise shielding and show be taken into account.


55
Yanan Zhang
Aerodynamics, Wind Energy,
Flight Performance and Propulsion

Agent-based modelling and simulation to evaluate safety of future unmanned aircraft system traffic

Chengpeng Jiang
Control & Simulation
Air Transport & Operation
Alexei Sharpanskykh
Henk Blom
c.jiang@tudelft.nl

Background

To enable the integration of UAS (Unmanned Aircraft System) into the airspace system and having this technology as part of daily operations, ConOps, rules and regulations have been proposed in Europe and USA.

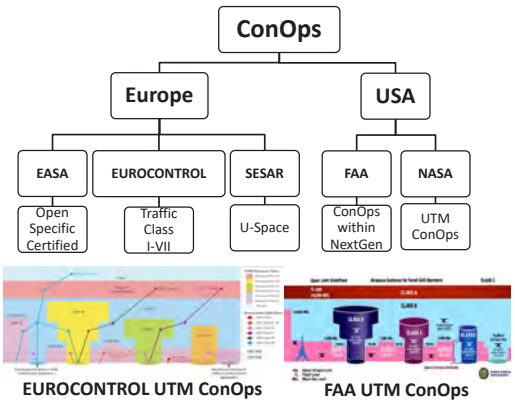

EUROCONTROL UTM ConOps

FAA UTM ConOps

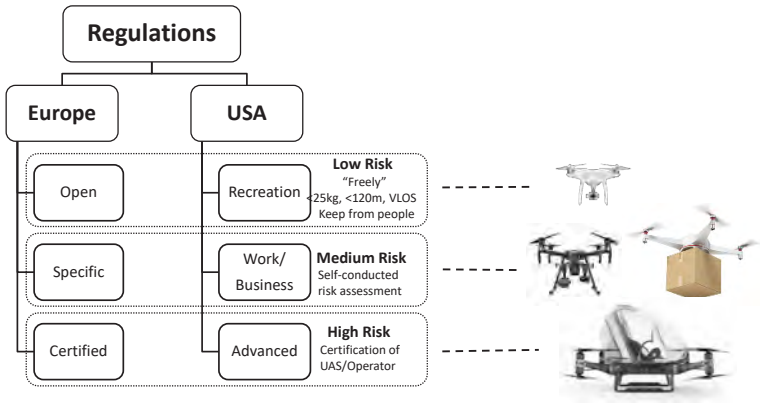

Problem Statement

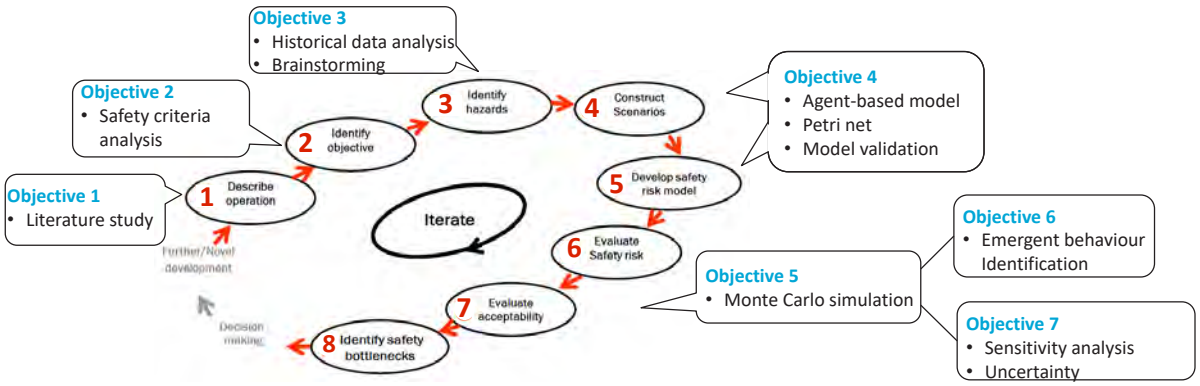

Case Study

Third-Party Risk of Urban Drone Dlivery

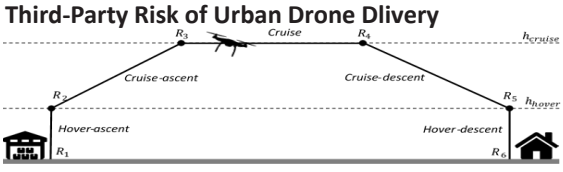

Single Drone Flight

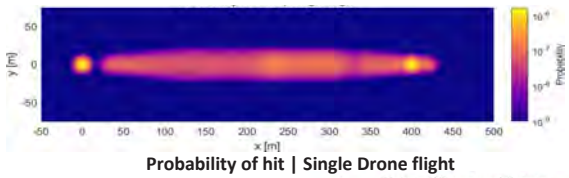

Probability of hit | Single Drone flight

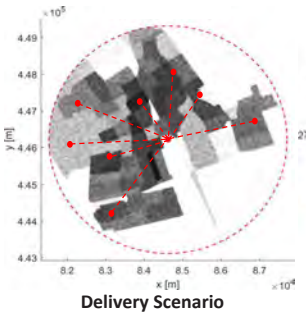

Delivery Scenario

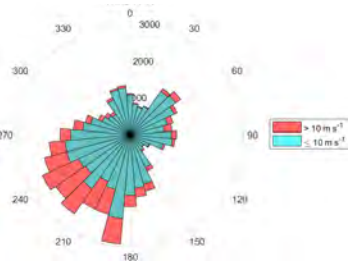

Wind Rose

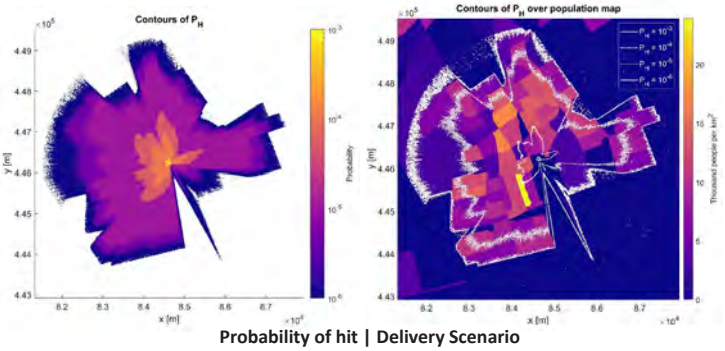

Probability of hit | Delivery Scenario

Evaluating Aircraft Maintenance Strategy: Agent-based Model and Stochastic Process

Juseong Lee
Aerospace Engineering
Air Transport and Operations
Daily supervisor: Dr. M.A. Mitici
Promotor: Prof. dr ir Max Mulder
J.Lee-2@tudelft.nl

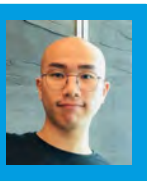

Motivation

Aircraft maintenance is key for efficient and safe aircraft operations. Through the improved sensors and data analysis technology, a new strategy called condition-based maintenance (CBM) is about to replace the traditional strategy called time-based maintenance (TBM). This research assesses the safety and efficiency of the new aircraft maintenance strategies using an agent-based model and stochastic process.

Agents in Aircraft Maintenance

Based on the study of aircraft maintenance practice, the following five agents are identified. Each agent is modeled based on their role, decision-making behavior, available information, and interaction with the other agents.

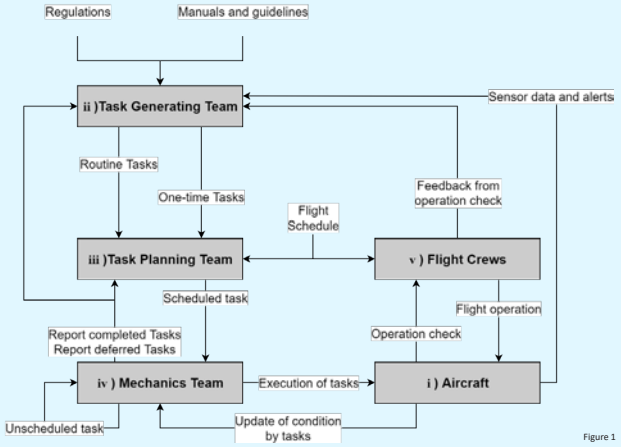

Figure 1

Degradation Model of Brakes

A case study is conducted for the maintenance of aircraft landing gear brakes, based on the operation data.

Degradation Model – Gamma Process

Degradation level of brakes X(t) can be modeled by the thickness of brake disks. X(t) increases by each flight cycles, following stochastic Gamma process[1]:

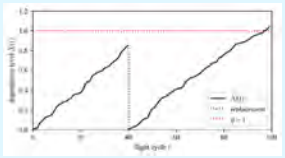

$$X(\tau_i^{\text{arr}}) - X(\tau_i^{\text{dep}}) \sim \text{Gamma}(a, b),$$

Incident Model

A wide-body aircraft with 8 brakes is considered. When more than two brakes on the same side are degraded too much, $X_i(t) > \eta$, it is regarded as an incident[2-3].

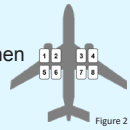

Figure 2

Maintenance Strategies

Four maintenance strategies are assessed in the case study.

1) TBM-Current interval of inspection
Inspect by interval, and replace if a brake is degraded too much.

2) TBM-Frequent interval of inspection
Inspect by more frequent interval.

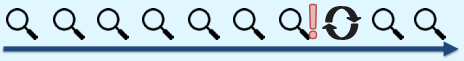

3) CBM-Sensor based Inspection
Start time-based inspections after sensor alert.

4) CBM-Sensor based Replacement
Replace when sensor data suggest zero Remained Useful Life (RUL).

Figure 3

Simulation Result

Monte Carlo simulation is conducted for the agents following four strategies for time horizon of 10 years.

Safety
- Number of incidents $N(t_H)$
- Time of the first incident $P(T(1))$

Efficiency
- Number of tasks performed
- Mean cycle to replace

	TBM-CI	TBM-FI	CBM-SI	CBM-SR
$E[N(t_H)]$	0.8248	0.0470	0.8377	0.0386

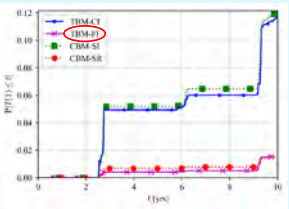

	TBM-CI	TBM-FI	CBM-SI	CBM-SR
Inspections	632.0	1272.0	802.8	-
Scheduled replacements	18.5	23.50	18.3	23.2
Unscheduled replacements	4.8	$\leq 10^{-4}$	4.9	-

	TBM-CI	TBM-FI	CBM-SI	CBM-SR
MCTR	1241.885	1234.115	1242.113	1239.042

Conclusion

Safety and efficiency indicators of four maintenance strategies are assessed using the proposed framework of agent-based model and stochastic process. This demonstrate the potential of use of simulation approach in assessment of aircraft maintenance.

Optimization of the decision parameters of maintenance strategies and the multi-criteria decision analysis are needed as the future work.

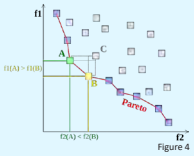

Figure 4

[1] J. M. van Noortwijk, A survey of the application of gamma processes in maintenance, Reliability Engineering and System Safety 94 (2009) 2-21.
[2] FAA Flight Operations Evaluation Board (FOEB), Master Minimum Equipment List (MMEL) Airbus A350-900 Series, All Models, 2017.
[3] FAA Flight Operations Evaluation Board (FOEB), Master Minimum Equipment List BOEING 787, 2015.
[Figure 4] Nojhan, https://en.wikipedia.org/wiki/Pareto_efficiency#/media/File:Front_pareto.svg

This research has received funding from the European Unions Horizon 2020 research and innovation programme under grant agreement No 769288.

Rare Event Simulation for Aircraft Collision Risk

Hao Ma
Aerospace Engineering
Control & Operations
Alexei Sharpanskykh
Henk Blom
Hao-2@tudelft.nl

Abstract

Commercial aviation is a complex, dynamic and safety critical system. Various elements such as Unmanned Aerospace System (UAS), commercial aircrafts, pilots, operating concepts, air traffic regulations, Air Traffic Controllers (ATCs), weather conditions and National Airspace System (NAS) capacity need to be considered. Moreover, this system is continuously changing/evolving/improved for enhanced safety and efficiency. To be able to understand the full implications of introducing change in any part of Air Traffic Management (ATM), agent-based modelling and Monte Carlo simulation are used. However, due to the impressive size and complexity of these systems, Standard Monte Carlo simulation requires a considerable amount of time and computational power. Therefore, simulation acceleration techniques, such as Interacting Particle System (IPS) combined with Markov jump process, are employed to enable an efficient analysis of applications in advanced ATM.

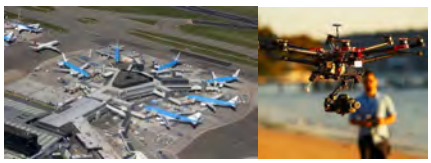

Fig.1. *Commercial aviation-complex and safety critical system*

Motivation

- Understand **interdependencies** between the technical subsystems together with incumbent operational and institutional frameworks;
- Understand and model how **architectural and design choices** influence the system and its various behaviours;
- Assess safety risk of complex ATM system;
- Assess safety risk/performance of new concepts;
- Safety is built in at the **capacity-level** required;
- UAS is expected to be **integrated** within the NAS.

Fig.2. *Agent based modelling and rare-event simulation for aircraft collision risk*

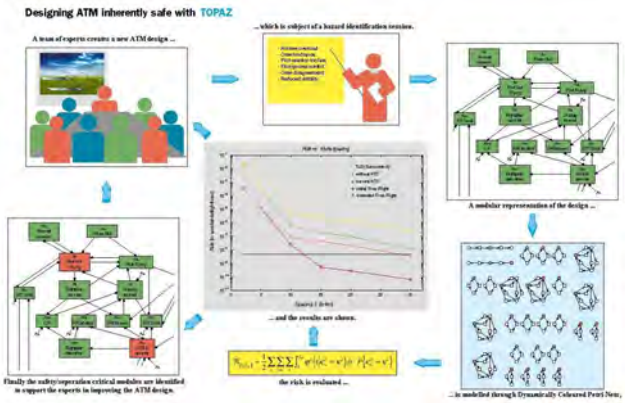

Agent-based Modelling

- Petri nets are a graphical paradigm for the formal description of the logical interactions among system components.
- Petri nets can be extended by associating time with the firing of transitions, resulting in Timed Petri nets

Existing Simulation Acceleration Technique

- Estimate the probability that a strong Markov process hits a given "small" subset within a given time period;
- Taking advantage of an appropriately nested sequence of closed subsets and then start simulation from outside to inside so that a rare event (accident/conflict) occurs

My initial contribution

- Develop an improved method in accelerating rare event simulations for an stochastic system with random jumps.

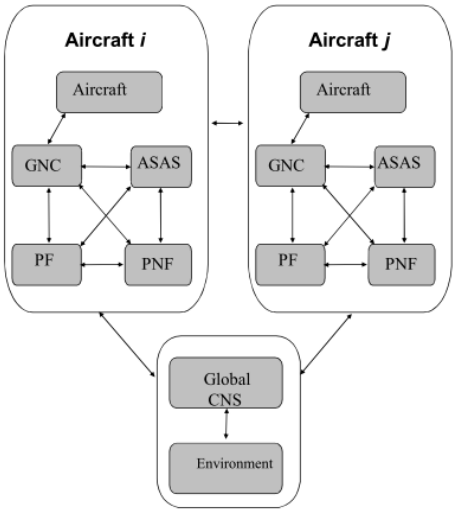

Fig.3. *Interactions between the agents*

Example & Results

Scenario:

Controller A controls UAS A in dense fog situation. Controller A sees another static UAS B for the first time if UAS A is at distance 1000m from UAS B. The reaction time of Controller A has a probability density function which satisfies experiential distribution. It is also assumed that UAS A can stop immediately. The velocity of UAS A is 100/3 m/s.

Question:

Estimate the probability that the UAS A hits UAS B.

Table 1 *Comparison Monte Carlo, existing IPS and novel IPS method using 50 simulation times*

λ	*Analytical Result*	Monte Carlo	Existing Method	Novel Method
0.1	2.478×10^{-3}	0	0.0028	0.0025
0.2	6.144×10^{-6}	0	3.603×10^{-6}	6.153×10^{-6}
0.3	1.522×10^{-8}	0	0	1.523×10^{-8}
0.4	3.775×10^{-11}	0	0	3.752×10^{-11}
0.5	9.357×10^{-14}	0	0	9.119×10^{-14}

What is resilience of aerospace sociotechnical systems?

Matt Vert

Air Transport and Operations
Alexei Sharpanskykh
Max Mulder
m.p.j.vert@tudelft.nl

Let's say you are interested in a system in particular. A system where both **human** and **technology** interact together

For instance, an aerospace system, like an international **airport** in Netherlands or a human **space shuttle** to Mars

You have heard somewhere, although you can't recall where exactly, that **resilience** is something desirable

The problem is: you have NO IDEA what **resilience** is...

I have got a good news for you: you are at the best place to know what it is!

To understand what is resilience, you need to first ask yourself 2 main questions:

Question 1- What is exactly your system? This will be the **core** and the boundaries of your model

Question 2- What should your system achieve? This will be related to the **performance** indicators of your system

Nope, there's no third question.

After answering these 2 questions, here is what is resilience:

Resilience is the capacity of the system to maintain high performance indicators while facing unexpected disruptions

I know what you are thinking. You are thinking: "Wow! This would be AMAZING for my system!"

You are thinking as well: "But what capabilities should my system have to be resilient?"

Here is the answer: your system should be capable to adapt. In other words, it should have an **adaptive capacity**

Now, you will ask me: "Please Matt, tell me what is the adaptive capacity!"

OK.

To be able to adapt to unexpected disruptions, your system should possess the following **cognitive** mechanisms:

- **Situation Awareness**
- **Analysing**
- **Sensemaking**
- **Creative problem-solving**
- **Planning**
- **Learning**
- **Coordination**
- **Monitoring**
- **Naturalistic decision-making**

And your system should possess as well:

- **Resources**

When disruptions occur, the right understanding of the situation and the **intelligent** use of **resources** will maintain a high performance of the system

You may wonder: is resilience like **robustness** or resistance?

No! Your system will be **robust** if it is able to cope with **known** disruptions. Meaning the performances won't decrease because of the existing procedures, rules, plans, buffers, redundancies...

While resilience is about facing **unexpected** disruptions!

Resilience is about reasoning

Let's say your are interested in a system in particular. How can you investigate the resilience quantitatively ?

You want to model and quantitatively assess resilience of your aerospace sociotechnical system? Let me know and let's work together!

Oh... this is the end of this poster unfortunately

DEPARTMENT OF AERODYNAMICS, WIND ENERGY, FLIGHT PERFORMANCE AND PROPULSION

The Aerodynamics, Wind Energy, Flight Performance & Propulsion (AWEP) Department contributes to the future of aircraft and wind turbines, with a nucleus in aerodynamics. The future sustainability of air transport depends greatly on innovations. We need to reduce significantly our energy consumption, our emissions and our dependence on fossil fuels.

A good proportion of the innovations we need are in the fields of aerodynamics, flight performance and propulsion. The relationship between aircraft and wind turbines is reflected in, for example, the fact that aircraft propulsion systems and wind turbines are both rotating wing systems with inverted operations. The turbine design directs towards huge, robust machines for application offshore and in energy-generating kites.

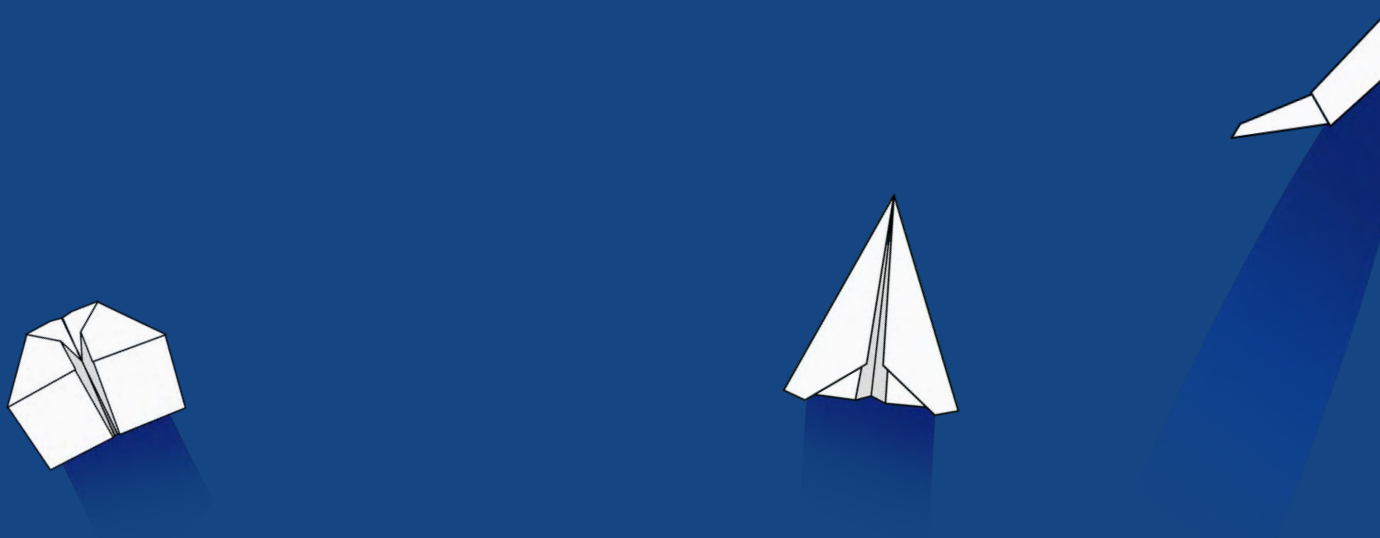

AERODYNAMICS

Jordi Casacuberta Puig
Alessandro D'Aguanno
Mohamad Fathi
Gabriel González Saiz
Weibo Hu
Varun Jain
Constantin Jux
Luis Laguarda Sanchez
Xiaodong Li
Christoph Mertens
Kaisheng Peng
Alberto Felipe Rius Vidales
Edoardo Saredi
Alexander Spoelstra
Wouter Terra
Yi Zhang
Giulia Zoppini

FLIGHT PERFORMANCE AND PROPULSION

Nitish Anand
Federica Ascione
Leonardo Castellanos G.
N. B. Chandrasekaran
Biagio Della Corte
Andrea Giuffré
Francesco Mazza
Rishikesh Sampat
Sumit Tambe
Francesco Tosto

WIND ENERGY

Hugo Mourão Bento
Livia Brandetti
Bedassa R. Cheneka
Delphine De Tavernier
Yunusi Fuerkaiti
Edoardo Grande
Ming Huang
Chihoon Hur
Sharif Khoshmanesh
Lourenco T. L. Pereira
Mihir Kishore Mehta
Jingna Pan
Mark Schelbergen
Julia Steiner
Christopher Teruna
Yanan Zhang

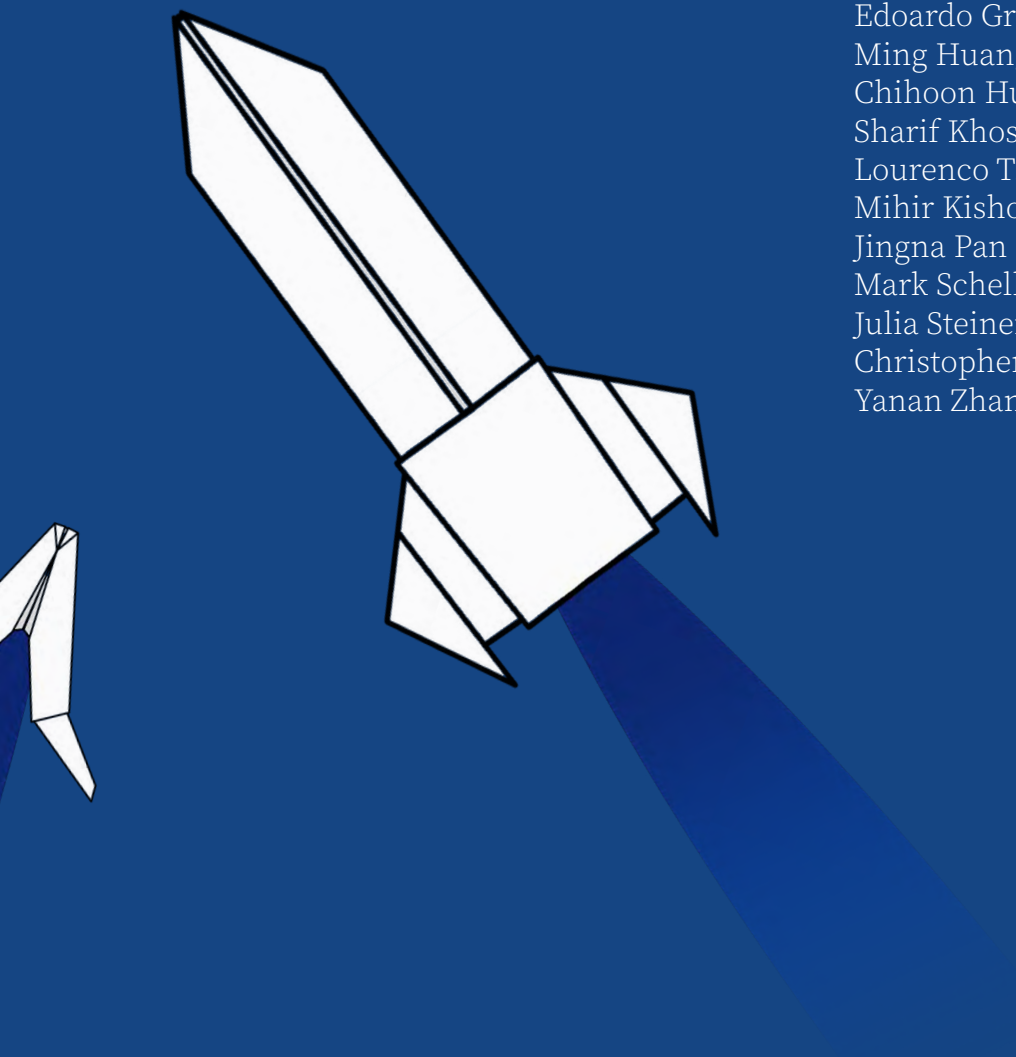

Numerical study of the crossflow instability

PhD Candidate
Jordi Casacuberta Puig
Department AWEP
Section Aerodynamics
Promotor Prof. Dr. Hickel
Co-promotor Dr. Kotsonis
J.CasacubertaPuig@tudelft.nl

Motivation

Improving the efficiency of aircrafts is of major priority due to environmental concerns involving noise contamination and air pollution [1]. Skin friction drag in subsonic transport aircraft represents approximately 50% of total drag [2]. It is therefore of interest to achieve fully laminar flow on the wings. Even though laminar flow control techniques are employed to delay or suppress the laminar-turbulent transition process, these techniques show poor performance in real flight conditions. A main reason is that *realistic* wings feature surface imperfections. Although roughness significantly alters the transition mechanisms as compared to a smooth case, little is known on the underlying physics and an in-depth investigation is required.

We study computationally the effect of two-dimensional surface roughness in the form of steps on the laminar-turbulent transition process on swept aircraft wings under the stationary crossflow instability.

Methodology

At the current stage of the research, a benchmark case of the crossflow instability developing on a smooth surface without excrescences has been developed. Numerically, we model the wing as a flat plate with an imposed favorable pressure gradient. One instability spanwise wavelength is considered, with periodic boundary conditions imposed at the transverse boundaries.

The instantaneous flow field is decomposed into a steady-state solution (the base flow) and a perturbation field:

$$\underbrace{\mathbf{q}(\mathbf{x},t)}_{\text{flow field}} = \underbrace{\mathbf{q}_\mathrm{s}(\mathbf{x})}_{\text{base flow}} + \underbrace{\mathbf{q}'(\mathbf{x},t)}_{\text{perturbations}}$$

Direct Numerical Simulations (DNS) of the base and the instantaneous flow fields are computed, and the dynamics of modal perturbations are assessed.

Results

The base flow is spanwise invariant. The base flow velocity profile orthogonal to the inviscid streamline features an inflection point near the wall, which gives rise to a strong inviscid instability. It manifests in the instantaneous flow as **stationary co-rotating vortices**, whose axes of rotation are practically aligned with the incoming inviscid streamline. Figure 1(*b*) shows the structure of the crossflow vortices, characterized as green isosurface of Q-criterion. Figure 1(*a*,*c*), the projected planes of Figure 1(*b*), illustrates the wavy pattern that is induced as a consequence of the streamwise-developing crossflow perturbation. The real proportions of the computational domain are portrayed in Figure 2. The boundary layer thickness at the inflow is denoted by h, and the inflow free-stream velocity by u_∞.

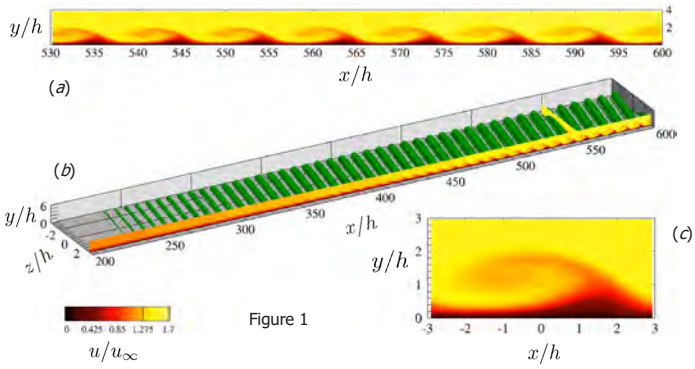

Figure 1

Figure 2

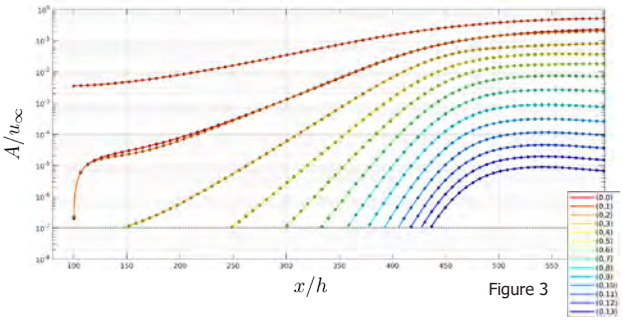

Figure 3

Figure 3 shows the streamwise evolution of the amplitude of steady instability modes obtained from the DNS. The red line represents the primary crossflow mode, which is prescribed at the inflow boundary condition. The strong non-linear interaction between the **primary mode**, the **mean-flow distortion** and the **high-order harmonics** leads to the non-linear saturation of the system for large x/h. The shear that develops in the distorted flow field is prone to highly energetic and explosive secondary instabilities.

Future work

In future stages of the research, DNS will reproduce on-going experimental work, with roughness in the form of forward-facing steps mounted on the wing.

[1] M. Jahanmiri. Aircraft drag reduction: an overview. Research report 2011:02, 2011.
[2] J. J. Thibert, J. Reneaux, and V. Schmitt. Onera activities on drag reduction. Office National d'Études et de Recherches Aérospatiales, 1990.

Experimental Investigation of Transonic Buffet

Alessandro D'Aguanno
Department: AWEP
Section: Aerodynamics
Daily supervisor: F.F.J. Schrijer
Promotor: B.W van Oudheusden
A.Daguanno@tudelft.nl

Motivation

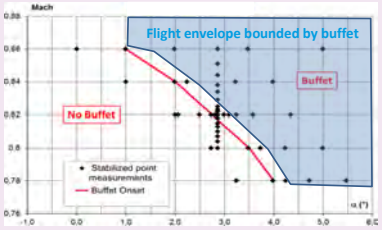

Adapted from *Dandois, 2016, Physics of Fluids*

- Transonic buffet is a phenomenon which limits the performance of civil aircrafts, bounding the flight envelope to lower values of Mach number and angle of attack (figure above).
- Regulations do not allow an acceleration, due to buffet, higher than 0.2 g.

Physical mechanism of Transonic Buffet

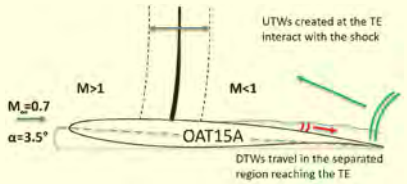

- Oscillation of a shockwave on the suction side of a wing/airfoil.
- Shockwave sustained by a feedback mechanism.
- Shockwave exchanging energy with pressure waves (UTWs) created at the trailing edge in order to satisfy the Kutta condition.

Experimental investigation

Experiments carried out in the transonic wind tunnel of TU Delft on the OAT15A airfoil (left) for fully developed buffet conditions:

- Ma=0.7
- α=3.5°
- Re= 2 x 10^6

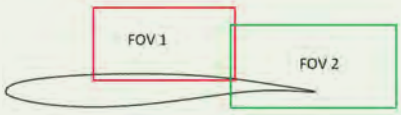

High Speed PIV has been adopted in order to quantify the velocity field.
Two cameras with an acquisition frequency of 4.65 KHz have been used in the regions shown on the left.

Phase average

$$u(x,t) = \bar{u}(x) + u'(x,t) + u_{Phase}(x)$$

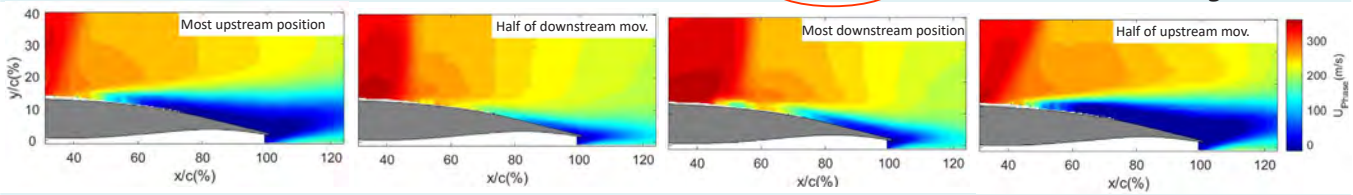

Thanks to the good periodicity of buffet, a phase average based on the shock position is evaluated. In the figures above the average flow velocity field (obtained from the PIV data) is shown for four buffet phases, highlighting the change in shock position and extent of the separated area.
A more complete statistical analysis (which does not only consider the shock position) has been accomplished by means of a modal decomposition.

Proper Orthogonal Decomposition

$$u(x,t) = \bar{u}(x) + u'(x,t) = \bar{u}(x) + \sum_{n=1}^{N} \sqrt{\lambda_n}\phi_n(x)c_n(t)$$

Spatial Modes

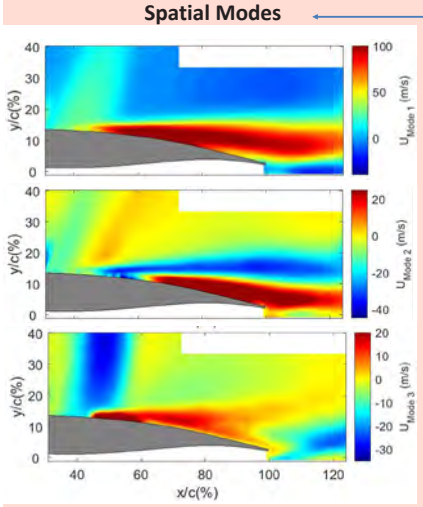

The first 3 modes account for more than 85% of the total energy.

- First mode associated with variations in the shock and separated oscillation area
- Second mode associated with the asymmetrical behaviour of buffet
- Third mode associated with oscillations of higher order

Time Coefficient

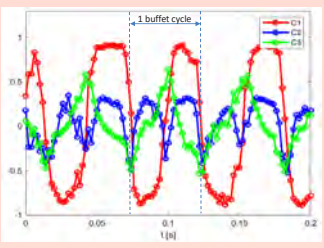

Each spatial mode has an associated contribution in time which is described by the time coefficients C1,C2,C3.

- C1 switches from a positive value, during the upstream mov., to a negative one in the downstream mov.
- The second mode (C2) is activated when the shock is in its turning point.
- C3, as the shock position, changes gradually during the buffet cycle.

Power Spectral Density

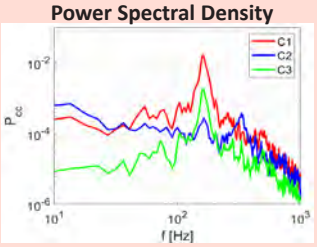

The Power Spectral Density associated with the time coefficient behaviour shows that each of the first 3 modes has a peak at 160 Hz (buffet frequency).

POD demonstrated to be an effective tool in scrutinizing the feedback mechanism of transonic buffet by taking into account all of its main elements (shock position, separated area, convection of vortices etc.). A more detailed study will be directed to the understanding and the origin of the UTWs and DTWs.

High-fidelity simulations of reacting and non-reacting multiphase flows at transcritical pressure

Mohamad Fathi
Aerospace Engineering
Aerodynamics
Stefan Hickel
Dirk Roekaerts
m.fathi@tudelft.nl

Motivation a significant portion of modern energy conversion systems works based on the injection of cryogenic compressed liquids into high-pressure combustion chambers. The pressure usually exceeds the critical pressure of conventional propellants and is called transcritical pressure. In addition to the effects on the phase change phenomena at transcritical pressures, the thermo-transport properties of the fluid also significantly deviate from those computed based on the ideal gas assumption. Hence, simulations of transcritical flows are a very challenging task.

the transcritical Spray A of the Engine Combustion Network (ECN) has received considerable attention in the community since experimental and theoretical findings, questioned the established paradigm of typical spray atomization (primary and secondary breakup, evaporation of droplets) on the one hand, and usage of a dense fluid mixing without considering two-phase phenomena with diminishing surface tension on the other hand. Here, we used this spray as our benchmark in the computations.

Non-reacting case for validation of spray modeling, we studied the non-reacting Spray A where the pure n-dodecane at low temperature of 363 K is injected into the warm pre-burn (without oxygen) combustion chamber which contains nitrogen, carbon dioxide, and water vapor at temperature of 900 K and transcritical pressure of 60 bar.

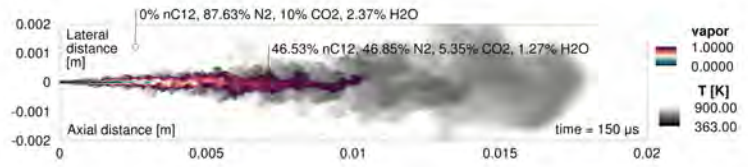

Fig1: An instantaneous snapshot of the temperature field, superimposed by the vapor mole fraction distribution which indicates the two-phase region as well as the liquid penetration length.

Reacting case warming up of the combustion chamber is carried out by means of a premixed combustion of acetylene, hydrogen, oxygen and nitrogen before the n-dodecane injection. For the reacting case, a combination that results in 15% of oxygen (molar based) and 900 K ambient temperature has been simulated.

Suitable reduced chemical mechanism for high-fidelity simulations, the reaction chemistry requires a significant size reduction such that the number of transported scalars is maintained at a reasonable level. Here, we utilized an optimized two-step mechanism (Hakim et al, 2018) for the computations.

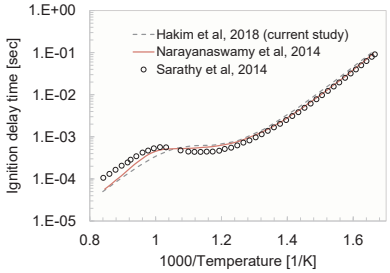

Fig2: Auto-ignition delay time for the stoichiometric mixture of the fuel and oxidizer of Spray A, it is predicted by the optimized two step mechanism and the state-of-the-art detailed and reduced mechanisms.

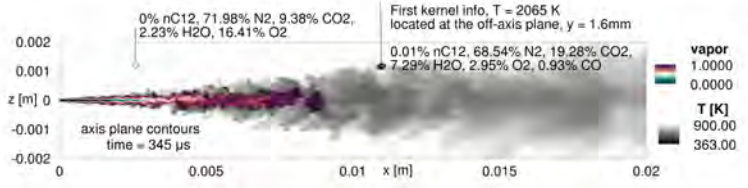

Fig3: An instantaneous snapshot of the temperature field, superimposed by the vapor mole fraction distribution at the axis plane (y = 0). First kernel information is also shown in the figure.

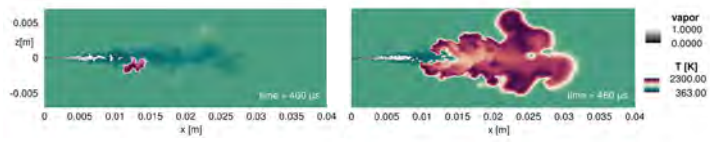

Fig4: Temporal sequence of the flame propagation after autoignition phenomena. Snapshots of the temperature field at the axis plane (y = 0) overlapped with two phase region.

Diffuse-interface method we solve the three-dimensional compressible multi-component Navier-Stokes equations in a fully conservative (FC) formulation with a finite volume (FV) method that uses a single-fluid approach to describe single-phase liquids and gases as well as two-phase mixtures.

Real thermodynamics for computational efficiency and for accurate representations of properties near the critical point, the RKPR EOS which is a three-parameter cubic state equation, has been used here.

$$p = \frac{\rho R_u T}{M_w - b\rho} - \frac{a\rho^2}{(M_w + \delta_1 b\rho)(M_w + \delta_2 b\rho)}$$

Following relationship can be derived for the evaluation of the internal energy based on the ideal and non-ideal parts:

$$e = e_0 + \frac{T\left(\frac{\partial a}{\partial T}\right) - a}{(\delta_1 - \delta_2) b M_w} \ln\left(\frac{M_w + \delta_1 b\rho}{M_w + \delta_2 b\rho}\right).$$

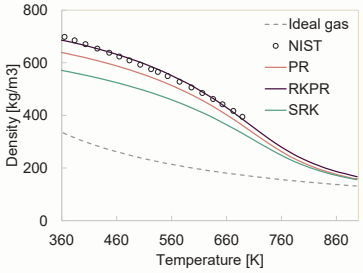

Fig5: Density prediction for pure n-dodecane at a pressure of 6 MPa for different cubic EOS models along with NIST data as a reference.

Vapor-liquid equilibrium We check the stability of the mixture, and accordingly we carry out the phase splitting calculations by means of a new thermodynamic tool called volume function in a very efficient reduced space (Fathi and Hickel, 2020).

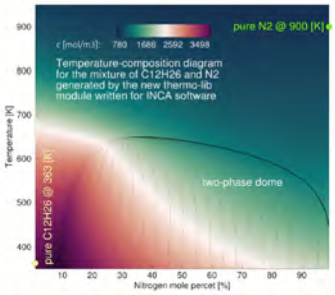

Fig6: Phase diagram for the binary mixture of nC_{12} and N_2 along with the thermodynamic conditions of the injectant and chamber.

References

[1] Hakim, et al. (2018). Probabilistic parameter estimation in a 2-step chemical kinetics model for n-dodecane jet autoignition. CTM, 22(3), 446-466.
[2] Fathi and Hickel (2020). Rapid multi-component phase-split calculations using volume functions and reduction methods. AIChE, 2001.06285.

AWEP

Towards the experimental closure of Collar's triangle with Lagrangian Particle Tracking

Gabriel González Saiz
Aerospace Engineering
Aerodynamics Section
Supervisors: Dr. A. Sciacchitano
Dr. B. van Oudheusden
Promotor: Prof. Dr. F. Scarano
G.GonzalezSaiz@tudelft.nl
Starting date: 15th October 2018

Motivation

The latest innovations in **composite materials** have encouraged their application in the aerospace industry, as a mean of reducing weight and fuel consumption. Light-weight composite structures are also more flexible and, thus, more prone to fluid-structure interaction, making aeroelastic phenomena more relevant.

In their interaction, fluid and solid are coupled through loads, which makes the measurements of loads crucial. With the current techniques, **flow and structural measurements are performed separately** with intrusive systems, which restricts the validation of computational approaches.

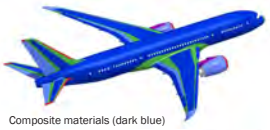

Composite materials (dark blue) in the Boeing 787

Micro air vehicle (MAV)

Objective

The aim of the project is to propose a diagnostics methodology capable of **experimentally obtaining loads present in aeroelastic phenomena** (i.e. aerodynamic, elastic, and inertial loads) and thus, closing the dynamic FSI equations.

Lagrangian Particle Tracking (LPT)

Also called Particle Tracking Velocimetry (PTV), this technique achieves **to obtain the positions and velocities of individual flow tracers**, at a given acquisition frequency.

Though, it is commonly used for fluid measurements, in which the flow is seeded with a low concentration of particles (compared to PIV), it offers potential advantages when applied to simultaneous measurements of fluid and structure.

Recorded snapshots — Volumetric reconstruction — Tracked data

Similarly to the fluid tracers, the structure is marked with a grid of points that are also recorded by the cameras.

Experimental setup

Aerodynamic forces

Surface pressure on the panel

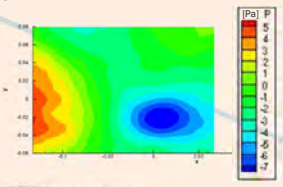

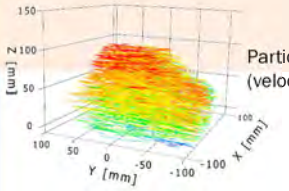

Particle tracks (velocity)

Rigid-body aerodynamics

Collar's Triangle

$F_{aero} + F_{elastic} = F_{inertial}$

Static aeroelasticity

Mechanical vibration

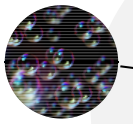

Helium Filled Soap Bubbles

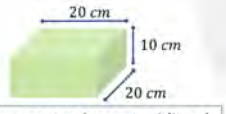

Measurement volume ➡ 4 liters!

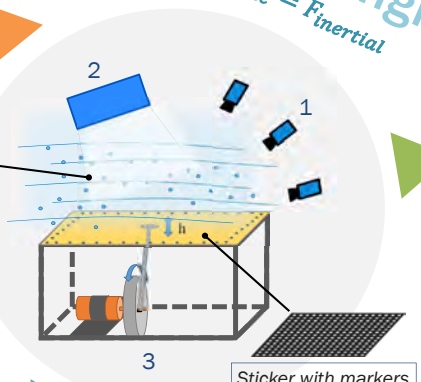

Displacement from marker positions

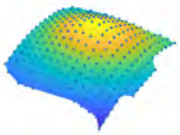

Elastic forces

Strain, ε_x

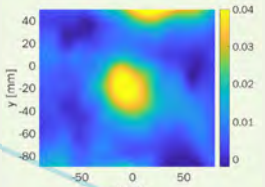

Panel height, $z\ [mm]$

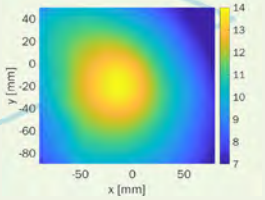

Inertial forces

Velocities and accelerations of the surface markers are regularized in time and space

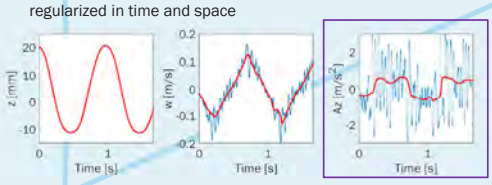

$F_{inertial} = A_z \cdot dm$

1. Tomographic system 3 high-speed cameras capture flow tracers and surface markers simultaneously
2. Illumination system White high-power LEDs to illuminate the domain
3. Actuation system DC motor moving the flexible panel at the center location

References

- Adrian, R. J. (1991). Particle-imaging techniques for experimental fluid mechanics. *Annual review of fluid mechanics*, *23*(1), 261-304.
- Krein, A., & Williams, G. (2012). Flightpath 2050: Europe's vision for aeronautics. Innovation for Sustainable Aviation in a Global Environment: Proceedings of the Sixth European Aeronautics Days, 63.
- Collar, A. R. (1946). The expanding domain of aeroelasticity. The Aeronautical Journal, 50(428), 613-636.

TUDelft ONERA DLR HOMER

AWEP

Dynamics of a Supersonic Flow over a Backward-facing Step

Weibo Hu
W.Hu-2@tudelft.nl
Department: AWEP
Section: Aerodynamics
Supervisor & Promoter: Stefan Hickel
Co-supervisor: Bas van Oudheusden

Introduction

Supersonic flow over a backward-facing step **(BFS)** features various unsteady flow phenomena, including **separation**, **reattachment**, **laminar-turbulent transition** and **shock wave/boundary layer interactions (SWBLI).** In contrast with a natural transition initiated by **Tollmien-Schlichting (T-S) waves**, the transition over BFS usually involves **Kelvin-Helmholtz (K-H) instability**. In terms of SWBLI, the upstream boundary of the separation bubble is stationary and only a reattachment shock is present in this case, different from the canonical incidence shock case.

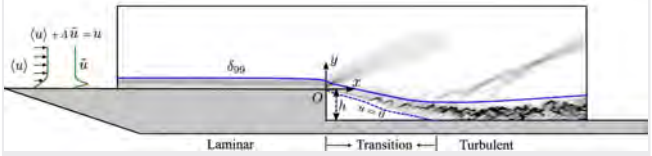

Schematic of a supersonic flow over a BFS.

The **transition process** and **unsteady SWBLI** are scrutinized by a well-resolved **large-eddy simulation (LES)**. A **spectral analysis** is employed to detect the dominant frequencies of unsteadiness. **DMD** is then utilized in order to relate these frequencies to the corresponding underlying flow phenomena.

Numerical setup

h	L_x	L_y	L_z	U_∞	Ma_∞
3mm	$110\delta_0$	$33\delta_0$	$16\delta_0$	469.85 m/s	1.7
p_∞	Re_∞	T_0	p_0	δ_0	$Re_{\delta_{in}}$
20259 Pa	1.3718×10^7 m^{-1}	300 K	1×10^5 Pa	1 mm	13718

Main geometry and flow parameters of the current case.

$$q' = A\tilde{q} = A(\tilde{q}_r cos\theta - \tilde{q}_i sin\theta), \qquad \theta = \alpha_r x + \beta z - \omega t, \mathrm{A} = 0.026$$

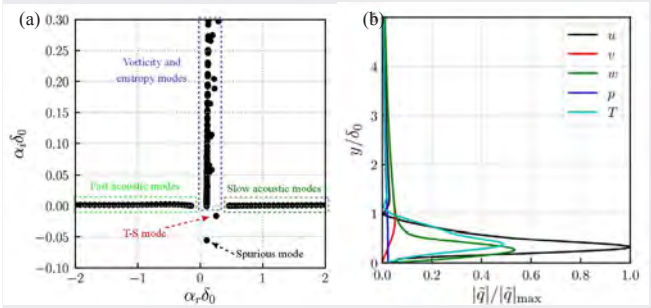

(a) Eigenvalue spectra and (b) the wall-normal disturbances of the local least-stable T-S mode obtained from linear stability theory at $\omega^\delta = 0.1016$ and $\beta^\delta = 0.3927$.

Transitional regime

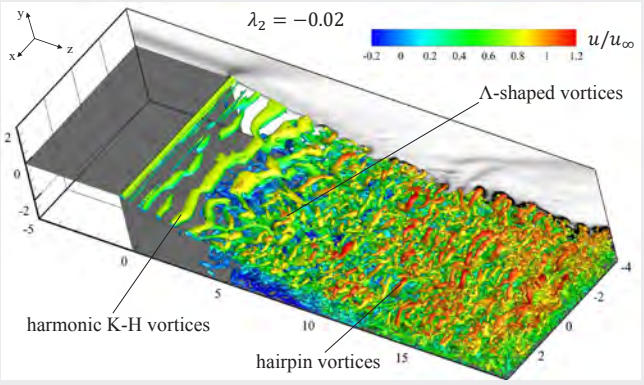

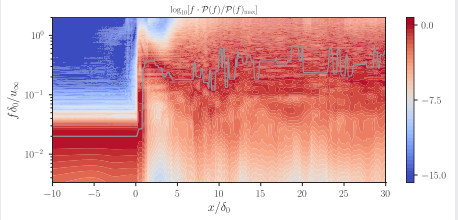

- Primary K-H modes
- Subharmonic waves
- Secondary modes
- Broad frequency spectrum

Turbulent regime

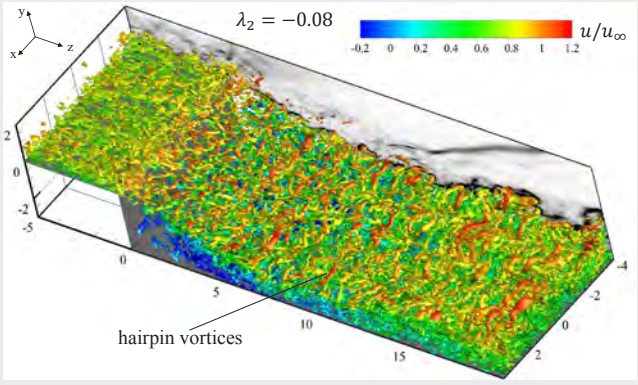

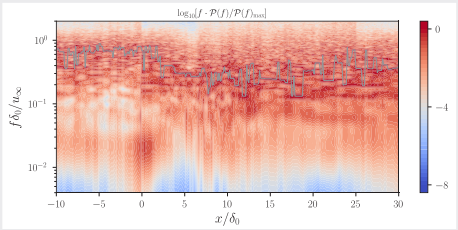

- No K-H vortices
- Stronger shock waves
- Higher dominant frequency
- Low-frequency contents present

Frequency-weighted power spectral density map of maximum pressure signals.

Flapping motion of shock and breathing of the separation bubble

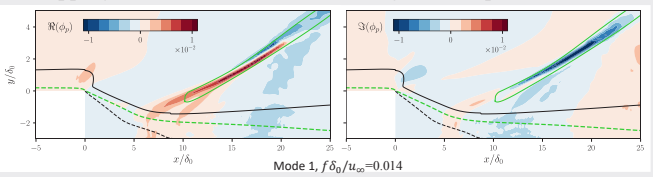

Large vortices shedding

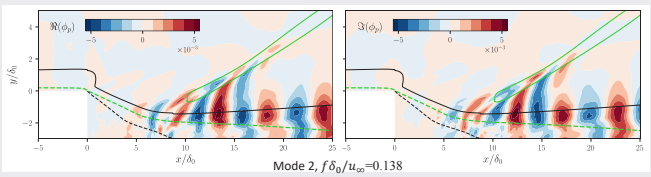

Real and imaginary parts of three selected dynamically important modes from DMD, indicating contours of modal pressure fluctuations.

An *n*-level domain decomposition formulation for finite element methods

PhD Candidate: Varun Jain
Department: Aerospace Engineering
Section: Aerodynamics
Supervisor: Dr. M. I. Gerritsma
Promotor: Dr. S. Hickel
Contact: v.jain@tudelft.nl

Abstract:

In classic domain decomposition methods Lagrange multipliers are introduced at the interface of broken spaces to impose continuity of solution across the elements. The discrete Lagrange multiplier problem is a reduced problem and therefore computationally cheap. However, in case of large number of discontinuous elements the interface system in itself becomes too large and expensive to solve.

In this work, we propose an extension to the classic methods, where you can divide the domain in macro elements and sub-elements within each macro elements. The Lagrange multipliers between the macro elements can be solved first – which is a smaller λ system. And then Lagrange multipliers between the sub elements can be solved for in parallel. In general, you can add n-layers of Lagrange multipliers with each subsequent layer being cheaper to solve.

Furthermore, we exploit the use of dual spaces as test functions such that the continuity constraint between the elements and the Lagrange multipliers is a local and topological metric free relation. The matrix representations for connections (at all levels) are independent of shape and size of the elements, and consists of 1, -1 and 0s only. We will illustrate this scheme with a numerical example on mixed formulation of Poisson equation using high order mimetic spectral element method.

Continuous domain

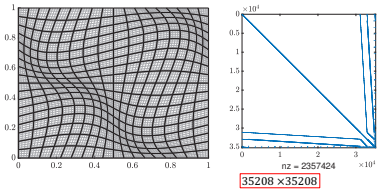

1-level decomposition

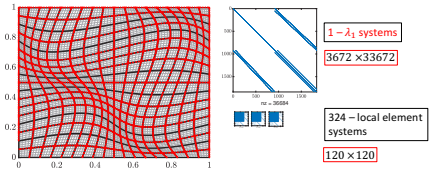

2-level decomposition

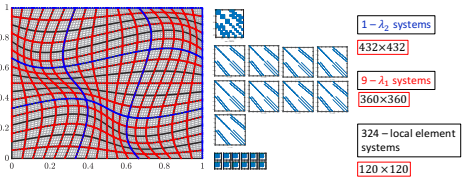

Mulitilevel domain decomposition

The Lagrange functional(s)

$$\mathcal{L}_0(\phi,q;f) := \int_K \frac{1}{2}|q|^2 dK + \int_K \phi(\nabla\cdot q - f)\,dK - \int_{\Gamma_D} \hat{\phi}(q\cdot n)\,d\Gamma - \int_{\Gamma_N} \lambda_5(\hat{q}\cdot n)\,d\Gamma$$

$$\mathcal{L}_1(\phi,q;f) := \int_K \frac{1}{2}|q|^2 dK + \int_K \phi(\nabla\cdot q - f)\,dK + \int_{\Gamma_1} \lambda_1(q\cdot n) - \int_{\Gamma_D} \hat{\phi}(q\cdot n)\,d\Gamma - \int_{\Gamma_N} \lambda_5(\hat{q}\cdot n)\,d\Gamma$$

$$\mathcal{L}_2(\phi,q;f) := \int_K \frac{1}{2}|q|^2 dK + \int_K \phi(\nabla\cdot q - f)\,dK + \int_{\Gamma_1} \lambda_1(q\cdot n)d\Gamma + \int_{\Gamma_2} \lambda_2(q\cdot n)d\Gamma - \int_{\Gamma_D} \hat{\phi}(q\cdot n)\,d\Gamma - \int_{\Gamma_N} \lambda_5(\hat{q}\cdot n)\,d\Gamma$$

$$\mathcal{L}_5(\phi,q;f) := \int_K \frac{1}{2}|q|^2 dK + \int_K \phi(\nabla\cdot q - f)\,dK + \int_{\Gamma_1} \lambda_1(q\cdot n)d\Gamma + \int_{\Gamma_2} \lambda_2(q\cdot n)d\Gamma + \ldots + \int_{\Gamma_5} \lambda_5(q\cdot n)d\Gamma - \int_{\Gamma_D} \hat{\phi}(q\cdot n)\,d\Gamma - \int_{\Gamma_N} \lambda_5(\hat{q}\cdot n)\,d\Gamma$$

The variational formulation

$$\begin{cases} (u,q) + <\nabla\cdot u,\phi> + <u\cdot n,\lambda_1> + <u\cdot n,\lambda_2> + \cdots + <u\cdot n,\lambda_5> = <u\cdot n,\hat{\phi}> & \forall\, u\in H(div;K) \\ <\varphi,\nabla\cdot q> = <\varphi,f> & \forall\,\varphi\in H^1(K) \\ <\mu_1,q\cdot n> = 0 & \forall\,\mu_1\in H^{\frac{1}{2}}(\Gamma_1) \\ <\mu_2,q\cdot n> = 0 & \forall\,\mu_2\in H^{\frac{1}{2}}(\Gamma_2) \\ \vdots \quad\quad \vdots & \\ <\mu_5,q\cdot n> = <\mu_5,\hat{q}\cdot n> & \forall\,\mu_5\in H^{\frac{1}{2}}(\Gamma_5) \end{cases}$$

The algebraic formulation

$$\begin{bmatrix} \mathbb{M}^{(d-1)} & \mathbb{E}^{2,1^T} & \mathbb{E}_{N_1}^T & \mathbb{E}_{N_2}^T & \cdots & \mathbb{E}_{N_5}^T \\ \mathbb{E}^{2,1} & & & & & \\ \mathbb{E}_{N_1} & & & & & \\ \mathbb{E}_{N_2} & & & & & \\ \vdots & & & & & \\ \mathbb{E}_{N_5} & & & & & \end{bmatrix} \begin{bmatrix} q \\ \phi \\ \lambda_1 \\ \lambda_2 \\ \vdots \\ \lambda_5 \end{bmatrix} = \begin{bmatrix} \hat{\phi} \\ f \\ 0 \\ 0 \\ \vdots \\ \hat{q}\cdot n \end{bmatrix}$$

$\mathbb{E}_{N_i}$ have local support and are independent of the shape and size of element.
At each macro element level !!!

where, $\mathbb{E}_{N_i}$ are incidence matrices of the type:

The above system can be efficiently evaluated using static condensation method, where

$$\lambda_i = \left(\mathbb{E}_i\mathbb{A}_i\mathbb{E}_i^T\right)^{-1}\left(\mathbb{E}_i\mathbb{A}_i\mathbb{F}_{i+1}\right) \quad \text{, where}$$

$$\mathbb{F}_i = \mathbb{F}_{i+1} - \mathbb{E}_i^T\lambda_i$$

$$\mathbb{A}_{i+1} = \mathbb{A}_i\left(\mathbb{I} - \mathbb{E}_i^T\left(\mathbb{E}_i\mathbb{A}_i\mathbb{E}_i^T\right)^{-1}\mathbb{E}_i\mathbb{A}_i\right)$$

Test problem: Darcy flow - manufactured solution

Optimal convergence

Domain of the test problem is given by, $\Omega \in [0,1]^2$.

The RHS term is given by,

$$f = -\nabla\cdot\mathbb{K}\nabla\phi_{ex}$$

where,

$$\mathbb{K} = \frac{1}{x^2+y^2+0.1}\begin{pmatrix} 10^{-3}x^2+y^2+0.1 & (10^{-3}-1)xy \\ (10^{-3}-1)xy & x^2+10^{-3}y^2+0.1 \end{pmatrix}$$

$$\phi_{ex} = \sin(2\pi x)\sin(2\pi y)$$

The boundary conditions are given by: $\Gamma_D = \phi_{ex}|_{\partial\Omega}$ and $\Gamma_N = \emptyset$.

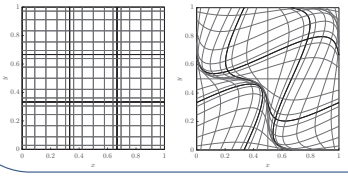

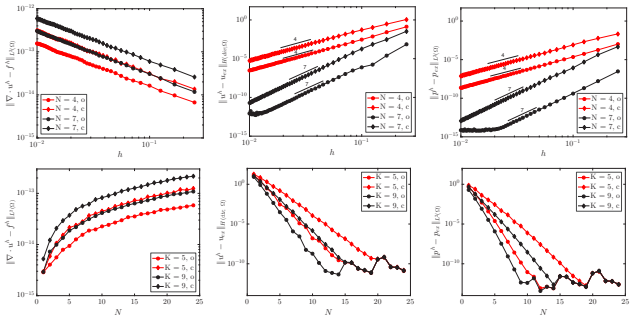

Application I :

Potential flow around a porous airfoil for wind turbines

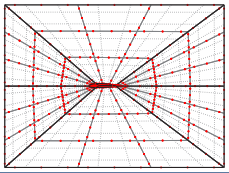

Domain boundaries have to be far to avoid any interference

But no interesting physics near domain boundaries !

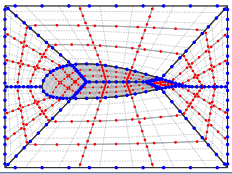

First - solve for blue Lagrange multipliers

Second – solve for red Lagrange multipliers in parallel

Third – solve for internal degrees of freedom

Application II :

Benchmark reservoir modeling case – SPE10

60 ×220 ×85 = 1.122 × 10^6 cells

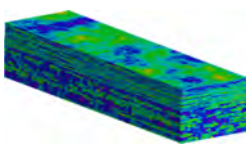

References:

[1] Jain, V., Zhang, Y., Palha, A., Gerritsma, M.I.: Construction and application of algebraic dual polynomial representations for finite element methods. arXiv:1712.09472v1, submitted to CAMWA.

AWEP

Robotic volumetric PIV

Name	**Constantin Jux**
Department	AWEP
Section	Aerodynamics
Daily supervisor	A. Sciacchitano
Promotor	F. Scarano
Email	C.Jux@tudelft.nl

Surface & pressure measurements on 3D objects

Background & motivation

Pressure is, next to shear stress, the only mechanism to exert a force onto an object moving through a fluid. Knowledge on the surface pressure distribution can thus be instrumental in an aerodynamic optimization process. Common instruments for surface pressure measurements are wall tappings or pressure sensitive paint (PSP). Whereas the latter can only be used for high speed applications, probing large models with taps at a desirable resolution often results in complex and costly test models.

A valid alternative is presented by particle image velocimetry (PIV): measuring the velocity field, the pressure field can be derived through the momentum equation. The robotic volumetric PIV system introduced by our group in 2018, is particularly well suited for measurements around large and complex test models.

An issue which arises, in particular when dealing with flexible models, is the knowledge about the precise surface location. Evaluating the pressure distribution on an object which deforms under aerodynamic loading requires the exact knowledge of its shape. To this end an approach is investigated to reconstruct the model geometry from the velocity field measurements.

Target

The aim of this study is the development of a dedicated strategy that allows for the simultaneous 3D shape reconstruction of a test model, and the time-averaged static pressure distribution on its surface by means of robotic volumetric PIV.

Test case

The approach has been assessed on a 15 cm-diameter sphere model at 10 m/s in the Open Jet Facility. The sphere contains surface pressure taps for reference.

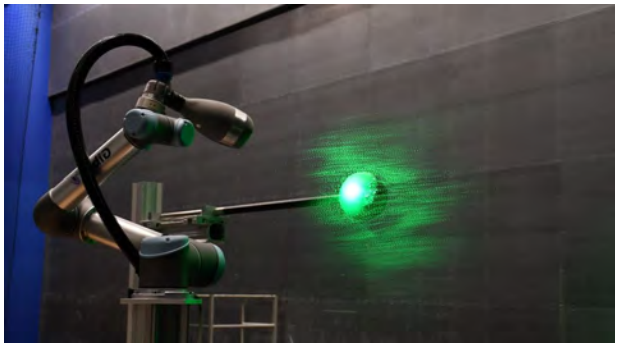

Fig. 1 Experimental setup in OJF

Surface reconstruction

The object shape is modeled by sampling the PIV tracer particles in vicinity of the model surface. The sampling relies on the uniformity of the particle distribution, and is conceptually illustrated below.

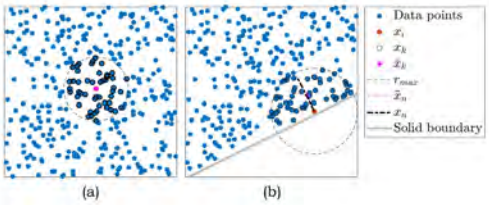

Fig. 2 Principle of tracer-based interface detection

The above data sampling identifies tracers along the fluid-solid interface, along with an approximate wall-normal vector. This provides the required input for a Poisson-type surface reconstruction, illustrated for the sphere case below.

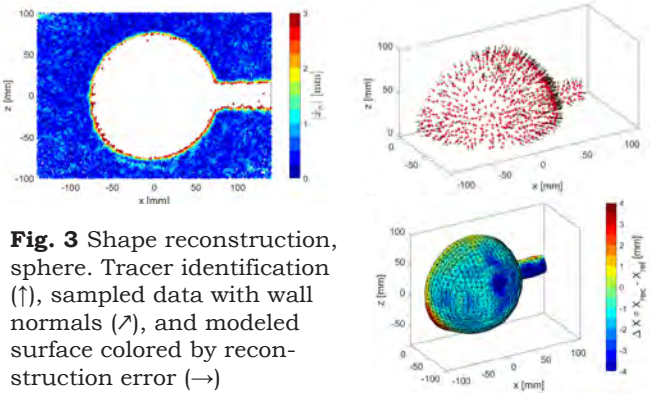

Fig. 3 Shape reconstruction, sphere. Tracer identification (↑), sampled data with wall normals (↗), and modeled surface colored by reconstruction error (→)

Pressure evaluation

The surface pressure distribution is evaluated in a three-part approach:

1. Bernoulli's equation provides the far-field pressure.
2. Spatial marching integration of $\nabla\bar{p}$ yields the static pressure in the remaining domain.
3. Extrapolation of the pressure field onto the model results in the desired surface pressure distribution.

The pressure evaluation method is expected to be published soon (under revision), whereas the surface reconstruction approach will only be presented at conference level this year.

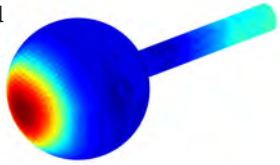

→ **Scan QR-code for selected research output** ←

Numerical investigation of a shock-wave/turbulent-boundary-layer interaction over a compliant panel

Luis LAGUARDA SANCHEZ
AWEP – Aerodynamics (2nd year)
Supervisors
Stefan HICKEL
Ferry SCHRIJER
Bas van OUDHEUSDEN
Contact
L.LaguardaSanch@tudelft.nl

Motivation

- Rocket propulsion systems are integral to global communication, scientific research and space exploration
- An essential component of the rocket engine is the nozzle, converting internal energy of combustion gases into propulsive force
- Maximum nozzle efficiency is achieved when discharge pressure matches ambient pressure (column shaped exhaust, Figure 1a)
- However, matched conditions are restricted to high altitudes, so during startup and initial climbing phase, the nozzle operates at over-expanded conditions (discharging at a lower pressure than ambient, Figure 1b)
- This operating condition is characterized by complex shock patterns, shock-turbulence interactions and boundary layer separation (Figure 1e), and results in unsteady asymmetric loads deforming the nozzle
- The situation is exacerbated when such a non-linear interaction between flow and structure self-amplifies (Figures 1c,d), degrading structural integrity and potentially yielding failure by fatigue

Objectives

Our goal is to improve our understanding of such dynamic processes (and thus allow more efficient nozzle designs) by means of numerical (this poster) and experimental investigations. We focus in particular on the dynamics of shock-wave/turbulent-boundary-layer interactions, a highly dynamic process responsible for the flow separation inside the nozzle.

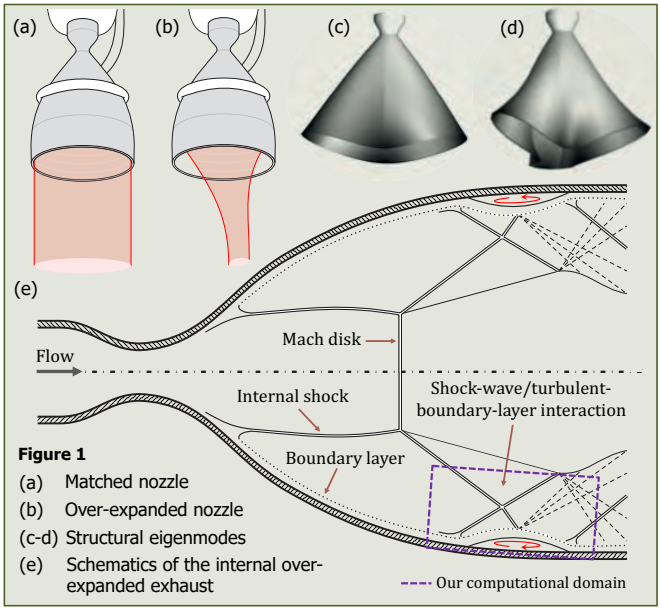

Figure 1
(a) Matched nozzle
(b) Over-expanded nozzle
(c-d) Structural eigenmodes
(e) Schematics of the internal over-expanded exhaust

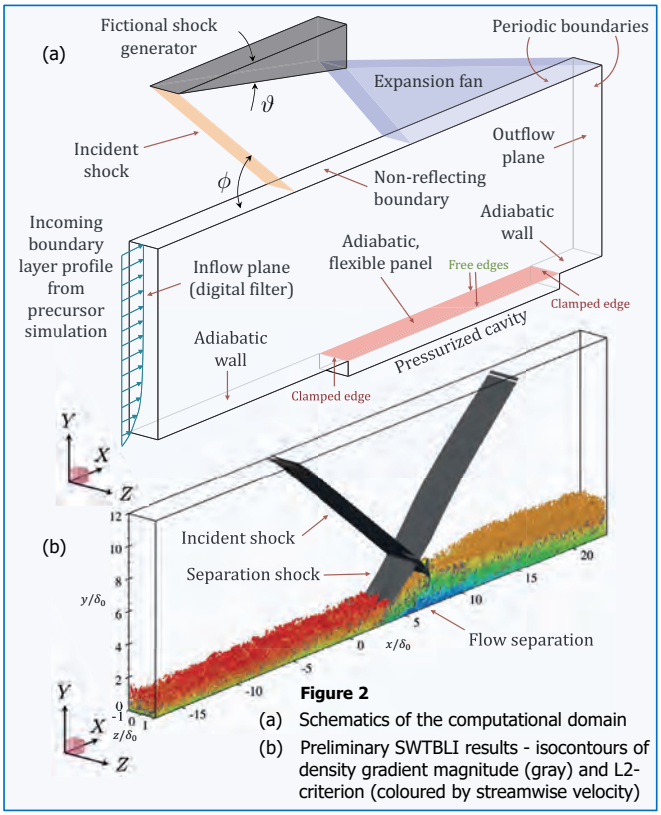

Figure 2
(a) Schematics of the computational domain
(b) Preliminary SWTBLI results - isocontours of density gradient magnitude (gray) and L2-criterion (coloured by streamwise velocity)

Methodology

Our numerical investigation is based on:

- A Large-Eddy Simulation (LES) of the baseline shock-wave/turbulent-boundary-layer interaction (SWTBLI) without deformable structures in order to fully characterize its dynamics (long integration times required for an accurate analysis of its characteristic low-frequency unsteadiness). Figure 2b shows the basic SWTBLI topology simulated on a coarse mesh,
- And a second LES simulation of a SWTBLI over a flexible panel (a sketch of the computational domain is shown in Figure 2a) in order to investigate the dynamic panel response and how the fluid-structure coupling modulates the characteristics of the baseline SWTBLI

Geometrical and aerodynamic parameters have been chosen to ensure experimental feasibility in TU Delft wind tunnels. A summary of the latter is presented in the following table:

M_0	p_0	T_0	U_0	ϑ	δ_0	Re_{δ_0}
2	3.5 bar	288.15 K	507 ms^{-1}	10.66°	5.2 mm	238×10^3

Simulations are conducted with our in-house solver INCA, operating on Cartesian grids and employing the cut-cell immersed boundary method to represent embedded geometries. To simulate the panel response, INCA is coupled to the finite-element based structural solver CalculiX following a loosely coupled approach by means of a Dirchlet-Neumann partitioning. Schematics of the algorithm is shown below, were flow imposes tractions on structure (Neumann BC) while the solid defines kinematic constraints (displacements and velocities, Dirichlet BC) on the flow:

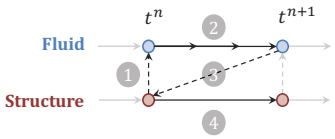

1. Transfer kinematic constraints
2. Advance fluid in time
3. Transfer tractions
4. Advance structure in time

- Hickel, S., Egerer, C. P., & Larsson, J. (2014). Subgrid-scale modeling for implicit large eddy simulation of compressible flows and shock-turbulence interaction. *Physics of Fluids*, *26* (10), 106101.
- Pasquariello, V., Hickel, S., & Adams, N. A. (2017). Unsteady effects of strong shock-wave/boundary-layer interaction at high Reynolds number. *Journal of Fluid Mechanics*, *823*, 617-657
- Spottswood, S. M. et al. (2019). Exploring the response of a thin, flexible panel to shock-turbulent boundary-layer interactions. *Journal of Sound and Vibration*, *443*, 74-89.

To take home

- This is work in progress on shock-wave/turbulent-boundary layer and fluid structure interaction representative of nozzle flows
- Currently performing high-fidelity LES simulations at previously unavailable (and computationally challenging) flow conditions
- We aim to obtain unprecedented agreement between simulations and experiments

Online Reduced-Order Model and its Application on Adjoint-based Mesh Adaptation for Large Eddy Simulation

Name: **Xiaodong Li**
Department: AWEP
Section: Aerodynamics
Promotor: Stefan Hickel
Daily Supervisor: Steven J. Hulshoff
X.Li-12@tudelft.nl

1. Why do we need mesh adaptation?

Large Eddy Simulation (**LES**) has the potential to deliver reliable flow predictions for cases involving mixing layers, large pressure gradients or high unsteadiness, which play an important role in the study of practical applications. It is not only crucial but also challenging for LES to define a computational mesh for obtaining an accurate solution with tractable computing cost. Constructing such meshes, however, usually involves experience and trials even for engineering experts. In order to tackle this difficulty, we pursue the use of **adjoint-based adaptive mesh refinement** (**AMR**) to make LES affordable for engineering problems. An AMR approach based on the adjoint method is shown below.

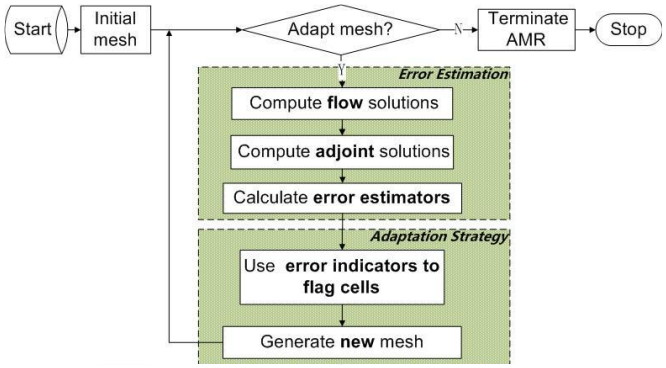

2. How to improve the efficiency for LES?

When applying adjoint-based AMR to unsteady problems, the flow problem is advanced forward in time while adjoint problem is solved backward in time. Due to the nonlinearity of Navier-Stokes equations, solving adjoint problem requires storage of the primal flow solutions. Since large averaging periods are needed for most statistical outputs of interest, the required storage quickly becomes prohibitive for practical problems. In order to make adjoint-based AMR affordable for LES, a reduced-order model (ROM) is introduced to represent the flow system in a low-order space. An enhanced online algorithm implemented by **incremental** singular value decomposition **(SVD)** enables the construction of **POD-based ROM** to be more efficient for complex problems without storing flow solutions, which is stated as follows:

Algorithm 1 Enhanced incremental weighted SVD

Input: $U = V\Sigma W^\intercal, V \in \mathbb{R}^{n\times k}, \Sigma \in \mathbb{R}^{k\times k}, W \in \mathbb{R}^{m\times k}$, $c \in \mathbb{R}^n, M \in \mathbb{R}^{n\times n}$, nModes

1: **Project a new column into an existing space:** $h = c - VV^\intercal Mc$, $p = (h^\intercal Mh)^{1/2}$, $j = h/p$.

2: **Neglect the small projection,** $Q = \begin{bmatrix} \Sigma & V^\intercal Mc \\ 0 & p \end{bmatrix}$.

3: **Apply standard SVD analysis on an updated matrix** $Q = V_Q \Sigma_Q W_Q^\intercal$:

$$[U \quad c] = [V \quad j]\, Q \begin{bmatrix} W & 0 \\ 0 & 1 \end{bmatrix}^\intercal = [V \quad j] V_Q \Sigma_Q \left(\begin{bmatrix} W & 0 \\ 0 & 1 \end{bmatrix} W_Q \right)^\intercal = V_u \Sigma_Q W_u^\intercal .$$

4: **Truncate on the selected number of POD Modes:**

$k = \text{nModes}, \quad \Sigma = \Sigma_{(1:\text{nModes},1:\text{nModes})}, \quad V = V_{u(:,1:\text{nModes})}, \quad W = W_{u(:,1:\text{nModes})}$.

5: **Neglect small singular values.**

6: **Re-orthogonalize the modes if necessary.**

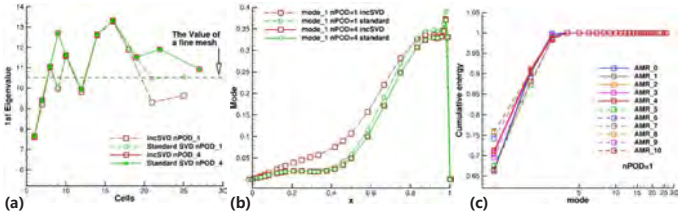

*The results, **(a)**Eigenvalue evolution and **(b)**Distribution of first POD mode at 10th AMR level, from online ROM (incSVD) are compared to those from standard ROM with one and four POD modes, respectively. **(c)** Cumulative energy during one-mode ROM-based AMR.*

3. Flow reconstruction from online ROM

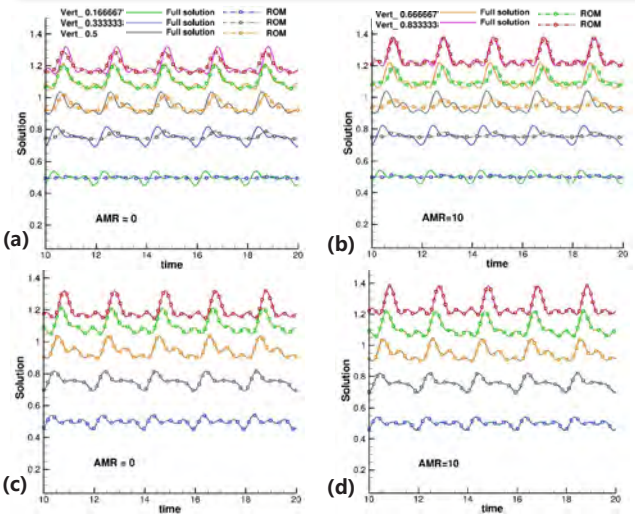

*The comparison between actual flow solutions and reconstructed solutions from online ROM when using one and four POD modes in two AMR levels, respectively. **(a)** One-mode ROM at first AMR level, **(b)** One-POD mode ROM at 10th AMR level, **(c)** our-mode ROM at first AMR level, **(d)** One-mode ROM at 10th AMR level.*

4. How about its performance?

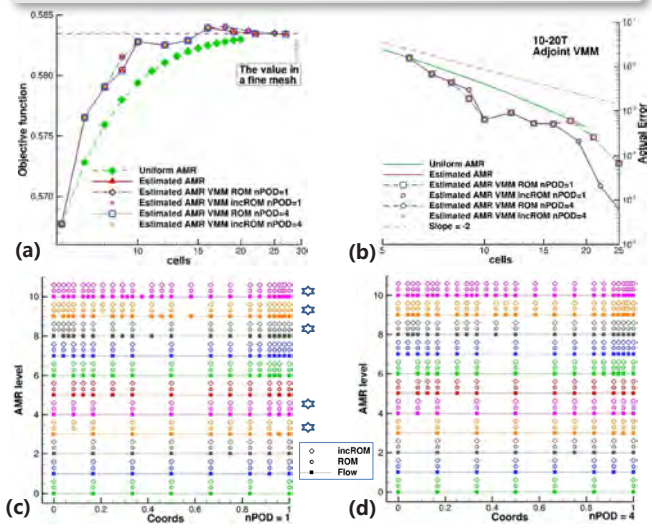

*Comparisons among uniform refinement and various AMR approaches based on full-order solutions, standard ROM, and online ROM(incROM), about **(a)** approximations of an output quantity, **(b)** the convergence of corresponding errors, **(c)** mesh refinement pattern with one mode, and **(d)** mesh refinement pattern with four modes.*

5. Conclusions and future work

- Adjoint-based AMR for LES is verified to improve the efficiency of computing the objective function.
- Using a truncated POD-based ROM does not affect the accuracy of the AMR in LES, which has been validated for a Burgers problem with a multi-frequency forcing term.
- The results imply that this new ROM-driven AMR will be useful for improving the efficiency of LES in more challenging problems.

Enabling Aeroelasticity Research with Large-Scale Volumetric PIV

Christoph Mertens
AWEP Department
Aerodynamics Section
Supervisors: Jurij Sodja
and Andrea Sciacchitano
Promotor: Bas van Oudheusden
C.Mertens@tudelft.nl

Motivation

The development of improved measurement techniques for wind tunnel experiments is primarily concerned with optical techniques, because they are non-intrusive and simplify the design of the experimental model. However, the investigation of dynamic aeroelasticity problems requires the application of multiple measurement systems, to measure the inertial and elastic forces as well as the aerodynamic force. This typically reduces the amount of information that can be extracted and results in complex and expensive setups. This research aims at providing a methodology to determine the three forces in a dynamic aeroelastic interaction based on measurements with a single system: Large-scale volumetric PIV.

Methodology

Combined measurements of the flow field and the structural deformation in wind tunnel experiments are performed with PIV using Helium-filled soap bubbles (HFSB) as flow tracer particles and fiducial markers painted on the model to track the structural motion. Both can be measured and analysed with the same measurement hardware and software. The experimental models in the two tests conducted so far are a pitching rigid wing and flexible wing subjected to gusts. The main research challenge is to determine the forces from the measurement results.

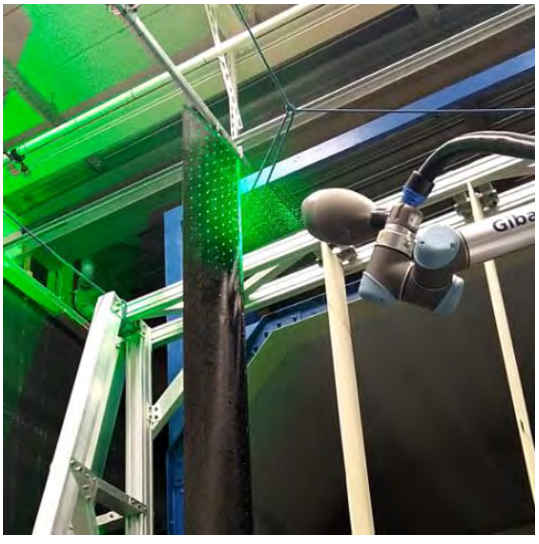

Figure 1: Combined measurements of HFSB flow tracers and structural markers with Robotic PIV on a flexible wing subjected to gusts in the OJF

Results

The unsteady lift force determined from PIV measurements on a pitching rigid wing is shown in figure 2 in comparison to reference measurements from installed pressure transducers. The structural load on a flexible wing subjected to a gust, reconstructed from the marker tracking data with a simple structural model, is shown in figure 3 in comparison to reference measurements with a force balance.

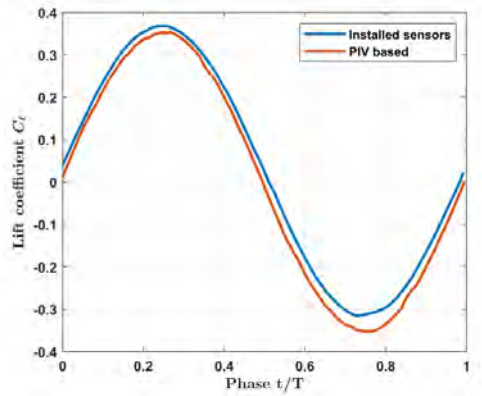

Figure 2: Aerodynamic force on a pitching wing

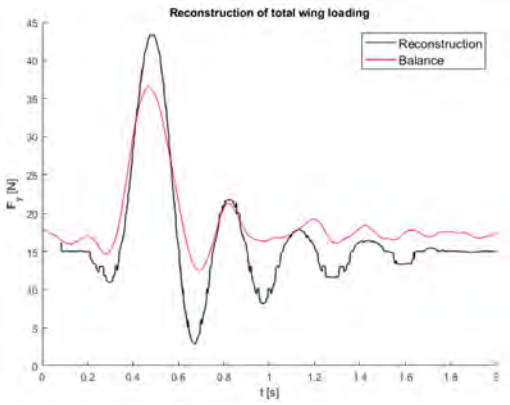

Figure 3: Structural force on a flexible wing during a gust encounter

Conclusions and Outlook

The determination of the aerodynamic force with PIV works well, the differences to the reference data can be explained with limitations in the experimental procedure. The determination of the structural force based on the marker tracking data currently only provides qualitative agreement. Improved structural models for the determination the forces will be tested in the future.

Plasma-based Control of Crossflow Instabilities

PhD candidate :Kaisheng
Department: AWEP
Section: Aerodynamics
Promotor: Marios Kotsonis
Co-promotor: Francesco Avallone
K.Peng@tudelft.nl

Motivation

The air flow around modern aircrafts with swept angle usually leads to the particular three-dimensional flow named crossflow. The resulting crossflow component generates primary CF (crossflow) instabilities and also distorts the mean flow. As the crossflow develops, the secondary instabilities are triggered, which eventually leads to turbulence and breakdown. So, if there is a way to suppress the cross flow, the transition can be delayed .

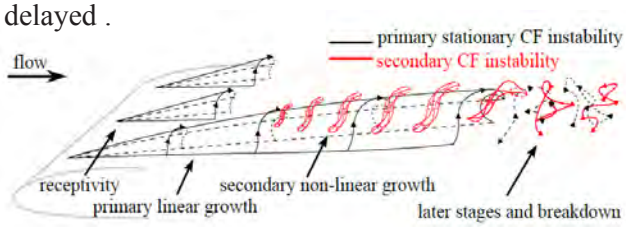

Plasma flow control

While working under gas ionization, the plasma actuator generates a body force that locally accelerates the surrounding fluid. Because they are fully electronic without moving parts and also flexible in changes of discharge characters, it shows promising application in flow control.

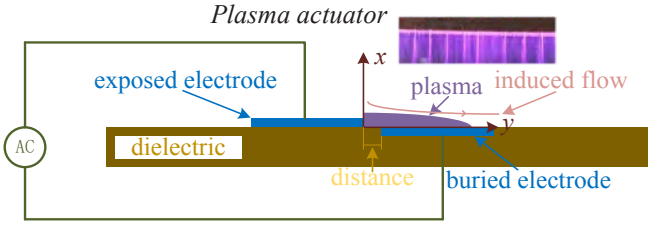

Problem in PA control

Though PA (plasma actuator) already shows a promising application on transitional flow control, there is still a considerable lack of knowledge about the effects of PA on CF. One important problem of plasma control is the low frequency disturbance. Even driven by high frequency AC power, they not only interact with CFI, but also introduce the unsteady disturbances to the receptivity

Traveling CF receptivity experiment

A carefully designed experiment is currently conducted, trying to understand the behaviors of different frequency disturbances introduced by PA.
A PA array is designed with each located at different chord. PA electrodes are sprayed with silver paint and a 500μm thick PET foil is used as the dielectric.
IR camera are used to give a general idea of transition movement visualization. As hotwire (HW) has a recording frequency more than 200KHz, it's possible to obtain the receptivity of different frequency disturbances.

PA array

Experiment set-up

Preliminary experiment results

IR results

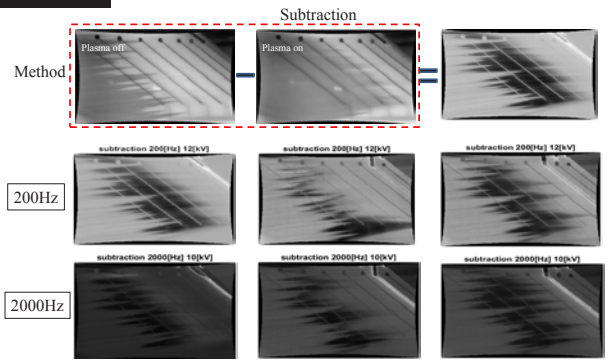

HW results (PA1)

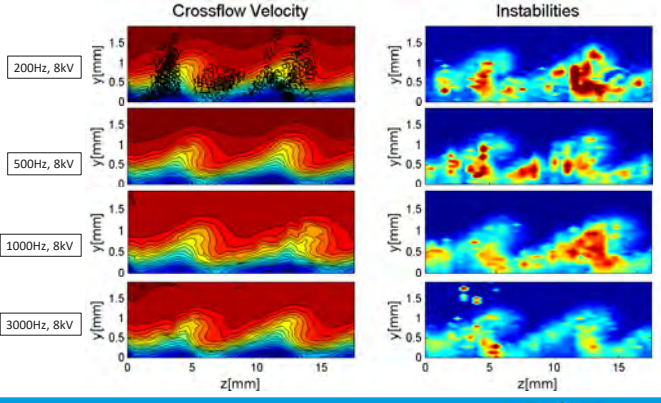

Impact of a Forward Facing Step Surface Irregularity on Swept-Wing Transition

Candidate: ir. Alberto Felipe Rius Vidales
Department: AWEP
Section: Aerodynamics
Daily Supervisor: Dr. Marios Kotsonis
Promotor: Prof.dr. Fulvio Scarano

Motivation

1920 2018

Environmental Impact

2018
Worldwide 4.3 billion passengers[1]
Total commercial aircraft[3] ≈ 20k

2037
Worlwide 8.2 billion passengers[2]
Total commercial aircraft[3] ≈ 45k

Reduce Skin-Friction drag by Laminar Flow Control[4]

Projected Market Growth

Limited by non-smooth surfaces due to aircraft skin joints[4]

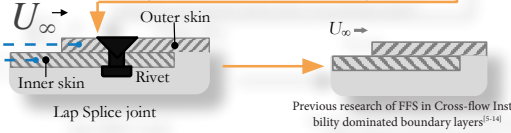

Previous research of FFS in Cross-flow Instability dominated boundary layers[5-14]

Schematic of a Lap-Splice panel joint and resulting conceptualised FFS surface irregularity.

Experimental Setup

- Experiments at TU Delft Low Turbulence Tunnel ($Tu/U_\infty \leq 0.03\%$)
- In-house design 45° swept-wing model (M3J). At test conditions ($\alpha = 3°$ and $Re_{cx} = 2.17 \times 10^6$), cross-flow is the dominant instability in the laminar-to-turbulent boundary-layer transition process [15].
- Three FFS (h_s= 346, 444 and 707 μm) tested using Polyethylene Terephthalate (PET) surface add-ons.
- One array of DREs (λ_z= 8 mm) was installed at the leading edge.
- Two IR cameras (A-> Wide-view , B-> Zoom-view) image the pressure side of the model.
- HWA (CTA) boundary-layer measurements acquired using an automated traversing system.
- The HWA measurements cover span-wise planes parallel to the leading edge (z) and along the corresponding local wall-normal direction (y) at several stream-wise stations (x/c_x).

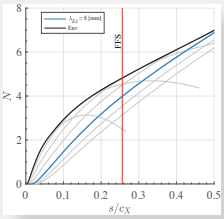

LST N-Factor Calculations indicating the N-Factor envelope and the DREs forced mode (λ_z= 8 mm) .

ID	h_s [μm]	σ_{h_s} [μm]	R_{k,h_s} [μm]	$x_{0,FFS}/c_x$	$\lambda_{z,D}$ [mm]	d_D [mm]	k_D[μm]	x_D/c_{x_D}
C-ST	-	-	0.20	-	-	-	-	-
C-TR	-	-	0.02	-	8	2	200	0.02
FFS-B	346	3	0.08	0.25	8	2	200	0.02
FFS-C	444	3	0.06	0.25	8	2	200	0.02
FFS-D	707	5	0.02	0.25	8	2	200	0.02

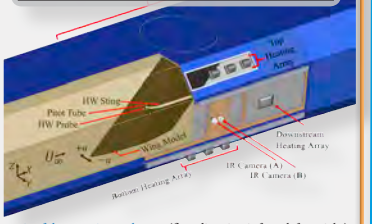

Schematic of the experimental setup (flow direction is from left to right)

Observations

HWA measurements for clean case(C-TR) at x/c_x = 0.25 (FFS Location)

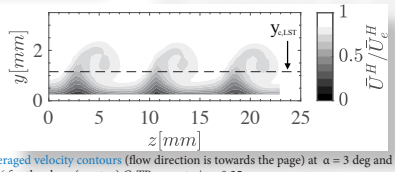

Time-averaged velocity contours (flow direction is towards the page) at α = 3 deg and Re_{cx} = 2.17×10^6 for the clean (no step) C-TR case at x/c_x = 0.25

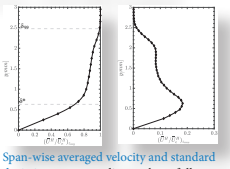

Span-wise averaged velocity and standard deviation corresponding to three-full stationary vortices.

HWA planes and IR measurements for clean and FFS cases

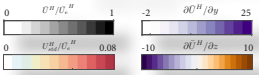

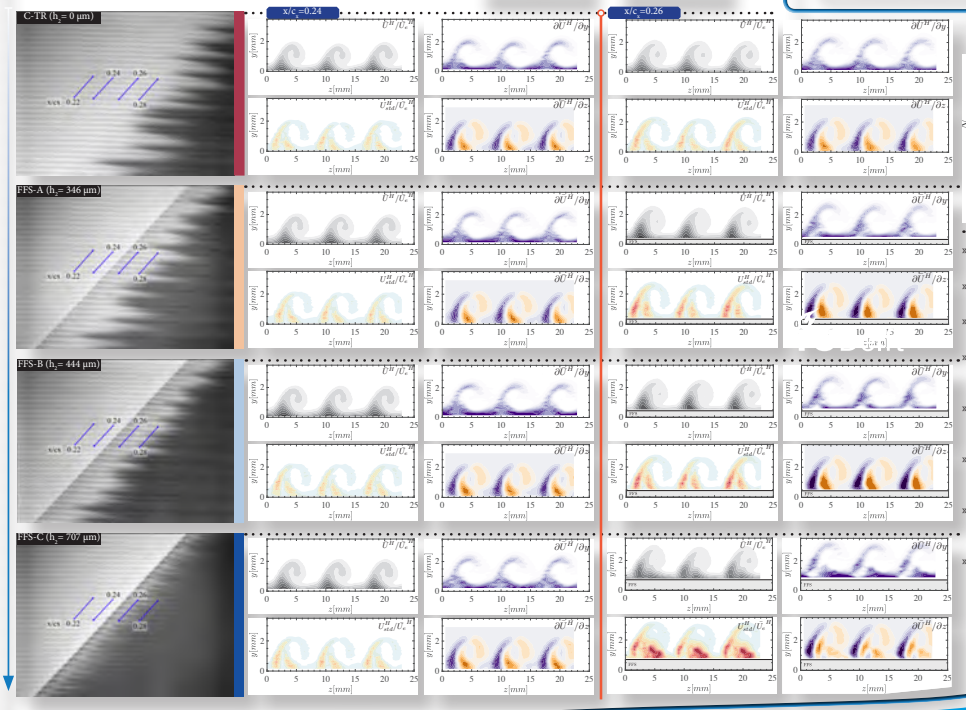

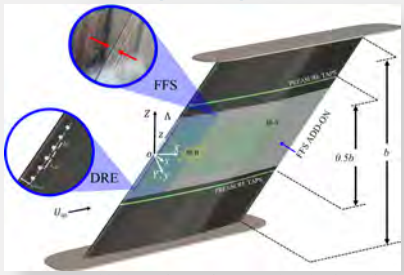

M3J Swept wing model diagram, showing the un-swept (X,Y,Z) and swept (x,y,z) coordinate systems, FFS add-on, location of DREs and pressure taps.

N-Factor (HWA) calculations based on maximum of the mode shape profiles, the analysis considers three CFVs.

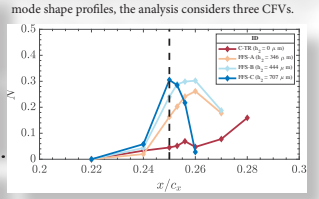

- A subcritical behavior is observed for FFS-A (h_s= 346 μm) and FFS-B (h_s= 444 μm).
- A supercritical behavior is observed for the FFS-C (h_s= 707 μm) as BL transition occurs at the step location.
- The LST estimated cross-flow vortex core-height[8] ($y_{c,LST}$) provides a first-order size estimation of the CFVs.
- In this study, using the cross-flow core-height as criteria for the FFS interaction with the CFVs results in an overestimation of the allowable step height.
- As the FFS height increases, there is a stronger stream-wise growth of the CFI mode, which leads to an earlier saturation.
- Downstream of the FFS there is an increase in the velocity fluctuation levels at the locations of type I and III modes. This is not evident for the type II mode.
- IR measurements for FFS-C (h_s= 707 μm) indicate that a series of "fork-type" structures are present in the vicinity of the FFS which require further study.
- To fully understand the interaction between the FFS and CFVs, more in-depth studies are required.

REFERENCES

AWEP

TU Delft EMBRAER

Multi-Δt 3D-PTV based on Reynolds decomposition

PhD Candidate: Edoardo Saredi
Department: Aerospace Engineering
Section: Aerodynamics
Co-promotor: Dr. A. Sciacchitano
Promotor: Dr. F. Scarano
Contact: e.saredi@tudelft.nl

Motivation:

The advent of Robotic Volumetric PIV, together with the usage of Helium Filled Soap Bubbles, have opened the possibility to perform PIV measurement within volumes that have reached sizes of order of m^3. This achievement permits to envisage its usage for industrial PIV.

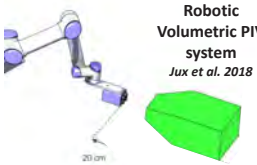

Robotic Volumetric PIV system
Jux et al. 2018

State-Of-The-Art methodology

Time-Resolved measurement
+
Shake-The-Box PTV algorithm

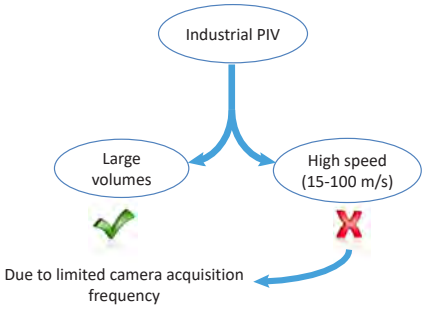

To overcome the limitation imposed by the limited camera maximum acquisition frequency, a new methodology has been proposed:

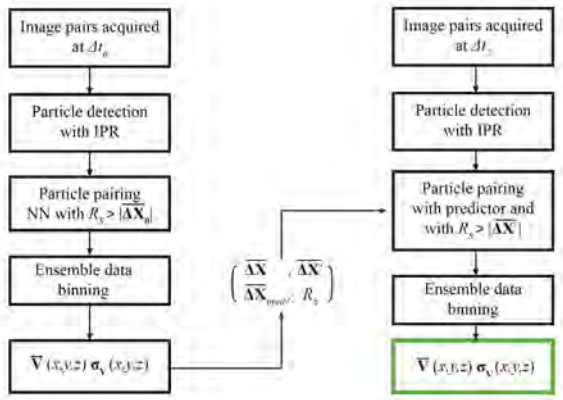

A set of two double-pulse double frame acquisitions is acquired, one with low pulse-separation time Δt_1 and one with a higher pulse separation time Δt_2. From the first acquisition, an estimator of the tracers velocity can be obtained invoking the Reynolds decomposition of the flow velocity:

$$\boldsymbol{U} = \overline{\boldsymbol{u}} + \boldsymbol{u}'$$

The information obtained is then used to increase the percentage of percentage of correct pairing of the second acquisition:

- $\overline{\boldsymbol{u}}$ is used to predict the expected particle position
- $\boldsymbol{u}'$ is used to evaluate the adequate radius of search.

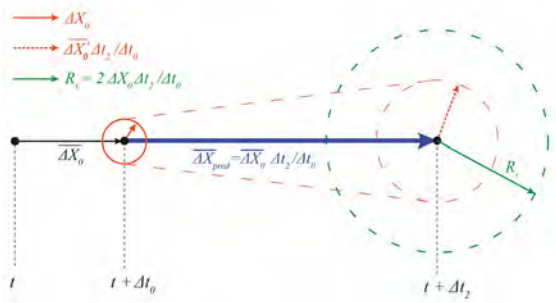

The methodology has been applied to several test cases.

The results here presented show the C-pillar vortices created by an Ahmed body with a back surface with slant angle 25° .

The comparison is made between STB, single-step (Δt = Δt0) and two multi-step analyses: Δt2 = Δt0 and Δt2 = 10·Δt0 respectively. The C-pillars vortices visualization using the single-step analysis suffers from random fluctuations appearing in the entire measurement domain. The multi-step analysis at shortest time separation exhibits some noise reduction, ascribed to the reduction of incorrect pairings when a displacement predictor and a smaller search radius are used. When the pulse separation is extended, with Δt2 = 10·Δt0, noisy fluctuations are considerably attenuated and a more regular vorticity iso-surface is obtained, in better agreement with the STB analysis.

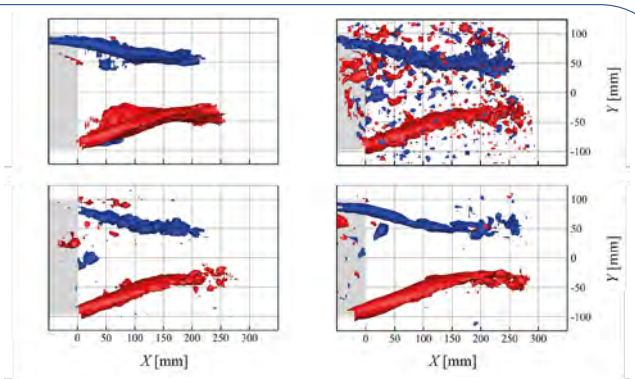

Iso-surface of $\overline{\omega}_x = \pm 250$ Hz (blue: positive, red: negative) in the object reference frame. (top-left) STB (top-right) single-step at Δt_0 (bottom-left) multi-step with $\Delta t_2 = \Delta t_0$ (bottom-right) multi-step with $\Delta t_2 = 10{\cdot}\Delta t_0$.

AWEP

Ring of Fire

On-site aerodynamic drag measurements

Alexander Spoelstra
AWEP
Aerodynamics
Dr. Andrea Sciacchitano
Prof. Dr. Fulvio Scarano
a.m.c.m.g.spoelstra@tudelft.nl

1 2 3 4

Background & motivation

Most experimental research in sport aerodynamics is performed in wind tunnels. Despite the fact that the situation to be simulated (e.g. a cycling or running athlete) is dynamic, the problem is often simplified reverting to a stationary scaled model to match the constraints posed by the wind tunnel size and the measurement techniques used for the aerodynamic analysis.
This project realizes a measurement apparatus, referred with the name "Ring of Fire" (RoF), that quantifies the aerodynamic drag of full-scale athletes during sport action. It uses large-scale Particle Image Velocimetry (PIV) to visualize the flow field and applies an air flow momentum balance to estimate the drag of the moving athlete. The measurement system was shown to provide the drag of an individual cyclist during sport action and returned a quantitative visualization of the flow field in the wake [1]. However, in most race events, athletes ride in close proximity to each other, thus benefitting from a significant reduction in aerodynamic drag [2]. For this reason, in this work, the Ring of Fire system is deployed to evaluate the effects of cyclists' position and their relative size on the aerodynamic drag.

Measurement system

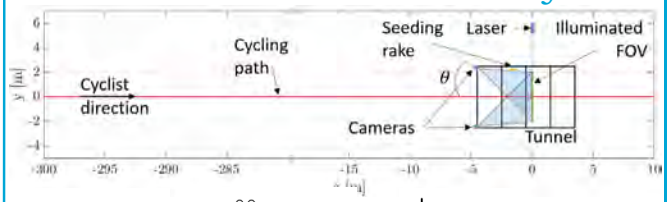

- Photron Fast CAM SA1
- θ = 50°
- 1024 x 1024 pixels
- 20µm pixel pitch
- 35mm objectives

- Helium filled soap bubbles
- Diameter 0.3 mm
- Time response 10 µs

- Quantronix Darwin Duo
- Nd:YLF (2 × 25 mJ at 1 kHz)
- Acquisition frequency 1kHz

Test parameters

Three athletes were asked to perform a series of individual test as well as different drafting tests. Throughout the drafting tests, the sequence of the athletes and the separation between them was varied. The longitudinal and lateral separations varied respectively between 0.35 m and 0.85 m and between 0 m and ±0.20 m.

Table 1. Subjects' anthropometric characteristics and individual drag area.

Subject	S1	M1	L1
Height [m]	1.75	1.85	1.92
Mass [kg]	60	70	69
Frontal area [m²]	0.360	0.337	0.316
Drag area [m²]	0.211 ± 0.011	0.177 ± 0.004	0.201 ± 0.005

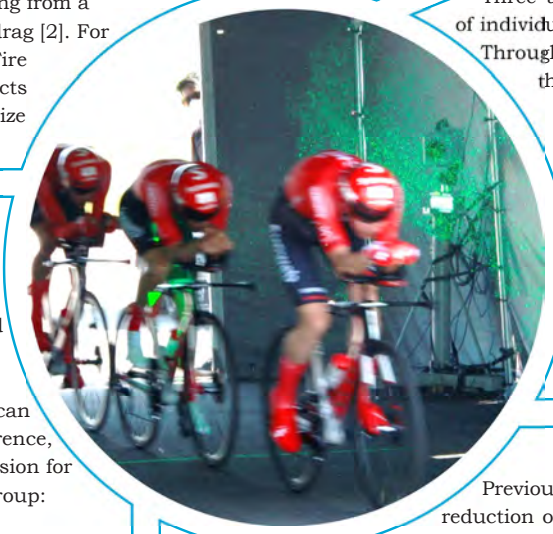

Working principle

The drag evaluation through the RoF follows that of the previous work [1]. The drag of a group can be determined by invoking the conservation of momentum across surfaces S_1 and S_3. The momentum and velocity changes can be written in the cyclists frame of reference, enabling to derive the following expression for the instantaneous drag of the entire group:

$$D(t) = \rho \left[\iint_{S_1} (U_{env,1} - U_C)^2 dS - \iint_{S_3} (U_{wake,2} - U_C)^2 dS \right] + \iint_{S_1} p dS - \iint_{S_3} p dS$$

Momentum term — Pressure term

The drag of the individual cyclists can be calculated in the same way, namely by enforcing the conservation of momentum across surfaces S_1 and S_2 for the leading cyclist, and across surfaces S_2 and S_3 for the drafting cyclist.

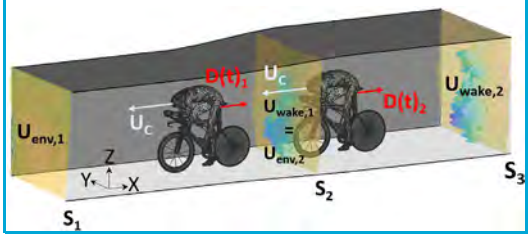

Results

Previous investigations have mentioned a drag reduction of the lead cyclist of 3% - 5% [3]. The accuracy of the RoF drag measurements is not sufficient to measure these kind of differences. Therefore the analysis of drag reductions solely focuses on the drafting cyclists. Within the measured spectrum, the savings for the drafting cyclist range from 27% to 66%. The aerodynamic advantage decreases as lateral and longitudinal separation between riders is increased, where the lateral distance is found to be more relevant. Furthermore, it is observed that the larger the isolated drag area of the leading cyclist is, the larger the benefit for the drafting cyclist.

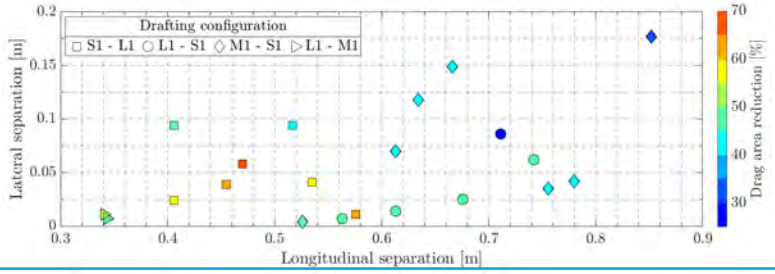

[1] Spoelstra, A., de Martino Norante, L., Terra, W., Sciacchitano, A., & Scarano, F. (2019). On-site cycling drag analysis with the Ring of Fire. *Experiments in Fluids, 60*(6), 90. doi:10.1007/s00348-019-2737-y
[2] Barry, N., Burton, D., Sheridan, J., Thompson, M., & Brown, N. A. T. (2015). Aerodynamic drag interactions between cyclists in a team pursuit. Sports Engineering, 18(2), 93-103. doi:10.1007/s12283-015-0172-8
[3] Blocken, B., Toparlar, Y., van Druenen, T., & Andrianne, T. (2018). Aerodynamic drag in cycling team time trials. Journal of Wind Engineering and Industrial Aerodynamics, 182, 128-145. doi:10.1016/j.jweia.2018.09.015

TU Delft

TEAM Sunweb · LaVision · WABCO · sportzone · NWO

AWEP

Cyclist near-wake Reynolds number effects & drag crisis distribution

Wouter Terra
AWEP Department
Aerodynamics Section
Supervisor Dr. A.Sciacchitano
Promotor Prof. Dr. F. Scarano
w.terra@tudelft.nl

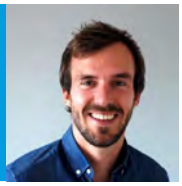

Motivation

Reduction of the aerodynamic drag of elite cyclists improves their performance. This may be achieved, based on the principle of the **drag crisis** of a bluff body, applying textured fabrics on the different areas (legs, arms etc.) of the rider's suit. To decide for the best fabric, the local **critical Reynolds number Re_c** on the bare athlete's body needs to be determined, which is the point of minimum drag coefficient.

Conventionally, Re_c is estimated from measurements on isolated cylinders in cross flow. Cyclist flow, however, is more complex and 3D and the critical flow conditions is expected to be distorted by, among others, limb junctions and wake interactions. This work aims to determine Re_c from **measurements on a cyclist** mannequin to establish a better understanding what governs the cyclist drag crisis.

Experiments

- Open Jet facility wind tunnel of TU Delft
- Full-scale, polished surface cyclist replica installed on time-trial bike
- Robotic volumetric Particle Image Velocimetry (PIV) measuring flow field around large/complex geometry
- Experiments repeated at U_∞ = [5 10 15 20 25] m/s to determine local drag crisis

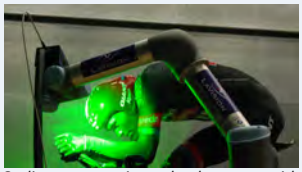

Cyclist mannequin and robot arm with PIV system imaging and illuminating Helium-filled soap bubble seeding

Conclusions

- Cyclist near-wake governed by streamwise vortices and wake interactions (in addition to limb taper)
- Minimum aerodynamic drag condition evaluated from variation of local wake width
- Critical velocity distribution obtained along upper arm and leg
- Results serve to improve low-drag skinsuits in the future

Drag crisis of a cylinder in cross flow (figure reproduced from Achenbach and Heinecke 1980).

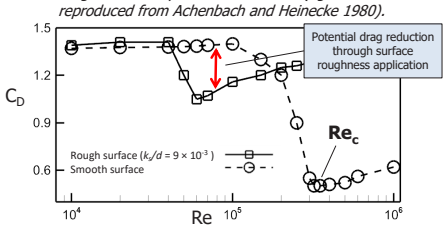

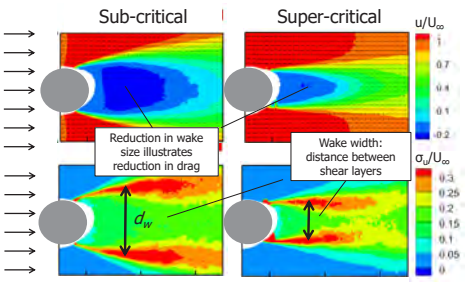

Mean non-dimensional streamwise velocity (top) and turbulence (bottom) across a cylinder

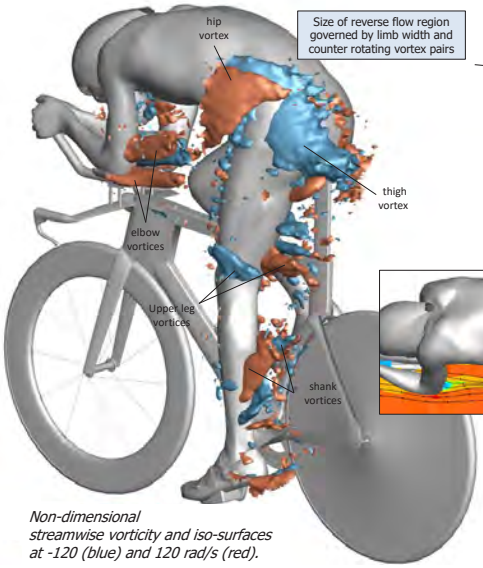

Non-dimensional streamwise vorticity and iso-surfaces at -120 (blue) and 120 rad/s (red).

Mean streamwise velocity (left) and fluctuations (right)

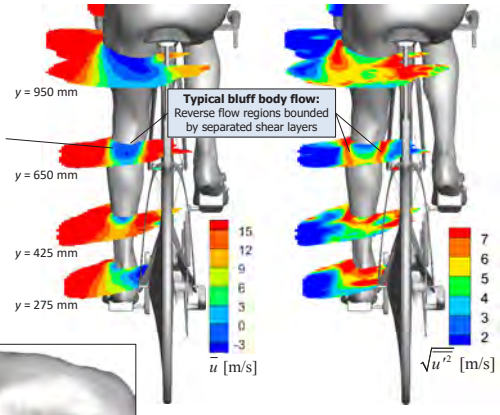

*Non-dimensional streamwise velocity downstream of the **leg** (top; horizontal planes) and **arm** (bottom; vertical plane)*

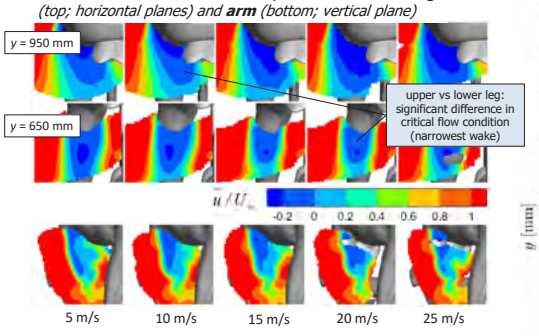

*Distribution of **wake width** (left) and **critical velocity** (right)*

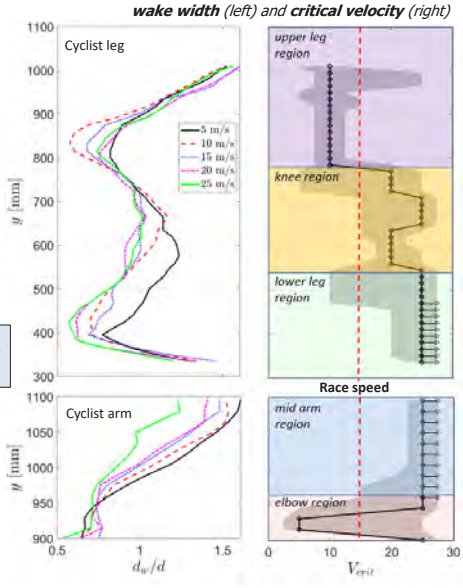

Methods

The drag coefficient of a cyclist limb section cannot be measured by a force balance. Instead, the **wake width** can be evaluated locally and can also be related to C_D (along the critical flow regime; e.g. Rodriguez et al. 2015):

$$\frac{C_{D,1}}{C_{D,2}} = \alpha_d \frac{d_{w,1}}{d_{w,1}}$$

where $\alpha_d \sim 2$ is an empirical constant, d_w is the wake width and subscript 1 and 2 refer to sub- and super-critical Reynolds number, respectively.

Instead of the critical Reynolds number, the **critical velocity, V_c** is used in this work, which allows a direct comparison to the race speed. The critical velocity then corresponds to U_∞ with the smallest wake width.

Terra W., Sciacchitano A., Scarano F. (2020) Cyclist Reynolds number effects and drag crisis distribution. J Wind Eng Ind Aerodyn (under review)

Hybrid mimetic spectral element method

With applications towards CFD

Yi Zhang
AWEP
Aerodynamics
Daily supervisor: Marc Gerritsma
Promotor: Stefan Hickel
y.zhang-14@tudelft.nl

Introduction & motivation & objective

Mimetic methods are numerical methods that aim to preserve fundamental properties of the continuous problems, like conservation laws (for example, conservation of mass in fluid), at the discrete level, and the mimetic spectral element method (MSEM) is a novel arbitrary order mimetic method. The key feature of the mimetic spectral element method is that it uses basis functions satisfying de Rham complex,

$$\mathbb{R} \hookrightarrow H^1(\Omega) \xrightarrow{\nabla} H(\mathrm{curl};\Omega) \xrightarrow{\nabla\times} H(\mathrm{div};\Omega) \xrightarrow{\nabla\cdot} L^2(\Omega) \longrightarrow 0,$$

and its dual complex,

$$0 \longleftarrow H^1(\Omega) \xleftarrow{\nabla\cdot^*} H(\mathrm{curl};\Omega) \xleftarrow{\nabla\times^*} H(\mathrm{div};\Omega) \xleftarrow{\nabla^*} L^2(\Omega) \hookleftarrow \mathbb{R}.$$

However, mixed formulation together with high order methods generally lead to large and full systems. An effective way to overcome this drawback is to use the hybrid finite element method, a domain decomposition method which breaks up the problem into smaller sub-problems.

⊛ Poisson problem

A Lagrangian formulation of the Poisson problem is given as:

$$\mathcal{L}(\boldsymbol{u},\phi;f) = \frac{1}{2}\langle \boldsymbol{u},\boldsymbol{u}\rangle + \langle \phi, (\mathrm{div}\,\boldsymbol{u} + f)\rangle - \left\langle \hat{\phi}, \boldsymbol{u}\cdot\boldsymbol{n}\right\rangle,$$

where $\boldsymbol{u} \in H(\mathrm{div};\Omega)$, $\phi \in \left[L^2(\Omega)\right]'$, $f \in L^2(\Omega)$, $\hat{\phi} \in H^{1/2}_{00}(\Gamma_D)$. The corresponding weak form is expressed as: Find $\boldsymbol{u} \in H(\mathrm{div};\Omega)$ and $\phi \in \left[L^2(\Omega)\right]'$ such that

$$\begin{cases} \langle \boldsymbol{u},\boldsymbol{v}\rangle + \langle \phi, \mathrm{div}\,\boldsymbol{v}\rangle = \left\langle \hat{\phi}, \boldsymbol{v}\cdot\boldsymbol{n}\right\rangle & \forall \boldsymbol{v} \in H(\mathrm{div};\Omega), \\ \langle \varphi, \mathrm{div}\,\boldsymbol{u}\rangle = -\langle \varphi, f\rangle & \forall \varphi \in \left[L^2(\Omega)\right]', \end{cases}$$

We can hybridize this problem, which gives the hybrid weak formulation: For $f \in L^2(\Omega_k)$ and $\hat{\phi} \in H^{1/2}_{00}(\Gamma_{kD})$, find $\boldsymbol{u} \in H(\mathrm{div};\Omega_k)$, $\phi \in \left[L^2(\Omega_k)\right]'$ and $q \in H^{1/2}_{00}(\partial\Omega_k\backslash\Gamma_{kD})$, such that

$$\begin{cases} \langle \boldsymbol{u},\boldsymbol{v}\rangle + \langle \phi, \mathrm{div}\,\boldsymbol{v}\rangle - \langle q, \boldsymbol{v}\cdot\boldsymbol{n}_k\rangle = \left\langle \hat{\phi}, \boldsymbol{v}\cdot\boldsymbol{n}_k\right\rangle & \forall \boldsymbol{v} \in H(\mathrm{div};\Omega_k), \\ \langle \varphi, \mathrm{div}\,\boldsymbol{u}\rangle = -\langle \varphi, f\rangle & \forall \varphi \in \left[L^2(\Omega_k)\right]', \\ -\langle p, \boldsymbol{u}\cdot\boldsymbol{n}_k\rangle = 0 & \forall p \in H^{1/2}_{00}(\partial\Omega_k\backslash\Gamma_{kD}). \end{cases}$$

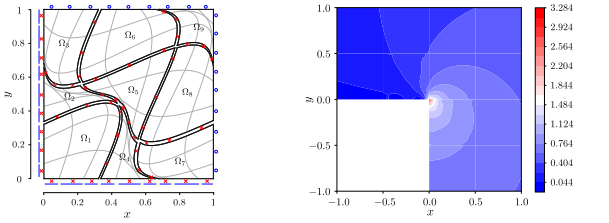

Figure 1: Examples of results. Left: An example of the division of a domain into subdomains and the connection with Lagrange multipliers. Right: The well capture of the singularity in a potential flow test case.

⊛ Linear Elasticity

A hybrid variational formulation for the linear elasticity problem is expressed as

$$\mathcal{L}(\boldsymbol{\sigma},\boldsymbol{u},\boldsymbol{\omega};\boldsymbol{f},\widehat{\boldsymbol{u}}) = \sum_m \left[\frac{1}{2}(\boldsymbol{\sigma}, C\boldsymbol{\sigma})_{\Omega_m} - \langle \widehat{\boldsymbol{u}}, \boldsymbol{t}\rangle_{\partial\Omega_m\cap\Gamma_{\boldsymbol{u}}} + (\boldsymbol{u}, D\boldsymbol{\sigma} + \boldsymbol{f})_{\Omega_m} - (\boldsymbol{\omega}, R\boldsymbol{\sigma})_{\Omega_m}\right] - \sum_{ij}\langle \boldsymbol{\lambda}, \boldsymbol{t}_i + \boldsymbol{t}_j\rangle_{\Gamma_{ij}},$$

which will give rise to the following weak formulation:

$$(\overline{\boldsymbol{\sigma}}, C\boldsymbol{\sigma})_{\Omega_m} + (\boldsymbol{u}, D\overline{\boldsymbol{\sigma}})_{\Omega_m} - (\boldsymbol{\omega}, R\overline{\boldsymbol{\sigma}})_{\Omega_m} - \sum_n \langle \boldsymbol{\lambda}, \overline{\boldsymbol{t}}\rangle_{\Gamma_{mn}} = \langle \widehat{\boldsymbol{u}}, \overline{\boldsymbol{t}}\rangle_{\partial\Omega_m\cap\Gamma_{\boldsymbol{u}}}, \forall\, \overline{\boldsymbol{\sigma}} \in [H_0(\mathrm{div};\Omega_m;\partial\Omega_m\cap\Gamma_{\boldsymbol{t}})]^3,$$

$$\begin{aligned} &(\overline{\boldsymbol{u}}, D\boldsymbol{\sigma})_{\Omega_m} = -(\overline{\boldsymbol{u}}, \boldsymbol{f})_{\Omega_m}, && \forall\, \overline{\boldsymbol{u}} \in \left[L^2(\Omega_m)\right]^3, \\ &-(\overline{\boldsymbol{\omega}}, R\boldsymbol{\sigma})_{\Omega_m} = 0, && \forall\, \overline{\boldsymbol{\omega}} \in \left[L^2(\Omega_m)\right]^3, \\ &-\langle \overline{\boldsymbol{\lambda}}, \boldsymbol{t}_i + \boldsymbol{t}_j\rangle_{\Gamma_{ij}} = 0, && \forall\, \overline{\boldsymbol{\lambda}} \in \left[H^{1/2}_{00}(\Gamma_{ij})\right]^3. \end{aligned}$$

We test the our hybrid MSEM using an arch bridge which has a crack developing from the bridge bottom at the middle surface. The material properties E and ν are set to $E = 400$ and $\nu = 0.3$. The two side walls are considered as fixed walls. A uniform load $\widehat{\boldsymbol{t}} = \{\widehat{\sigma}_{xx}\ \widehat{\sigma}_{xy}\ \widehat{\sigma}_{xz}\}^{\mathsf{T}} = \{\widehat{\sigma}_{xx}\ 0\ 0\}^{\mathsf{T}}$, where $\widehat{\sigma}_{xx} = -\sin(\frac{\pi y}{4})e^{-(y-2)^2}$, is applied on the bridge floor.

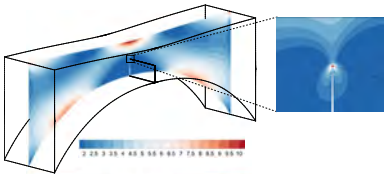

Figure 2: A test case that simulates a cracked bridge. At the crack root, extreme stress is observed.

⊛ Stokes problem

We consider the a Lagrangian for Stokes problem in velocity-vorticity-pressure formulation:

$$\mathcal{L}(\boldsymbol{\omega},\boldsymbol{u},p;\boldsymbol{f},g,\widehat{\boldsymbol{u}}\times\boldsymbol{n},\widehat{p}) = \frac{1}{2}(\boldsymbol{\omega},\boldsymbol{\omega})_\Omega - \langle \boldsymbol{\omega}, \widehat{\boldsymbol{u}}\times\boldsymbol{n}\rangle_{\Gamma_{\boldsymbol{u}\times\boldsymbol{n}}} - (\boldsymbol{u}, \nabla\times\boldsymbol{\omega} - \boldsymbol{f})_\Omega + (p, \nabla\cdot\boldsymbol{u})_\Omega - \langle \widehat{p}, \boldsymbol{u}\cdot\boldsymbol{n}\rangle_{\Gamma_p},$$

where $\boldsymbol{\omega} \in H_0(\mathrm{curl},\Omega;\Gamma_{\boldsymbol{\omega}})$, $\boldsymbol{u} \in H_0(\mathrm{div},\Omega;\Gamma_{\boldsymbol{u}\cdot\boldsymbol{n}})$, $p \in L^2(\Omega)$, and $f \in [L^2(\Omega)]^3$, $g \in L^2(\Omega)$, $\widehat{\boldsymbol{u}}\times\boldsymbol{n} \in TH^{1/2}_{00}(\Gamma_{\boldsymbol{u}\times\boldsymbol{n}})$, $\widehat{p} \in H^{1/2}_{00}(\Gamma_p)$ are given. Note that the trace of $\boldsymbol{\omega} \in H_0(\mathrm{curl},\Omega;\Gamma_{\boldsymbol{\omega}})$ is in $\left[TH^{1/2}_{00}(\Gamma_{\boldsymbol{u}\times\boldsymbol{n}})\right]'$ and the trace of $\boldsymbol{u} \in H_0(\mathrm{div},\Omega;\Gamma_{\boldsymbol{u}\cdot\boldsymbol{n}})$ is in $\left[H^{1/2}_{00}(\Gamma_p)\right]'$. Variations with respect to $\boldsymbol{\omega}$ gives rise to

$$(\boldsymbol{\omega},\overline{\boldsymbol{\omega}})_\Omega - (\boldsymbol{u}, \nabla\times\overline{\boldsymbol{\omega}})_\Omega = \langle \overline{\boldsymbol{\omega}}, \widehat{\boldsymbol{u}}\times\boldsymbol{n}\rangle_{\Gamma_{\boldsymbol{u}\times\boldsymbol{n}}}, \quad \forall \overline{\boldsymbol{\omega}} \in H_0(\mathrm{curl},\Omega;\Gamma_{\boldsymbol{\omega}}).$$

Variations with respect to $\boldsymbol{u}$ gives rise to

$$(\overline{\boldsymbol{u}}, \nabla\times\boldsymbol{\omega})_\Omega - (p, \nabla\cdot\overline{\boldsymbol{u}})_\Omega = (\overline{\boldsymbol{u}}, \boldsymbol{f})_\Omega - \langle \widehat{p}, \overline{\boldsymbol{u}}\cdot\boldsymbol{n}\rangle_{\Gamma_p}, \quad \forall \overline{\boldsymbol{u}} \in H_0(\mathrm{div},\Omega;\Gamma_{\boldsymbol{u}\cdot\boldsymbol{n}}).$$

Variations with respect to p gives rise to $(\overline{p}, \nabla\cdot\boldsymbol{u})_\Omega = 0, \forall \overline{p} \in L^2(\Omega)$.

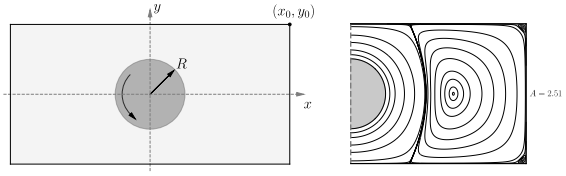

Figure 3: An example result: Creepy flow in a rectangle box with a rotating cylinder.

⊛ Navier-Stokes equations (NSE)

For 3D NSE, we aim to conserve mass, kinetic energy and helicity using the following scheme.

System 1 Assume $\boldsymbol{\omega}_2 \in H(\mathrm{div};\Omega)$ is a weak vorticity solution of the NSE and, therefore, is known. Given $\boldsymbol{f} \in \left[L^2(\Omega)\right]^3$, if $\boldsymbol{\omega}_1, \boldsymbol{u}_2, P_3 \in H(\mathrm{curl};\Omega)\times H(\mathrm{div};\Omega)\times L^2(\Omega)$ satisfy

$$\begin{aligned} &\left(\frac{\partial \boldsymbol{u}_2}{\partial t}, \boldsymbol{\epsilon}_2\right) + (\boldsymbol{\omega}_2\times\boldsymbol{u}_2, \boldsymbol{\epsilon}_2) + \nu(\nabla\times\boldsymbol{\omega}_1, \boldsymbol{\epsilon}_2) - (P_3, \nabla\cdot\boldsymbol{\epsilon}_2) = (\boldsymbol{f}, \boldsymbol{\epsilon}_2), && \forall \boldsymbol{\epsilon}_2 \in H(\mathrm{div};\Omega), \\ &-(\boldsymbol{u}_2, \nabla\times\boldsymbol{\epsilon}_1) + (\boldsymbol{\omega}_1, \boldsymbol{\epsilon}_1) = 0, && \forall \boldsymbol{\epsilon}_1 \in H(\mathrm{curl};\Omega), \\ &(\nabla\cdot\boldsymbol{u}_2, \epsilon_3) = 0, && \forall \epsilon_3 \in L^2(\Omega), \end{aligned}$$

then $\boldsymbol{\omega}_1, \boldsymbol{u}_2, P_3$ weakly solve the NSE.

System 2 Assume $\boldsymbol{\omega}_1 \in H(\mathrm{curl};\Omega)$ is a weak vorticity solution of the NSE and, therefore, is known. Given $\boldsymbol{f} \in \left[L^2(\Omega)\right]^3$, if $P_0, \boldsymbol{u}_1, \boldsymbol{\omega}_2 \in H^1(\Omega)\times H(\mathrm{curl};\Omega)\times H(\mathrm{div};\Omega)$ satisfy

$$\begin{aligned} &\left(\frac{\partial \boldsymbol{u}_1}{\partial t}, \boldsymbol{\epsilon}_1\right) + (\boldsymbol{\omega}_1\times\boldsymbol{u}_1, \boldsymbol{\epsilon}_1) + \nu(\boldsymbol{\omega}_2, \nabla\times\boldsymbol{\epsilon}_1) + (\nabla P_0, \boldsymbol{\epsilon}_1) = (\boldsymbol{f}, \boldsymbol{\epsilon}_1), && \forall \boldsymbol{\epsilon}_1 \in H(\mathrm{curl};\Omega), \\ &-(\nabla\times\boldsymbol{u}_1, \boldsymbol{\epsilon}_2) + (\boldsymbol{\omega}_2, \boldsymbol{\epsilon}_2) = 0, && \forall \boldsymbol{\epsilon}_2 \in H(\mathrm{div};\Omega), \\ &-(\boldsymbol{u}_1, \nabla\epsilon_0) = 0, && \forall \epsilon_0 \in H^1(\Omega), \end{aligned}$$

then $P_0, \boldsymbol{u}_1, \boldsymbol{\omega}_2$ weakly solve the NSE. Combining above two weak formulations gives a huge system that satisfies

- Mass conservation for $\boldsymbol{u}_2$, $\nabla\cdot\boldsymbol{u}_2 = 0$,
- $\boldsymbol{\omega}_2 = \nabla\times\boldsymbol{u}_1$. Therefore, $\nabla\cdot\boldsymbol{\omega}_2 = 0$,

and, in the absence of body force and viscosity,

- Kinetic energy conservation for both $(\boldsymbol{u}_1, \boldsymbol{u}_1)$ and $(\boldsymbol{u}_2, \boldsymbol{u}_2)$.
- Helicity conservation for both $(\boldsymbol{u}_1, \boldsymbol{\omega}_1)$ and $(\boldsymbol{u}_2, \boldsymbol{\omega}_2)$.

A staggered temporal discretization removes the non-linearity, decrease the computation cost and get these conservations satisfied at the discrete level.

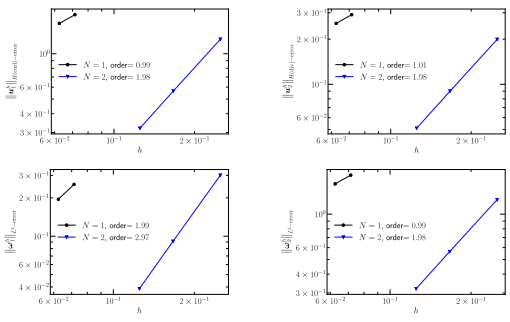

Figure 4: Some results of a manufactured solution test case. Optimal convergence rates are observed.

Conclusions

We have proposed a hybrid mimetic spectral element method. It decomposes the domain into discontinuous elements (subdomains). With the framework, conservation laws can be preserved at the discrete level.

AWEP

Experimental Investigation of Roughness Receptivity of Swept Wing Transition

PhD Candidate : Giulia Zoppini
Department : AWEP
Section : Aerodynamics
Promotor : Dr. Marios Kotsonis
Copromotor : Dr. Daniele Ragni
Contact : G.Zoppini@tudelft.nl

1.MOTIVATION

Swept wings are widely spread on civil and transport aircrafts.

Delaying their flow transition to turbulence, can improve their aerodynamic efficiency leading to a lower fuel consumption long with a cost and pollution decay due to flight travels.

2.INTRODUCTION

On **swept wings**, transition is due to **crossflow instabilities** (**CFV**), that develop on the wing as crossflow vortices (**CFV**).

They are strongly influenced by external roughness and turbulence. These are linked to the instability onset through the **receptivity process**, investigation subject of this project.

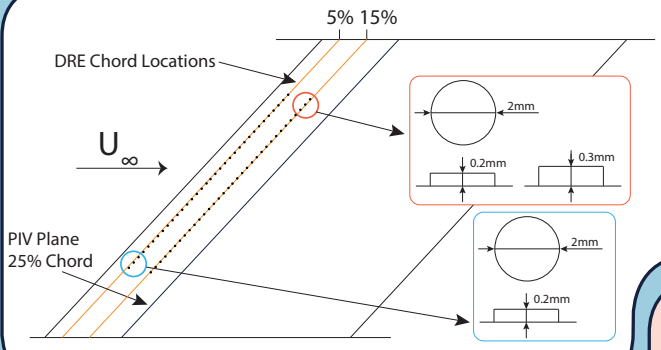

3. METHODOLOGY

To study roughness receptivity, cylindrical elements (**DRE**) are periodically distributed along the wing span.

The effect of a **shift** of their application point and a change in their **height** are here investigated through Infrared Thermography and 2D PIV. The collected data show the influence of such changes on transition front location and vortex growth.

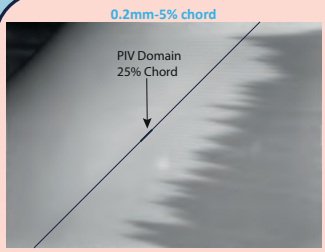

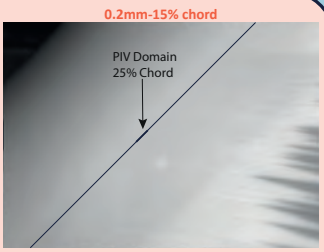

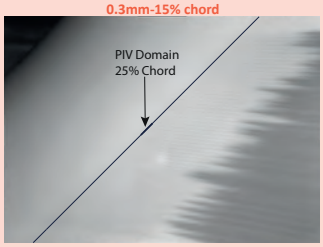

4. RESULTS

The IR and PIV images show the effects of a DRE downstream shift and an height increse.

The **downstream shift** is seen to cause a transition delay and the development of weaker vortices on the wing, as can be seen by the reduced contrast between lighter and darker stripes. A shift in DRE location seems to shift the whole CFV growth and evolution.

The **height increase** instead leds to a transition advance, and insuces stronger stability. This can be linked to the higher disturbances initial amplitude they introduce. They seem to have similar effect to an upstream forcing with smaller heights.

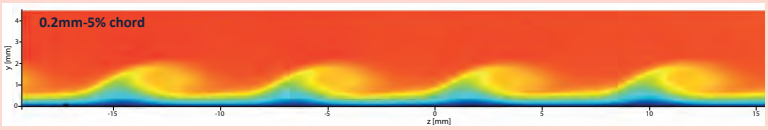

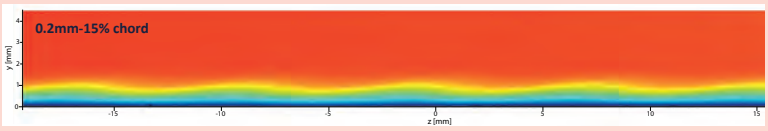

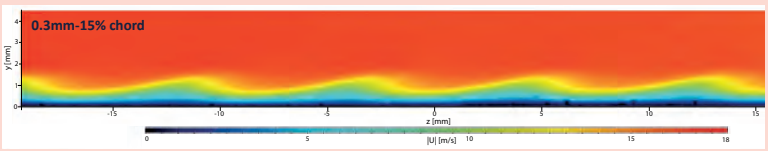

5. CONCLUSION

From this preliminary results, the important role of receptivity in CFI onset and development can be confirmed.

The analysis of all tested cases is expected to lead to the reconstruction of a transition and CFI growth map to compare with literature.

The obtained results will be investigated to identify a configuration suitable to be further studied through spatio-temporal investigations to describe the DRE ements near flow.

References

Saric, Carrillo, Reibert. Leading-edge roughness as a transition control mechanism, 6th AIAA.

Kurz, Kloker. Mechanisms of flow tripping by discrete roughness elements in a swept-wing boundary layer, JFM, 2016.

Serpieri, Kotsonis. Three-dimensional organisation of primary and secondary crossflow instability. JFM, 2016.


Promoting human-ma
in highly automated air

Wall-treatments for closed-section wind-tunnel aeroacoustic experiments

Hugo Mourão Bento
AWEP
Wind Energy Research Group
Francesco Avallone
Daniele Ragni
Mirjam Snellen
H.F.MouraoBento@tudelft.nl

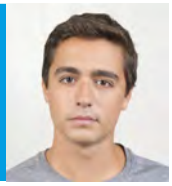

Motivation

Wind tunnels (WT):

- Open-jet → Better aeroacoustic measurements
- Closed-section → Higher aerodynamic fidelity

Open jet example, A-tunnel, TU Delft [1]

Closed-section example, LTT, TU Delft [2]

Goals

Improvement of closed-section WT

- Mitigation of the reflections
- Reduction of wall boundary layer (BL) radiated noise
- Reduction of wall BL hydrodynamic noise

→ Analysis of the aerodynamic characteristics of the modified test section

Methodology

Flow-off experiments:
- study of the reflection/absorption coefficient of lining materials.

A-tunnel (open-jet) experiments:
- study of wall BL radiated noise,
- wall BL hydrodynamic pressure fluctuations,
- and aerodynamic characteristics of wall treatments.

Computational simulations:
- study of the aerodynamic characteristics of the wall treatments,
- and validation of the experiments.

LTT (closed-section) tests:
- study of the overall gain in signal to noise ratio for aeroacoustic measurements, considering reference sound sources, e.g.:
  - streamlined speaker,
  - laser based plasma,
  - reference wind turbine airfoil.

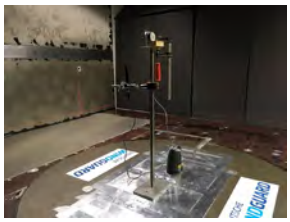

Speaker placed inside the WT, flow-off experiment

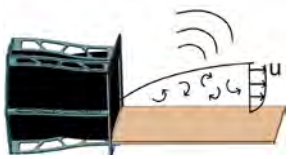

A-tunnel setup: study of flat plate BL radiated and hydrodynamic noise

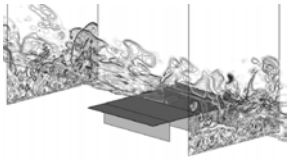

DNS simulation of a large eddy break up device, adapted from [3]

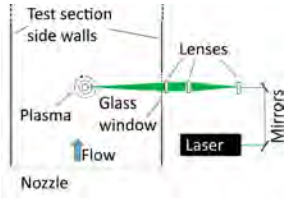

Laser based plasma sound source, adapted from [4]

Outcome

Guidelines for designing improved closed wind tunnel test sections for aeroacoustic measurements.

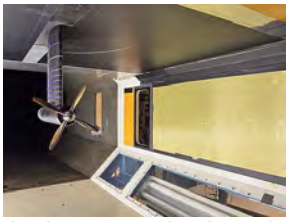

Closed test section with Kevlar panels, to reduce reflections, LTT, TU Delft, [2]

Closed test section seen from outside, LTT, TU Delft

References

[1] Rubio Carpio, A., et al. "On the role of the flow permeability of metal foams on trailing edge noise reduction." *2018 AIAA/CEAS Aeroacoustics Conference*. 2018
[2] Merino-Martinez, R., et al. "Acoustic measurements of a DU96-W-180 airfoil with flow-misaligned serrations at a high Reynolds number in a closed-section wind tunnel." *Proceedings of the 7th International Conference on Wind Turbine Noise: Rotterdam*. 2017.
[3] Spalart, P. R., et al. "Direct numerical simulation of large-eddy-break-up devices in a boundary layer." *International Journal of Heat and Fluid Flow* 27.5 (2006): 902-910.
[4] Szoke, Máté, et al. "Characterization of Hybrid Wind Tunnel Environments Using Laser-Induced Acoustic Sources." *AIAA Scitech 2020 Forum*. 2020.

AWEP

TU Delft

NWO

Experimental testing of variable loads on a vertical axis wind turbine

Livia Brandetti
AWEP – Wind Energy
Promotor: C.J. Ferreira
Co-promotor: S.J. Watson, J.W. van Wingerden
L.brandetti@tudelft.nl

Introduction

The performance of Vertical Axis Wind Turbine (VAWT) is complex due to the 3D unsteady aerodynamics. Additional complexities are introduced by a sudden change in the wind speed (i.e. gust). These variable loads are investigated with an experimental campaign in the Open Jet Facility of TUDelft University.

Methodology

The model is a two-bladed H-Darrieus VAWT, equipped with active individual blade pitch control. Dynamic inflow conditions are realised by dynamic thrust. The flow velocity is measured instantaneously with hotwire upwind and downwind the rotor.

Results

The axial velocity at tip speed ratio of 4 follows the load variation (i.e. a multi-sinusoidal pitch with 5° degree amplitude). The induction of the turbine can be controlled by the change of pitch of its blades, once considering a time delay based upon the flow convection in the wake.

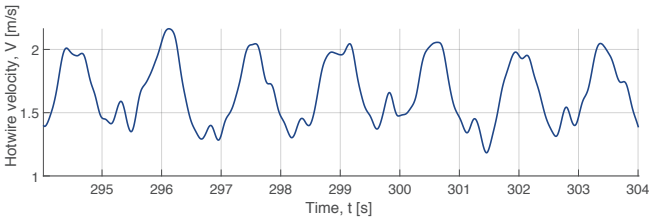

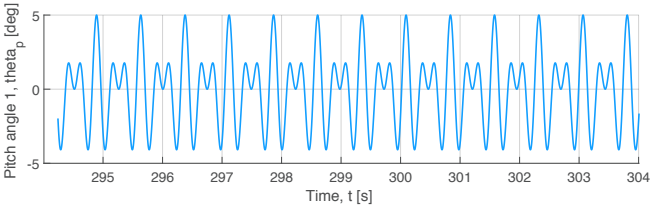

Scan me to discover more!

This research is part of the Arkom-Tulyp Wind project and is sponsored by RVO, the Netherlands Enterprise Agency, under a Hernieuwbare Energie (Sustainable Energy) subsidy.

AWEP

Wavelet-based Algorithm to Detect Wind Power Ramps

Name: Bedassa R. Cheneka
Department: AWEP
Section: Wind Energy
Promotor: Simon J. Watson
Co-promotor: Sukanta Basu
b.r.cheneka@tudelft.nl

Introduction

- Wind power ramps are the large and fast variation of wind power
- The detection of wind power ramps valuable in the deployment of wind power
- Wind power ramps characters include
  - Duration (D)
  - Magnitude (M)
  - Rate (R) $= \frac{M}{D}$

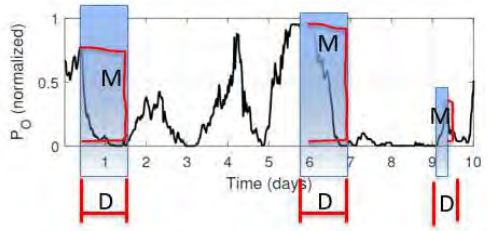

Problem Statements

- Variable ΔP (change in power) and Δt (change in time) defined wind power ramps

$$\Delta P = P(t + \Delta t) - P(t)$$

- For instance [1] defined wind power ramps when there is a change in wind power
  - 75% of rated power within 3hours
  - 65% of rated power within 1hour

Objectives

- Develop a realistic algorithm that automatically detects wind power ramps characters (duration, magnitude and rate)

Wavelet-based Algorithm

A wavelet-based algorithm which is a holistic approach that detects wind power ramps is developed by a combination of

1. Wavelet transform function
2. Surrogate data method (random shuffling)

1. *Wavelet transform function*

- The signal **x(t)** is filtered with a wavelet function (φ) with shifting in time **(b)** and a scaling **(a)** parameters to generate wavelet coefficients ($W_X(a,b)$)

$$\varphi(x) = \begin{cases} 1 & 0 \le x \le \frac{1}{2} \\ -1 & \frac{1}{2} \le x \le 1 \\ 0 & otherwise \end{cases} \qquad W_X(a,b) = \frac{1}{\sqrt{a}} \int_{-\infty}^{\infty} x(t)\varphi\left(\frac{t-b}{a}\right)$$

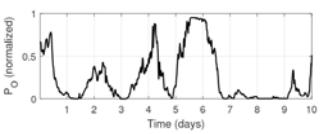

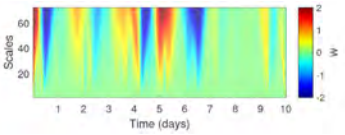

2. *Random Shuffling*

Generate N analogue data that keeps certain statistical properties of data

- It preserves the histogram density of the original data (P_o)
- But it destroys the linear property (auto-correlation) of the data
- Then, wavelet coefficient (W_s) is generated for surrogate data (P_S)

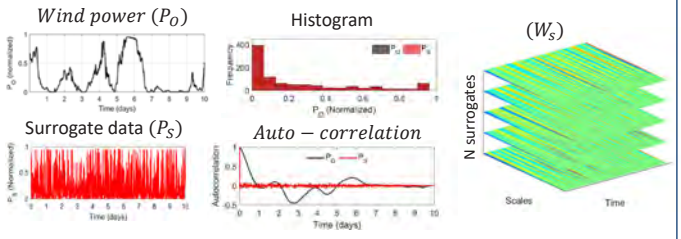

Hypothesis Testing

We have develop a hypothesis testing between (W) and (W_s) at a given significant level (α)

$$W(a,t) \ge W_S(a,(N \times t,\alpha) = \begin{cases} W(a,t) & Power\ ramps \\ 0, & not\ a\ power\ ramps \end{cases}$$

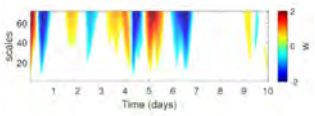

Power ramps Indices (Pr_i)

Power ramp indices are the weighted averaged of the discriminated W

$$Pr_i(t) = \frac{1}{a}\sum_{j=1}^{a} W_j(t)$$

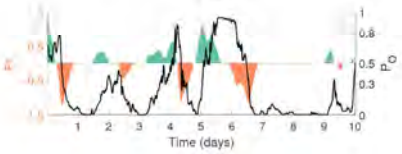

Conclusions

- The wavelet-based algorithm realistically detects wind power ramps characters
- The power ramp indices is a useful tool that is comparable with wind power ramps magnitude

[1] Cutler, N., Kay, M., Jacka, K., and Nielsen, T. S.: Detecting, categorizing and forecasting large ramps in wind farm power output using meteorological observations and WPPT, Wind Energy, 10, 453–470, https://doi.org/10.1002/we.235, 2007

THE 3D EFFECTS OF A VERTICAL-AXIS WIND TURBINE

DELPHINE DE TAVERNIER

AWEP - Wind Energy
Daily supervisor: Carlos Ferreira
Promotor: Gerard van Bussel
d.a.m.detavernier@tudelft.nl

Introduction

Although horizontal-axis wind turbines are widely studied and have proven their technological capabilities, researchers are constantly seeking for affordable renewable energy sources. Vertical-axis wind turbines might be promising alternatives when considering floating, far-offshore applications. Their lower centre of gravity, omni-directionality and easy scalability make them good candidates. However, the technological gap between VAWTs and HAWTs is wider than ever. A crucial step to evaluate their potential is to advance the modelling.

Objective

Most of the VAWT research is performed in 2D, however, the 3D flowfield is significantly different. Depending on the research goal it might be crucial to include 3D effects. With this motivation, a study is performed to identify the 3D effects of a vertical-axis wind turbines.

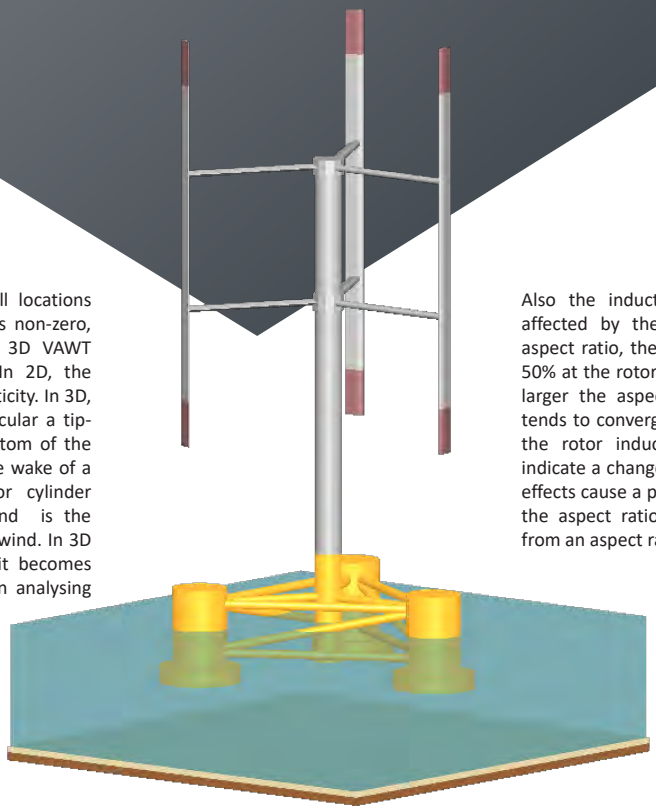

Wake induction

Because vorticity is created at all locations where the curl of the forcefield is non-zero, the vorticity field of a 2D and 3D VAWT actuator cylinder are different. In 2D, the wake consists only out of shed vorticity. In 3D, also trailing vorticity, and in particular a tip-vortex is shed at the top and bottom of the turbine. This makes that in 2D, the wake of a uniformly normal-loaded actuator cylinder with all load concentrated upwind is the same as if all load would be downwind. In 3D this is no longer true and thus it becomes important to include 3D effects in analysing the VAWT wake.

Rotor induction

Also the induction at the actuation surface is affected by the 3D effects. Depending on the aspect ratio, the normal induction may vary up to 50% at the rotor edges from the 2D induction. The larger the aspect ratio, the more the induction tends to converge to the 2D induction. Changes in the rotor induction for a similar loading case indicate a change in power coefficient. As such, 3D effects cause a power loss up to 15% depending on the aspect ratio and load configuration. Starting from an aspect ratio of 5, this loss is negligible.

AWEP

DO YOU WANT TO SEE MORE? BRING THIS POSTER TO LIVE!

1. Install the *Artivive* app
2. Launch the *Artivive* app and stand 1.5m from the poster
3. Hold your smartphone over the poster

TU Delft

Sound Propagation in Complex Environments for Urban Air Mobility

PhD Candidate: Yunusi Fuerkaiti
Department: Awep
Section: Wind Energy
Supervisors: Dr. F. Avallone, Dr. D. Ragni
Promotor: Prof. dr. D. Casalino
Contact: y.fuerkaiti@tudelft.nl

Research context

Figure 1: Conceptual illustration of Urban Air Mobility operations [4].

Urban Air Mobility (UAM) developers have anticipated that **electrical aircraft**, automation, and telecommunications driven by **Unmanned Aircraft System (UAS)** will enable novel Vertical Takeoff and Landing (VTOL) aircraft to provide UAM services in the early **2020's** [1].

UAM researchers highlight **aeroacoustic noise** as one of the **threats** to the implementation of large-scale UAM [2].

VTOL aircraft noise reduction can be achieved through **low noise aircraft and trajectories and urban planning** [3].

Source prediction

Source noise levels are predicted in two steps:
i) flow field computation with high-fidelity simulation.
ii) sound field computation using Ffowcs-Williams and Hawkings (FW-H) acoustic analogy.

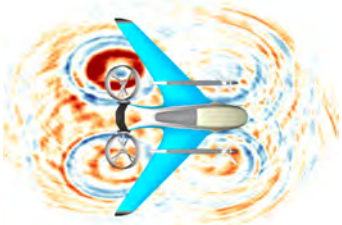

Figure 2: Sound field around the 3Ds eVTOL model [5].

Urban environment

Sound propagation in urban environment will be studied using the Lattice- Boltzmann Method (LBM).

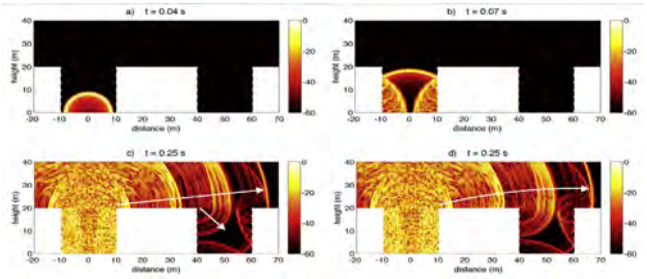

Figure 5: Snapshots of wave propagation in a section of an urban area. a) Direct sound wave, b) Sound is reflected by building facades, c) Sound is diffracted into the nearby street canyon, d) Sound is refracted due to a mean atmospheric wind speed profile [6].

References:
[[1] Parker D. Vascik, R. John Hansman, "Scaling Constraints for Urban Air Mobility Operations: Air Traffic Control, Ground Infrastructure, and Noise".
[2]P. D. Vascik and R. J. Hansman, "Evaluation of Key Operational Constraints Affecting On-Demand Mobility for Aviation in the Los Angeles Basin: Ground Infrastructure, Air Traffic Control and Noise". [3]A. Filippone, " Aircraft noise prediction".
[4] D. P. Thipphavong et al. "*Urban Air Mobility Airspace Integration Concepts and Considerations*".
[5]D. Casalino, W. C. P. Van der Velden, G. Romani, "Community Noise of Urban Air Transportation Vehicles".
[6]Maartin Hornix, "Ten questions concerning computational urban acoustics".
[7]Vinaykumar Kurakula, " A GIS-Based Approach for 3D Noise Modelling Using 3D City Models".

Noise footprint computation

Noise footprint of the eVTOL vehicle is computed with Noise Hemisphere Database (NHD) approach and ray acoustics. The ray acoustics enables prediction of sound field at receivers in an inhomogeneous medium.

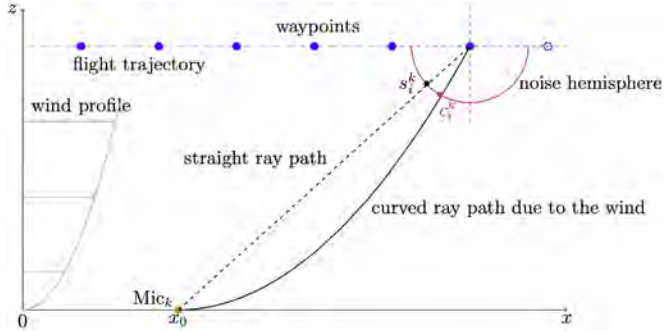

Figure 3: Illustration of the NHD-based noise footprint calculation procedure for an inhomogeneous atmosphere.

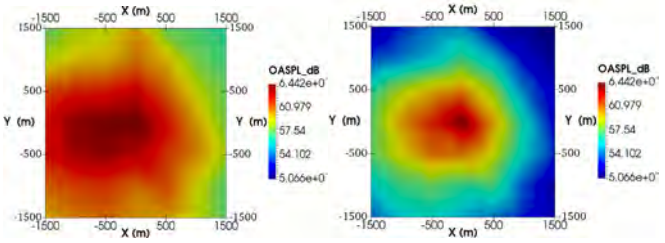

Figure 4: Noise footprint of the 3DS eVTOL over a flat terrain in an ideal atmosphere (left) and in an inhomogeneous atmosphere (right).

3D noise mapping with GIS

Geographical Information System (GIS) based 3D noise maps will be studied by converting the noise footprint data into noise rasters and integrating it into a GIS environment.

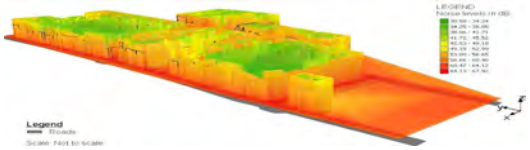

Figure 6: A GIS based 3D noise map for a building area between two roads [7] .

AWEP

TU Delft

Aeroacoustic study of low-Reynolds propellers for UAV applications

PhD Candidate: Edoardo Grande
Department: AWEP
Section: Wind Energy
Supervisors: Dr. F. Avallone, Dr. D. Ragni
Promotor: Prof. dr. D. Casalino
Contact: e.grande@tudelft.nl

INTRODUCTION

UAVs (Unmanned Aerial Vehicle) are developing incredibly fast, both for military and commercial applications. The use of UAVs is limited by their noise generation levels. Either for acoustic furtivity in military operations, or noise pollution in civilian use in proximity of populated areas, **noise reduction** of UAV propellers is a **goal to achieve**.

EXPERIMENTAL TEST-RIG

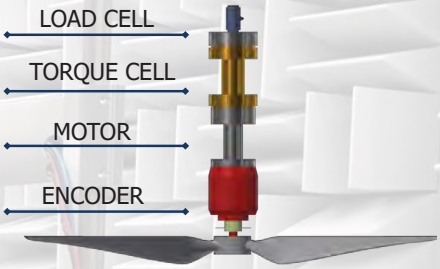

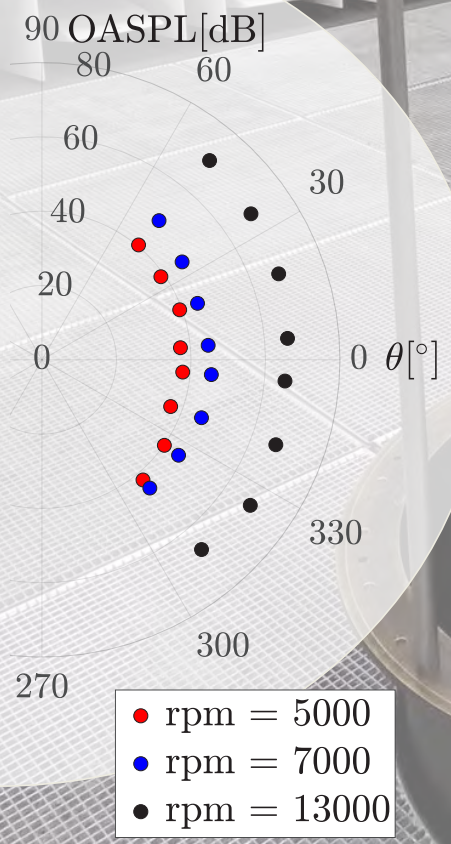

NOISE SPECTRA

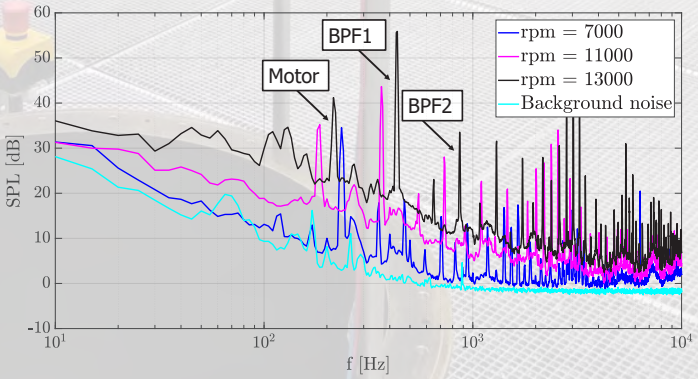

AWEP

TU Delft

AIRBUS DEFENCE & SPACE

Experimental study of the wake behind planar actuator surfaces

MING HUANG
Department: AWEP
Section: Wind Energy
Promotors: Carlos Ferreira
Fulvio Scarano, Andrea Sciacchitano
M.Huang-1@tudelft.nl

Background

Vertical vs Horizontal axis wind turbine (VAWT vs HAWT)

Advantages:

- Omni-directionality
- Lower center of gravity

These advantages make VAWT promising for more efficient off-shore wind farm application.

However, the aerodynamic efficiency of VAWT in the wind farm scale needs to be demonstrated.

Adapted from the work of R. Bos

Objectives

- Simplified HAWT model

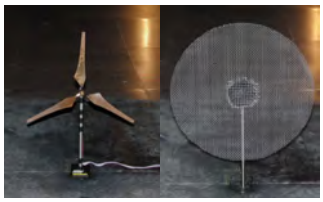

Aubrun et al., 2013

Kyle Charmanski et al., 2014

Porous plates are often adopted as actuator discs to represent HAWT.

- Simplified VAWT model

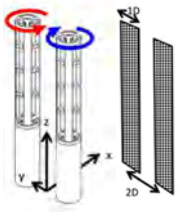

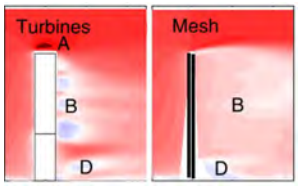

Craig et al., 2017

Discrepancies in the velocity fields of actuator rectangle are reported.

Shape effect of planar actuator surface?

Method

- Actuators in our experiment

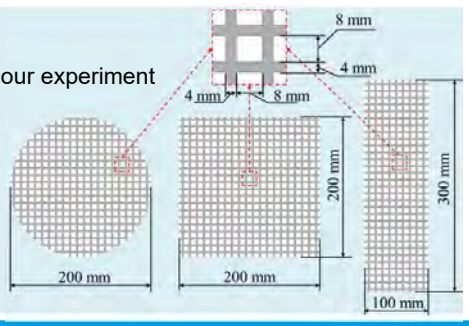

Porosity: 44%

- Robotic PIV setup

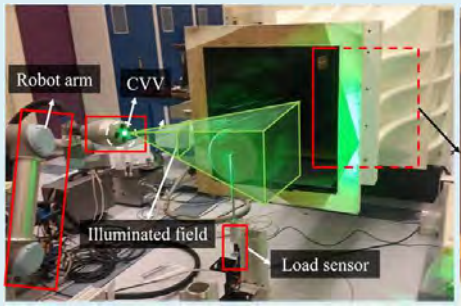

- W-Tunnel: open-jet, section size of 0.6 m × 0.6 m
- Coaxial volumetric velocimeter (CVV)
- Robotic system
- Helium-filled soap bubbles (HFSB) seeding system

- Field of view

Top-view

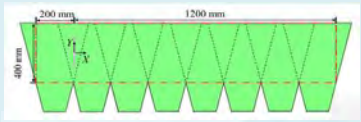

Front-view

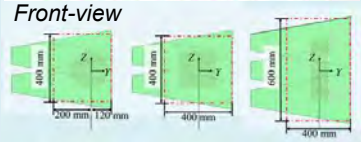

- Thrust Measurement

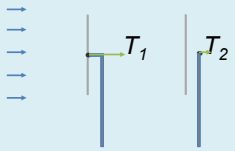

	T [N]	C_T
Circular	0.46 ± 0.01	0.92 ± 0.02
Square	0.55 ± 0.01	0.87 ± 0.02
Rectangular	0.44 ± 0.01	0.93 ± 0.02

Results

- Velocity field in the median plane: top view

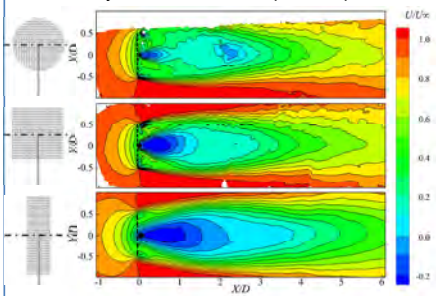

- Deceleration region (upstream) rectangle>square≈circle
- Recirculation region rectangle>square>circle
- Velocity recovery circle>square>rectangle
- Wake expansion rectangle>square≈circle

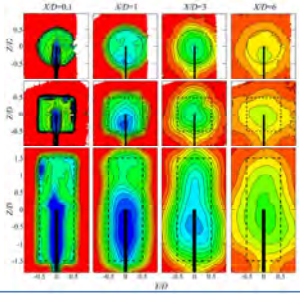

Actuator shape strongly affects:
- velocity recovery
- expansion rate
- wake cross-sectional shape

Conclusions

Actuator shape has
-- small effect on C_T
-- significant effect on the wake development

AWEP

The necessity to develop a new dynamic inflow model in yaw

PhD Candidate: Chihoon Hur
Department: AWEP
Section: Wind Energy
Supervisor Carlos Simão Ferreira
Gerard Schepers (TNO)
Promotor: Carlos Simão Ferreira
Contact: c.hur@tudelft.nl

Background

- Horizontal Axis Wind Turbines (HAWTs) experience more frequent yaw misalignments due to various novel approaches to utilize active yaw control in order to maximize power production [1].
- A combined dynamic wake model for yawed flow does not exist yet. Furthermore, in the AVATAR project [2]. fully coupled aero-elastic tools using 10 different engineering models, including yaw and dynamic inflow models, are simulated. Results in the project show that BEM suffer from significant deficiencies.

Objective

- **To Evaluate dynamic phenomena in yaw, using high fidelity CFD approach for yawed flow with dynamic loading and comparing it against state-of-the-art engineering models.**
- **Eventually, to determine if a new dynamic inflow model in yaw is necessary.**

Approach

- Using state-of-the-art engineering models, vortex and CFD models explained in the literature [3, 4], induction fields are compared at different yaw angles and varying loads as described in the table below.

	Case I	Case II	Case III	Case IV
Yaw angle	0 deg	30 deg	0 deg	30 deg
Base C_T	0.6			
Load type	Constant load		Step load ($\Delta C_T = +0.1$), cyclic load ($\Delta C_T =+ 0.1$, fr $= 0.1$)	
Models	Yaw momentum model (Øye), PWVM, FWVM, CFD model		Dynamic inflow models (Pitt-Peters, ENC, Øye, Yu's linear and non-linear model) CFD model	

Results

- Since current dynamic inflow models expect no yaw angle, induction fields from those models in upwind part and downwind part are same, while CFD results show a significant difference with respect to y/D position as seen results from Case Ⅳ.
- Because downwind part of actuator disc is deeper in the wake, the phase delay is slower than upwind part.

Case Ⅱ : Induction field at disc

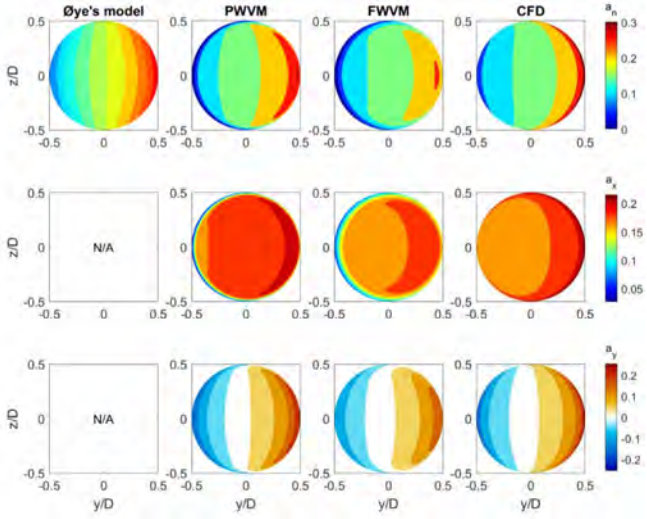

Case Ⅲ : Induction field at inner and outer point

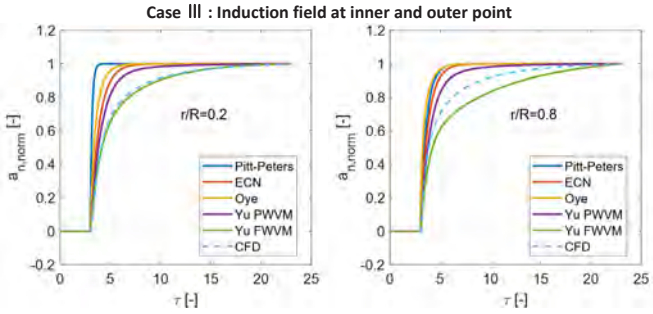

Case Ⅳ: Induction field at upwind and downwind point

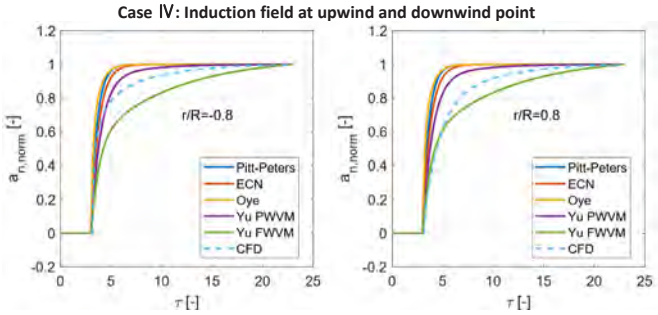

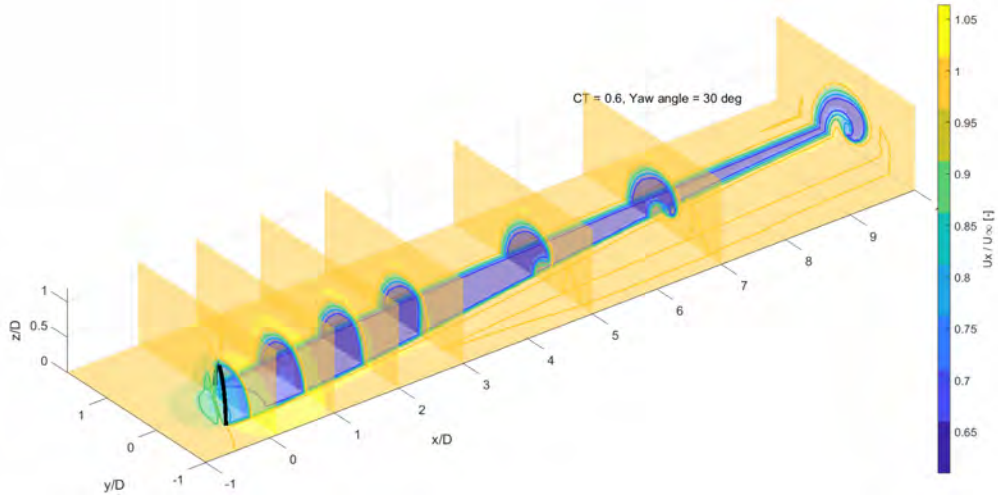

Conclusions

- **Current yaw momentum models and dynamic inflow models are implemented and analyzed with vortex and CFD models.**
- **It is required to create a new dynamic inflow model in yaw to take dynamic asymmetric wake development into account.**

References

[1] Paul Fleming, Pieter MO Gebraad, Sang Lee, Jan-Willem van Wingerden, Kathryn Johnson, Matt Churchfield, John Michalakes, Philippe Spalart, and Patrick Moriarty. Simulation comparison of wake mitigation control strategies for a two-turbine case. Wind Energy, 18(12):2135–2143, 2015

[2] Alvaro Gonzalez, Ainara Irisarri, Helge Madsen, Torben Juul Larsen, Koen Boorsma, Michael Schwarz, Marion Reijerkerk, and Dimitris Manolas. Comparison of models with respect to load analysis in extreme yaw of the innwind.eu and avatar rwt's. , Petros Chasapogiannis (Ed), NTUA, 2016.

[3] Chihoon Hur, Tom Berdowski, Carlos Simao Ferreira, Koen Boorsma, and Gerard Schepers. A review of momentum models for the actuator disk in yaw. In AIAA Scitech 2019 Forum, page 1799, 2019.

[4] Wei Yu, Delphine Tavernier, Carlos Ferreira, Gijs AM van Kuik, and Gerard Schepers. New dynamic-inflow engineering models based on linear and nonlinear actuator disc vortex models. Wind Energy, 2019.

TU Delft

AWEP

Using damping measurements in a thick adhesive joint of a wind turbine blade to detect damage

Sharif Khoshmanesh
AWEP
Wind Energy
Supervisor: S.Watson/D.Zarouchas
Promotor: S.Watson
s.khoshmanesh@tudelft.nl

Introduction

Deploying a sophisticated condition monitoring system could reduce the levelised cost of energy (LCOE) for an offshore wind farm with low accessibility. With the increasing size of offshore wind turbine blades, the necessity for a blade monitoring system is ever more pressing due to the large downtime associated with failure and the high replacement cost.

Motivation

In vibration-based methods, the most advanced damage detection techniques rely on measurements of stiffness. In a complex structure like a wind turbine blade, changes in stiffness may not be significant unless severe damage occurs. In a wind turbine blade, changes in material damping are more sensitive than changes in stiffness to such as delamination in the spar cap, transverse cracks and de-bonding in adhesive joints.

Results

Four distinctive stages of damage can be seen: Stage 1 - transverse cracks and delamination in vicinity of cracks are initiated; Stage 2 - cracks are saturated; Stage 3 - de-bonding of the adhesive from the fibre laminates is initiated; Stage 4 - fibres pull out and failures occurs.

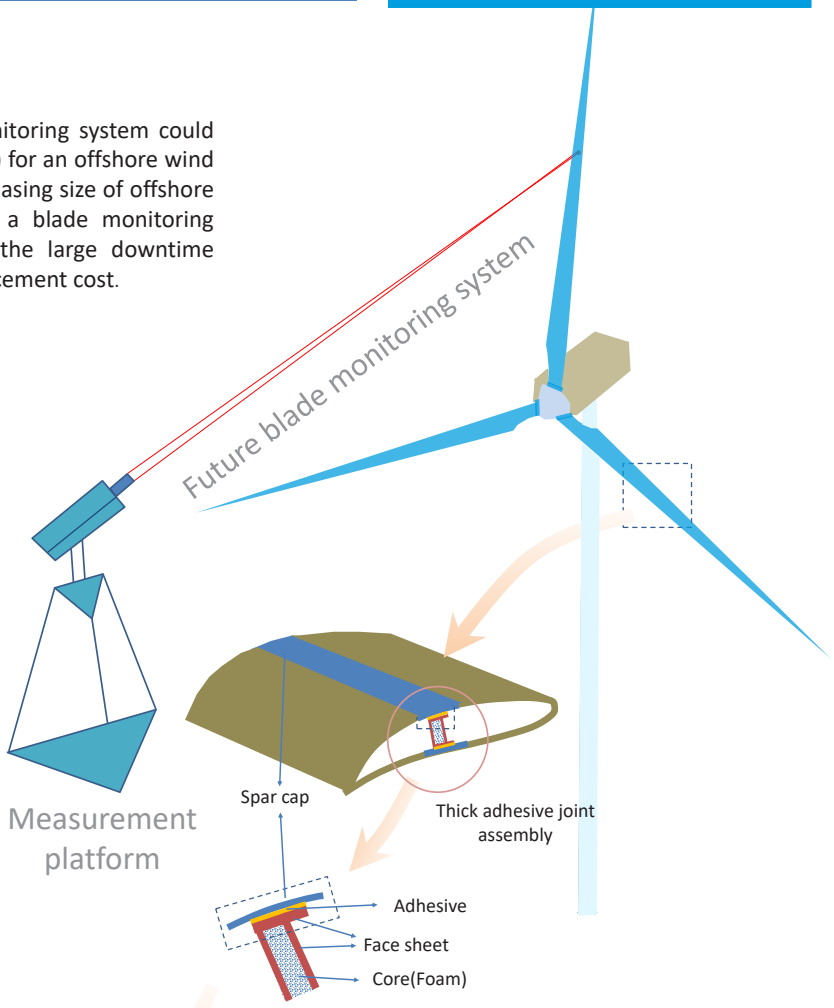

Methodology

A fatigue tension test and a vibration test are carried out on a thick adhesive joint to identify the variation of the damping property during the fatigue lifetime.

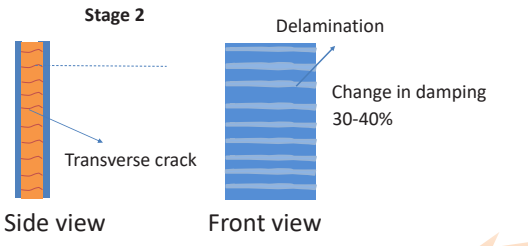

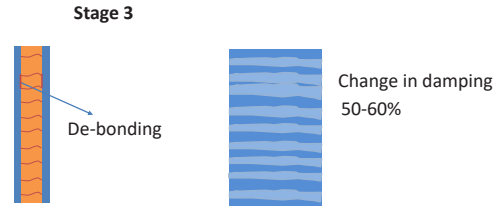

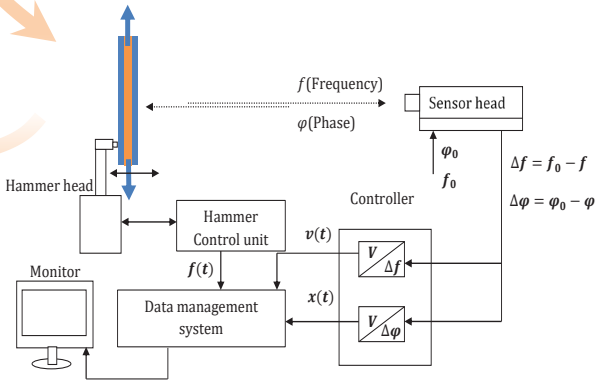

AWEP

Trailing-edge noise reduction for wind turbines

PhD Candidate: Lourenco T. L. Pereira
Department : AWEP
Section : Wind Energy
Supervisors : Dr. D. Ragni, Dr. F. Avallone
Promotor : Prof. Dr. F. Scarano
Contact : l.t.limapereira@tudelft.nl

Background

Turbulent boundary layer trailing-edge noise is caused by scattering of pressure fluctuations at the sharp trailing edge [1]. Devices such as trailing-edge serrations can be employed to reduce **trailing-edge noise**, i.e. by shaping the TE in a sawtooth-like geometry. Serrations avoid the **coherent scattering** of the turbulent structures.

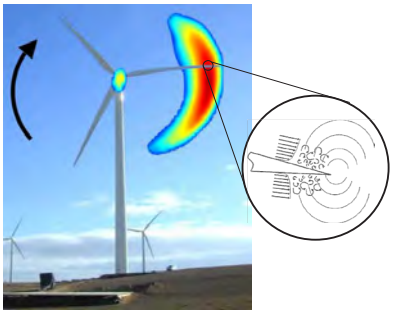

Noise sources in a wind turbine, [1] and [2].

Improving noise reduction performance requires information from both the acoustic and aerodynamic fields. High resolution spatio-temporal flow data are needed for studying the flow surrounding the trailing-edge serration.

- Pressure fluctuations;
- Correlation length;
- Convection velocities.

Aerodynamic → **Acoustic**

- Frozen turbulence assumption (serration geometry not considered);
- No effect from blade loading.

- Models do not predict a limit for serration angle;
- Requires model of the aerodynamic data on stream and spanwise wavenumbers.

Goals

The aim of this PhD is to

- Improve understanding and predictions of trailing edge noise reduction by serrations in wind turbines;
- Explore novel techniques to measure the unsteady flow close to the trailing edge.

Methodology

Time-resolved 3D-PIV + pressure reconstruction using Helium Filled Soap Bubbles (HFSB):

- Large volumes;
- Assimilation of data from sparse particle positions.

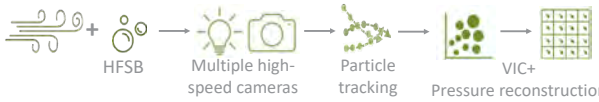

Experiments are performed on a flat plate model with trailing edge flaps and exchangeable trailing-edge inserts. Aerodynamic measurements are carried at the W-Tunnel facility and acoustic measurements at the A-Tunnel.

Results

1. Mean flow characterization

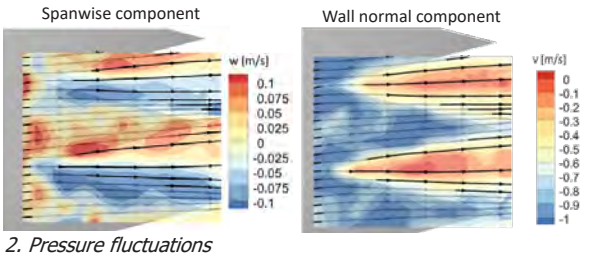

2. Pressure fluctuations

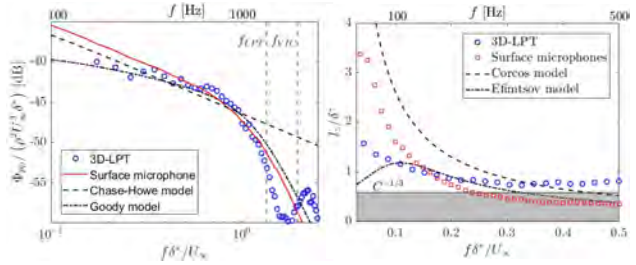

3. Acoustic measurements

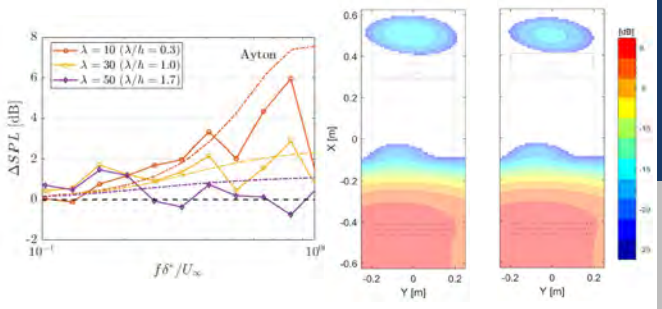

References

[1] Oerlemans, S., Sijtsma, P., and Lopez, B. M., "Location and quantification of noise sources on a wind turbine". Journal of sound and vibration, 2007.

[2] Barone, M. F. , and Franklin, M. "Survey of techniques for reduction of wind turbine blade trailing edge noise". Technical Report, 2011.

Smart Mitigation of flow-induced Acoustic Radiation and Transmission for reduced Aircraft, Surface traNSport, Workplaces and wind enERgy noise

This project has received funding from the **European Union's Horizon 2020** research and innovation program under the **Marie Skłodowska-Curie grant** agreement No 722401

H2020 MARIE SKŁODOWSKA-CURIE ACTIONS

Wind Turbine Design for Hybrid Renewable Energy Systems (HRES)

Name: Mihir Kishore Mehta
Department: Aerospace
Section: Wind energy
Daily supervisor: Michiel Zaaijer & Dominic von Terzi
Promotor: Dominic von Terzi & Simon Watson
m.k.mehta@tudelft.nl

What would a wind turbine optimized specifically for HRES look like?

HRES are power generating systems that use a renewable energy source along with a conventional source or multiple renewable energy sources with/without storage, operating in a grid-connected or an islanded mode.

HRES

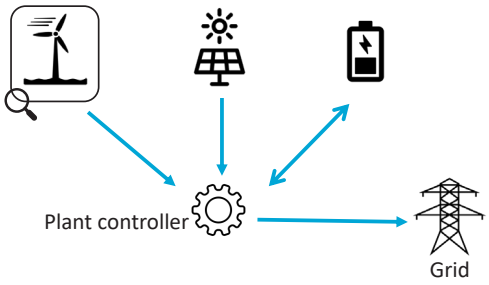

Why HRES?

Reduced power intermittency

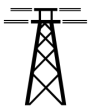

Better grid infrastructure usage

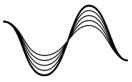

Higher generation-load correlation

Increased revenue from energy arbitrage

Some relevant HRES scenarios

- Off grid wind-solar-battery storage for meeting the local demand curve.
- Utility scale wind-solar-battery storage for electricity market (regular markets + ancillary services market) with grid congestion issues.
- Wind-hydrogen hybrid for the energy market at large including electricity and heat.

Sample ideas for turbine design

A low-cost night-time turbine for a better fit with solar

Low wind speed turbines with a low specific power

Wind turbine with integrated electrolyzers for hydrogen production

Optimization Tool

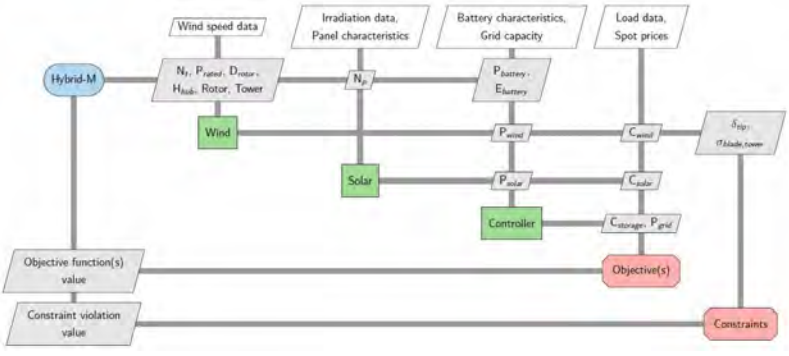

Wind-Solar hybrid: System sizing trade-offs

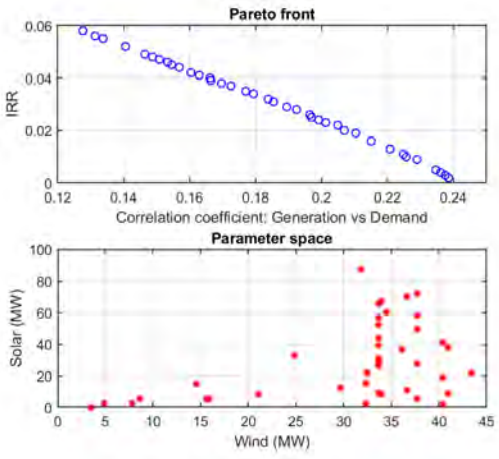

A Multi-disciplinary optimization tool will be developed, that combines holistic HRES design with detailed wind turbine design, to determine the most optimal wind turbine configuration for specific HRES. The dissemination of this knowledge will enable wind turbine manufacturers and hybrid wind farm developers to meet the demands of the TSO and the society in the most beneficial way.

AWEP

TU Delft

DUWIND TU Delft Wind Energy Institute

Numerical and Experimental Analysis of the Aerodynamics and Design of the Lift-drag Combined Vertical Axis Wind Turbine

Name: Jingna Pan
Department: AWEP
Section: Wind Energy
Promotor: Carlos J. Simao Ferreira
Co-promotor: Alexander van Zuijlen
Contact: J.Pan-1@tudelft.nl
Year: 1 2 3 4

1. Introduction

- Drag-type vertical axis wind turbines [1] have the features of simple structure, low noise, good self-starting performance. These characteristics allow them to be suitable for most small and medium-sized utilization; for example, to be integrated with residential and commercial buildings for energy production [2]. However, their tip speed ratio and efficiency are low.
- For lift-type vertical axis wind turbines [3], efficiency and corresponding tip speed ratio are high. However, the turbine start-up is challenging.

Fig. 1(a) Drag-type VAWT [4]

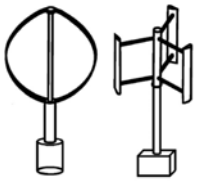

Fig. 1(b) Lift-type VAWT [4]

- Among the two types of wind turbine, the problems of start performance, aerodynamic output, dynamic stall, and structural safety and stability are complemented [5]. Aiming at solving these problems, this research will focus on the operation of the combined lift-drag Vertical Axis Wind Turbine.
- To analyze the complex and unsteady aerodynamic flow associated with a wind turbine, computational fluid dynamics (CFD) is an attractive and powerful method. However, it requires significant computational resources. To improve simulation efficiency, a vortex model will also be employed.

2. Objective

- This research will focus on the aerodynamic flow around the combined lift-drag vertical axis turbine, aiming to develop physical insight to improve the rotor design and increase annual energy productions.
- The improved numerical method through a hybrid Eulerian-Lagrangian model allows the decoupling of the different scales of vorticity.
- The research will demonstrate the suitability of this approach for highly complex vortical flows.

3. Methodology

① The first step is to generate high-fidelity (OpenFOAM) and mid-fidelity (Vortex Model) reference simulations, and validate them with existing experimental data.
② The second step is to develop a hybrid Eulerian-Lagrangian solution to analyze the viscous, turbulent flow around the blades. The Lagrangian method could solve the flow in the far-field region, and the Eulerian method could solve the flow in the near-wall region.
③ The third step is to conduct wind tunnel experiments (including Particle Image Velocimetry) to validate the whole numerical method.

4. Initial Research

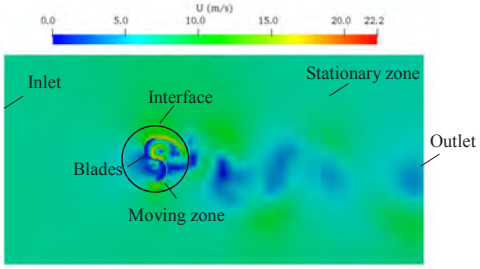

Fig. 2 Schematic and velocity field of the computational domain

In the early stage, a 2D drag-type rotor case is studied using OpenFOAM. The computational domain is divided into two parts: a moving zone and a stationary zone. Fig. 3 compares the power coefficient c_p for different tip speed ratios of the simulation with that of an experiment [6]. The initial results show some agreement with the experimental results. However, there are discrepancies at TSR=1.0, which will be studied further.

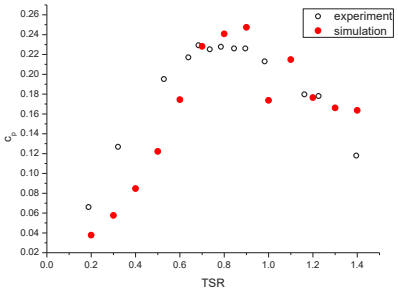

Fig. 3 Comparison of power coefficient for experiment and simulation

5. Current Work

Currently, OpenFOAM is validated to be able to deal with the aerodynamic flow in a 2D vertical axis wind turbine. Different numbers of mesh are generated to verify mesh independency. A vortex model is needed to simulate far-field flow. Therefore, we are currently studying the fundamental equations of the flow problem and obtaining solutions under specific assumptions.

6. References

[1]Chen T Y , Chen Y Y . Developing a Vortical Stator Assembly to Improve the Performance of Drag-Type Vertical-Axis Wind Turbines. *Journal of Mechanics*, 2015, 31(06):693-699.
[2]Jian C , Zhou-Zhou Z , Hong-Tao X U . Research status of drag-type vertical axis wind turbine. *Energy Engineering*, 2017.
[3]Chen J , Yang H , Yang M , et al. A comprehensive review of the theoretical approaches for the airfoil design of lift-type vertical axis wind turbine. *Renewable and Sustainable Energy Reviews*, 2015, 51:1709-1720.
[4] Kozak, Peter. Effects of Unsteady Aerodynamics on Vertical-Axis Wind Turbine Performance. 2004.
[5]Scheurich F , Fletcher T M , Brown R E . Simulating the aerodynamic performance and wake dynamics of a vertical-axis wind turbine. *Wind Energy*, 2011, 14(2):159-177.
[6]Fujisawa, N., Gotoh, F. Visualization study of the flow in and around a Savonius rotor. *Experiments in Fluids,* 1992.

AWEP

Dissecting a pumping cycle

of Kitepower's development system

Mark Schelbergen
Department: AWEP
Section: Wind Energy
Supervisor: Roland Schmehl
Promotor: Simon J. Watson
M.Schelbergen@tudelft.nl

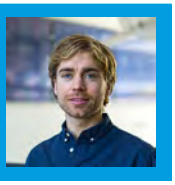

Pumping Airborne Wind Energy System

Kitepower's system uses ground-based power generation, also known as a pumping mode system. The pumping cycle consists primarily of a reel-out and reel-in phase, in which power is generated and consumed. The kite is retracted using only a fraction of the energy produced during the traction phase, yielding positive net energy production.

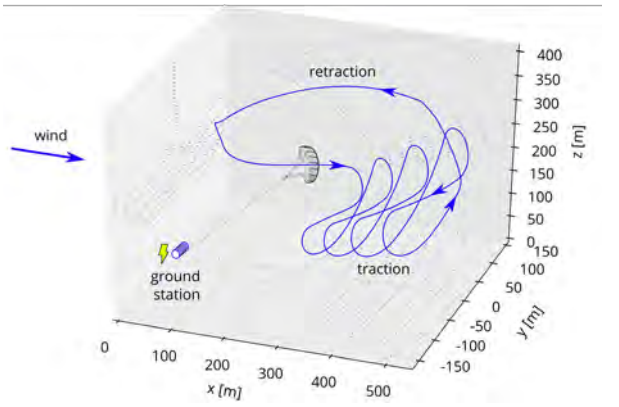

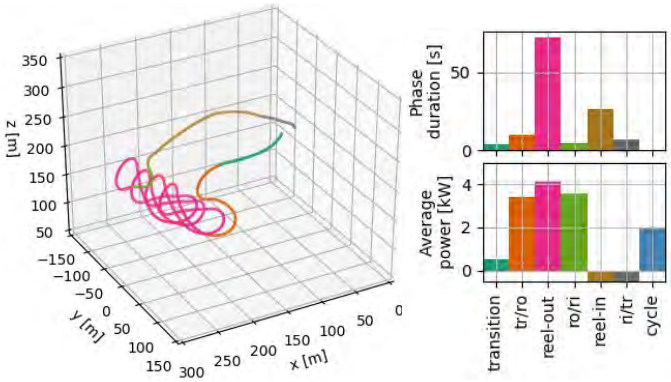

Flight test data

Measurements from flight tests are analysed for identifying inefficiencies in the operation of the system and validating performance models. On 8-10-2019, Kitepower's 25 m² kite was flown in moderate wind conditions. A representative pumping cycle is selected for further analysis.

Identification of kite's aerodynamic coefficients

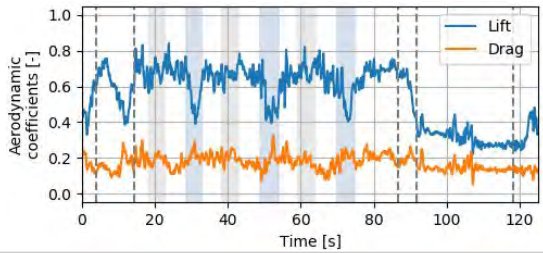

Wind conditions

The wind speed at the kite is in general higher than at the ground and is not directly measured, but estimated from the apparent wind speed. Some spread is expected due to the varying wind, on top of that, measurement errors and assumptions in the calculation result in additional spread. The latter shows by the relatively high spread during turns (purple points). The spread for the full flight test is substantially larger.

Reconstructed wind speeds

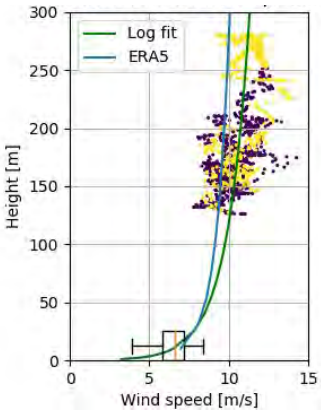

Identification of aerodynamics and validation of performance models

Identifying and validating models is problematic since the system can not be tested in a controlled environment, its behaviour is greatly influenced by the continuously changing wind, and only an estimate of the wind speed is available.

Comparison between measured and simulated data

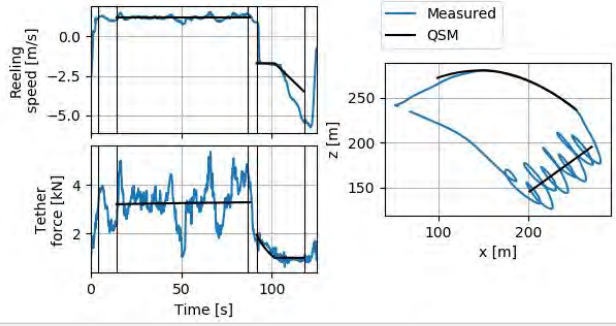

Publications

[1] Airborne Wind Energy Resource Analysis – P. Bechtle, M. Schelbergen et al. (2019), Renewable Energy
[2] Clustering wind profile shapes to estimate airborne wind energy production - M.Schelbergen et al. (2020), WESD

Photo and flight test data provided by Kitepower B.V. (www.kitepower.nl).

Received financial support by the project REACH (H2020-FTIPilot-691173), funded by the European Union's Horizon 2020 research and innovation programme under grant agreement No. 691173.

DATA-DRIVEN TURBULENCE MODELING FOR WIND FARMS

Julia Steiner
AWEP
Wind Energy
Axelle Viré, Richard Dwight
Simon Watson
j.steiner@tudelft.nl

Why is it important? Optimal wind farm layout and control strategy during operation are crucial for cost-effective wind farm design and operation. Both of these aspects require accurate and efficient wind farm flow and actuator models.

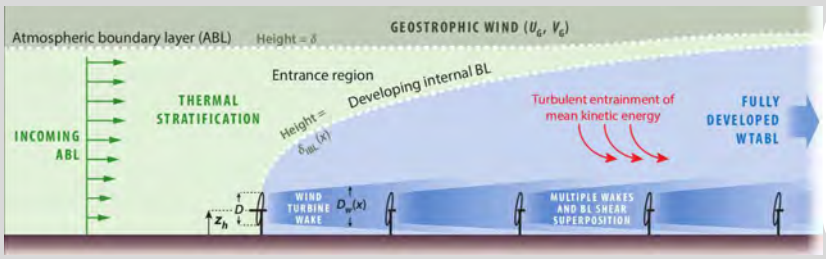

Limitations Choice of models is a trade-off between accuracy and cost. Currently, the state of the art are Large Eddy Simulations (LES). But these models are too expensive to be used for practical applications. Reynolds-Averaged Navier-Stokes (RANS) based turbulence models are cheaper, but have structural shortcomings and existing corrections do not generalize.

Objective Improve RANS based flow & turbine load predictions for stratified flows in wind farms.

Methodology Use a data-driven approach to improve RANS turbulence models. Time-averaged LES data can be used to derive correction terms for RANS models. Then, machine learning can be used to generalize the corrections beyond the training data.

Setup LES database and time-average relevant fields

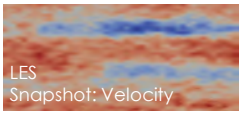

- Build case database using LES
- Time-average fields such as velocity $\overline{u}$, pressure $\overline{p}$, pressure & turbine forcing $\overline{f}$, turbulent kinetic energy k and turbulence anisotropy tensor b_{ij}

Setup RANS counterpart simulations

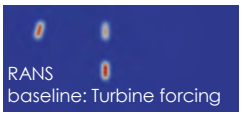

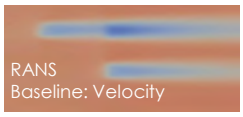

- Setup RANS simulation that complement LES database
- Use inflow & forcing from LES
- Use similar turbine model

Solve RANS turbulence equations with frozen flow field from LES to get ideal correction terms

$$\frac{D\overline{u}_i}{Dt} = -\frac{1}{\rho_0}\frac{\partial \bar{p}}{\partial x_i} + \nu\frac{\partial^2 \overline{u}_i}{\partial x_j^2} + \frac{\partial \bar{\tau}_{ij}}{\partial x_j} + \overline{f}_i$$

Reynolds stress definition

$$\tau_{ij} = 2k\left(b_{ij} + \frac{1}{3}\delta_{ij}\right) \overset{\text{def}}{=} 2k\left(-\frac{\nu_t}{k}S_{ij} + b_{ij}^{\Delta} + \frac{1}{3}\delta_{ij}\right)$$

Transport eqn for turbulent kinetic energy k and its dissipation ϵ

$$\frac{Dk}{Dt} = P_k + P_k^{\Delta} - \epsilon + D_k$$

$$\frac{D\epsilon}{Dt} = \left[C_{\epsilon 1}\left(P_k + P_k^{\Delta}\right) - C_{\epsilon 2}\epsilon\right]\frac{\epsilon}{k} + D_\epsilon$$

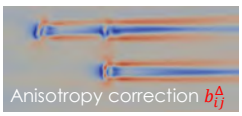

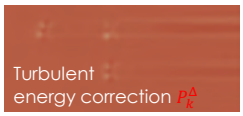

- Solve turbulent transport equations from the RANS model with frozen velocity field from LES
- Get correction terms for the Reynolds stress anisotropy tensor b_{ij}^{Δ} and for the turbulent kinetic energy production P_k^{Δ}
- Correction terms ensure that the velocity and turbulence intensity field predicted by RANS will agree with the mean LES field
- See resulting correction terms on the left

Use symbolic regression to generalize correction terms

$$b_{ij}^{\Delta}(S_{ij}, \Omega_{ij}) = \sum_{i=1}^{10}\alpha_n(I_m)T_{ij}^{(n)}$$

$$\alpha_n(I_m) = \sum_{j=1}^{M} B_{jn}\theta_j \text{ with}$$

$$B_{jn} = [I_1, I_2^2, \sin(I_1), I_3^2 I_5, \dots]$$

$$\Theta = \min_{\widehat{\Theta}}\left\|\mathbf{B}\widehat{\Theta} - b\right\| + \lambda\rho\left\|\widehat{\Theta}\right\| + \frac{1}{2}\lambda\rho(1-\rho)\left\|\widehat{\Theta}\right\|^2$$

- Use integrity basis of ten base tensors $T_{ij}^{(n)}$ and five invariants I_m to model correction terms
- Only the construction of b_{ij}^{Δ} is shown, but the approach is very similar for P_k^{Δ}.
- Find expression for $\alpha_n(\dots)$

Integrate correction terms into RANS model

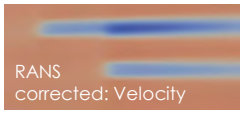

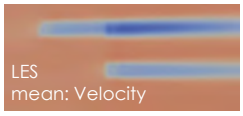

- Corrected RANS velocity field is shown alongside the LES mean field
- Difference is minimal.

SOURCES
ABL picture: Stevens, R. & Meneveau, C.: Flow Structure and Turbulence in Wind Farms, Annual Review Fluid Mechanics, 2017.
Integrity basis: Pope, S.B.: A more general effective-viscosity hypothesis. Journal of Fluid Mechanics, 1975.
Correction framework: Schmelzer, M. et al .: Machine Learning of Algebraic Stress Models using Sparse Symbolic Regression. Flow Turbulence and Combustion, 2019.

TU Delft

AWEP

Porous Treatments for Reducing Interaction Noise in Turbofans

PhD Candidate: Christopher Teruna
Department : AWEP
Section : Wind Energy
Supervisors : Dr. D. Ragni, Dr. F. Avallone
Promotor : Prof. Dr. D. Casalino
Contact: c.teruna@tudelft.nl

1. PROBLEM STATEMENT

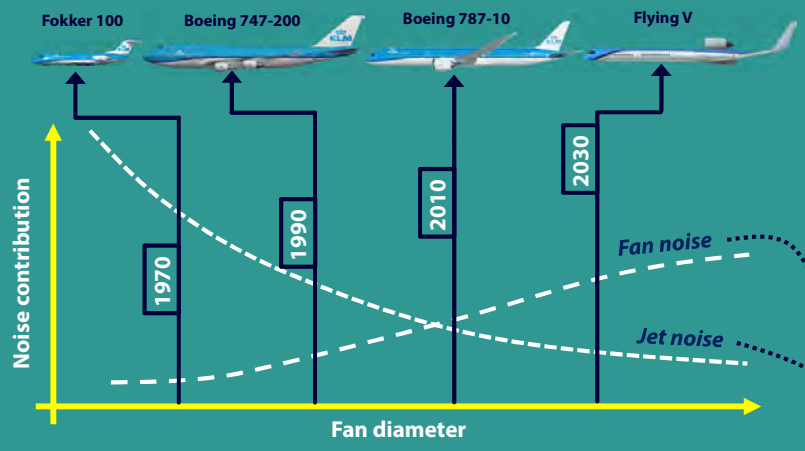

Turbofans are increasing in size to achieve higher fuel efficiency and to reduce jet noise. However, a wider fan is noisier and eventually becomes the dominant noise source inside the engine. In particular, the noise arises from the aerodynamic interaction between the *fan wake* and *outlet-guide vane (OGV)* [1,2].

Cutaway of a high-bypass turbofan

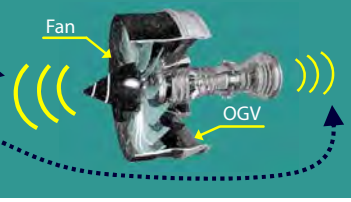

2. OUR RESEARCH

Porous material[3]

- Ni-Cr-Al metal foam
- 90% porosity
- 5% of the tensile strength of Al-7075

Concept

a. **OGV blade with porous tip**

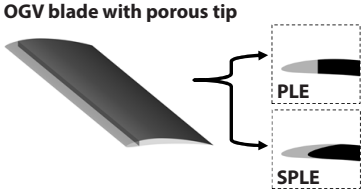

b. **OGV blade with serrated-porous tip**

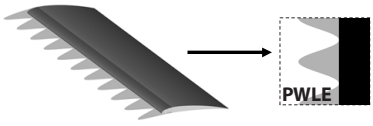

Analysis

Rod wake – airfoil [4] **interaction simulation**

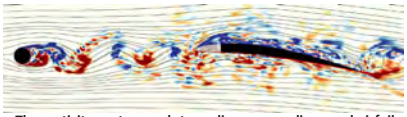

The vorticity contour and streamline surrounding a rod-airfoil

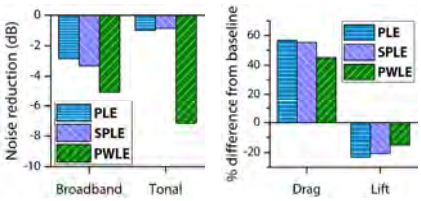

Noise reduction and aerodynamic performance penalty

3. WHAT WE FOUND

- The application of porous material to reduce wake-interaction noise is promising with *up to 7 dB* noise reduction for a reference case.
- The *serration shape* is relevant for improving both aerodynamic and acoustic performance of the porous leading-edge.
- Porous treatments might also be applicable for addressing noisy airframe components, such as landing-gear struts or high-lift devices.

REFERENCES

1. Teruna, C., Casalino, D., Ragni, D., & Avallone, F. "Numerical Analysis of a Linear Cascade Model for Rotor-Stator Interaction Aeroacoustics". 2018 AIAA/CEAS Aeroacoustics Conference (p. 4189), 2018.
2. Casalino, D., Avallone, F., Gonzalez-Martino, I., & Ragni, D. "Aeroacoustic study of a wavy stator leading edge in a realistic fan/OGV stage". *Journal of Sound and Vibration*, 442, 138-154, 2019.
3. Carpio, A. R., Martínez, R. M., Avallone, F., Ragni, D., Snellen, M., & van der Zwaag, S. "Experimental characterization of the turbulent boundary layer over a porous trailing edge for noise abatement". *Journal of Sound and Vibration*, 443, 537-558, 2019.
4. Jacob, M. C., Boudet, J., Casalino, D., & Michard, M. "A rod-airfoil experiment as a benchmark for broadband noise modeling. Theoretical and Computational Fluid Dynamics", 19(3), 171-196, 2005.

Smart Mitigation of flow-induced Acoustic Radiation and Transmission for reduced Aircraft, Surface traNSport, Workplaces and wind enERgy noise

This project has received funding from the European Union's Horizon 2020 research and innovation program under the Marie Skłodowska-Curie grant agreement No 722401.

H2020 MARIE SKŁODOWSKA-CURIE ACTIONS

AWEP

Wind turbine blade fault detection: An aeroacoustics approach

Yanan Zhang
Department: AWEP
Section: Wind Energy
Daily supervisor: Dr. Francesco Avallone
Promotor: Prof.dr. Simon Watson
Contact: Yanan.Zhang@tudelft.nl

1. Introduction

Wind turbine blade is vulnerable to be damaged due to its structure and operating environment. As existing researches reported, the repair time of the blade is even longer when the damage occurs than other parts of the wind turbine which influence the power output and economic benefits of the wind farm. However, there are some limitations using existing mechanical approaches (e.g. vibration-related approaches) and material approaches (e.g. stress and fatigue analysis) to directly detect the blade damage when the wind turbine is operating.

The wind turbine aeroacoustics noise is affected by the blade conditions, which provides a potential metric to detect the blade faults. In this research, a new approach based on the wind turbine aeroacoustics noise measurement is attempted to wind turbine blade fault detection and condition monitoring. The fault features are extracted from the measured data. The fault is then recognized by using the fault features we get. Further, the wind turbine blade damage development and health condition are monitored using the fault recognition knowledge.

2. Methodology

➢ Research objectives

- How to extract the features related to the faults from the acoustic signals we get from the microphone array;
- How to recognize the fault using the extracted features;
- How to monitoring the blade damage development and health condition using the knowledge of the fault recognition.

➢ Approach

- Using the non-stationary time-frequency analysis to extract features related to the faults from the microphone array signals;
- Using the intelligent classification algorithms to recognize the fault on the basis of the extracted features;
- Using the machine learning and data-driven related methods to monitor the blade damage development and health condition.

3. Experiment & test

➢ Aeroacoustics measurement for airfoils with given faults

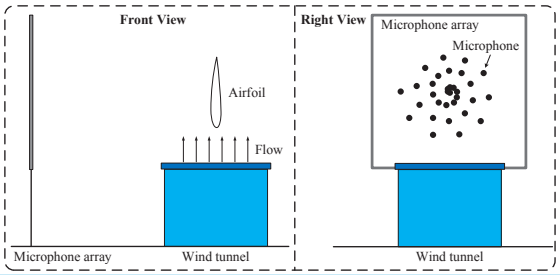

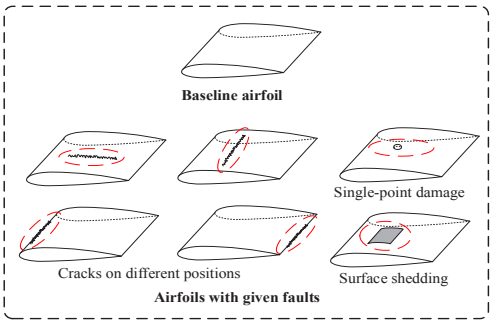

➢ Aeroacoustics measurement for small-scale wind turbine with faults on the blade

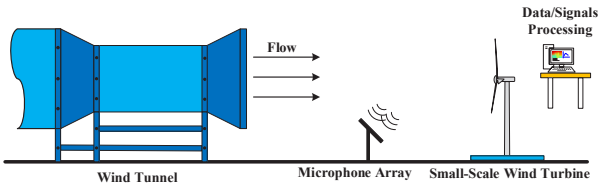

➢ Test in field

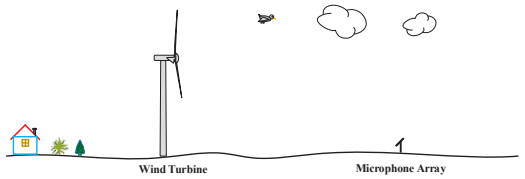

4. Future work

- To finish the airfoils experiment and compare the time-frequency differences between the baseline airfoil and the airfoils with given faults and then conclude the features set of the faults;
- To know the basic characteristics of the faults (e.g.: category, position, damage levels): on the one hand, to finish the small-scale wind turbine experiment and use the beamforming to find the damage positions, and on the other hand, to use the intelligent classification algorithms to find the different faults and determine the damage levels;
- To design the blade condition monitoring algorithms for the purpose of monitoring the damage development, and to employ the proposed approach to the field wind turbines, meanwhile to solve some practical issues e.g. robustness of the algorithms.

References:

[1] Yang, W., et al. (2017). "Structural health monitoring of composite wind turbine blades: challenges, issues and potential solutions." IET Renewable Power Generation 11(4): 411-416.
[2] Ramachandran, R. C., et al. (2014). "Wind turbine noise measurement using a compact microphone array with advanced deconvolution algorithms." Journal of Sound and Vibration 333(14): 3058-3080.
[3] White, E., et al. (2011). Leading-Edge Roughness Effects on 63 (3)-418 Airfoil Performance. In 49th AIAA Aerospace Sciences Meeting including the New Horizons Forum and Aerospace Exposition (p. 352).

3D Adjoint-Based Turbomachinery Shape Optimization Framework using a CAD-Based Blade Parametrizer.

Name. : Nitish Anand
Department : AWEP
Section : FPP
Daily Supervisor: Matteo Pini
Promotor. : Piero Colonna
E-Mail. : n.anand@tudelft.nl

Motivation

Automated 3D-turbomachinery blade design poses a lot of practical challenges, some of them being:

1) Solving complex fluid dynamics in the flow passage to obtain performance values (**J**),
2) Managing larger number of design variables (***α***), required to represent the blade shape,
3) Computationally expensive Optimization.

In this work, a **cost-effective** method to perform a **3D shape optimization** using **open-source** tools is presented.

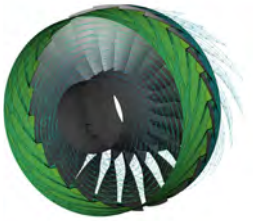

Design chain

$\boldsymbol{\alpha}$ → Parametrization → Grid deformation → Flow solver → $\mathbf{J}$

ParaBlade $\frac{\mathrm{d}\mathbf{X}_{\mathrm{surf}}}{\mathrm{d}\alpha}$

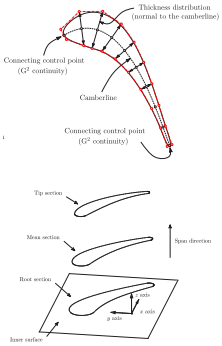

- Blade and sections are constructed using **B-Splines**.
- Provides a **rich design space** for the optimizer.
- Computes **CAD-sensitivity** required for gradient-based optimization.

Grid Deformation $\frac{\mathrm{d}\mathbf{X}}{\mathbf{X}_{\mathrm{surf}}}$

The volumetric grid is deformed is each design step by using a linear elasticity model. The surface deformation ($\mathbf{X}_{\mathbf{surf}}$) acts like a Dirichlet boundary condition for the volumetric grid ($\mathbf{X}$).

$$\mathbf{K}\Delta\mathbf{X}^k = \mathbf{T}\Delta\mathbf{X}^k_{\mathrm{surf}}$$

The sensitivity of the volumetric grid ($\mathbf{X}$) with surface grid ($\mathbf{X}_{\mathbf{surf}}$) is computed using **Algorithmic Differentiation**.

SU2 - Code $\frac{\mathrm{d}J}{\mathrm{d}\mathbf{X}}$

The performance of the turbine cascade is obtained by solving RANS equations in the discretized flow domain. The turbulence equations are closed using one equation Spalart-Allmaras model.

The **discrete-adjoint** solver computes the sensitivity of the objective function ($\mathbf{J}$) with respect to the volumetric grid ($\mathbf{X}$).

Gradient Assembly and Validation

$$\frac{\mathrm{d}J}{\mathrm{d}\alpha} = \frac{\mathrm{d}J}{\mathrm{d}\mathbf{X}}\frac{\mathrm{d}\mathbf{X}}{\mathrm{d}\mathbf{X}_{\mathrm{surf}}}\frac{\mathrm{d}\mathbf{X}_{\mathrm{surf}}}{\mathrm{d}\alpha}$$

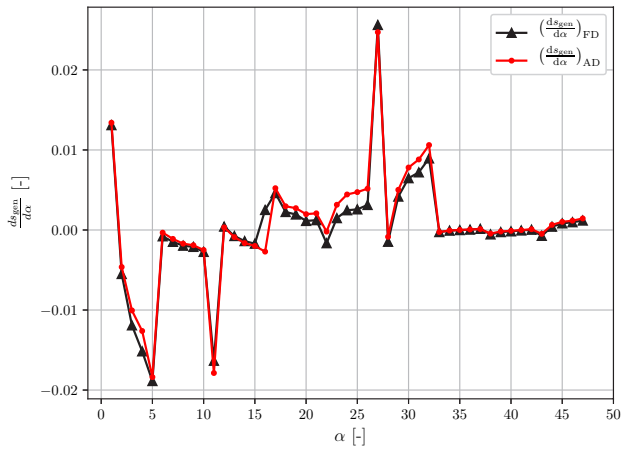

Results

Optimization based on discrete-adjoint(AD) is 24x faster than its finite difference(FD) equivalent.

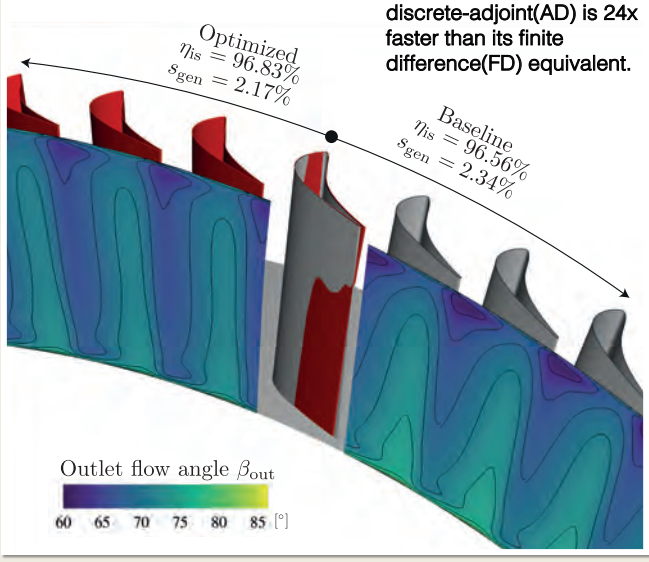

AWEP

NEDEFA: Novel Electrically Driven Environmental Control System for Aircraft

Federica Ascione
Department: AWEP
Section: FPP
Supervisor: Carlo De Servi
Promotor: Piero Colonna
F.ascione@tudelft.nl

Introduction

ACARE strategic roadmap research: reduction of **CO2 emissions** by 75%

Airline fuel efficiency increase: development of *more electric aircrafts*

Cabin environmental control system (ECS): air conditioning as the largest consumer of non-propulsive power

Vapor compression cycle (VCC) refrigeration system: alternative to the traditional **Air Cycle Machine (ACM)**

Resources

High speed centrifugal compressor Courtesy of Aeronamic

- High speed centrifugal **compressor** (AERONAMIC)
- Working **fluids** and **mixtures** models (3M – Asimptote)
- **System design** modeling MODELICA
- **Test rig** design and commissioning

Research Objectives

VCC system **design** and multi-point **optimization**

- Configuration
- Working fluid
- Target aircraft size and mission

Experimental set-up

- Test rig: VCC optimal configuration
- Experimental data: validation numerical model

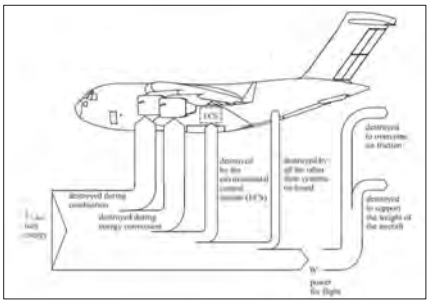

Contributions of exergy destruction on an aircraft (J. Vargas – A. Bejan)

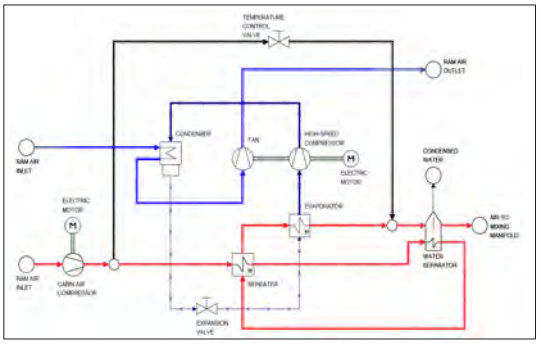

Vapor compression cycle ECS system model

ECS **global performance** evaluation metric

- thermodynamic efficiency
- weight and drag penalty

↓

Fuel Consumption

Conclusions

Proof of concept of the **VCC system as an alternative to the traditional ACM for ECS**, in terms of:

Lower fuel consumption
Higher thermodynamic efficiency

References

[1] Martinez, I. (2014). Environmental control system in aircraft.
[2] Vargas, J. V., & Bejan, A. (2001). Integrative thermodynamic optimization of the environmental control system of an aircraft. *International journal of heat and mass transfer*, *44*(20), 3907-3917.

AWEP

Spatiotemporal CARS measurements in the Recirculation Zone of Bluff-Body Stabilized Premixed Methane/Air Flames

Leonardo Castellanos G.
Faculty of Aerospace Engineering
FPP group
Dr.ir. G. A. Bohlin
Prof.dr.ir. P. (Piero) Colonna
L.J.Castellanosgonzales@tudelft.nl

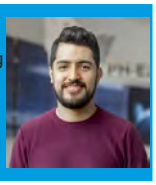

Research Framework

- Recirculation zones facilitate combustion within high speed reactive flows.
- The mixing occurring between the low-temperature reactants and the products can act as a flame stabilizing mechanism.
- Through the shaping of these recirculation zones much of the emissions (e.g. NOx, CO, etc.) can be reduced.

Fig. 1: Premixed methane/air flame at lean conditions, stabilized with circular bluff body .

Coherent anti Stokes Raman spectroscopy (CARS) is a laser diagnostics technique, which allows for the measurement of temperature in reactive flows with the highest levels of accuracy and precision.

- Most accurate technique:
  Inaccuracy ~2-3%
  Single shot precision ~4-5%
- Non-intrusive, in-situ probe.
- Signal is temperature dependent, with the population of excited rotational quantum states following the Boltzmann distribution.

Methodology

- The two-beams (fs-pump/Stokes and ps-probe) are produced from a single ultrafast amplifier system.

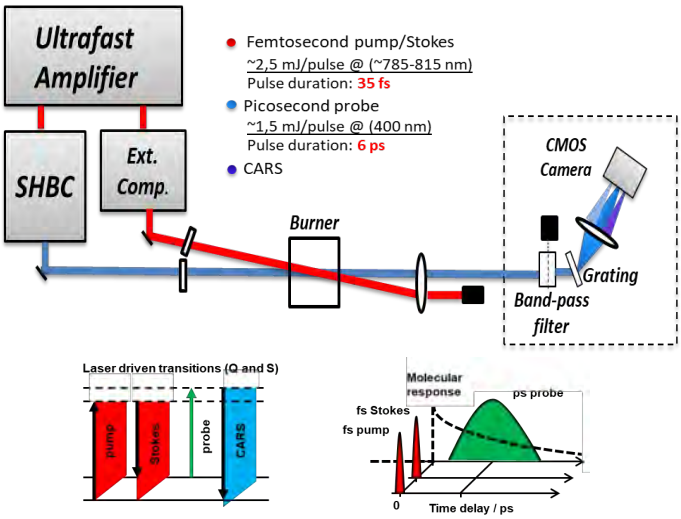

- A coherent imaging spectrometer has been developed which allows for the simultaneous spatial-, temporal-, and spectral-resolution of CARS signals (~1-3 mm, 1kHz, ~1200 cm-1).

Results

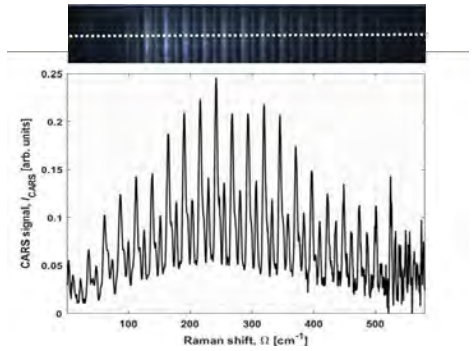

Fig. 3: (a) A snap-shot recording of a one-dimensional CARS signal displaying spatial vs. spectral information at the detector. (b) N_2 CARS spectrum recorded in the product gas of a premixed methane/air flame. The temperature is ~2070 K evaluated by a least-square library spectral fitting routine.

Acknowledgement: Financial support provided by the Netherlands Organization for Scientific Research (NWO), obtained through a Vidi grant in the Applied and Engineering Sciences domain (AES) (15690).

Experimental Investigation of Non-Ideal Compressible Fluid Dynamic Effects

N.B.Chandrasekaran
AWEP
Propulsion & Power
Dr. Bertrand Mercier
Prof. P. Colonna
n.b.chandrasekaran@tudelft.nl

Nonclassical Flow Dynamics

- Departure from ideal-gas behaviour near saturation conditions in the dense-vapour and liquid-vapour thermodynamic region
- Fundamental derivative (Γ) characterizes gas dynamics – negative Γ denotes inversion in fluid dynamic behavior [1]

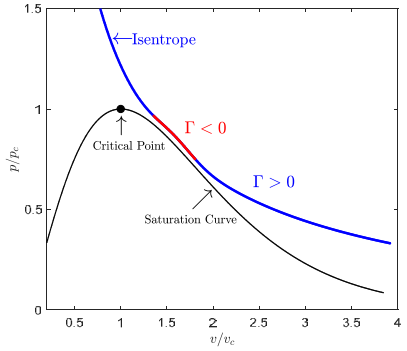

Fig.1: P-v plot showing non-classical thermodynamic region close to saturation

Experiments in Non-Ideal Flows

- Flexible Asymmetric Shock Tube (FAST) consists of Charge Tube (CT) with high pressure gas separated from Reservoir by a glass-disk diaphragm

Fig.3: Flexible Asymmetric Shock Tube

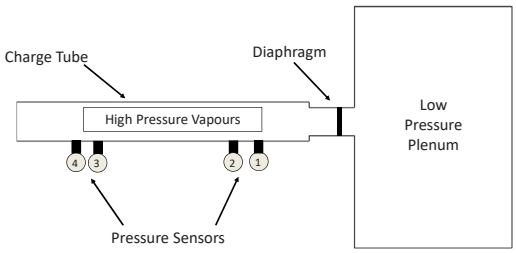

Fig. 4: Schematic of FAST Experiment [3]

- When the disk is broken, the dense gas expands into the LPP and a rarefaction shock is expected to propagate into the CT [2]
- Wave speed calculated by time-of-flight method using pressure sensor data → enables Γ estimation

$$\textit{Wave speed} = \frac{\textit{Distance between two sensor pairs}}{\textit{Time taken by wave to cover this distance}}$$

Γ and shockwaves [2]

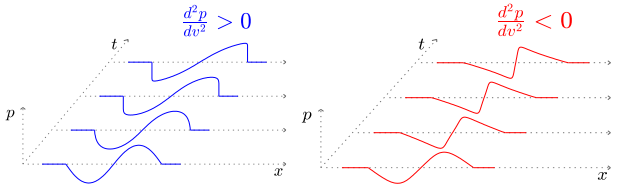

Fig.2: Wave Steepening in the ideal and non-ideal cases

Γ>0	$dP>0 \Rightarrow dw>0$ $dP<0 \Rightarrow dw<0$	Compression shock Rarefaction (isentropic) fan	Classical
Γ=0	$\forall dP \Rightarrow dw=0$	Stationary wave profile	
Γ<0	$dP>0 \Rightarrow dw<0$ $dP<0 \Rightarrow dw>0$	Compression (isentropic) fan Rarefaction shock	Nonclassical

Research Objectives

- Demonstrate the formation of first-of-its-kind rarefaction shockwave in dense gas vapours of D6
- Perform measurements in the nonclassical thermodynamic region to improve fluid-dynamic models for better fluid characterization

Improving fluid models through experiments

- Speed of sound data can be used to extract density, specific heat capacity, etc. – connected through non-linear relations [3]
- Knowledge of thermodynamic properties across different *p*, *T* enables developing accurate equations of state (EoS)
- To measure precisely the speed of sound in D6 in the critical region, and to support experiments with the FAST – **Acoustic Resonator**

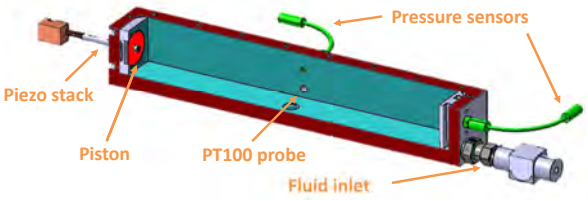

Fig. 5: Schematic of Acoustic Resonator

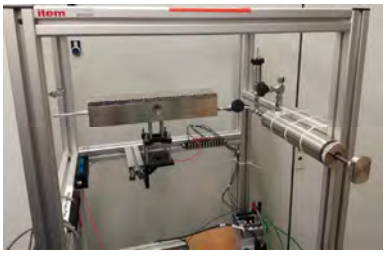

Fig. 6: Acoustic Resonator Setup

References

[1] N. Nannan, A. Guardone, and P. Colonna, *On the fundamental derivative of gas dynamics in the vapor–liquid critical region of single-component typical fluids*, Fluid Phase Equilibria **337**, 259 (2013).

[2] C. Zamfirescu, A. Guardone, and P. Colonna, *Admissibility region for rarefaction shock waves in dense gases*, Journal of Fluid Mechanics **599**, 363 (2008).

[3] Bijedic, Muhamed, and Sabina Begic. 2014. "Thermodynamic Properties of Vapors from Speed of Sound." Journal of Thermodynamics.

AWEP

Experimental Investigation of Bondary-Layer-Ingestion Aircraft

Biagio Della Corte
Department: AWEP
Section: FPP
Daily supervisor: Arvind Rao
Promotor: Leo Veldhuis
B.DellaCorte@tudelft.nl

Boundary Layer Ingestion

How it works:
- Engine operates on low-energy flow (boundary layer).
- Boundary layer is accelerated and “re-energised”.
- Viscous dissipation in the wake is reduced.

Pros:
- Potential aero-propulsive benefit.
- Broader design space.

Cons:
- Detrimental aerodynamic interaction (drag increases)
- Fan operates in non-uniform inflow conditions (performance penalty, vibrations and noise)

Experiment

Goal:
- What is the mechanical power balance across the propulsor?

Constrains:
- Isolate the major interaction effect (fuselage boundary layer) from other distortions (wings, tail)

Setup:
- Axisymmetric fuselage
- Symmetric wings
- Representative fan design

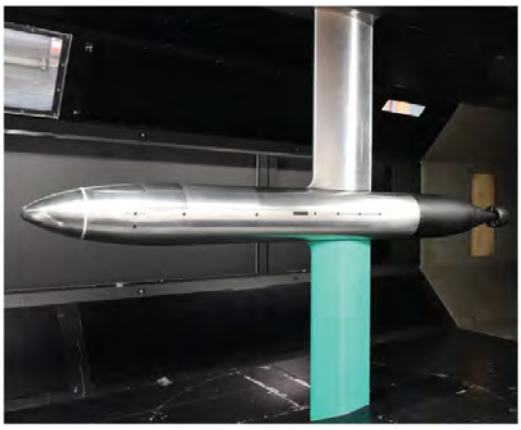

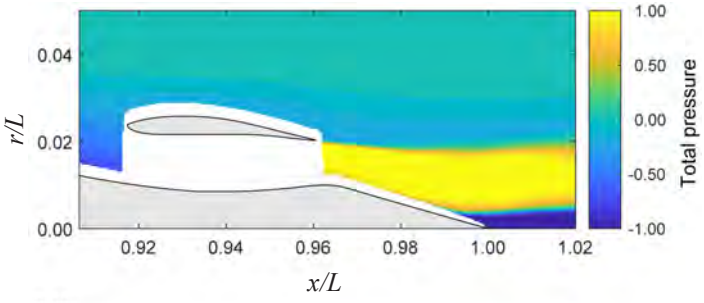

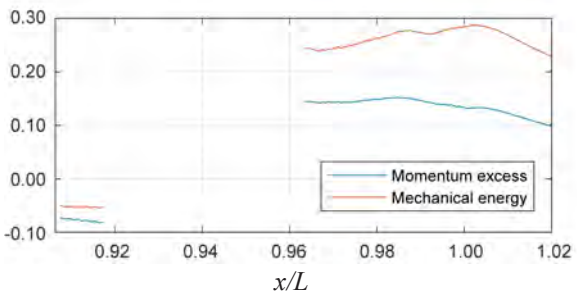

Results

- Velocity data obtained with PIV.
- Pressure inferred from the PIV field.

→ Total pressure distribution in the flow.

- Velocity + total pressure field

→ Momentum flux
→ Drag—thrust equilibrium

→ Mechanical energy flux
→ Energy deficit of the boundary layer
→ Power spent by the engine
→ Residual wake energy

This work was conducted within the CENTRELINE project, which has received funding from the European Union’s Horizon 2020 research and innovation programme under Grant Agreement No. 723242.

AWEP

Next-Gen Aircraft Environmental Control System based on the Inverse Organic Rankine Cycle

Andrea Giuffré*, Matteo Pini and Piero Colonna.
AWEP, Flight Performance & Propulsion

*a.giuffre@tudelft.nl

Motivation

Direct emissions from aviation account for 3% of the EU's total greenhouse gas emissions. The efficiency of aero-engines is approaching a plateau, whereas the traditional ECS architecture is sub-optimal from an energetic perspective.

1) The ECS accounts for 75% of secondary power consumption.
2) A bleedless engine architecture can reduce the total fuel consumption of about 1%, 3%, 4.5% for a regional, midrange and long range aircraft, respectively [1].
3) The inverse ORC concept can improve the ECS thermodynamic efficiency up to 800% with respect to the traditional Air Cycle Machine (ACM) architecture.

High-Speed Compressor

Key challenges:
1) Optimization of fluid-dynamic performance with 10% rotor tip gap.
2) Axial thrust minimization to allow the use of gas bearings.
3) Structural optimization to ensure safe operation up to 200 krpm.
4) Influence of working fluid non-ideality (NICFD).

High-speed centrifugal compressor: assembly (left), size comparison with equivalent scroll compressor (right). Courtesy of Aeronamic.

Preliminary Results

ACM optimization for performance comparison with iORC.

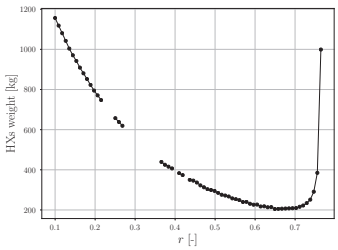

Optimal heat load distribution for ACM weight minimization:

$$r = \frac{T_{bleed} - T_{HX1,out}}{T_{bleed} - T_{cab}}$$

Research Roadmap

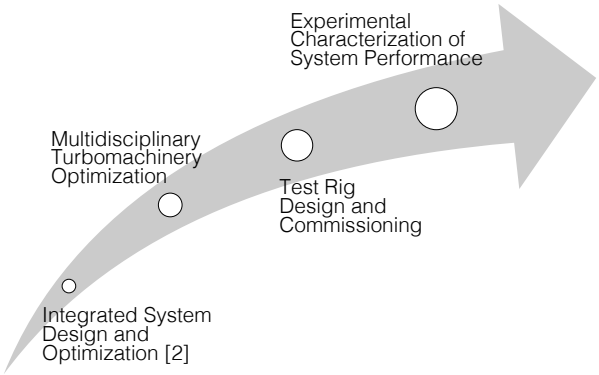

Inverse Organic Rankine Cycle

Key challenges:
1) Selection of the optimal working fluid/mixture.
2) Optimization of system architecture: number of pressure levels, compression intercooling, gas removal.
3) System integration at aircraft level.

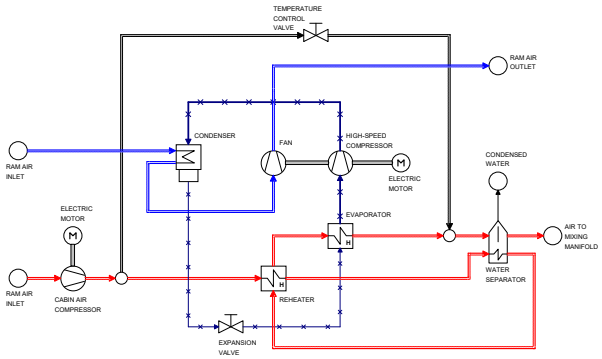

Layout of an electrically driven ECS based on the inverse ORC.

References

[1] Chakraborty, I., and Mavris, D. N., 2016. "Assessing Impact of Epistemic and Technological Uncertainty on Aircraft Subsystem Architectures". Proceedings of the 16th AIAA Aviation Technology, Integration, and Operations Conference.

[2] Vargas, J. V. C., and Bejan, A., 2001. "Integrative Thermodynamic Optimization of the Environmental Control System of an Aircraft". International Journal of Heat and Mass Transfer.

AWEP

Improved thermometry precision in fs/ps RCARS with simultaneous referencing of the excitation efficiency

Francesco Mazza
AWEP
Propulsion and Power
Dr.ir. G. A. Bohlin
Prof.dr.ir. P. Colonna
f.mazza@tudelft.nl

Research framework:

- Coherent anti-Stokes Raman spectroscopy (CARS) is a laser diagnostic technique for thermometry and species detection in combustion [I, II].
- In pure-rotational CARS (RCARS), three photons undergo mixing with the internal rotational energy levels of the probed molecules, yielding a forth photon with coherent "laser-like" properties (Fig. 1). CARS is a non-linear optical process, which is described in terms of the third-order susceptibility [I]:

$$\chi^{(3)}_{\mathrm{CARS}} = \chi_{\mathrm{Resonant}} + \chi_{\mathrm{NR}}$$

  - χ_{Resonant} is the resonant signal, which carries the information about the temperature and species in the sample.
  - χ_{NR} is the non-resonant signal, due to the instantaneous response of the molecular electronic configuration.
- The non-resonant signal can be employed to map the efficiency of the two-photon excitation, in the frequency domain.

Research Aim:

- Simultaneous recording of both the resonant and non-resonant components of the CARS signal, to further push the precision of the thermometry (species detection) below ~1% (~5%). The current scheme allows for shot-to-shot referencing of the two-photon excitation efficiency.

Research Methodology:

- Simultaneous detection of the two signals through polarisation control: the resonant and non-resonant signals have different polarisation orientation (Fig. 2) [III]:

$$\tan\beta = -\frac{\sin\phi}{2\cos\phi} \quad \text{Resonant signal}$$

$$\tan\delta = \frac{\sin\phi}{3\cos\phi} \quad \text{Non-resonant signal}$$

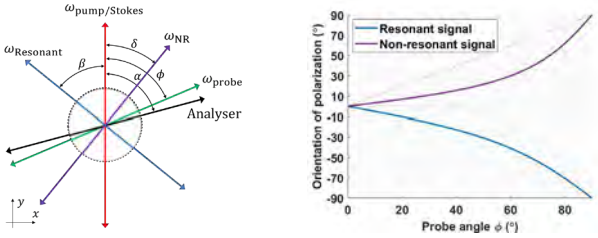

Fig. 2: Relative polarisation orientation for the resonant and non-resonant CARS signals, as a function of the probe polarisation orientation with respect to the pump/Stokes fields.

- A polarization splitter splits the CARS beam into the resonant and non resonant components, which are then collected in two detection channels (Fig. 3-4).
- Half-wave plates provide control over the polarisation orientation in the two channels.

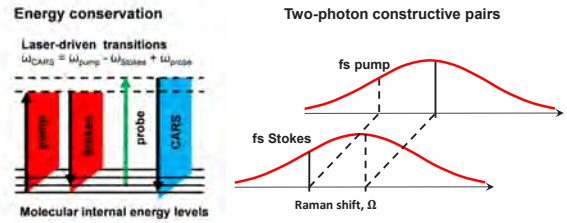

Fig. 1: Schematics of the two-photon excitation process, employed in the preparation of the rotational coherence in the sample (dual broadband CARS).

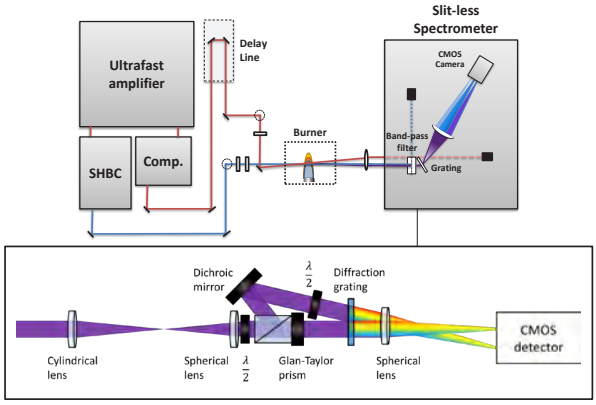

Fig. 3: Schematics of the ultrafast CARS diagnostics system and detail of the detection subsystem, w/ polarisation optics for the dual channel signal acquisition.

Results:

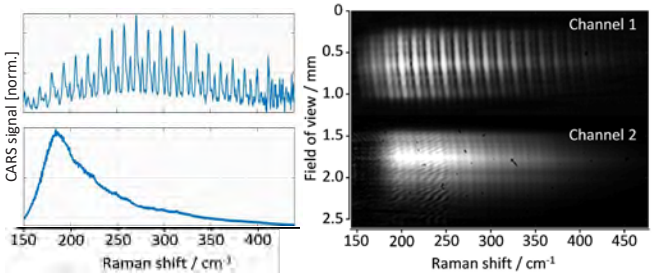

Fig. 4: Resonant and non-resonant CARS signal acquired simultaneously in the CMOS detector in the first and second channel, respectively. The CARS signal was generated and recorded in a methane/air flame in stoichiometric conditions.

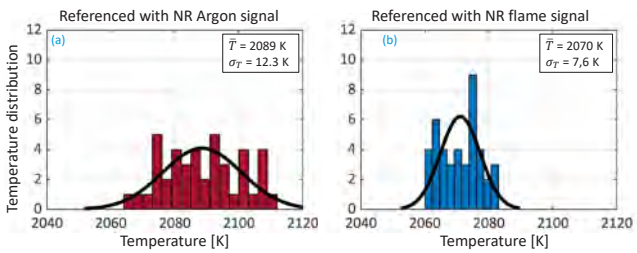

Fig. 5: Probability density functions (pdf) of 100 single-shot evaluated temperatures, acquired in the product gases of a premixed methane/air flame (Φ=1). The two pdfs are computed from resonant spectra normalized with the non-resonant signal acquired in Argon (a) and in the second channel of the flame spectra (b).

References:

I. A. C. Eckbreth, "*Laser Diagnostics for Combustion Temperature and Species*", 2nd ed., (Gordon and Breach: Amsterdam, 1996).
II. S. P. Kearney, "Hybrid fs/ps rotational CARS temperature and oxygen measurement in the product gases of canonical flames", Combustion and Flames **162**, 1748-1758 (2015).
III. F. Vestin, M. Afzelius, P.E. Bengtsson, "Development of rotational CARS for combustion diagnostics using a polarization approach", Proceedings of the Combustion Institute **31** (2007) 833–840.

Acknowledgement: Funding provided by NWO (AES) – Netherlands Organization for Scientific Research (Vidi grant)

Turbulence Characteristics of Jet in Co-flow

Rishikesh Sampat
Department: AWEP
Section: Propulsion and Power
Daily supervisor: Dr. ir. F. F. J. Schrijer
Promotor: Dr. A. G. Rao
Contact: R.P.Sampat@tudelft.nl

Introduction:

- Flameless Combustion is a concept that has potential for very low NOx emissions. Hence our interest to integrate it in aero-engines. Typically, the flame is invisible to the naked eye.
- The jet in coflow(Fig 1) is a commonly used configuration to achieve the mixing of hot products of combustion with fresh reactants to achieve this regime of combustion. We study the flow characteristics of this configuration.

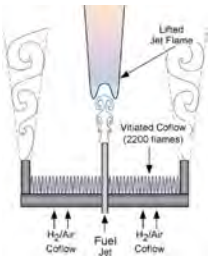

Fig1: Jet in hot co-flow to create Flameless Combustion conditions

Experiment:

- Jet created with pipe supplied with pressurized air. The coflow is created using a wind tunnel. Both streams are seeded.
- Planar PIV measurement.
- Statistics obtained over 5000 images.
- Cases presented:C2.5(Free jet), C12.65(Low co-flow), C18(High co-flow)

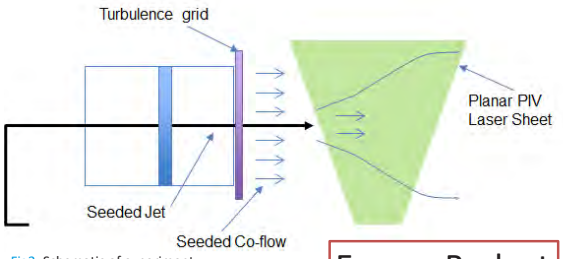

Fig2: Schematic of experiment

Results:

- Jet centreline velocity in Fig 3 shows a faster decay for cases with higher co-flow.
- Jet in co-flow shows earlier "Mixing transition", Fig 4, which is identified by an increase of Taylor scale Reynolds number beyond 100[1].

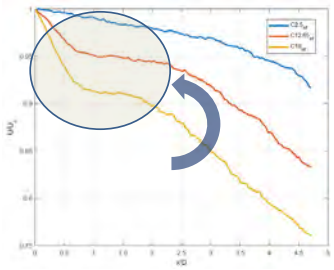

Fig3: Jet Centerline Velocity

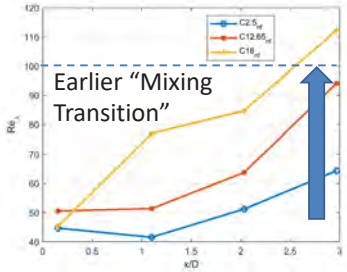

Fig4: Taylor Scale Reynolds number

- Budget of mean kinetic energy(MKE) and turbulent kinetic energy(TKE)[2].

- **MKE:** $\frac{\partial \bar{E}}{\partial t} + U_j \frac{\partial \bar{E}}{\partial x_j} = \frac{\partial}{\partial x_j}\left(-\frac{U_j P}{\rho_0} + 2\vartheta U_i \overline{S_{ij}} - \overline{u_i u_j} U_i\right) - 2\vartheta \overline{S_{ij} S_{ij}} + \overline{u_i u_j} \frac{\partial U_i}{\partial x_j}$

Time rate of change following mean flow | Pressure Transport | Viscous Transport | Turbulent Transport | Viscous Dissipation | Loss to turbulence/ turbulence production

- **TKE:** $\frac{\partial \bar{e}}{\partial t} + U_j \frac{\partial \bar{e}}{\partial x_j} = \frac{\partial}{\partial x_j}\left(-\frac{\overline{pu_j}}{\rho_0} + 2\vartheta u_i \overline{S'_{ij}} - \frac{1}{2}\overline{u_i u_i u_j}\right) - 2\vartheta \overline{S'_{ij} S'_{ij}} - \overline{u_i u_j} \frac{\partial U_i}{\partial x_j}$

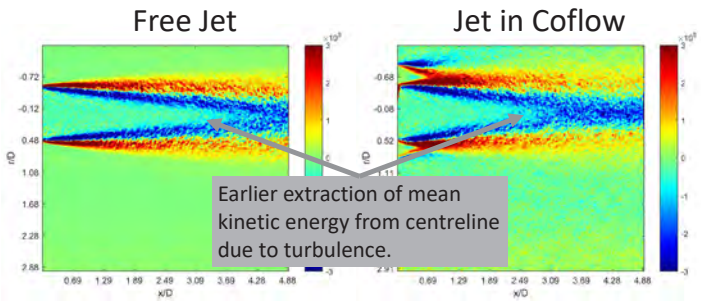

Fig5: Mean Kinetic Energy Turbulent transport.

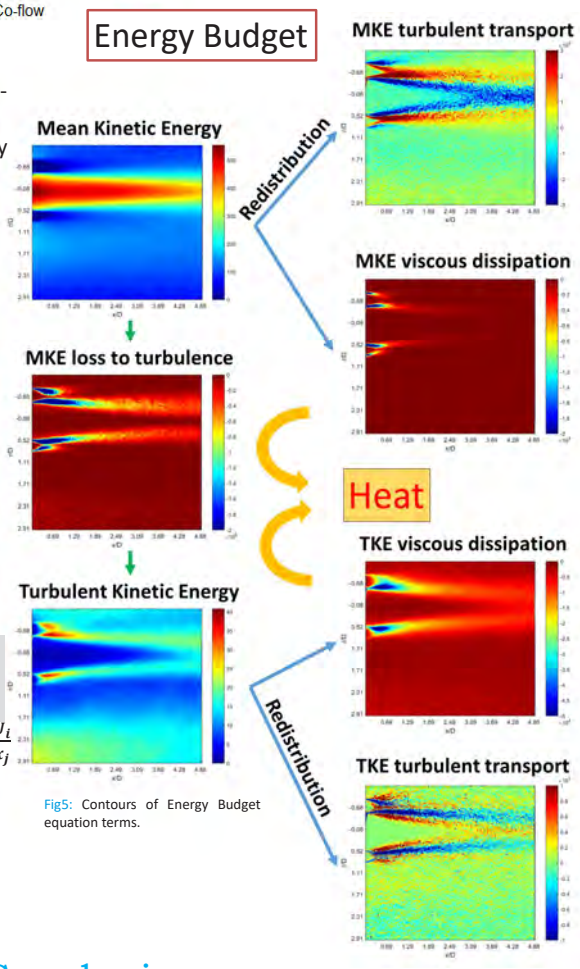

Fig5: Contours of Energy Budget equation terms.

Conclusion:

- The co-flow leads to earlier mixing transition and faster decay of velocity of the jet compared to a free jet.
- The recirculation zone formed around the nozzle lip by the co-flow contributes significantly to energy exchange.
- As shown from the budget, the turbulent transport plays a significant role in mean centreline velocity decay in jet in co-flow.

References:

1] Paul E. Dimotakis. The mixing transition in turbulent flows. Journal of Fluid Mechanics, 409:69–98, 2000.
2] Rodrigo R. Taveira and Carlos B. da Silva. Kinetic energy budgets near the turbulent/non turbulent interface in jets. Physics of Fluids, 25(1), 2013.

AWEP

Boundary layer instability over a rotating slender cone under non-axial inflow[1]

Name: Sumit Tambe
Department: AWEP
Section: FPP
Supervisors: Arvind G Rao
Ferry Schrijer
Promoter: Leo Veldhuis
s.s.tambe@tudelft.nl

Centrifugal instability leads to the formation of spiral vortices over a rotating slender cone.

The vortex growth depends on local Reynolds number Re_l and rotational ratio S.

$$Re_l = \frac{lu_e}{\nu} \qquad S = \frac{r\omega}{u_e} \qquad \kappa = \frac{2U_\infty^2}{\omega\nu}$$

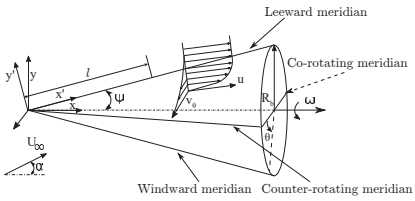

During their amplification, spiral vortices bring outer high momentum (slightly colder) flow near the wall. This increases the amplitude of surface temperature fluctuations.

Under non-axial inflow, spiral vortices are still formed, but their appearance and growth are delayed.

The distorted scales under non-axial inflow suppress the formation of spiral vortices.

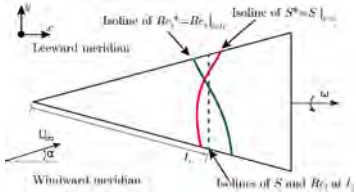

Senstitivity of spiral vortex wavenumber n to the distorted scales is quantified here as: $\frac{1}{\kappa}\cdot\frac{dn}{dS}$.

At higher local Reynolds number and rotational ratio, the decreased sensitivity allows the formation of spiral vortices, despite the distorted scales.

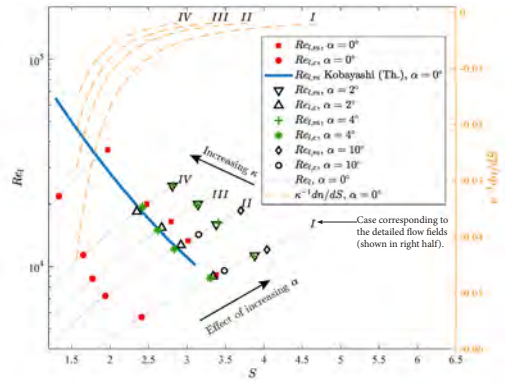

Axial inflow, $\alpha = 0°$, case I

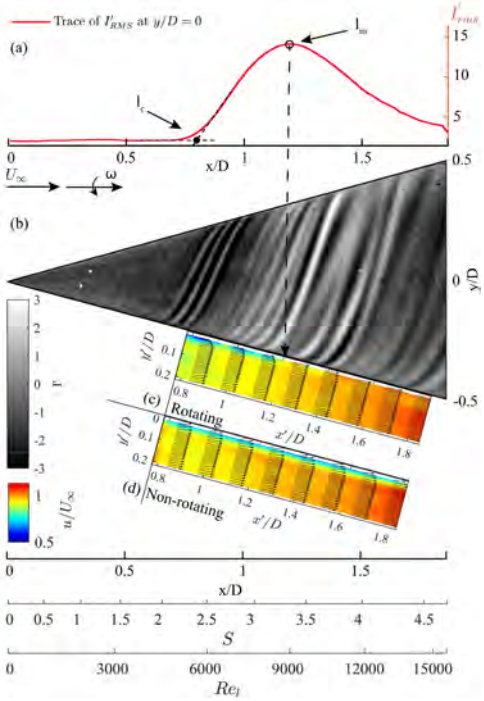

RMS of surface temperature fluctuations (over 2000 images)

Instantaneous temperature footprints of spiral vortices (POD reconstruction following a method [2])

Mean velocity fields (PIV)

Non-axial inflow, $\alpha = 4°$,case I

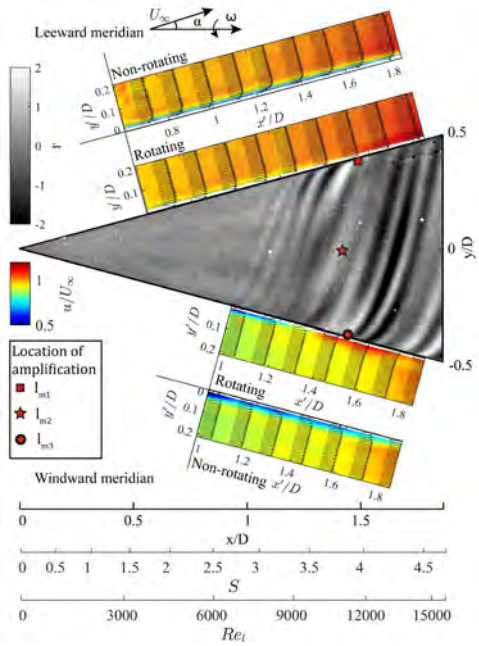

Mean velocity fields (PIV)

Instantaneous temperature footprints of spiral vortices (POD reconstruction following a method [2])

Mean velocity fields (PIV)

References:
1. Sumit Tambe, Ferry Schrijer, Arvind G Rao, Leo Veldhuis, Boundary layer instability over a rotating slender cone under non-axial inflow, *Journal of Fluid Mechanics* (manuscript submitted).
2. Tambe, S., Schrijer, F., Rao, A.G. et al. An experimental method to investigate coherent spiral vortices in the boundary layer over rotating bodies of revolution. *Experiments in Fluids* 60, 115 (2019). https://doi.org/10.1007/s00348-019-2756-8
3. Kobayashi, R., Kohama, Y. & Kurosawa, M. 1983 Boundary-layer transition on a rotating cone in axial flow. *Journal of Fluid Mechanics* 127, 353-364.

Non Ideal Compressible Fluid Dynamics: 1D Framework and Design Guidelines for Non-conventional Turbomachinery

Francesco Tosto
AWEP
FPP – Propulsion & Power
Supervisor: dr. Matteo Pini
Promotor: prof. Piero Colonna
f.tosto@tudelft.nl

Background and Motivation

Propulsion and power applications like Organic Rankine Cycle (ORC) and supercritical CO_2 systems, for example, operate with **non ideal fluids** in proximity of the critical point.
Real gas effects can thus have an impact on the performance of the components of these systems.

Fig. 1: Distribution of Γ on the p-V plane for siloxane D6

The complex internal fluid dynamics of these flows is governed by the **fundamental derivative of gas dynamics[1] (Γ)**:

$$\Gamma = 1 + \frac{\rho}{c}\left(\frac{\partial c}{\partial \rho}\right)_s$$

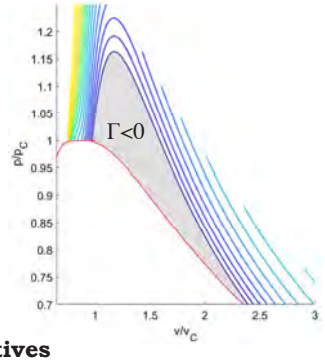

Project Scope and Objectives

- Development of a **quasi 1D theoretical framework** for Non Ideal Compressible Fluid Dynamics (**NICFD**)
- Investigate and quantify the NICFD effects on losses in turbomachinery using **physics-based loss models**
- Provide **design guidelines** for turbomachinery operating with non conventional fluids using similitude theory

Quasi 1D framework

Creation of a **quasi 1D theoretical framework** for NICFD applications by exploiting the definition of **influence coefficients** according to Shapiro[2]

Aim: to relate changes in flow variables to:
- ✓shaft work
- ✓cross-section area
- ✓heat addition
- ✓wall friction

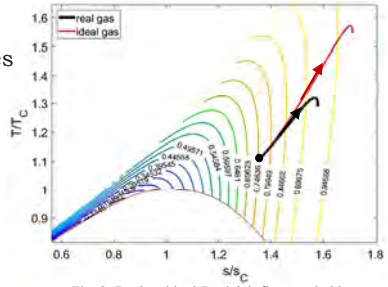

Fig. 2: Real vs ideal Rayleigh flow at choking conditions on a Ts diagram for CO_2. Iso-Z contours are also plotted (Z=pv/RT)

Example: Rayleigh flow

$$\frac{dM}{M} = \frac{\gamma+1}{2(1-M^2)}\frac{dq}{c_pT} \qquad \frac{dM}{M} = \frac{\Gamma(\beta_pT)}{1-M^2}\frac{\cancel{dq}}{c_pT}$$

Ideal gas **NICFD**

Physics-based loss model

Gas non-ideality is measured by the **gradient of compressibility factor** Z and **fundamental derivative** Γ along the transformation.

Empirical-based loss models are derived and tuned for standard turbomachinery.
A general **physical-based** loss model[3] is required to evaluate the **impact of NICFD on entropy generation**.

Fig. 3: Z and Γ variation for D6 in dense gas region

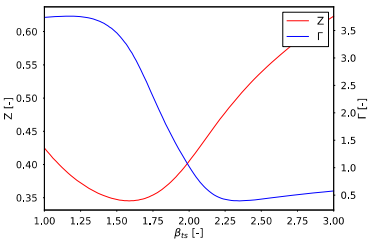

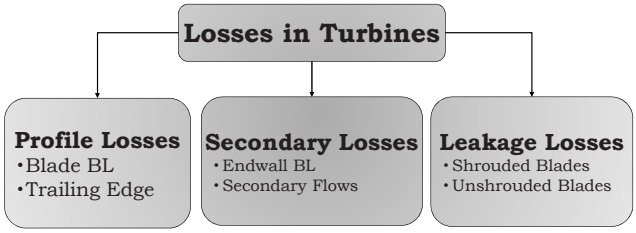

Design guidelines

Standard **similitude theory** can be **extended** to describe a turbomachine with generic architecture operating with real gas.

$$\eta_{tt} = f\left(K_{is}, \phi, r^*, VR, \frac{R_0}{R_2}, \frac{R_3}{R_2}, Re, P_r, T_r, \boldsymbol{\sigma}, \boldsymbol{\pi}\right)$$

A design code based on the generalized similitude theory is implemented.
The results are used to draw **design guidelines** for **non conventional turbomachines**.
Validation will be performed with **CFD**.

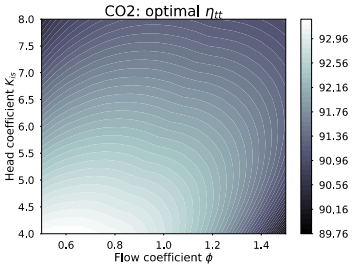

Bibliography

1.Thompson, P.A., *A Fundamental Derivative in Gasdynamics*, Physics of Fluids- PHYS FLUIDS. 14. 1843-1849, 1971.
2.Shapiro A. H., *The Dynamics and Thermodynamics of Compressible Fluid Flow*, Volume 1, The Ronald Press Company, New York, 1953.
3.Denton J.D., *Loss Mechanisms in Turbomachines*, Journal of Turbomachinery; (United States). 115:4. 10.1115/93-GT-435, 1993.

AWEP

PHOTO GALLERY

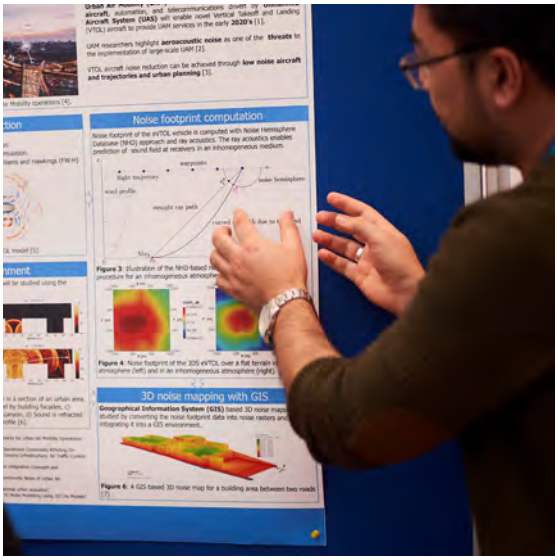

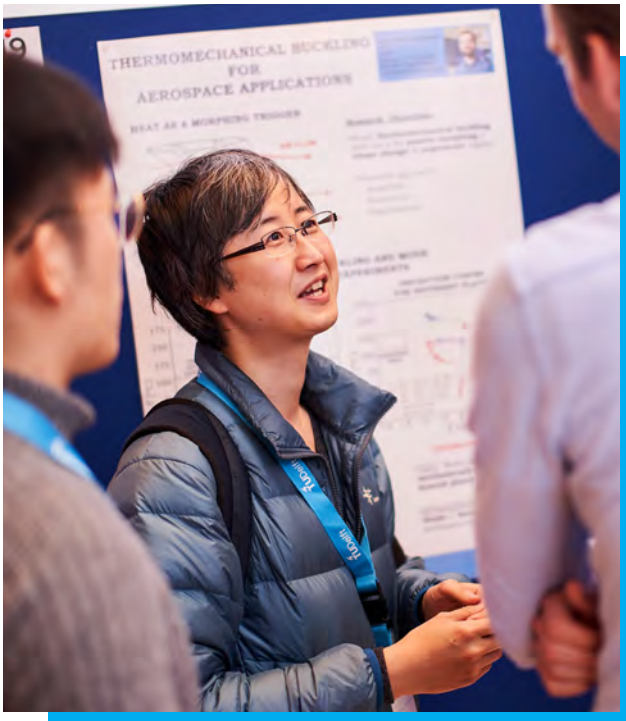
THERMOMECHANICAL BUCKLING
FOR
AEROSPACE APPLICATIONS






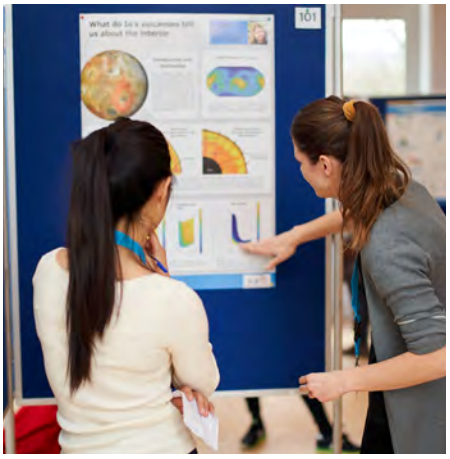
101


Damage diagnostics utilizing sensor data fusion




PhD Academia Event 2020
DATE
LOCATION
PROGRAMME
TUDelft


49